Heinrich Heine
Universität Düsseldorf

JÜLICH
Forschungszentrum

Polarized Proton Beams From Laser-induced Plasmas

Inaugural Dissertation

for the attainment of the title of doctor
in the Faculty of Mathematics and Natural Sciences
at the Heinrich Heine University Düsseldorf

presented by

Anna Hützen, M. Sc.

from Neuss

Düsseldorf, January 2021

JuSPARC

from the Institute for Laser and Plasma Physics
at the Heinrich Heine University Düsseldorf

and the Peter Grünberg Institute (PGI-6, Electronic Properties)
at Forschungszentrum Jülich

Published by permission of the
Faculty of Mathematics and Natural Sciences at
Heinrich Heine University Düsseldorf

Supervisor: Prof. Dr. rer. nat. Markus Büscher
Co-supervisor: Prof. Dr. rer. nat. Axel Görlitz

Date of the oral examination: July 16, 2021

Declaration of Authorship

I declare under oath that I have produced my inaugural dissertation

"Polarized Proton Beams from Laser-induced Plasmas"

independently and without any undue assistance by third parties under consideration of the "Principles for the Safeguarding of Good Scientific Practice at Heinrich Heine University Düsseldorf".

Ich versichere an Eides Statt, dass die Dissertation

„Polarized Proton Beams from Laser-induced Plasmas"

von mir selbständig und ohne unzulässige fremde Hilfe unter Beachtung der „Grundsätze zur Sicherung guter wissenschaftlicher Praxis an der Heinrich-Heine-Universität Düsseldorf" erstellt worden ist.

Düsseldorf, January 28, 2021

Place, Date

Anna Hützen

Remember to look up at the stars and not down to your feet. Try to make sense of what you see and wonder about what makes the universe exist. Be curious.

— Stephen Hawking

Kurzfassung

Im Rahmen dieser Arbeit wurde ein Konzept zur experimentellen Realisierung der lasergetriebenen Beschleunigung spinpolarisierter Protonen erarbeitet. Dieses umfasst neben umfangreichen 3D Particle-In-Cell (PIC)-Simulationen einschließlich Spindynamik auch den Aufbau und die Inbetriebnahme eines polarisierten Targets.

Zur erstmaligen numerischen Vorhersage des Grades der Strahlpolarisation eines lasergetriebenen Plasmabeschleunigers wurden 3D PIC-Simulationen unter Berücksichtigung von Spineffekten auf dem Jülicher Supercomputer JURECA durchgeführt. Dazu wurde die Thomas-Bargmann-Michel-Telegdi (T-BMT)-Gleichung, die die Spinpräzession in elektromagnetischen Feldern beschreibt, in den Virtual Laser Plasma Lab (VLPL)-Code implementiert. Analytische Abschätzungen zeigen, dass der Sokolov-Ternov-Effekt und der Stern-Gerlach (SG)-Effekt einen vernachlässigbaren Einfluss auf die Spindynamik bei der laserinduzierten Protonenbeschleunigung haben.

Die Simulationsarbeiten beinhalten mehrere Studien, anhand derer untersucht wurde, welche Laser- und Targetkonfigurationen, sowie welche Beschleunigungsmechanismen zu Energien im MeV-Bereich bei möglichst hoher Strahlpolarisation führen. Ein wesentliches Ergebnis dieser Simulationen ist, dass, unter experimentnahen Voraussetzungen im Intensitätsregime eines Multi-PW-Lasers, eine Energie von etwa 100 MeV durch eine zweistufige Beschleunigung in Gas bei einem Polarisationsgrad von bis zu $\sim 80\,\%$ erreicht werden kann.

Insbesondere zeigen die Simulationen, dass die Protonenspins bereits vor dem Beschleunigungsprozess ausgerichtet sein müssen, um polarisierte Protonenstrahlen zu erzeugen. Dies erfordert ein vorpolarisiertes Gastarget, das in einem für die Laser-Plasma-Beschleunigung geeigneten Aufbau experimentell realisiert wurde.

In Anlehnung an die Arbeiten der Gruppe von T. P. Rakitzis von der Universität Kreta wurde ein Gastarget, basierend auf der dynamischen Polarisation von Halogenwasserstoffen, hier HCl- und HBr-Gas, von Grund auf neu konzipiert und in Betrieb genommen. Unter Verwendung einer nicht-magnetischen Gasdüse mit einem Hochgeschwindigkeits-Piezoventil wird das Gas in eine Interaktionskammer injiziert, wobei eine Gasdichte von etwa $10^{19}\,\mathrm{cm}^{-3}$ erzielt wird. Durch die Wechselwirkung der Fundamentalwellenlänge des *Ju*SPARC_Mira Nd:YAG-Lasersystems und seiner zirkular polarisierten fünften Harmonischen mit dem Gas werden spinpolarisierte Wasserstoffatome mittels Photodissoziation erzeugt. Infolge von Hyperfeinstruktur-Oszillationen wird die Polarisation zwischen den Elektronen und Protonen binnen 350 ps übertragen. Erste Messungen zu ihrer Kernpolarisation wurden mit einem Lamb-Shift Polarimeter (LSP) durchgeführt. Machbarkeitsstudien zum erstmaligen Nachweis von laserbeschleunigten polarisierten Protonenstrahlen im 100 MeV-Bereich werden nun für den 10 PW Laser der Shanghai super-intense Ultrafast Laser Facility (SULF) vorbereitet.

Basierend auf den gewonnenen Erkenntnissen mit Protonen wurde abschließend ein Konzept zur Erzeugung von polarisierten Elektronenstrahlen mittels Plasma-Wakefield-Beschleunigung ausgearbeitet, mit dem langfristigen Ziel, einen polarisierten Multi-GeV Elektron-Positron-Collider zu entwickeln.

Abstract

Within the scope of this thesis, a scheme for the experimental realizability of spin-polarized laser-driven proton acceleration has been worked out, involving extensive 3D Particle-In-Cell (PIC) simulations incorporating spin dynamics as well as the setup and commissioning of a polarized target.

3D PIC simulations including spin effects have been performed on the Jülich supercomputer JURECA to numerically predict the degree of beam polarization from a laser-driven plasma accelerator for the first time. To do so, the Thomas-Bargmann-Michel-Telegdi (T-BMT) equation characterizing the spin precession in arbitrary electromagnetic fields has been implemented in the Virtual Laser Plasma Lab (VLPL) code. Analytical estimates show that the Sokolov-Ternov effect and the Stern-Gerlach (SG) effect have negligible influence on the spin dynamics in laser-induced proton acceleration.

The simulation work includes a set of several studies clarifying which laser and target configurations, as well as which acceleration mechanisms, result in acceleration energies in the MeV range at preferably high beam polarization. A crucial result of these simulations is that under near-experimental conditions in a multi-PW laser intensity regime, an energy of about 100 MeV can be achieved by a two-stage acceleration in gas, while maintaining the polarization at a degree of up to $\sim 80\,\%$.

Thus, to produce polarized proton beams, the proton spins must already be aligned before the acceleration process, as further simulations demonstrate. This requires a pre-polarized gas target to be experimentally implemented in a setup suitable for laser-plasma acceleration.

Following the studies published by the group of T. P. Rakitzis from University of Crete, a gas-jet target, based on the dynamic polarization of hydrogen halides, i.e., HCl or HBr gas, has been designed from scratch and commissioned. Applying a non-magnetic nozzle with a high-speed piezo valve, the gas is injected into an interaction chamber to create a gas density in the range of approximately $10^{19}\,\mathrm{cm}^{-3}$. The interaction of the fundamental wavelength of the *Ju*SPARC_Mira Nd:YAG laser system and its circularly polarized fifth harmonic with the gas generates spin-polarized hydrogen atoms in a photo-dissociation process. Due to hyperfine-structure oscillations the polarization is transferred between the electrons and protons within 350 ps. First measurements on their nuclear polarization have been carried out with a Lamb-Shift Polarimeter (LSP). Proof-of-principle demonstrations for the first-time detection of laser-accelerated polarized proton beams in the 100 MeV range are now being prepared for the 10 PW laser at Shanghai super-intense Ultrafast Laser Facility (SULF).

Based on the gained experience with protons, a concept for the generation of polarized electron beams via plasma wakefield acceleration has been developed, with the long-term goal to pave the way towards a polarized multi-GeV electron-positron collider.

Contents

List of Figures

List of Tables

List of Abbreviations

ABS Atomic Beam Source

ANKE Apparatus for Studies of Nucleon and Kaon Ejectiles

BA Booster Amplifier

BBO Beta Barium Borate

COSY COoler SYnchrotron

CPA Chirped Pulse Amplification

CPU Central Processing Unit

ELI-NP Extreme Light Infrastructure - Nuclear Physics

ES Electron Spectrometer

FCU Frequency Conversion Unit

FDTD Finite Difference Time Domain

PHELIX Petawatt High-Energy Laser for heavy Ion eXperiments

FPFE Finite Phase-Fluid Element

FZJ Forschungszentrum Jülich

HDF Hierarchical Data Format

HHUD Heinrich Heine University Düsseldorf

IKP Nuclear Physics Institute

IP Image Plate

JSC Jülich Supercomputing Centre

JURECA Jülich Research on Exascale Cluster Architectures

***Ju*SPARC** Jülich Short-pulsed PArticle and Radiation Center

JUWELS Jülich Wizard for European Leadership Science

KDP Potassium Dihydrogen Phosphate

LG Laguerre-Gaussian

LLNL Lawrence Livermore National Laboratory

LSP Lamb-Shift Polarimeter

LWFA Laser WakeField Accelerator

MA Multi-pass Amplifier

MPI Message Passing Interface

MVA Magnetic Vortex Acceleration

OAP Off-Axis Parabola

PA Power Amplifier

PWFA Plasma WakeField Accelerator

PGI Peter Grünberg Institute

PIC Particle-In-Cell

QED Quantum Electrodynamics

QCD Quantum Chromodynamics

RCF RadioChromic Film

RF Radio Frequency

SBS Backward-stimulated Brillouin Scattering

SG Stern-Gerlach

SIOM Shanghai Institute of Optics and Fine Mechanics

SLM Single Longitudinal Mode

SSH Secure Shell Protocol

SULF Shanghai super-intense Ultrafast Laser Facility

T-BMT Thomas-Bargmann-Michel-Telegdi

TNSA Target Normal Sheath Acceleration

TP Thompson Parabola

VLPL Virtual Laser Plasma Lab

1 Introduction and Motivation

Spin-polarized particle beams are of outstanding importance in nuclear and particle physics as they are commonly used for scattering experiments to explore the structure and interaction of matter or to test the standard model [1–3]. Especially, the composition of sub-atomic particles like protons is investigated to gain further knowledge of QCD as our standard theory of the strong interaction [4] or to probe the nuclear spin structure [5]. Beyond that, polarized particle beams are beneficial to get additional insights of nuclear reactions [6], to study symmetry violation and evaluate new asymmetries, to quantify quantum numbers of new particles [3, 7–9] or to investigate the dynamics of molecules [10, 11].

The technique for generating polarized beams depends largely on the type of particles and their energies. For stable particles, like electrons or protons, polarized sources with subsequent acceleration in a linear accelerator or a synchrotron can be employed. During the acceleration of polarized beams in conventional circular accelerators, depolarizing spin resonances have to be balanced by the use of complex correction techniques maintaining the beam polarization [12, 13].

In any case, the acceleration of charged particles still relies on conventional particle accelerators, which are normally very large in budget and scale. Following the argumentation of Schlenvoigt et al. in Ref. [14], the method of acceleration bases on the use of longitudinal electric fields oriented along the beam direction, induced via either capacitors or microwaves in RF cavities. Such accelerators, however, are limited by their surface damage thresholds: once the electric field in the cavities overruns about 50 MV/m, conduction band electrons from the material are field-ionized, resulting in a performance reduction of the accelerator. High particle energies can in fact only be achieved by the additional acceleration length, the reason for the often strikingly large dimensions of state-of-the-art accelerators. In contrast to conventional accelerators, laser-induced plasmas, created during the interaction of ultra-short, ultra-intense laser pulses with a suitable target, may lead to electric field strengths up to TV/m. As a consequence of the extremely high energy density of such ultra-short pulses, the particles to be accelerated interact directly with the strong electromagnetic fields of the laser and the energy coupling between the laser field and the plasma is very efficient. Thus, the particles obtain significant kinetic energies over sub-mm distances, by many orders of magnitude shorter than in conventional RF-driven accelerators. Therefore, the goal is to develop and bring into operation the next generation of highly compact, cost-effective accelerators that use plasma as the accelerating medium [14–16].

To date, laser-plasma based particle accelerators are capable of generating both, high-energetic electron and proton beams: in 2019 the production of electron beams with quasi mono-energetic peaks up to 7.8 GeV using a 20 cm long laser-heated capillary discharge waveguide was demonstrated with intense laser pulses of 0.85 PW peak power at the Lawrence Berkeley National Laboratory [17]. For protons, up to now, only acceleration energies approaching the 100 MeV range have been achieved [18–20]. While most of the experimental results were obtained in the Target Normal Sheath Acceleration (TNSA) regime (cf. Sec. 3.2.1), higher energies are expected to be produced by using innovative target technologies ranging from nm-scale solid density foils to near-critical density slabs, gas, and liquid jets as well as employing advanced regimes of laser-particle acceleration [21]. As an additional advantage, these laser-induced beams meet a number of extraordinary properties like ultra-short pulse duration in the order of the laser pulse [22–24], outstanding emittance values [25] and high peak currents [14].

Although concepts based on laser-driven wakefield acceleration have been strongly advanced in recent years, one largely unexplored aspect is how the particle spins are affected by the enormous electromagnetic fields associated with the plasma, and the principal mechanisms that may lead to the generation of highly polarized beams. There are several possible scenarios, for example: i) the spin of the accelerated beam particles can be aligned by the magnetic fields, ii) a spin alignment due to the asymmetric spin-flip amplitudes in the radiation reaction regime, or iii) the spins are too inert and, thus, a short acceleration has no impact on the spin alignment. If the latter applies, throughout the whole acceleration process the polarization would be conserved, but a pre-polarized target is required. Within the context of the *Ju*SPARC project at Forschungszentrum Jülich (FZJ), the production of laser-driven polarized particle beams is being pursued together with the development of advanced target technologies [26–32].

For the buildup of a nuclear polarization in the plasma, two effects are currently discussed: i) the polarization is produced by a spin-flip according to the Sokolov-Ternov effect, which is induced by the magnetic fields of the incident laser pulse (cf. Sec. 4.3.2). ii) The magnetic field gradients of the SG force may also yield the generation of polarization for two opposite beam trajectories (cf. Sec. 4.3.3) [33]. Besides these two phenomena, all particle spins precess around the laser or plasma magnetic fields, as specified by the T-BMT equation (cf. Sec. 4.3.1).

Within the scope of this work, polarized laser-induced proton acceleration is addressed since i) our group has already gained experience with polarized proton acceleration [34], ii) protons are potentially less depolarized during acceleration as compared to electrons due to their higher mass, and, iii) a suitable tool for proton polarimetry is at hand.

The goal of this PhD thesis is the elaboration of a concept as well as first experimental tests towards the experimental realization of a laser-plasma based accelerator for polarized proton beams. To do so, the following tasks have been set to deal with within this dissertation:

- Numerical studies of which laser and target parameters as well as which acceleration mechanisms yield higher energies in laser-induced proton acceleration.
- Clarification of the questions: how can polarized beams be generated? Which target technology is promising and how can it be implemented experimentally?
- Identification of the mechanisms that could lead to polarization and depolarization effects during laser-plasma based acceleration and classification of their relevance for the planned experiments on polarized proton acceleration.
- Implementation of the identified mechanism into a PIC code and tests of correct operation.
- 3D PIC simulations accurately predicting the experimental results to the planned experiment for the production and observation of a polarized laser-accelerated proton beam.
- Development of a novel experimental setup for a polarized target including all relevant components, commissioning of the whole setup as well as first tests and measurements on the degree of proton polarization using an adequate tool for polarimetry.
- Identification of a suitable laser system for the acceleration of the polarized proton beam.

After an introduction into the theoretical background relevant for this thesis, these tasks will be elaborated and suitable solutions will be presented in Secs. 5 ff.

2 Modern High-Intensity Lasers

Not least because of the 2018 Nobel Prize in Physics being awarded to Professors Donna Strickland and Gerard Mourou for the development of the technique of Chirped Pulse Amplification (CPA) [35], scientific questions concerning laser applications have received more public attention than ever before. In the framework of this thesis, laser-accelerated protons are investigated in terms of their acceleration mechanism and the gained energy. This chapter provides a short overview of the laser principle as well as the technological development of high-intensity lasers worldwide which is necessary to emphasize the importance of laser-induced particle acceleration as a decisive alternative to conventional accelerators. In this context, the Shanghai super-intense Ultrafast Laser Facility (SULF) will be presented, where one of the most powerful systems worldwide with 10 PW will soon go into user operation, so that our group can perform its experiments on polarized proton acceleration there.

2.1 The laser principle

Lasers are used as radiation sources mainly in science, medicine and technology. The term *laser* is an acronym for light amplification by stimulated emission of radiation. Nowadays, the expression laser also represents a technical device using the mentioned principle.

The elementary process for realizing a laser is the stimulated emission, which was first postulated by Albert Einstein in 1917. Together with absorption and spontaneous emission, it is one of the three fundamental interactions between quantum mechanical systems and photons. A photon is the light quantum carrying the smallest energy possible $E_{\mathrm{ph}} = h\nu$ with Planck's constant h and frequency ν. Regarding a two-level system, an incoming photon generates a resonant transition from excited state $|1\rangle$ with discrete energy E_1 into ground state $|0\rangle$ with lowest possible energy E_0, whereby emitting a second photon with energy E_{ph}. Because photons are bosons, both photons can be identical with respect to their frequency, phase, polarization and direction of propagation. Thus, increasing the number of photons leads to an amplification of light [36, 37].

Depending on the transition probabilities, the atom drops from the excited state $|1\rangle$ into the ground state $|0\rangle$ releasing the energy $\Delta E = h\nu = E_1 - E_0$ because of energy conservation in a process called spontaneous emission. In contrast to stimulated emission, spontaneous emission occurs randomly without any external influence and induces incoherent radiation. Thus, stimulated emission has to be the dominant process for a certain light amplification since absorption, spontaneous emission and stimulated emission occur simultaneously.

However, when the laser medium is in thermal equilibrium, the photon density in the exited state N_1 is smaller than in the ground state N_0 due to Boltzmann statistics and, thus, the photon number decreases exponentially with time. Only if $N_1 > N_0$, i.e., a so-called occupation inversion prevail, the number of photons can increase with time and the light can be amplified, as applies

$$N_1 = N_0 \exp\left(\frac{-(E_1 - E_0)}{k_{\mathrm{B}} T}\right) , \tag{2.1}$$

where k_{B} is the the Boltzmann constant and T is the temperature. Since in a pure two-level system only a direct excitation from E_0 to E_1 is possible, no population inversion can be achieved

by optical pumping. Therefore, a laser has to be operated in non-equilibrium ($T < 0$) to reach population inversion. This can be realized with multi-level systems, e.g., with a four-level system, in which most laser systems are operated today [38].

The first laser ever built was a ruby solid-state laser realized by Theodore Maimann in 1960. Besides gas and dye lasers, solid-state devices belong to the most commonly used lasers. The active medium of such lasers is made of crystals or glasses with the size of a few centimeters. They are doped with optically active ions, such as transition metals like Cr^{3+} or rare earths like Nd^{3+}. Laser transitions take place between the energy levels of inner unfilled electron shells. These transitions are quite sharp because they are unaffected by the field of the surrounding crystal. Using solid-state laser systems, one can obtain extremely high powers up to 10 PW, e.g., with a Ti:Sa laser system at the Shanghai Institute of Optics and Fine Mechanics (SIOM) [38, 39].

According to Schlenvoigt et al. [14], today's state-of-the-art laser systems have the capability to apply about 300 J of energy within a pulse duration of about 30 fs and a focal spot size of about 5 μm, achieving ultra-high light intensities I_L exceeding the $10^{22}\,\mathrm{Wcm}^{-2}$ range according to

$$I_\mathrm{L} = \frac{E_\mathrm{L}}{t_\mathrm{L} A_\mathrm{foc}} \ , \tag{2.2}$$

with the released amount of laser energy E_L in a very short time interval t_L to a very tiny spot size A_foc. Until today there is only one technique that makes it possible to generate such high intensities, the so-called Chirped Pulse Amplification (CPA) [35]. Here, ultra-short but spectrally broad laser pulses having pulse durations in the range $t_\mathrm{L} \sim 10\,\mathrm{fs}$ and initially containing only nano-joules of energy are produced by a mode-locked, dispersion-compensated optical oscillator. To amplify these pulses without damaging the amplifier by excessive pulse power or energy, they are first temporally stretched in dispersive elements by imprinting a positive chirp (similar to 2^nd-order dispersion) onto the pulse. This leads to pulse durations of 100's of ps such that the now long and less intense pulses can be amplified to several joules. In order for the pulses to be re-compressed to ultra-short durations, all spectral components must receive the same gain during the amplification procedure. Only a few available laser media meet this requirement, such as Ti:Sa, Nd:Glass or Yb:CaF_2, which limits the laser wavelengths λ_L to the near-infrared. By applying the inverse dispersion, the pulses are finally compressed back to ultra-short durations. The pulses generated in this way can have multi-TW power and find a wide range of applications, such as laser-induced particle acceleration [14].

2.2 High-intensity laser facilities

The scientific quest for ever higher laser powers and intensities has led to more and more high-intensity laser systems being built and operated worldwide. Already in 1996, the world's first petawatt laser was put together while re-purposing one beamline of the existing Nova Nd:glass laser facility at Lawrence Livermore National Laboratory (LLNL). The system operated for three years and delivered 1.5 PW with an energy of up to 680 J to target [40]. Figure 2.1 depicts a world map of ultrahigh intensity laser facilities in 2020 taking into account all labs operating systems, which have a peak power of at least 10 TW or produce light that can be focused to an intensity of $10^{19}\,\mathrm{Wcm}^{-2}$ or higher [41].

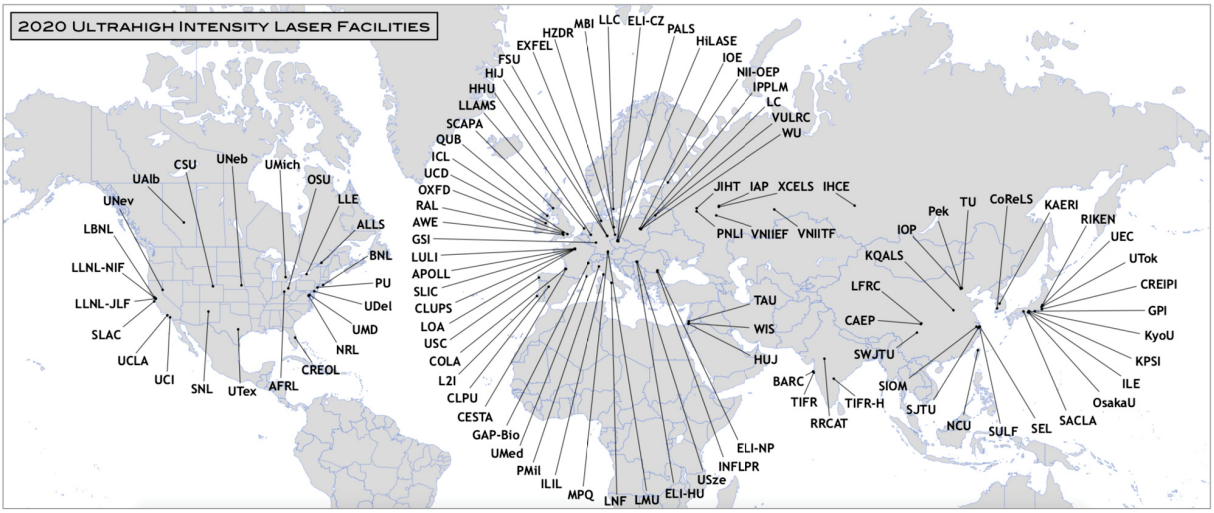

Figure 2.1: World map of ultrahigh intensity laser facilities in 2020. All represented labs operate laser systems, which have a peak power of at least 10 TW or produce light that can be focused to an intensity 10^{19} Wcm^{-2} or higher [41].

It is remarkable that this map was practically empty just a few years ago. In 2009, there were only a few ultra-high intensity laser systems throughout the world: 16 in the USA, 13 in Europe and Russia and 12 in Asia. There are now 174 such systems worldwide. Also evident is the leading role of Europe in this field with respect to the number of facilities. However, also Asia has a long history of operating ultra-high power facilities and has been pioneers in their development and application. Particularly China has seen the greatest growth internationally in the development of such systems and their implementation. Looking into the future, special attention will have to be paid to the further development of the following two aspects: delivering higher peak powers for fundamental research and higher average powers crucial for applications [42].

Modern high intensity lasers can be characterized by several properties, like e.g., laser power P_L, peak intensity I_peak, pulse duration t_L, wavelength λ_L or repetition rate, to mention just a few. Table 1 exemplifies four multi-TW/PW laser facilities with their current properties. For comparison, the *Ju*SPARC_Mira system is listed, which is operated at FZJ and is used in the course of this work to polarize an initially unpolarized proton beam (cf. Sec. 8). The generation of secondary particles results from the interaction of the respective laser system with a target. The

Table 1: Examples for today's multi-TW/PW laser systems with current properties. The *Ju*SPARC_Mira system is listed for comparison.

	*Ju*SPARC_Vega	SULF	PHELIX	ARCTURUS	*Ju*SPARC_Mira
amplifier	Ti:Sa	Ti:Sa	Nd:glass	Ti:Sa	Nd:YAG
P_L [TW]	1	10000	500	300	$3{\cdot}10^{-6}$
I_peak [Wcm^{-2}]	$3{\cdot}10^{18}$	$>10^{22}$	$2{\cdot}10^{21}$	$4.5{\cdot}10^{19}$	$\approx 10^{13}$
t_L [ps]	0.03	0.03	$0.5-20$	0.025	170
λ_L [nm]	800	800	1053	800	213, 1064
rep. rate [Hz]	1000	1/180	single shot	10	5
2ry particles	γ (XUV), e$^-$	p (MeV)	p, ions (10 MeV)	p (MeV)	p (eV)

*Ju*SPARC_Vega laser is the first TW system that was put into operation at FZJ during my time as a PhD student and is used at the PGI-6 for investigating higher harmonics generation and electron acceleration [31]. At the PHELIX laser as well as at the ARCTURUS system essential research results have been acquired in recent years (cf. Sec.4.5), on which this work is based. The ARCTURUS laser is a two-beam Ti:Sa system operated by the institute for laser and plasma physics at Heinrich Heine University Düsseldorf (HHUD), and can deliver a total system power exceeding 200 TW onto target [43]. At the Helmholtz Centre GSI, the Petawatt High-Energy Laser for heavy Ion eXperiments (PHELIX) kilojoule glass laser system is especially used for ion acceleration experiments [44]. The 10 PW laser at SULF, described in detail in the following section, is of particular interest since the experimental work and theoretical studies in this thesis will be used to prepare for the final experiments at this laser facility (cf. Sec. 2.2.1).

2.2.1 Shanghai super-intense ultrafast laser facility at SIOM

Substantial advances in ultra-short and ultra-intense laser technology have led numerous laboratories to develop PW-class laser systems with the challenging goal to investigate laser-matter interactions in a relativistic regime. In a joint effort of SIOM and ShanghaiTech University, a new laser facility has been brought to operation. The Shanghai super-intense Ultrafast Laser Facility (SULF), also known as Xi-He laser facility, is located in the Pudong District of Shanghai and aims to generate the most powerful laser pulse with peak power up to 10 PW. It contains a 10 PW, an 1 PW and a 100 TW beamline. Each beam is guided to one out of three target areas constructed underground for the study of the dynamics of materials under extreme conditions, ultra-fast sub-atomic physics and ultra-fast chemistry. The 10 PW ultra-intense laser facility can provide physical conditions for research on nonlinear strong-field optics, laser-plasma physics, nuclear photonics and strong-field QED. It should be mentioned that another 10 PW laser system pursuing similar science goals is already in operation at the Extreme Light Infrastructure - Nuclear Physics (ELI-NP) facility [45].

The designed focused laser intensity of the 10 PW laser is above $10^{22}\,\mathrm{Wcm}^{-2}$. Thus, a high temporal contrast of about 10^{-11} is required at full peak power. A suitable simplified layout of the 10 PW laser system at SULF is shown in Fig. 2.2. The system is based on a double-CPA scheme. A pulse from a commercial Ti:Sa CPA laser with kHz repetition rate passes through a nonlinear pulse cleaner, which links the two CPA stages. Then, it is stretched to approximately 2 ns by an Öffner stretcher in order to reduce chromatic aberrations and improve the temporal contrast. Next, a Dazzler is implemented, to perform simultaneous and independent spectral phase and amplitude shaping of ultra-fast laser pulses. After the Dazzler, four Multi-pass Amplifiers (MAs) intensify the signal beam to 8 J with 1 Hz repetition rate. Using two Power Amplifiers (PAs) and a final Booster Amplifier (BA), the signal beam is further amplified, achieving a maximum energy of 339 J. For this purpose, six high-energy pump lasers with output pulse energy of about 100 J and repetition rate of one shot per 3 minutes have been developed and are used as pump sources for the power amplifiers and the booster amplifier. They support an amplified energy beyond 300 J and a pulse duration of ~ 25 fs. Finally, the vacuum compressor compresses the pulse duration to 21 fs and the maximum pulse peak power can reach 10 PW [42, 46].

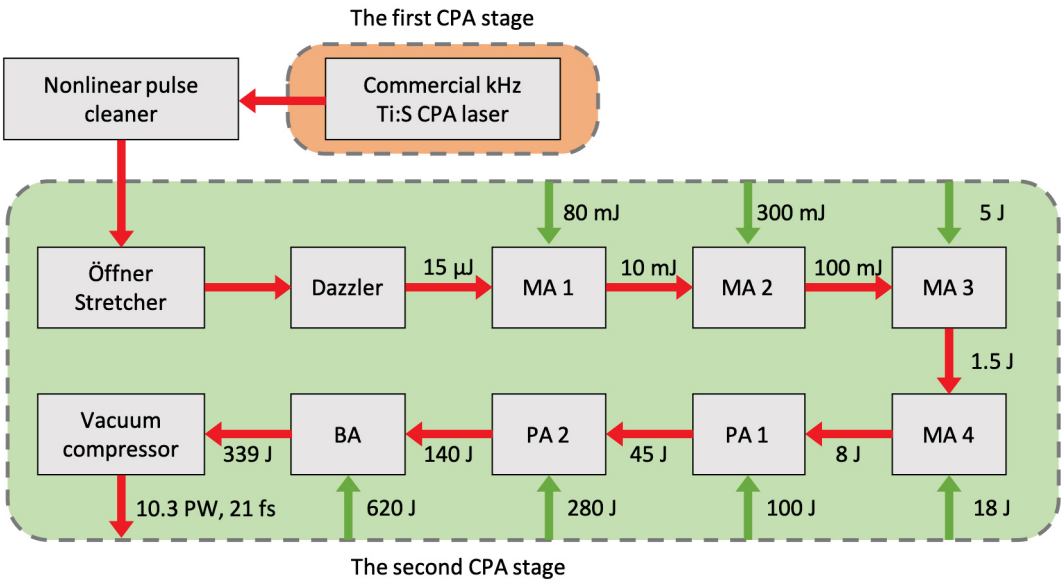

Figure 2.2: Layout of the SULF-10 PW laser system including Multi-pass Amplifiers (MAs), Power Amplifiers (PAs) and a Booster Amplifier (BA), adapted from Ref. [46].

Back in 2017, pulses with 5.4 PW peak power were reported in a specifically developed prototype facility [47]. Already about one year later, an amplified pulse energy of 339 J from the Ti:Sa amplifiers was achieved, which can support a peak power of 10 PW [48]. Meanwhile, the 1 PW laser system with repetitive rate of 0.1 Hz and a nanosecond 300 J Nd:glass laser system has been built and put into trial experimental operation.

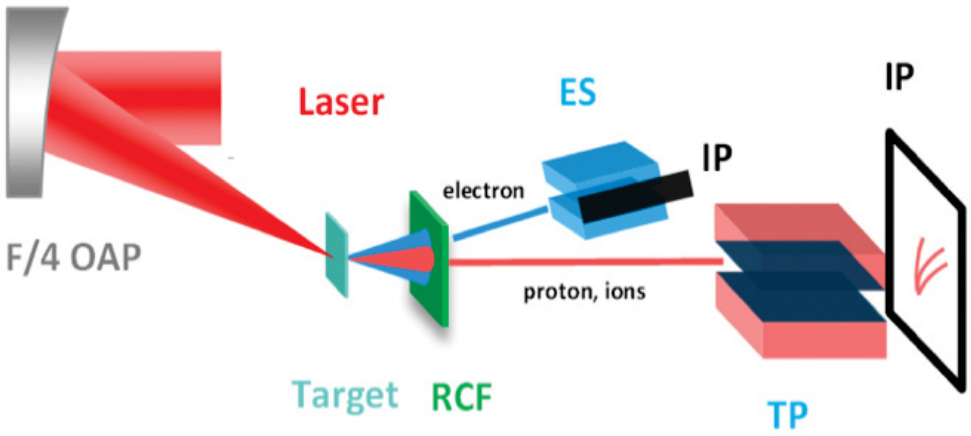

Figure 2.3: Schematic view of the setup for laser proton acceleration at SIOM. The ultra-intense laser is focused onto the target by the Off-Axis Parabola (OAP). Diagnostics include a RadioChromic Film (RCF) stack, a Thompson Parabola (TP) spectrometer, Image Plates (IPs) and an associated Electron Spectrometer (ES) [49].

Besides the development of state-of-the-art laser systems, SIOM also has great expertise in the research field of laser-induced proton acceleration, both theoretically and experimentally. On the experimental side, the group has demonstrated ~ 10 MeV laser-driven proton acceleration using a 800 nm circularly polarized laser pulse with a peak intensity of $6.9{\cdot}10^{19}$ Wcm^{-2} interacting with an ultra-thin plastic foil target. A mono-energetic peak at 9 MeV of high flux

has been observed. The optical setup inside the interaction chamber and various diagnostics tools including a RadioChromic Film (RCF) stack, a Thompson Parabola (TP) spectrometer, Image Plates (IPs) and an associated Electron Spectrometer (ES) have also been developed (cf. Fig.2.3) [49]. These will be used in the first phase of our joined experiments to evaluate both, the energy and the angular distribution, of the accelerated protons. In the second phase a polarimeter for the measurement of the degree of polarisation will be mounted similar to the experiments at the ARCTURUS laser system (cf. Fig. 4.8).

3 High-Intensity Laser-Plasma Acceleration

This section focuses on the physical background of high-intensity laser-plasma interactions. First, a short description of the fundamentals of laser-plasma physics is provided, which is the basis for understanding the acceleration mechanisms in laser-induced plasmas. In the following, the three mechanisms of laser-driven proton acceleration, which are of relevance for this thesis, are introduced: Target Normal Sheath Acceleration (TNSA), the acceleration in the bubble regime, and Magnetic Vortex Acceleration (MVA). In this context, the current status of the laser-driven proton acceleration is outlined. Subsequently, each mechanism is characterized, the corresponding regimes are defined with regard to laser and target parameters, and finally, the advantages and disadvantages are evaluated.

3.1 Fundamentals of laser-plasma physics

The acceleration of particles in laser-plasma accelerators is often based on the generation of so-called plasma waves. A plasma is defined as a (partly) ionized gaseous, electrically conductive and outwardly electrically neutral mixture of charged and uncharged particles, which interact by collisions. It is created under the condition that a fraction of the electrons has kinetic energies, which exceed the ionization potential, i.e., above a few eV. In plasmas, there is a weak coupling between pairs of particles, but there are strong collective interactions as can also be concluded from the following three properties: i) the Debye length λ_D, defining the characteristic length, over which the electrical potential will decrease in magnitude by $1/\exp(1)$, is small compared to the typical size of the plasma. ii) The plasma parameter $\Lambda \equiv n \cdot 4/3 \cdot \pi\lambda_\mathrm{D}^3$, i.e., the number of particles in a sphere with radius equal to the Debye length, is large. Here, n defines the particle density of the plasma. iii) The time between collisions is long as compared to the period of plasma oscillations since the electron plasma frequency is large in comparison to the electron-neutral collision frequency (see, e.g., the textbook by K. Nishikawa and M. Wakatani [50]).

With a focused, highly energetic and very short pulsed laser, plasma waves can be induced, which are driven by the so-called ponderomotive force: averaged over one laser cycle, the ponderomotive force pushes electrons away from regions of high intensity. After the pulse, the electrons strive back to the remaining ions. However, the electrons are not completely stopped again, partly shoot beyond the focal region and then return. This oscillating dipole creates an electrostatic Langmuir plasma wave for a very short time. The ponderomotive force can be derived from the equation of motion of a single point-like particle with mass m and charge q according to the Lorentz force law (cgs units)

$$\frac{\mathrm{d}\mathbf{p}}{\mathrm{d}t} = q\Big(\mathbf{E}_\mathrm{L} + \frac{\mathbf{p}}{mc} \times \mathbf{B}_\mathrm{L}\Big) \ , \tag{3.1}$$

where $\mathbf{p}(t) = \gamma m\mathbf{v}$ is the relativistic momentum, γ the relativistic Lorentz factor, $\mathbf{v}$ the particle velocity and $\mathbf{E}_\mathrm{L}$ and $\mathbf{B}_\mathrm{L}$ are the electric and magnetic fields of the laser pulse. Throughout this thesis bold symbols are used for vector quantities. As it is assumed that a laser has a pure electromagnetic potential, $\mathbf{E}_\mathrm{L} = -\partial\mathbf{A}_\mathrm{L}/\partial t$ applies and $\mathbf{B}_\mathrm{L} = \nabla \times \mathbf{A}_\mathrm{L}$ with the laser potential $\mathbf{A}_\mathrm{L} = A_0 \cos(\mathbf{k}\cdot\mathbf{r} - \omega_\mathrm{L} t)\mathbf{e}_\perp$. Here, $A_0 = (c/\omega_\mathrm{L})E_0$ with the electric field amplitude E_0, $\omega_\mathrm{L} = 2\pi c/\lambda_\mathrm{L}$ is the laser frequency with the laser wavelength λ_L and $\mathbf{k}$ is the wave vector, which absolute value is $2\pi/\lambda_\mathrm{L}$.

In the non-relativistic limit ($\beta = v/c \ll 1$ or $\gamma \approx 1$) the influence of the magnetic field on the motion of the electron can be neglected and as a result the vector product in Eq. 3.1 becomes small. Hence, only the electric force $\mathbf{F}_{\mathrm{el}} = e \cdot \mathbf{E}_{\mathrm{L}}$ determines the equation of motion of the oscillating electron and the normalized vector potential $\mathbf{a}$ is given by

$$\mathbf{a} = \frac{e\mathbf{A}_{\mathrm{L}}}{mc^2} \ . \tag{3.2}$$

It is smaller than one by definition and equal to the normalized transverse quiver momentum $\mathbf{p}_{\mathrm{q}}$ of the plasma electron in the laser field, i.e., $\mathbf{a} = \mathbf{p}_{\mathrm{q}}/(mc)$. The laser strength parameter $a_0 = eA_0/(mc^2)$ is the dimensionless peak amplitude of $\mathbf{a}$ and commonly used as it represents the "relativisticness" of the motion and is directly related to the laser intensity I_{L} by

$$I_{\mathrm{L}} = \pi c \cdot \left(\frac{a_0 m_{\mathrm{e}} c^2}{c\lambda_{\mathrm{L}}} \right)^2 \iff a_0 = 0.85 \cdot \left(\frac{I_{\mathrm{L}} \lambda_{\mathrm{L},\mu\mathrm{m}}^2}{10^{18}\,\mathrm{Wcm}^{-2}} \right)^{1/2} , \tag{3.3}$$

where $\lambda_{\mathrm{L},\mu\mathrm{m}}$ is the laser wavelength given in μm. In the non-relativistic regime $a_0 \ll 1$ and one finds that a_0 is the ratio of the amplitude of the quiver velocity $\mathbf{v}_{\mathrm{q}}$ to c. Intensities $a_0 \geq 1$ are considered as "relativistic intensities".

Averaging the Lorentz force in time over the fast oscillatory contributions from the laser, i.e., regarding just the pulse envelop, the second order motion gives the 3D ponderomotive force $\mathbf{F}_{\mathrm{pond}}$ in the non-relativistic limit. If considering that the electron momentum splits up according to $\mathbf{p} = \mathbf{p}_{\mathrm{q}} + \delta\mathbf{p}$, for $\mathbf{F}_{\mathrm{pond}}$ it holds

$$\mathbf{F}_{\mathrm{pond}} = -\frac{1}{2} m_{\mathrm{e}} c^2 \nabla \mathbf{a}^2 \ . \tag{3.4}$$

Here $\mathbf{v}_{\mathrm{q}} \approx \mathbf{p}_{\mathrm{q}}/m_{\mathrm{e}}$, $\partial \mathbf{p}_{\mathrm{q}}/\partial t \approx -e \cdot \mathbf{E}_{\mathrm{L}}$ and $\gamma \equiv 1$. Thus, in the non-linear regime, the quiver motion is still the leading order transverse motion of an electron, if $r_{\mathrm{L}} > \lambda_{\mathrm{p}} \gg \lambda_{\mathrm{L}}$. r_{L} is the laser focal spot size, $\lambda_{\mathrm{p}} = 2\pi c/\omega_{\mathrm{p}}$ is the plasma wavelength and $\omega_{\mathrm{p}} = (4\pi n_{\mathrm{e}} e^2/m_{\mathrm{e}})^{1/2}$ is the electron plasma frequency with n_{e} being the number density of electrons [51, 52]. The related ponderomotive potential reads as

$$\Phi_{\mathrm{pond}} = \frac{a_0^2}{4} m_{\mathrm{e}} c^2 \ . \tag{3.5}$$

From this equation it can be concluded that the envelope of the focused laser pulse effectively dominates the shape of the ponderomotive potential. The ponderomotive force causes a net push in the direction away from high intensities. In this way, a net momentum can be transferred to the electrons, particularly in laser propagation direction. The ponderomotive pressure is one of the main mechanisms for electrons to gain kinetic energy at relativistic intensities and, thus, plays a key role in both, electron and ion acceleration [14].

Laser-plasma interactions strongly depend on the plasma properties, in particular, the plasma frequency ω_{p} and, hence, the electron density n_{e}. The condition $\omega_{\mathrm{L}} = \omega_{\mathrm{p}} = \omega$ defines the critical density n_{c} as

$$n_{\mathrm{c}} = \frac{m_{\mathrm{e}}}{4\pi e^2} \cdot \omega^2 \ . \tag{3.6}$$

A laser with a given frequency ω_{L} can propagate through the plasma only when the plasma density does not exceed the critical value n_{c} ($\omega_{\mathrm{L}} > \omega_{\mathrm{p}}$). In that case the plasma is called un-

derdense ($n_e \ll n_c$), and plasma waves can be induced. An example are gas-jet targets with a typical electron density of $n_e = 10^{18} - 10^{19}\,\mathrm{cm}^{-3}$. In case of overdense plasmas ($\omega_p > \omega_L$), the laser pulse is reflected partially, while the absorbed component exponentially decreases. Here, laser-plasma interactions can lead to the generation of quasi-static fields, for example behind thin foil targets [52].

For relativistic intensities time-scales larger than the laser period lead to a relativistic mass increase of the electron. Thus, the electron rest mass m_e has to be replaced by the average relativistic mass $\overline{\gamma} m_e$ with $\overline{\gamma} = \langle\gamma\rangle \approx (1 + a_0^2/2)^{1/2}$. In addition, the ponderomotive force causes a local change of the plasma electron density [53]. The ponderomotive potential changes to

$$\Phi_{\mathrm{pond}} = \left(\sqrt{1 + a_0^2} - 1\right) m_e c^2 \ , \tag{3.7}$$

which is equal to the electron's relativistic kinetic energy gained from the laser field. Both afore mentioned effects modify the optical properties of the plasma at regions, where the laser pulse interacts with the plasma. This can result in an alternation of the laser pulse propagation and finally in a change of the laser pulse shape. In this context self-focusing and self-modulation are the most noteworthy mechanisms [14].

The 10 PW laser at SULF, for example, is designed to deliver pulses with an intensity of $I_L > 10^{22}\,\mathrm{W/cm^2}$ at a wavelength of $\lambda_L = 800\,\mathrm{nm}$. Here, the laser strength parameter $a_0 \approx 70$ yields a ponderomotive potential of at least $\Phi_{\mathrm{pond}} \approx 5{\cdot}10^{-12}\,\mathrm{J} \approx 31\,\mathrm{MeV}$.

3.2 Laser-driven acceleration mechanisms for protons

Based on simulations and theoretical work, in 1979 Tajima and Dawson have first demonstrated for electrons that an intense electromagnetic pulse induced by the linear ponderomotive force can create a wake of plasma oscillations [54]. They concluded that a laser-driven relativistic plasma can be appropriate for the development of compact accelerators, such as laser-driven ones. With the improvement to build more powerful lasers, concepts and first experiments on laser-induced particle acceleration have also been pushed forward since the 1990s.

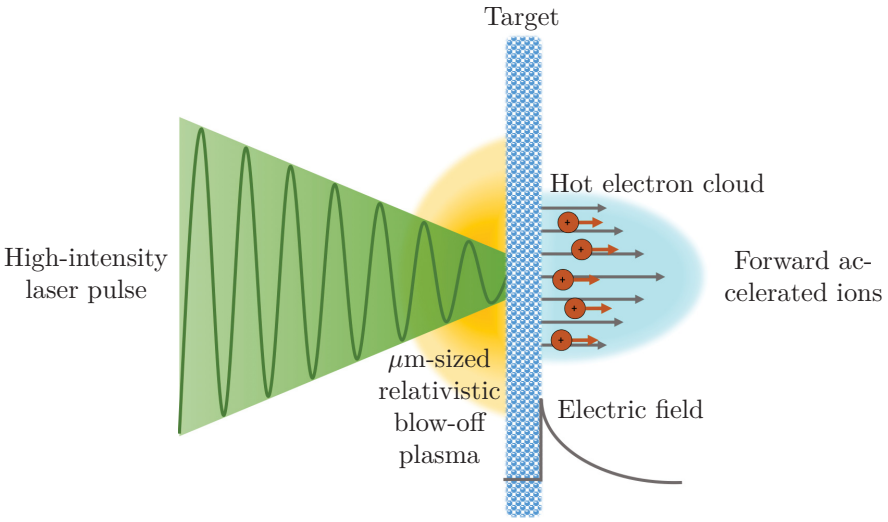

Figure 3.1: Simple scheme of a laser-driven ion accelerator.

In Fig. 3.1 a simple scheme of a laser-driven ion accelerator is presented. The main components of this kind of accelerator are a high-intensity short-pulse laser beam and a suitable target, e.g., a gas jet or a thin foil, positioned in a vacuum chamber. Due to the interaction of the laser with the target, a μm-sized relativistic plasma is generated. While plasma waves in under-critical gas targets can be used for particle acceleration, acceleration from foil targets is generally achieved as a result of the generated quasi-static fields. Due to their 2000 times higher mass, proton acceleration has so far been performed from schemes with quasi-static fields. In general, a distinction is made between two main forces induced by the laser beams in the plasma, which make it possible to accelerate ions to high velocities over short distances, namely the electromagnetic and the hydrodynamic forces. The latter dominate at low laser intensities ($\sim 10^{10} - 10^{15}\,\mathrm{Wcm}^{-2}$) and long laser pulses (from tens of ps to tens of ns), while the space-charge force induced by presence of strong laser field plays the decisive role at high ($> 10^{15}\,\mathrm{Wcm}^{-2}$) and relativistic ($> 10^{18}\,\mathrm{Wcm}^{-2}$) laser intensities. This thesis focuses on laser-driven particle acceleration at high and relativistic laser intensities and, hence, the acceleration by electromagnetic forces. The origin of the electromagnetic forces is the Lorentz force (cf. Eq. 3.1), which interacts with both, the plasma electrons and the plasma ions, whereas it is about 2000 times weaker for the latter. As the field strength generated during the acceleration process is extremely high, in the range of up to tens or even hundreds of GeV/cm, the particles are accelerated to high velocities ($v_\mathrm{i} \approx c$) over sub-mm distances. This is many orders smaller compared to conventional RF-driven accelerators paving the way to compact or even table-top setups. Further advantages of laser-driven accelerators over conventional accelerators, which can be directly attributed to the very dense and compact accelerated ion bunches, are the very high ion beam intensities and powers as well as the very short pulse duration of the ion pulse [55].

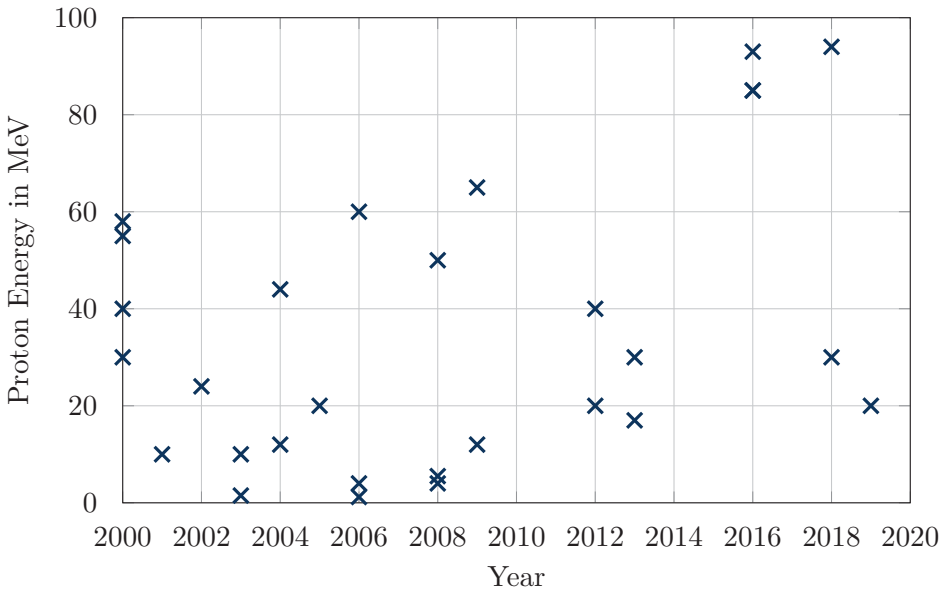

Figure 3.2: Development and status of laser-driven proton acceleration making use of quasi-static field and/or thin target foils (cf. App. A).

The investigation of generating energetic ions from laser-induced plasma has a long tradition and goes back to the 1960s [56, 57]. However, it was only at the turn of the millennium that a real breakthrough was achieved by demonstrating collimated forward-emitted proton

beams in the MeV range from thin foil targets irradiated by a short ($\leq 1\,\mathrm{ps}$) and high-intense laser pulse [55, 58–60]. Figure 3.2 displays the development and status of laser-driven proton acceleration concentrating on the energy of the accelerated protons since then. In the majority of the experiments shown, a foil target was used and the ions were accelerated according to the TNSA mechanism (cf. Sec. 3.2.1). Though, until today the 100 MeV energy level could not be broken. As a result, there is great demand for further acceleration mechanisms that promise higher energies (cf. Secs. 3.2.2 and 3.2.3).

In order to actually compete with conventional accelerators, laser-driven ones absolutely have to accelerate polarized particles. However, this has never been demonstrated experimentally so far and we are one of the few research groups that are not only working on theoretical but also on experimental objectives. For the various acceleration mechanisms, it is therefore mandatory to check that the polarization is maintained.

3.2.1 Target normal sheath acceleration

The Target Normal Sheath Acceleration (TNSA) mechanism was first proposed by Wilks et al. in 2001 [61]. It is most effective for the acceleration of light ions, especially protons, and is, generally speaking, a consequence of the large charge separation created by the hot electrons penetrating through the foil target and reaching its back side (cf. Fig. 3.3). In this most widely investigated scheme the acceleration process is based on three steps:

1. A high-intensity laser pulse having an incident angle α of typically 30° to 60° is first focused onto the target [62]. Due to the interaction with the overdense plasma, an energetic, hot electron contribution with a temperature of $T_{\mathrm{hot}} \approx 0.1 - 10\,\mathrm{MeV}$ is created.

2. The electrons propagate into the plasma and through the target. Typically, the foil targets are made from insulators, such as plastic, or metals with a thickness ranging from about $2\,\mu\mathrm{m}$ to $20\,\mu\mathrm{m}$. Solid metal targets are preferred due to the better transport of electrons resulting in an increased ion energy and higher ion beam quality.

3. On the rear surface electrons leave the target and form a Debye sheath resulting in a kind of capacitor. The induced electric field is $E_{\mathrm{ind}} \approx T_{\mathrm{hot}}/(e\lambda_{\mathrm{D}}) \approx 1 - 100\,\mathrm{GeV/cm}$, where λ_{D} is the Debye length. Hence, atoms at the rear surface are ionised and the generated ions are accelerated over distances $l_{\mathrm{acc}} \approx 10 - 50\,\mu\mathrm{m}$ to high energies. However, in reality usually only ions from a very thin layer ($\approx 2 - 10\,\mathrm{nm}$) are accelerated. To gain high ion beam intensities ($\approx 10^{18}\,\mathrm{Wcm^{-2}}$) and/or energy fluencies ($\approx 1\,\mathrm{MJcm^{-2}}$) either fairly high ion energies need to be achieved ($\geq 100\,\mathrm{MeV}$) or the total number of accelerated ions needs to be very large ($\approx 10^{12} - 10^{13}$). The maximum ion energy E_{max} in Mora's one-dimensional model including plasma expansion by charge separation [63–65] is given as

$$E_{\mathrm{max}} = 2k_{\mathrm{B}}T_{\mathrm{hot}} \ln^2\left(\tau + \sqrt{1+\tau^2}\right) \ , \tag{3.8}$$

where $\tau = \omega_{\mathrm{p,i}} t/\sqrt{2\exp(1)}$ with the ion plasma frequency $\omega_{\mathrm{p,i}}$, the Boltzmann constant k_{B} and the hot electron temperature T_{hot}. For the acceleration time t_{acc} is follows

$$t_{\mathrm{acc}} = 1,3 \cdot (t_{\mathrm{L}} + t_{\mathrm{min}}) \ , \tag{3.9}$$

with the laser pulse duration t_L and the constant value $t_{min} = 60\,fs$, which defines the minimum time the energy transfer from the electrons to the ions takes for laser intensities $I_L \geq 3{\cdot}10^{19}\,Wcm^{-2}$. Thus, for the 10 PW laser at SULF the acceleration time would be about 78 fs. Although the Mora model is only one-dimensional, it was applied to experimental data generated at more than ten high-intensity short-pulse laser systems over the world and can, therefore, be considered as a reference model [24, 55, 61, 66–69].

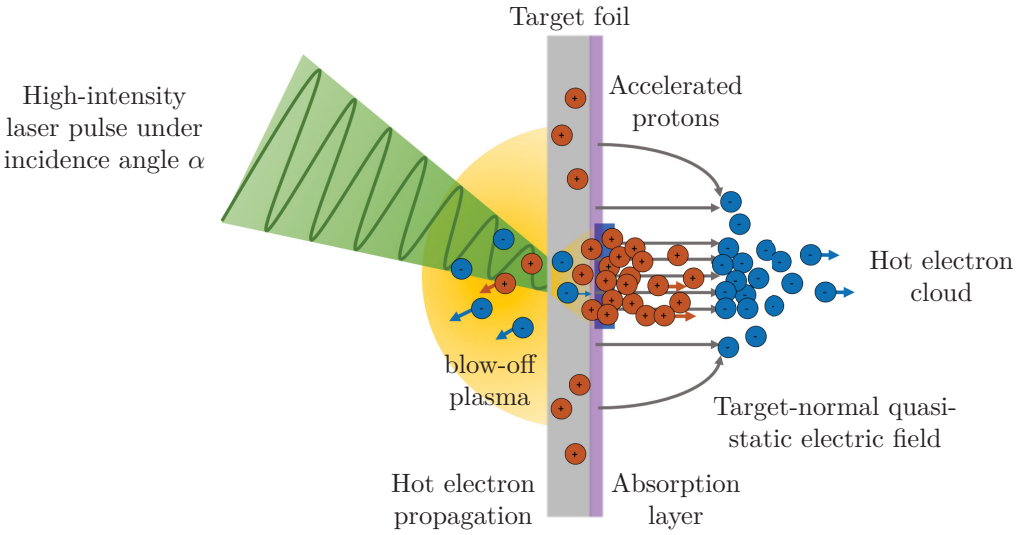

Figure 3.3: Simplified scheme of ion acceleration by the TNSA mechanism.

Like every scheme, the TNSA mechanism also has its pros and cons. The main advantages, also proven experimentally, are given in the following [55].

- The transverse intensity distribution of the ion beam is of extraordinary quality.
- The transverse emittance of the beam is fairly low.
- Requirements for the laser beam intensity and quality are moderate.

There are also considerable disadvantages of this acceleration mechanism [55].

- The ion energy spectrum is comparatively broad (quasi-Maxwellian like).
- The maximum ion energy scales with the laser intensity as $E_{max} \propto I_L^{0.5}$. Thus, E_{max} is limited to a few hundred MeV, since with this method a laser intensity of $10^{22}\,Wcm^{-2}$ cannot be exceeded.
- The areal ion density $\sigma_i < 10^{17}\,cm^{-2}$ at the source is relatively small.
- The laser-to-ions conversion efficiency η is just a few percent.
- The ion beam parameters and the laser-to-ions conversion efficiency η depends very much on the target rear surface quality.
- The very thin targets are difficult to handle, in particular regarding the precise positioning of the foils relative to the laser focus.

3.2.2 Bubble regime for particle acceleration

Laser-plasma interactions in the so-called "bubble" regime were first described for **electrons** by Pukhov et al. in 2002 [22]. They demonstrated in 3D PIC simulations that the interaction of a Laser WakeField Accelerator (LWFA) having ultra-relativistically intense pulses with an underdense gas plasma results in a breaking of the formed plasma wave already after the first oscillation [70]. For this to happen, a few further conditions have to be met: i) the laser pulse has to be shorter than the plasma wavelength $\lambda_\mathrm{p} = 2\pi c/\omega_\mathrm{p}$, where $\omega_\mathrm{p} = (4\pi n_\mathrm{e} e^2/m)^{1/2}$ is the plasma frequency and n_e denotes the electron density. ii) The excitation of the plasma wave is most efficient if the laser pulse completely fits into the first half of the wave. iii) The FWHM of the laser pulse should be equal to one-half of the plasma period. Thus, a plasma cavity – the bubble – can be generated given that the laser ponderomotive force and the electromagnetic fields define the electron dynamics as depicted in Fig. 3.4 [22, 70, 71].

- At the beginning of the interaction no bubble is formed yet since the shape of the cavity is only defined by the ponderomotive potential of the laser pulse.
- During the interaction, the electron-plasma cavity with a large ion charge located at its front is created. The bubble itself is virtually free from cold plasma electrons. While the cavity in the plasma nearly runs with the speed of light, the ions inside are immobile.
- The bubble boundary is limited by the electron sheath around the cavity.
- Near the middle plane passing through the cavity center, the transverse size of the cavity has its maximum. At the intercept with the bubble boundary the electron sheath contains a return current carried by the weakly relativistic electrons.
- A bunch of accelerated electrons is accumulated in the cavity behind the laser pulse at its central horizontal axis.

Regarding this density structure, three key features of the bubble regime emerge [22, 70, 71].

1. Instead of a periodic plasma wave as it applied to many other acceleration schemes, a cavity free from cold plasma electrons is created behind the incident laser pulse: during the laser-plasma interaction, the transverse ponderomotive force of the laser pulse expels the plasma electrons from the high intensity region, leaving behind the laser pulse and the plasma cavity, which is almost free from plasma electrons. As the ions barely move, a transverse quasi-static electric field is formed due to the charge separation. Thus, in the stationary lab frame, the background electrons mainly move sideways, while electrons trapped in the bubble follow the laser pulse. A return current sheath is generated and the bubble-like structure is stretched. At the boundary in the middle of the bubble the Lorentz forces from the cavity and from the bunch electrons compensate each other. After having overcome this balancing point, the electrons are now attracted by the Lorentz force. At the wave breaking region of the cavity they are pulled onto the central laser axis forming a channel. The trapping for electrons occurs most probably at the boundary of the domain since here the wake potential $\Phi = \gamma_0^{-1} < 1$ is minimal, where γ_0 is the Lorentz factor of the bubble [70]. As the electrons are trapped inside the accelerated phase of the bubble plasma field, an efficient acceleration to high energies inside the channel gets very likely.

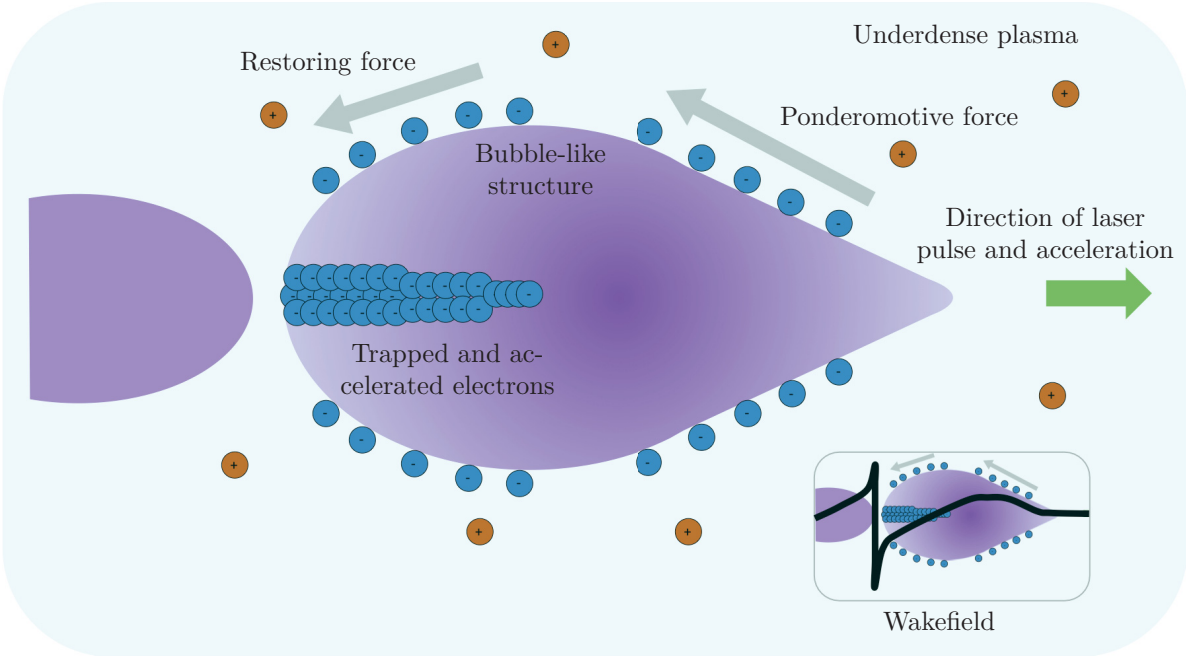

Figure 3.4: Simplified scheme of electron acceleration in the bubble structure. The black line in the insert shows the longitudinal (accelerating) electric field distribution on the symmetry axis.

2. A quasi mono-energetic spectrum from a dense bunch of relativistic electrons is generated. It has been found that the maximum energy of the accelerated electrons peaks at the cavity center and scales like [70]

$$\gamma_{\max} \approxeq 2\gamma_0^2\left(1+\frac{R^2}{4}\right) \approxeq \frac{1}{2}\gamma_0^2 R^2 \quad . \tag{3.10}$$

   The expression in the brackets represents the Hamiltonian describing the longitudinal motion of the trapped electrons, γ_0 is the Lorentz factor of the bubble and R is the radius of the cavity approximated by an ion sphere. In the trapping process the laser field is negligible as the trapping happens when the laser pulse has already passed and, thus, the laser field is small. The acceleration is a result of the longitudinal electric field of the plasma wave travelling with the laser pulse group velocity $v_{\mathrm{ph}}^{wake} = v_{\mathrm{g}} = c \cdot (1-\omega_{\mathrm{p}}^2/\omega_{\mathrm{L}}^2)^{1/2}$ with the laser frequency ω_{L}. Thus, a relativistic electron can ride this plasma wave while it stays in phase with the electric fields pointing into the laser propagation direction. However, the velocity of the cavity at its front is larger compared to that of its base because the sheath electrons near the base are collected by the bunch.

3. The high-intense laser pulse propagates in the homogeneous underdense plasma for many Rayleigh lengths without substantial spreading.

In 2007 Shen et al. extended the bubble acceleration scheme for **ion** acceleration in laser-driven plasma [72]. Compared to the bubble scheme for electrons, high-energetic ion beams in the so-called electron bubble-channel structure can be produced if i) a multi-petawatt laser system ($a_0 \geq 25$) is combined with ii) a gas target containing hydrogen and another ion species with a larger A/Z ratio (like, e.g., HCl or HBr gas).

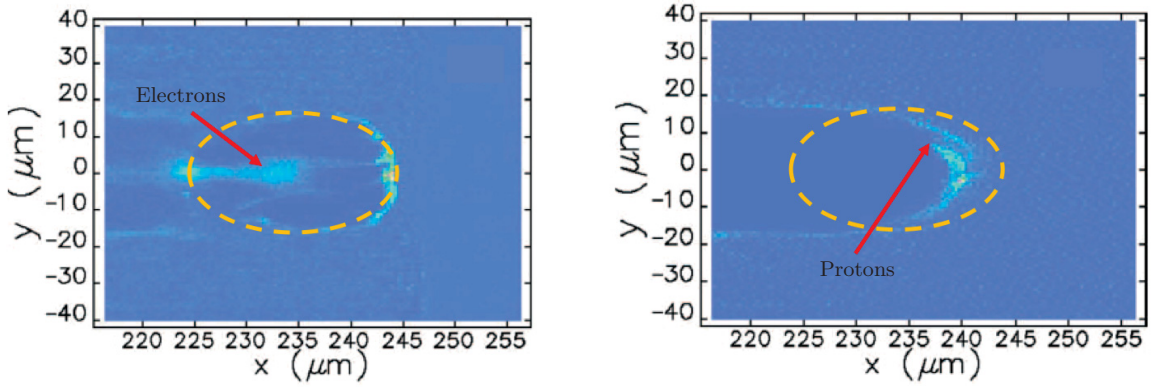

(a) Electron density contour plot at a simulation time of 854 fs.

(b) Proton density contour plot at a simulation time of 854 fs.

Figure 3.5: Principle of the electron bubble-channel structure shown in a 3D simulation using the PIC code VORPAL. For the simulations a hydrogen density of $1{\cdot}10^{20}\,\mathrm{cm}^{-3}$ and a tritium density of $1.4{\cdot}10^{21}\,\mathrm{cm}^{-3}$ has been chosen. The circularly polarized laser pulse has a wavelength of $0.8\,\mu$m, a normalized peak amplitude of $a_0 = 316/\sqrt{2}$, a length of $10\,\mu$m, and a FWHM spot size of $16\,\mu$m while entering from the left side of the simulation box and propagating in the x-direction, adapted from Ref. [72].

With foresight for the next generation of PW classes laser systems, Shen et al. carried out 3D simulations with the code VORPAL for a laser pulse of wavelength $0.8\,\mu$m, normalized peak amplitude $a_0 = 316/\sqrt{2}$, length $10\,\mu$m, and FWHM spot size $16\,\mu$m. The circularly polarized laser beam enters the simulation box of size $400\,\mu\mathrm{m} \cdot 80\,\mu\mathrm{m} \cdot 80\,\mu\mathrm{m}$ from the left side interacting with a plasma of electron density $1.4{\cdot}10^{21}\,\mathrm{cm}^{-3}$, hydrogen density $1{\cdot}10^{20}\,\mathrm{cm}^{-3}$ and tritium density of $1.4{\cdot}10^{21}\,\mathrm{cm}^{-3}$. For each species two particles per cell were simulated and there are $1200 \cdot 100 \cdot 100$ cells in the simulation window. Under these conditions it was found that the protons are accelerated in the electron bubble-channel structure. As can be seen from Fig. 3.5, the plasma density structure is a combination of an electron bubble and an ion channel with a low-density tail, extending to the plasma edge. The accelerated electrons are trapped at the rear and in the center of the bubble-like structure (cf. Fig. 3.5a), whereas protons are wakefield-trapped and accelerated at the high-density front of the ionic channel as depicted in Fig. 3.5b.

As the heavy ions react with some delay to the built up charge-separation field, an ultra-intense electrostatic field is generated as a result of electron charge-depletion at the channel centre. Not the heavy ions are trapped, but only the protons, moving with and surfing on the longer-lasting electric field. Like that, the proton acceleration time is prolonged and they achieve large energy gain. Thus, the heavy ions in the plasma are a crucial component for proton acceleration to happen. An acceleration of unpolarized protons to a maximum energy of several GeV is predicted, e.g., Shen et al. found protons being accelerated to up to 27 GeV in a H/T plasma [72].

In another simulation study with comparable parameters and a H/T gas with $5.2{\cdot}10^{20}\,\mathrm{cm}^{-3}$ background plasma density, Shen et al. show that protons in a small target located in an under-dense high-mass plasma can be accelerated by the wakefield to energies of 38 GeV with small divergence angles [73]. Moreover, it was proven that near the front electron layer the transverse space-charge field is radially inward, while the direction is contrary elsewhere. The self-generated

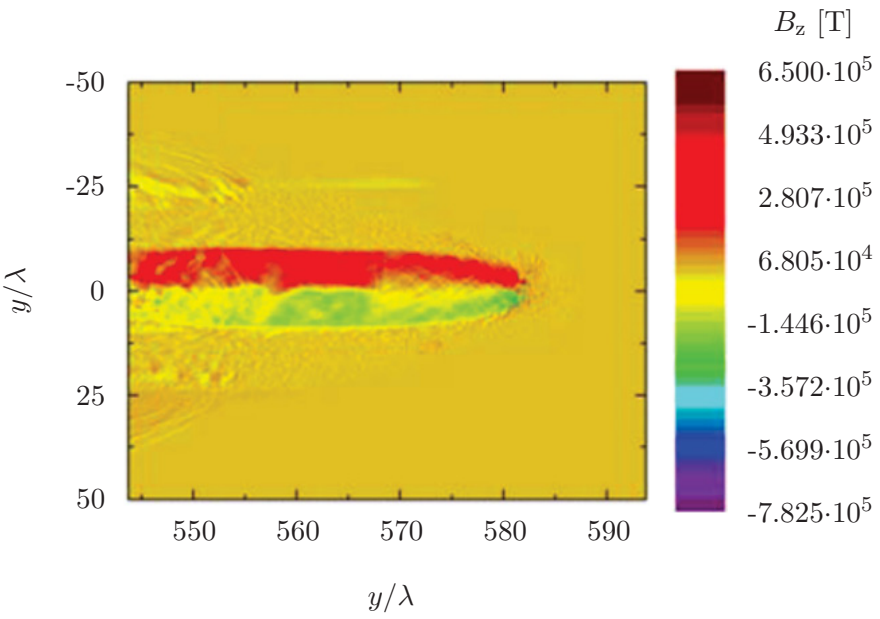

Figure 3.6: 2D simulation of the quasi-static self-generated magnetic field B_z with similar parameters compared to these ones presented in Fig. 3.5 and a H/T gas with $5.2{\cdot}10^{20}\,\mathrm{cm}^{-3}$ background plasma density using the PIC simulation code VORPAL, adapted from Ref. [73].

and quasi-static magnetic field B_z in the simulation window with a maximum of $B_z \approx 2.8{\cdot}10^5\,\mathrm{T}$ is presented in Fig. 3.6. From that the interaction time t_{int} of the accelerated protons with the magnetic field can be estimated as

$$t_{\mathrm{int}} = \frac{s}{v} = \frac{\text{target length}}{v_{\mathrm{proton}}} = \frac{1\,\mu\mathrm{m}}{c} = 3.3\,\mathrm{ps}\ . \tag{3.11}$$

For comparison, the typical time scale t_{spin} for the spin motion is given by

$$t_{\mathrm{spin}} = \nu_{\mathrm{Larmor}}^{-1} = \frac{2\pi}{\gamma B} = \frac{2\pi}{2.7 \cdot 10^8\,(\mathrm{Ts})^{-1} \cdot 280000\,\mathrm{T}} = 0.08\,\mathrm{ps}\ , \tag{3.12}$$

where γ is the Lorentz factor and $B = B_z$ from Fig. 3.6. Already from these calculations it is obvious that the interaction time between the magnetic field and the protons is sufficiently long to have spins aligned. Detailed information about the spin and its peculiarities are summarized in Sec. 4.

Note that these pioneering simulations from Ref. [72, 73] have been carried out more than a decade ago with very limited statistical accuracy. These simulations wait for using higher particle numbers and a higher resolution.

In the following, advantages of ion acceleration in the electron bubble-channel structure are presented.

- Possibility to also accelerate nuclear *polarized* ions due to the use of a gas target (cf. Sec. 9).
- Compared to other acceleration schemes, e.g., light pressure acceleration, much larger proton energies at the same laser intensity are predicted, which represents a major step towards the realization of laser-based accelerators.
- No sharp laser pulse front is needed, which facilitates the experimental realization.

There are also some considerable disadvantages, which have to be considered.

- Multi-petawatt laser systems ($a_0 \geq 25$) are required, which are only just being put into operation at a few institutes worldwide.
- There are no experimental confirmations of this mechanism yet.

3.2.3 Magnetic vortex acceleration

In 2D and 3D PIC simulations the MVA mechanism has been identified as an interaction of a laser pulse with a near-critical density target that is much longer than the laser pulse itself. Subsequently, a quasi-static magnetic field is created at the plasma-vacuum interface by the acceleration of electrons and the rise of the return current, resulting in efficient forward acceleration and collimation of ions as can be seen in Fig. 3.7 [74–76].

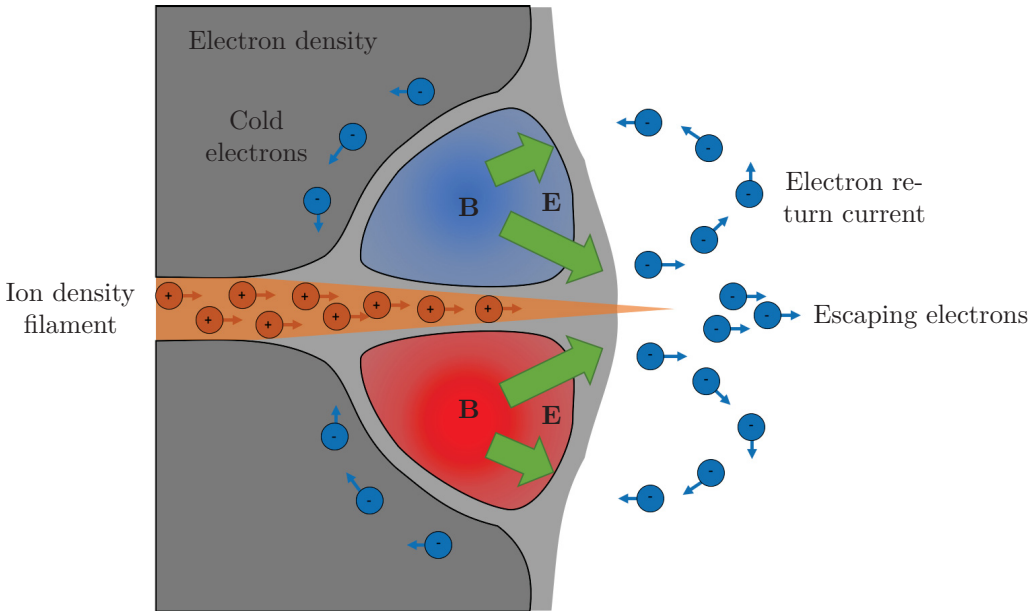

Figure 3.7: Simplified scheme of ion acceleration in the MVA mechanism.

Due to the interaction of a strongly focused laser pulse with the target, the ponderomotive force expels electrons and drives electron cavitation. It is suggested that near-critical density plasma targets have the advantage of higher laser-plasma coupling over other target types. Thereby, along the laser propagation axis, a low density channel is created in the electron plasma component. Ions remain at their initial position because of their larger mass. While the laser pulse propagates through this self-generated channel, electrons are trapped and accelerated in its wake. These fast electrons fall behind the laser front and form a thin filament on the central horizontal axis. They carry a strong axial fast current having an average of several MA as a result of the plasma lensing effect. In order to balance the fast current, a cold electron return current is generated maintaining the plasma quasi-neutrality. The magnitude of the strong azimuthal magnetic field caused by the rise of the return current is in the order of thousands of teslas. When leaving the channel at the back, the magnetic field expands into vacuum in the transverse direction and the electron current is dissipated. This magnetic field has the shape of a dipole in 2D and of a toroidal vortex in 3D and is generated along the channel and plasma-

vacuum interface. Following, the magnetic field displaces the electron component of the plasma causing a decrease of the electron density. As the responds of ions is much slower than that of electrons, a long-living positively charged region results. The corresponding electrostatic sheath has an electric field $E \approxeq \nabla B^2/(8\pi e n_\mathrm{e})$ accelerating and collimating the ions near the channel axis. In addition, the collimation is enhanced by the effect of forming an ion density filament in the paraxial region of the channel. The ions are accelerated at both sides of the plasma slab but in opposite directions due to the existing quasi-static magnetic field. The ion energy E_i per nucleon can be estimated by [77]

$$\frac{E_\mathrm{i}}{A} \approx \frac{Z}{A}\frac{mc^2 a_\mathrm{L}}{2\sqrt{2}}\frac{n_1}{n_2} \ , \tag{3.13}$$

where A and Z are the ion mass number and the ion charge, $a_\mathrm{L} = eA_\mathrm{L}/(mc)$ is the vector potential of the laser pulse (cf. Sec. 3.1) and n_1/n_2 is the density ration of the near-critical density plasma, respectively. To realize a long-living dipole vortex, $n_1/n_2 = 8$ is chosen, resulting in a simple energy scaling

$$E(\mathrm{MeV}) = 16.7\sqrt{P_\mathrm{L}} \ , \tag{3.14}$$

with the laser power P_L given in units of TW. Thus, a 100 TW-class laser is predicted to generate protons of about 200 MeV energy in the MVA mechanism. Hence, optimal parameters for the acceleration depend on the coupling of the laser energy to the self-generated channel in the target, the plasma slap density and thickness as well as on the laser pulse intensity [21, 74, 76–78].

It is important to note that the vortex structure is very different from the bubble structure, which is generated by electrons kicked aside by the high-intense laser pulse and recaptured by the electric field (cf. Sec. 3.2.1) [77].

Advantages of the MVA mechanism are among others:

- Good ion energy scaling with laser intensity comparable to TNSA.
- Good energy conversion efficiency.

For sure, there are also disadvantages like:

- Requirement of near-critical targets.
- No conclusive experimental demonstrations yet. In particular, it is difficult to discriminate MVA against TNSA.

4 Spin and Polarization of Particle Beams

The experiments with laser-accelerated polarized particle beams aim at the investigation how particle spins are influenced by the huge electromagnetic fields, which are inherently present in the plasma and what fundamental mechanisms may lead to the production of highly polarized beams. Firstly, the spin formalism and the polarization as a property of the entire particle beam are introduced. In the following, a detailed description of the three relevant mechanisms leading to a polarization buildup is provided: the T-BMT equation, the Sokolov-Ternov effect and the Stern-Gerlach (SG) effect. In order to measure the demonstrated effects, the so-called Lamb-Shift Polarimeter (LSP) is presented, which already has a long tradition at FZJ to measure the nuclear spin polarization. Finally, the status quo of experiments on laser-accelerated spin-polarized proton beams are outlined so that these results can be referred to in the next sections.

4.1 Spin formalism

As early as 1921, the so-called "quantization of direction" was discovered by Stern and Gerlach as a further property of atoms besides, e.g., mass and charge. In their famous experiment they sent a beam of atomic silver through an inhomogeneous magnetic dipole field and observed two discrete lines on a screen instead of the expected continuous distribution [79]. It prompted Goudsmit and Uhlenveck to suppose a "spin", another reason for the development of the quantum theory at these days in order to explain the fine structure of atomic spectra quantum-mechanically. They assigned a spin $\mathbf{s}$, similar to an intrinsic angular momentum $\mathbf{s} = (s_\mathrm{x}, s_\mathrm{y}, s_\mathrm{z})$ of the electrons of the atomic shell, which couples with the orbital angular momentum $\mathbf{L}$ to the total angular momentum $\mathbf{J} = \mathbf{s} + \mathbf{L}$ [80]. The spin operator $\mathbf{s}$ can be understood as normal angular momentum in the sense that the orbital angular momenta and spins satisfy the same (SO (3) or SU (2)) Lie algebra [81]. Thus, they are hermitian and unitary: $[s_\mathrm{i}, s_\mathrm{j}] = \epsilon_\mathrm{ijk} s_\mathrm{k}$ with the Levi-Civita tensor ϵ_ijk. For the corresponding eigenvalue equations with eigenfunctions $|sm\rangle$ applies:

$$s_\mathrm{z}|sm\rangle = \hbar m|sm\rangle \quad \text{and} \quad \mathbf{s}^2|sm\rangle = \hbar^2 s(s+1)|sm\rangle \quad . \tag{4.1}$$

m and $s(s+1)$ are eigenvalues to s_z and $\mathbf{s}^2 = s_\mathrm{x}^2 + s_\mathrm{y}^2 + s_\mathrm{z}^2$, where $s = 0,\ 1/2,\ 1,\ \ldots$ denotes the spin quantum number and $m = -s, -s+1, \ldots, +s$ the magnetic spin quantum number, whereby there are always $2s+1$ possible values for m. In the simplest case, i.e., $s = 1/2$, as it is the case for protons or electrons, there are only two eigenfunctions along the z-axis, namely those with $m = +1/2$ for spin projection "up" and $m = -1/2$ for spin projection "down". Using the Pauli matrices σ_x, σ_y, σ_z, which form a basis of the hermitian and unitary 2×2 matrices, the effect of the angular momentum operators on spin 1/2 states, $s_\mathrm{i} = \hbar/2 \cdot \sigma_\mathrm{i}$, $i \in x, y, z$, can be investigated [82–84].

4.2 Polarization of a particle beam

While the spin is a property of an individual particle, the polarization is a property of an entire ensemble or beam. Thus, the polarization vector $\mathbf{P} = (P_\mathrm{x},\ P_\mathrm{y},\ P_\mathrm{z})$ is defined as the statistical average of an ensemble of classical spin vectors $\mathbf{P} = \langle \mathbf{s} \rangle$. In the quantum mechanical view, the polarization component P_i, $i \in x, y, z$, of an ensemble of particles is the expectation value $\langle \sigma_\mathrm{i} \rangle$

of the Pauli operator σ_i over all particles

$$P_\mathrm{i} = \langle \sigma_\mathrm{i} \rangle = \mathrm{tr}(\rho \sigma_\mathrm{i}) \quad . \tag{4.2}$$

Here, $\rho = \sum_{i=1}^{n} P_\mathrm{i} \cdot |sm_\mathrm{i}\rangle\langle sm_\mathrm{i}|$ is a density operator, by which information about the quantum statistical ensemble are specified. The trace of the density operator is normalized to unity and evidently, $0 \leq P_\mathrm{i} \leq 1$. n characterizes the number of pure states, i.e., $n = 2$ for protons and electrons, and P_i is the probability of finding the i-th state in the ensemble. For a magnetic field aligned in z-direction, the polarization P_z of such an ensemble is given by

$$P_\mathrm{z} = \langle \sigma_\mathrm{z} \rangle = \mathrm{tr}(\rho \sigma_\mathrm{z}) = p_+ \langle +|\sigma_\mathrm{z}|+\rangle + p_- \langle -|\sigma_\mathrm{z}|-\rangle = p_+ - p_- = \frac{N_+ - N_-}{N_+ + N_-} \quad , \tag{4.3}$$

where $p_\pm$ is the probability to find a particle in the quantum state $|1/2, \pm 1/2\rangle$, i.e., $p_\pm = {}^{N_\pm}\!/_{(N_+ + N_-)}$, where $N = N_+ + N_-$ is the amount of all particles in the beam. If $p_+ = p_-$, $N_\pm$ for $m = \pm 1/2$ are also equal representing a particle beam of zero polarization, i.e., $P_\mathrm{z} = 0$ [83–85].

Furthermore, it is obvious that the polarization vector of several particles $\mathbf{P}$ is therefore a weighted sum of classical spin vectors $\mathbf{s}_\mathrm{i}$

$$\mathbf{P} = \frac{1}{N} \sum_{i=1}^{N} \mathbf{s}_\mathrm{i} \quad , \tag{4.4}$$

with N defining the number of particles in a given volume, e.g., a simulation cell, within a certain energy range, if the action angle

$$\alpha_\mathrm{max} = \max_\mathrm{i} \left[\arccos \left(\frac{\mathbf{P}_0 \cdot \mathbf{s}_\mathrm{i,f}}{|\mathbf{P}_0| \cdot |\mathbf{s}_\mathrm{i,f}|} \right) \right] \tag{4.5}$$

between the initial polarization $\mathbf{P}_0$ and the finial spin vectors $\mathbf{s}_\mathrm{i,f}$ stays small [85].

4.3 Polarization and depolarization effects

In order to clearly characterize both, polarization and depolarization effects, a consistent description of the relevant mechanisms involved is important. After a brief overview, the three decisive mechanisms, namely

- the spin precession according to the Thomas-Bargmann-Michel-Telegdi (T-BMT) equation
- the Sokolov-Ternov effect
- the Stern-Gerlach effect

are outlined within the following three sections. For a better readability the formulas are given in cgs units. A schematic overview over these three polarization processes is presented in Fig. 4.1.

If the individual particle spins are treated in a semi-classical limit, it is the T-BMT equation (cf. Sec. 4.3.1) that describes the spin precession around the local electromagnetic field lines in dependence of the single particles' motion. As soon as further physical processes are considered, the link to the particle motion and the temporal spin evolution must be defined. Figure 4.2 shows the schematic overview of the interplay between the single particle trajectory (blue),

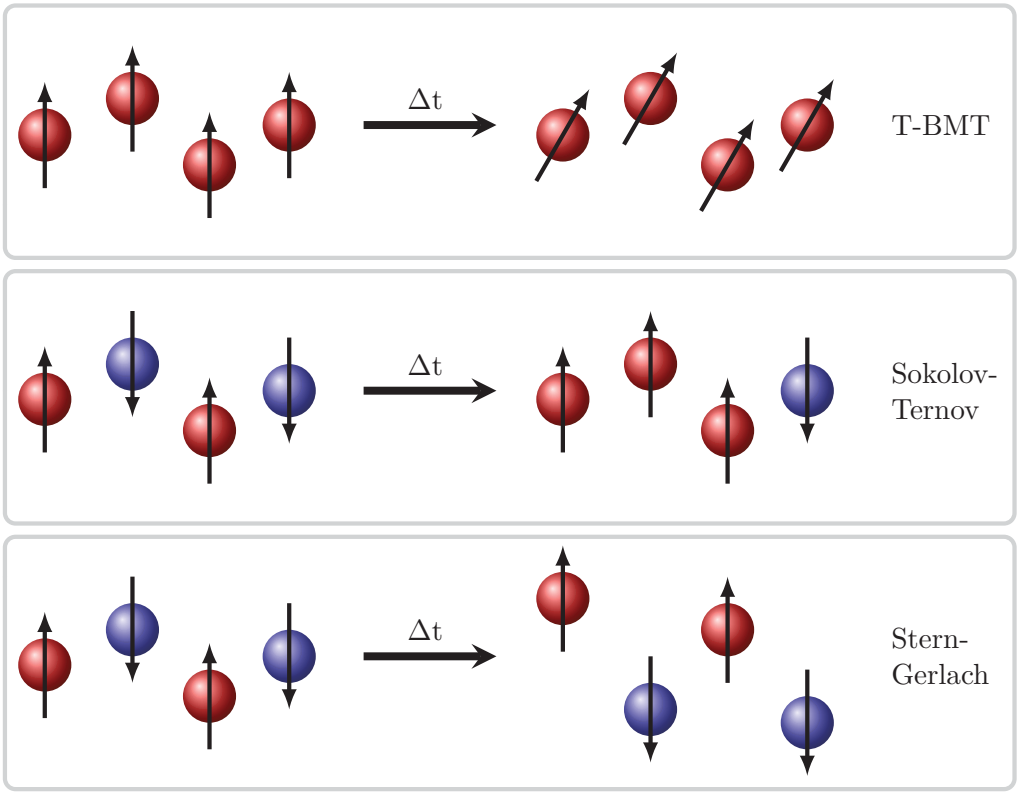

Figure 4.1: Schematic overview of the basic (de-)polarization processes for laser-driven particle beams. The red and blue spheres indicate the spin up and down states, respectively.
Top: time evolution for an initially fully polarized particle beam. The black arrows indicate the single particle spins, which are treated in a semi-classical limit following the T-BMT equation. The initial precession angles are observed under the action of a homogeneous magnetic field.
Middle: initially unordered spins individually flip in z-direction resulting in a certain polarization build up. The corresponding mechanism is known as the Sokolov-Ternov effect and is observed in circular electron accelerators.
Bottom: If the SG force acts constantly on an initially unpolarized and spatially unordered ensemble, the emergence of two polarized beams due to a spatial separation is expected.

the spin (green) and the radiation (yellow). In the non-QED regime, there is indeed a theory including the T-BMT equation that self-consistently describes the particle and spin motion in electromagnetic fields.

A direct coupling between single particle spins and radiation fields is covered in the context of quantum field theory. Within this theory, the mechanism describing the spontaneous self-polarization of an accelerated particle ensemble is known as the Sokolov-Ternov effect (cf. Sec. 4.3.2). The stochastic spin diffusion from photon emission is a non-deterministic process. It results in the rotation of the spin vector in the presence of a magnetic field by emitting a photon. The Sokolov-Ternov effect, which causes a spin flip, is widely used in classical accelerator physics to polarize electron beams in circular accelerators.

The Stern-Gerlach (SG) force (cf. Sec. 4.3.3) primarily effects the trajectory of a particle. If the particle energies are very high, radiation effects must also be taken into account. In most cases, the radiation-reaction force exceeds the SG force by far if the particles are relativistic (kinetic energies well above 1 GeV) or even ultra-relativistic (above 1 TeV). But for some cases, depending on the field configuration, the radiation-reaction force can be neglected compared

to the SG force (see e.g., Ref. [86]). The acceleration of charged particles is treated within the framework of the classical field theory in the classical and semi-classical limit. In this theory the back action of radiation on the particle motion as a result of the radiation-reaction force is explained.

Apart from that, spin precession is a deterministic process and, thus, can be investigated by treating the spin as an intrinsic electron magnetic moment [28, 30]. Another possible interpretation of this basic process is to introduce a spin-dependent radiation-reaction force analog to the Sokolov-Ternov effect, which characterizes a beam-filter mechanism similar to a combination of the SG and the radiation-reaction force [87].

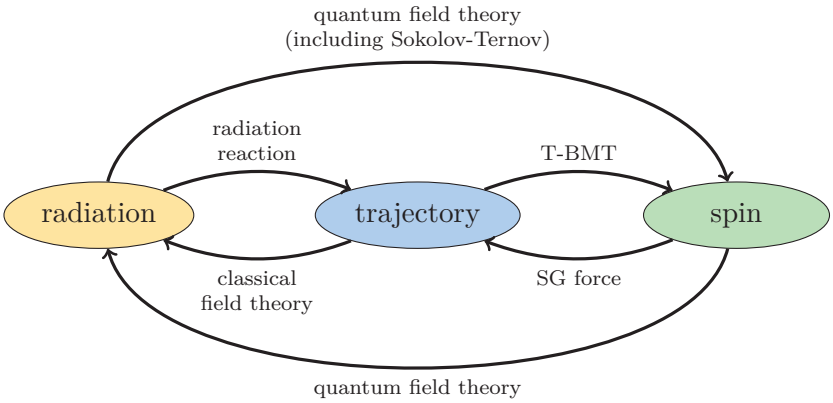

Figure 4.2: Schematic overview of the relations between radiation (yellow), single particle trajectory (blue) and spin (green). The black arrows indicate the basic physical process that connects two of these colored particle properties [30].

4.3.1 T-BMT equation

The classical dynamics for a charged spin particle is defined by the Thomas-Bargmann-Michel-Telegdi (T-BMT) equation for spin precession [88]. It was first introduced by Bargmann, Michel and Telegdi in 1959 using the Thomas approach and refers to the interaction of the magnetic dipole moment with external electromagnetic fields. Usually, the Foldy-Wouthuysen method is a matter of choice to understand the non-relativistic limit of the Dirac equation for problems, where the particle velocity is small. But it cannot be applied in presence of intense electromagnetic fields [89]. Another method would be the semi-classical limit [90] of the Dirac equation, given that the particle wavelength is small compared to the characteristic distance of the electromagnetic potential. It leads to a trajectory determined by the Lorentz force and an additional spin precession described by the T-BMT equation. Since the latter is preferred when dealing with relativistic velocities [91] it can be applied also for particles in laser fields to predict the rate of spin precession. In the following the T-BMT equation is derived for charged particles.

Following the discussion of Mane et al. in Ref. [85] for the derivation of the spin precession equation, the spin motion in any magnetic field $\mathbf{B}$ is a precession according to the interaction of the magnetic moment $\boldsymbol{\mu}$ of spin $\mathbf{s}$ with this field. In the relativistic case this assumption leads to the T-BMT equation, which describes the spin motion in arbitrary electric and magnetic fields. The equation of motion for an expectation value is given by the so-called Ehrenfest theorem [92]. Ehrenfest's theorem is a fundamental theorem of quantum mechanics valid in both, the

Schrödinger and the Heisenberg picture, in which the expectation value $\langle \hat{A} \rangle = \langle \psi | \hat{A} | \psi \rangle$ of the quantum operator $\hat{A}$ for a system in state $|\psi\rangle$ in the generalized from is

$$\frac{\mathrm{d}\langle \hat{A} \rangle}{\mathrm{d}t} = \left\langle \frac{\partial \hat{A}}{\partial t} \right\rangle + \frac{1}{i\hbar} \langle [\hat{A}, \hat{H}] \rangle \ , \tag{4.6}$$

where $\hat{H}$ is the Hamiltonian operator. Considering $\hat{A}$ being the spin operator $\hat{\mathbf{s}}$ for the Hamiltonian applying the Ehrenfest's theorem it follows

$$\hat{H} = -\hat{\boldsymbol{\mu}} \cdot \hat{\mathbf{B}} = \hat{\boldsymbol{\Omega}} \cdot \hat{\mathbf{s}} \ . \tag{4.7}$$

Here $\hat{\mathbf{B}}$ is the magnetic field, which is in principle also an operator, and $\hat{\boldsymbol{\Omega}}$ is the spin precession vector operator. Taking into account the commutator relation $[\hat{\mathbf{s}}, \hat{H}] = [\hat{\mathbf{s}}, \hat{\boldsymbol{\Omega}} \cdot \hat{\mathbf{s}}] = \mathrm{i}\hbar \hat{\boldsymbol{\Omega}} \times \hat{\mathbf{s}}$ and $\partial \hat{A} / \partial t = 0$ yields

$$\frac{\mathrm{d}}{\mathrm{d}t} \langle \hat{\mathbf{s}} \rangle = c \quad . \tag{4.8}$$

If $\hat{\boldsymbol{\Omega}}$ is constant, e.g., $\hat{\boldsymbol{\Omega}} = \Omega \mathbf{e}$, where $\mathbf{e}$ is a fixed unit vector, Eq. 4.8 simplifies to the equation of motion for a rigid-body spin precession

$$\frac{\mathrm{d}}{\mathrm{d}t} \langle \hat{\mathbf{s}} \rangle = \Omega \mathbf{e} \times \langle \hat{\mathbf{s}} \rangle \ , \tag{4.9}$$

with the solution starting from $t = 0$

$$\langle \hat{\mathbf{s}} \rangle_{\mathrm{t}} = \mathbf{e} \cdot \langle \hat{\mathbf{s}} \rangle_0 \, \mathbf{e} + \sin(\Omega t) \, \mathbf{e} \times \langle \hat{\mathbf{s}} \rangle_0 - \cos(\Omega t) \, \mathbf{e} \times (\mathbf{e} \times \langle \hat{\mathbf{s}} \rangle_0) \ . \tag{4.10}$$

This corresponds to a rotation around the axis $\mathbf{e}$ by the angle Ωt. Thus, the precession of a classical spin vector $\langle \hat{\mathbf{s}} \rangle$ describes the evolution of a spin state of a quantum system.

In classical accelerator physics, the spin depends on the orbital dynamical variables $\hat{\mathbf{x}}$ and $\hat{\mathbf{p}}$ (quantum operators) as follows

$$\frac{\mathrm{d}}{\mathrm{d}t} \langle \hat{\mathbf{s}} \rangle = \langle \hat{\boldsymbol{\Omega}}(\hat{\mathbf{x}}, \hat{\mathbf{p}}) \times \hat{\mathbf{s}} \rangle \ . \tag{4.11}$$

To calculate the expectation value $\hat{\boldsymbol{\Omega}}$ an auxiliary condition, the semi-classical approximation, is used. This approach refers to a theory, in which one part of a system is described quantum-mechanically, whereas the other is treated classically, e.g., external fields are treated to be constant, or when changing classically described as [93]

$$\langle \hat{\boldsymbol{\Omega}}(\hat{\mathbf{x}}, \hat{\mathbf{p}}) \rangle \approxeq \hat{\boldsymbol{\Omega}}(\langle \hat{\mathbf{x}} \rangle, \langle \hat{\mathbf{p}} \rangle) \ , \tag{4.12}$$

with the c-number expectation values of the position and momentum operator $\langle \hat{\mathbf{x}} \rangle$ and $\langle \hat{\mathbf{p}} \rangle$. $\langle \hat{\mathbf{x}} \rangle$ and $\langle \hat{\mathbf{p}} \rangle$ can be visualized by specifying a classical orbital theory, i.e., $\mathbf{x} \equiv \langle \hat{\mathbf{x}} \rangle$, $\mathbf{p} \equiv \langle \hat{\mathbf{p}} \rangle$ and $\mathbf{s} \equiv \langle \hat{\mathbf{s}} \rangle$. Transferred to the semi-classical approximation $\boldsymbol{\Omega}_{\mathrm{sc}} \equiv \boldsymbol{\Omega}(\mathbf{x}, \mathbf{p})$ is obtained, from which it follows that

$$\frac{\mathrm{d}\mathbf{s}}{\mathrm{d}t} \approxeq \boldsymbol{\Omega}_{\mathrm{sc}} \times \mathbf{s} \ . \tag{4.13}$$

Thus, the spin motion of a quantum system can be described by the classical spin vector $\mathbf{s}$ and the semi-classical spin precession vector $\boldsymbol{\Omega}_{\mathrm{sc}}$.

For a non-relativistic spin $\mathbf{s}$ the Hamiltonian is given by

$$H = -\boldsymbol{\mu} \cdot \mathbf{B} = -\frac{ge}{2mc} \mathbf{s} \cdot \mathbf{B} \ . \tag{4.14}$$

The magnetic moment $\boldsymbol{\mu}$ is an axial vector, which is proportional to the particle spin $\mathbf{s}$. The proportionality factor is determined by the mass m, the speed of light c, the charge e and the Landé factor of the particle g, respectively. For the spin precession movement yields

$$\frac{\mathrm{d}\mathbf{s}}{\mathrm{d}t} = \boldsymbol{\mu} \times \mathbf{B} \ . \tag{4.15}$$

Hence, the interaction of the magnetic moment $\boldsymbol{\mu}$ of a particle in an external magnetic field $\mathbf{B}$ causes a torque and, thus, a change of the particle spin over time. From the Dirac equation of quantum electrodynamics, which is valid for point-like particles, $g \approx 2$ results. With composite particles like the proton, additional magnetic moments occur due to the finite charge distribution, which are described by the gyromagnetic anomaly G, so that $g = 2(1 + G)$, with $G_{\text{proton}} = 1.792846$. Thus, $g_{\text{proton}} = 5.585694$. However, the g-factors of nucleons cannot be calculated precisely due to the non-perturbative nature of Quantum Chromodynamics (QCD).

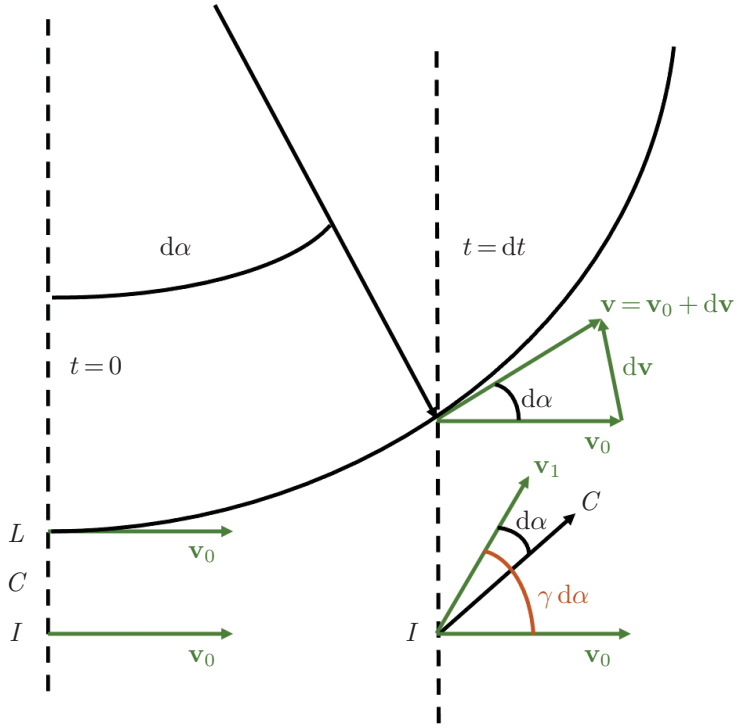

Figure 4.3: Coordinate system and initial frames for spin motion according to the T-BMT equation, adapted from Ref. [85].

Considering a particle with charge e moving with the relativistic velocity $\mathbf{v}$ in an electric field $\mathbf{E}$ and a magnetic field $\mathbf{B}$ in the laboratory system on a trajectory described by the Lorentz equation, for the momentum $\mathbf{p}$ considering $\boldsymbol{\beta} = \mathbf{v}/c$ it follows

$$\frac{\mathrm{d}\mathbf{p}}{\mathrm{d}t} = e\left(\mathbf{E} + \boldsymbol{\beta} \times \mathbf{B}\right) \ , \tag{4.16}$$

so that

$$\frac{\mathrm{d}\boldsymbol{\beta}}{\mathrm{d}t} = \frac{e}{mc\gamma}\left(\mathbf{E} - \mathbf{E}\cdot\boldsymbol{\beta}\boldsymbol{\beta} + \boldsymbol{\beta}\times\mathbf{B}\right) \ , \tag{4.17}$$

with the Lorentz factor $\gamma = 1/\sqrt{(1-\boldsymbol{\beta}^2)}$. For both frames the C and the I coordinate origins coincide with the laboratory frame L at $t=0$, as depicted in Fig. 4.3. The spin $\mathbf{s}$ is defined only for the particle rest frame C. That is why another rest-frame C' is introduced, defined as follows: first, a boost from the laboratory frame L to an intermediate frame F at velocity v_1 (arbitrary) is performed. Then, a second boost with velocity v_2, so that the combined Lorentz boost $\mathcal{L}(v_2)\mathcal{L}(v_1)$ gives the final particle velocity $v_\mathrm{t} = 0$. But the rest-frame spin $\mathbf{s}$ is not well-defined unless the Lorentz transformation from the laboratory frame to the particle rest frame is accomplished by a single boost. The particle then rotates under an angle $\mathrm{d}\boldsymbol{\alpha}$ at an infinitesimal time $t = \mathrm{d}t$ later, considered as a kinematic effect

$$\mathrm{d}\boldsymbol{\alpha} = \frac{\boldsymbol{\beta}\times\mathrm{d}\boldsymbol{\beta}}{\beta^2} = \frac{\boldsymbol{\beta}\times\dot{\boldsymbol{\beta}}}{\beta^2}\,\mathrm{d}t \ . \tag{4.18}$$

Here,

$$\frac{\boldsymbol{\beta}\times\dot{\boldsymbol{\beta}}}{\beta^2} = -\frac{e}{mc\gamma}\left[\mathbf{B}_\perp - \frac{\boldsymbol{\beta}\times\mathbf{E}}{\beta^2}\right] \ , \tag{4.19}$$

for a motion in prescribed external electric and magnetic fields with

$$\mathbf{B}_\parallel = \frac{\mathbf{B}\cdot\boldsymbol{\beta}\boldsymbol{\beta}}{\beta^2} \ , \qquad \mathbf{B}_\perp = \mathbf{B} - \mathbf{B}_\parallel = \frac{\boldsymbol{\beta}\times(\mathbf{B}\times\boldsymbol{\beta})}{\beta^2} \ . \tag{4.20}$$

$\mathbf{B}_\parallel$ denotes the components of the magnetic fields parallel and $\mathbf{B}_\perp$ perpendicular to the velocity $\mathbf{v}$, respectively. Under a Lorentz boost with the relativistic factor γ from the laboratory system to the moving systems at $t = 0$ applies

$$\mathbf{B}_\mathrm{C} = \gamma\left[\mathbf{B}_\perp - \boldsymbol{\beta}\times\mathbf{E}\right] + \mathbf{B}_\parallel \ . \tag{4.21}$$

The spin changes in a certain time interval $\mathrm{d}\tau = \mathrm{d}t/\gamma$ according to Eq. 4.15, by

$$(\mathrm{d}\mathbf{s})_\mathrm{I} = -\frac{ge}{mc}\,\mathbf{B}_\mathrm{C}\times\mathbf{s}\,\mathrm{d}\tau \ , \tag{4.22}$$

with the two introduced frames, the particle rest frame C and an initial frame I moving with particle velocity $v_{\mathrm{t}=0}$. In order to determine the spin change in the particle rest frame, it must be taken into account that C itself rotates relative to the initial frame under the angle $\mathrm{d}\phi$. This is obtained by subtraction

$$\mathrm{d}\mathbf{s} = (\mathrm{d}\mathbf{s})_\mathrm{I} - \mathrm{d}\phi\times\mathbf{s} \ . \tag{4.23}$$

Since the rest frame is oriented at the angle $-\,\mathrm{d}\alpha$ at time $\mathrm{d}t$ relative to the new velocity $v + \mathrm{d}v$ and since both directions rotate γ times faster in the moving initial system than in the laboratory system, one finds for the angle $\mathrm{d}\phi$

$$\mathrm{d}\phi = \gamma\,\mathrm{d}\alpha - \mathrm{d}\alpha = (\gamma - 1)\,\mathrm{d}\alpha \ . \tag{4.24}$$

Summing up the findings from the last equations yields

$$\mathrm{d}\mathbf{s} = \left[-\frac{e}{mc\gamma}\,\mathbf{B}_\mathrm{C} \times \mathbf{s} - \frac{\gamma - 1}{\beta^2}\,(\boldsymbol{\beta} \times \dot{\boldsymbol{\beta}}) \times \mathbf{s} \right] \mathrm{d}t \ , \tag{4.25}$$

which can also be written in the form

$$\frac{\mathrm{d}\mathbf{s}}{\mathrm{d}t} = -\boldsymbol{\Omega} \times \mathbf{s} \ . \tag{4.26}$$

Here, $\boldsymbol{\Omega}$ is the spin precession vector, which is defined as

$$\boldsymbol{\Omega} = \boldsymbol{\mu} \cdot \frac{\mathbf{B}_\mathrm{c}}{\gamma} + \omega_\mathrm{T} \ , \tag{4.27}$$

with the Thomas precession vector ω_T given by

$$\omega_\mathrm{T} = -\frac{\gamma - 1}{\beta^2}\,\boldsymbol{\beta} \times \dot{\boldsymbol{\beta}} = -\frac{\gamma^2}{\gamma + 1}\,\boldsymbol{\beta} \times \dot{\boldsymbol{\beta}} \ . \tag{4.28}$$

The spin precession vector $\boldsymbol{\Omega}$ in Eq. 4.27 consists of two terms. The first one describes a magnetic dipole interaction with the magnetic field of the rest frame, time-delayed by the factor γ. In the second term the Thomas precession (cf. Eq. 4.28), which occurs due to relativistic dynamics, is presented [88]. This term is independent of electric and magnetic fields and, thus, would even exist if the acceleration $\dot{\mathbf{v}}$ were caused due to gravitation or other non-electromagnetic forces [85, 94].

If particles with mass m, charge $q \cdot e$, magnetic moment anomaly $a = 2g - 1$ and velocity v move in an electromagnetic field $\mathbf{B}$, $\mathbf{E}$ with vanishing gradient, their spin vectors $\mathbf{s}_\mathrm{i}$ precess around the local electromagnetic fields and evolve according to the T-BMT equation as

$$\boldsymbol{\Omega} = -\frac{q \cdot e}{mc}\left[\Omega_\mathrm{B}\mathbf{B} - \Omega_\mathrm{v}\left(\frac{\mathbf{v}}{c} \cdot \mathbf{B}\right)\frac{\mathbf{v}}{c} - \Omega_\mathrm{E}\frac{\mathbf{v}}{c} \times \mathbf{E}\right], \tag{4.29}$$

where

$$\Omega_\mathrm{B} = a + \frac{1}{\gamma} \ , \qquad \Omega_\mathrm{v} = \frac{a\gamma}{\gamma + 1} \ , \qquad \Omega_\mathrm{E} = a + \frac{1}{1 + \gamma} \ . \tag{4.30}$$

Considering an N-particle ensemble, where all spin vectors precess coherently, a certain polarization changes its orientation in space but its absolute value is conserved provided that all particles saw the same electromagnetic field and moved on similar trajectories [30, 95, 96].

4.3.2 Sokolov-Ternov effect

The spontaneous buildup of self-polarization via the emission of spin-flip synchrotron radiation of relativistic and charged particles moving at high energy in a background guiding magnetic field is called radiative polarization, also known as the Sokolov-Ternov effect [85, 97–99]. The theoretical formulation of this effect was first developed by Ternov et al. in 1962 for large-scale storage rings stating that the photon emission couples to the particle-spin operator at the higher orders of Quantum Electrodynamics (QED) perturbation theory [97]. In 1964, Sokolov and Ternov expanded their theory and established a quantitative solution based on calculating the Dirac equation for the electron motion for initially unpolarized particles in a homogeneous

magnetic field [98]. They presented an exponentially behaving polarization buildup (starting from zero) in the vertical direction

$$P(t) = P_{\mathrm{s}} \cdot (1 - \exp(-t/\tau_{\mathrm{pol}})) \tag{4.31}$$

converging to the asymptotic (equilibrium) degree of the polarization $P_{\mathrm{s}} = {}^{8}\!/_{5\sqrt{3}} \simeq 0.924\,\%$ with a strongly energy dependant polarization buildup time $\tau_{\mathrm{pol}} \propto B^{-3}E^{-2}$ for a beam of energy E circulating in a uniform magnetic field B. Thus, the beam polarization can and does approach the theoretical limit. For positrons, the direction of the asymptotic polarization is parallel to the guiding magnetic field, while it is anti-parallel for electrons. Within their approach Sokolov and Ternov describe the radiation intensities for the spin-flip terms taking into account the spectral power density $\mathcal{P}(\omega)$, summing over the σ and π modes, as

$$W^{\uparrow\downarrow}(\zeta) = \int_0^\infty \mathcal{P}^{\uparrow\downarrow}(\zeta,\omega)\ \mathrm{d}\omega\ , \tag{4.32}$$

where $\zeta = \pm 1$ is the initial spin state and ω is the unit frequency. Accordingly, the number of spin-flip photons emitted per unit frequency per unit time is given by

$$\mathcal{N}^{\uparrow\downarrow}(\zeta,\omega) = \frac{\mathcal{P}^{\uparrow\downarrow}(\zeta,\omega)}{\hbar\omega}\ . \tag{4.33}$$

From that, the spin-flip transition probabilities per unit time, from up to down and vice-versa, are calculated as

$$p\pm = \int_0^\infty \mathcal{N}^{\uparrow\downarrow}(\zeta = \mp 1,\omega)\, d\omega\ . \tag{4.34}$$

Finally, the equilibrium degree of polarization is

$$P_{\mathrm{eq}} = \frac{N_+ - N_-}{N_+ + N_-} = \frac{p_+ - p_-}{p_+ + p_-}\ , \tag{4.35}$$

where the "up" and "down" spin populations are denoted by N_+ and N_-. In equilibrium, $N_+ p_- = N_- p_+$. Thus, the equilibrium polarization is only determined by the spin-flip amplitudes [85].

The Sokolov-Ternov effect was first experimentally observed with just a low polarization [100, 101] and later on optimized at several electron rings to generate a highly polarized beam during storage [102–107]. Thereby, it was also discovered that spin-polarized beams are subject to depolarizing resonances. Until today it is a great scientific challenge of spin dynamics to calculate the strengths of these depolarizing resonances, and to devise the ways, both theoretically and experimentally, to avoid, overcome and eliminate them [85].

Unlike electrons, protons emit no significant synchrotron radiation and, therefore, do not polarize spontaneously according to the theory of Sokolov and Ternov for large-scale storage rings. An interesting question is whether this also applies to the acceleration of particles in laser-plasma accelerators. The corresponding answer is given in our publication (Ref. [30]) and in Sec. 5.2.

4.3.3 Stern-Gerlach effect

In the original experiment by Stern and Gerlach [79] silver atoms from a source first were collimated with an aperture to shape a regular beam before they move through a spatial region, where an inhomogeneous magnetic field $\mathbf{B}(\mathbf{r})$ was applied. For the sake of simplicity, it is assumed that the components of the field and its gradients along one direction – hereafter the z-axis – are much larger than the components perpendicular to it, thus $\mathbf{B}(\mathbf{r}) = B_\mathrm{z}\mathbf{e}_\mathrm{z}$. In the inhomogeneous magnetic field every (silver) atom experiences a force

$$\mathbf{F} = -\nabla(\boldsymbol{\mu}\cdot\mathbf{B}) \approxeq \mu_\mathrm{z}\frac{\partial B_\mathrm{z}}{\partial z}\mathbf{e}_\mathrm{z} \propto s_\mathrm{z}\frac{\partial B_\mathrm{z}}{\partial z}\mathbf{e}_\mathrm{z} \ , \tag{4.36}$$

where $\boldsymbol{\mu} = -g\frac{\mu_\mathrm{B}}{\hbar}\mathbf{s}$ is the magnetic dipole moment of the atom, μ_z is its z-component and s_z is the z-component of the spin with the Landé factor g, μ_B is the Bohr magneton, $\hbar$ the reduced Planck's constant and $\mathbf{s}$ the spin vector.

Classically, one would expect that the orientation of the spins of the atoms at the exit of the source is arbitrary – no spatial direction is preferred. Accordingly, the z-component of the spin vector should take any value in a continuous interval $s_\mathrm{min} \leq s_\mathrm{z} \leq s_\mathrm{max}$, i.e., a continuous deflection spectrum is expected. This "classic" scenario is not confirmed experimentally. Instead, in an experiment with silver atoms only two spots were observed, which correspond to the values $s_\mathrm{z} = \pm\hbar/2$ of the spin component. Thus, in the SG experiment the quantization of the spin – or more precisely the value of the component of the spin along an (arbitrary) direction – is proven.

However, decades of experience with subatomic beams in conventional particle accelerators demonstrate that beams do not separate into spin "up" and "down" beamlets since the SG force is dominated by the Lorentz force for charged particles, even for non-relativistic systems. In relativistic systems, the magnitude of the SG force decreases very fast with increasing Lorentz factor γ and is completely dominated by the Lorentz force [85].

It is discussed in Sec. 5.3 if there is any chance to build up a certain polarization due to a beam separation according to the SG effect in a laser-plasma based accelerator.

4.4 Measurement of nuclear spin polarization

The measurement of the nuclear spin polarization of hydrogen atoms is a crucial research objective for the construction of a pre-polarized target for laser-induced proton acceleration. For this purpose the so-called Lamb-Shift Polarimeter (LSP) [108] is a very useful tool, since on the one hand the degree of polarization can be measured directly, i.e., within a few seconds, with high absolute accuracy and on the other hand a complete LSP is available for the execution of experiments. The LSP consists of six components shown in Fig. 4.4 and is based on the measurement of Lyman-α transitions after Stark quenching of meta-stable atoms whose Zeeman hyperfine states have been selected using a spin filter. In the following, the exact function of this polarimeter is explained in detail.

To measure the occupation numbers of the Lyman-α substates, the transition of all Zeeman states into the ground state $^2\mathrm{S}_{1/2}$ using the Lamb shift is required. Besides the fine structure and hyperfine structure splitting, the Lamb shift is a correction that was not predicted by the Dirac equation. This theory says that states with the same main quantum number n and the same total angular momentum quantum number j in the hydrogen atom are degenerate with

respect to the orbital angular momentum quantum number l. However, in 1947 Willi Eugene Lamb and Robert Curtis Retherford measured an energy difference between the $^2S_{1/2}$ ($l=0$) and $^2P_{1/2}$ ($l=1$) energy levels of the hydrogen atom of $1058\,\mathrm{MHz} = 4.4{\cdot}10^{-6}\,\mathrm{eV}$ [109]. This can be explained with an electromagnetic interaction of the orbiting electron with the virtual photons. Compared to the harmonic oscillator in quantum mechanics, the zero-point energy of the electromagnetic field deviates from the defined zero in QED. Thus, a perturbation of the Coulomb potential results in a change of the effective potential close to the nucleus ($r=0$). That is why mostly those orbitals with a large probability of the electron being located close to the nucleus, namely the s-orbitals, are affected. Today, the QED permits to calculate the Lamb shift more precisely than it can be measured.

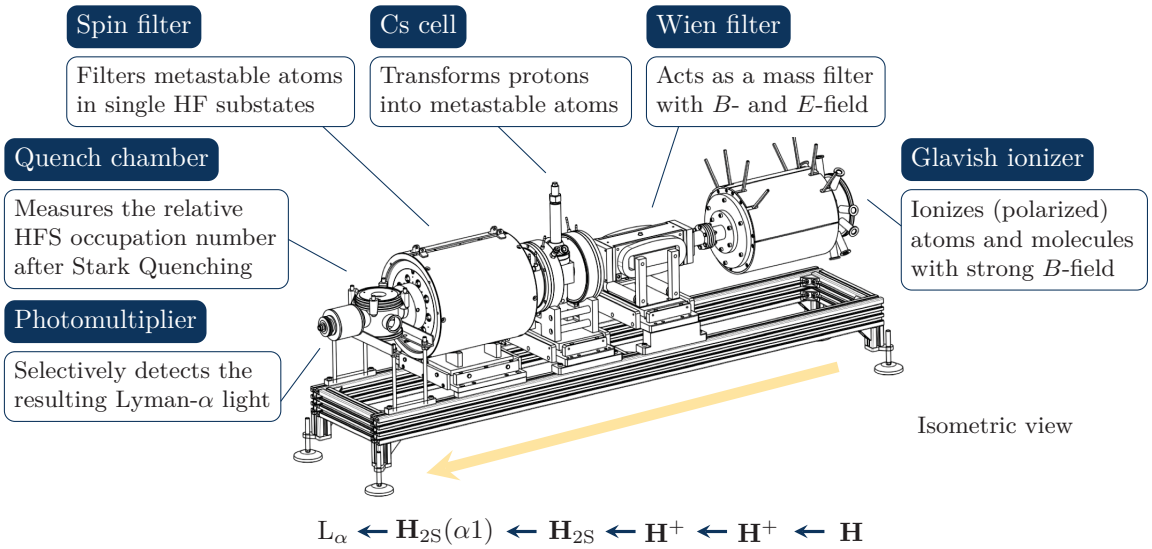

Figure 4.4: Schematic overview of the Lamb-Shift Polarimeter (LSP) [108] and its components for measuring the proton polarization.

The Breit-Rabi diagram in Fig. 4.5 shows the dependence of the binding energies of the individual hyperfine-structure states in the excited state with quantum number $n=2$ for hydrogen on an applied magnetic field. As can be seen from the figure, the Zeeman effect does not fully cover the influence of external magnetic fields. In the weak magnetic field, the Zeeman region, the nuclear spin $I=1/2$ and the total electron spin $J=1/2$ of the hydrogen atom couple to form the total spin $F=0$ or $F=1$, as $F=I+J$. Consequently, the spin projection m_F can take the values $m_\mathrm{F} \in [\text{-}1, 0, 1]$. The total spin F additionally induces a magnetic moment, which is aligned parallel, perpendicular or antiparallel to the applied magnetic field. This results in a slight modification of the binding energy of these three Zeeman states, so that the state $^2S_{1/2}$ is split into four substates, one for $F=0$ and three for $F=1$, characterized by the quantum numbers $|F, m_\mathrm{F}\rangle$. With the transition to stronger magnetic fields, the Paschen-Back region, J and I are aligned separately, since the coupling of core and shell spins breaks up accordingly. The four Zeeman states, characterized by the quantum numbers $|F, m_\mathrm{F}\rangle$, in turn form four substates

which, taking into account the general solution of the Schrödinger equation, are as follows

$$\begin{aligned}
&1. \quad |F=1, m_\mathrm{F}=+1\rangle = |m_\mathrm{J}=+1/2, m_\mathrm{I}=+1/2\rangle \\
&2. \quad |1,0\rangle = \frac{1}{\sqrt{2}}\Big[\sqrt{1+a}\,|+1/2,-1/2\rangle + \sqrt{1-a}\,|-1/2,+1/2\rangle\Big] \\
&3. \quad |1,-1\rangle = |-1/2,-1/2\rangle \\
&4. \quad |0,0\rangle = \frac{1}{\sqrt{2}}\Big[\sqrt{1-a}\,|+1/2,-1/2\rangle - \sqrt{1+a}\,|-1/2,+1/2\rangle\Big] \ .
\end{aligned} \tag{4.37}$$

Here, 1. and 3. are pure states, whereas the solutions 2. and 4. are mixed states defined by the mixing parameter a

$$a = \frac{B}{\sqrt{B_\mathrm{c}^2 + B^2}} = \frac{{}^{B}/_{B_\mathrm{c}}}{\sqrt{1+\left({}^{B}/_{B_\mathrm{c}}\right)^2}} \ , \tag{4.38}$$

which only depends on the external magnetic field B and the critical magnetic field strength

$$B_\mathrm{c} = \frac{\Delta E_\mathrm{HFS}}{2\mu_\mathrm{B}} = 6.347\,\mathrm{mT} \ , \tag{4.39}$$

for the $^2\mathrm{S}_{1/2}$ excited state. $\Delta E_\mathrm{HFS} = 7.34{\cdot}10^{-7}\,\mathrm{eV}$ is the energy difference of the hyperfine splitting in the absence of a magnetic field and μ_B is the Bohr magneton. Thus, $B \ll B_\mathrm{c}$ denotes a weak magnetic field, i.e., in the Zeeman region, while $B \gg B_\mathrm{c}$ specifies a strong field.

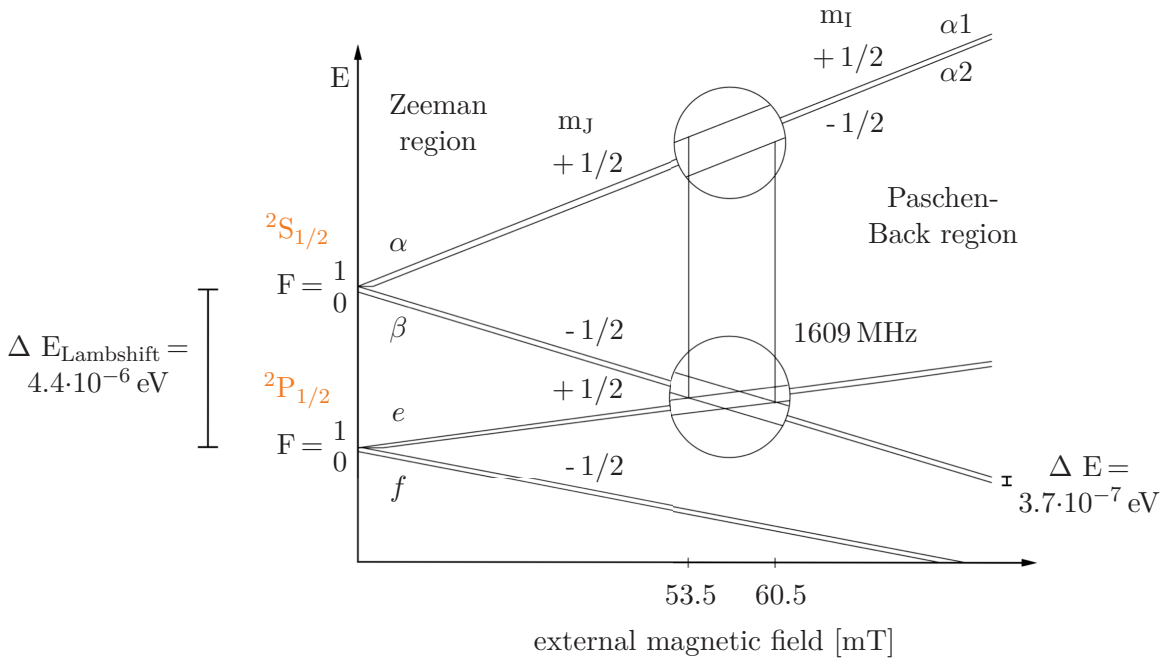

Figure 4.5: Breit-Rabi diagram for the excited state with quantum number $n = 2$ for hydrogen, adapted from Ref. [108].

Applying an external longitudinal magnetic field of 53.5 mT (Paschen-Back region) and a transverse electric field of about 10 V/cm combined with a radio frequency of 1.60975 GHz, whose peak width at half-height in the resonance chamber of the spin filter is about 1 MHz, results in an oscillation between the states $\alpha 1$ and $e1$ due to a strong coupling. This can be controlled with the RF power. The slightly shifted resonances of the $\alpha 2$ and $e2$ substates are responsible for a weaker coupling between these states and, thus, for the depopulation of the

$\alpha 2$ state via the short-living e state. Thus, only the $^2S_{1/2}$, $|m_J = +1/2,\ m_I = +1/2\rangle$ state of the hydrogen atom is transmitted through the spin filter, while all other states are quenched into the ground state. If the high frequency is switched off at the end of the spin filter, all remaining atoms in the $e2$ state also decay into the ground state and only the $\alpha 1 = |m_J = +1/2,\ m_I = +1/2\rangle$ state remains occupied. Likewise, only the $\alpha 2 = |m_J = +1/2,\ m_I = -1/2\rangle$ state of the hydrogen atom is transmitted at 60.5 mT. Therefore, ramping the magnetic field of the spin filter allows metastable atoms to pass through the spin filter at 53.5 mT ($\alpha 1$) and 60.5 mT ($\alpha 2$) only. By counting these residual atoms the nuclear polarization of the incoming atoms can be deduced with the LSP.

It should be mentioned that an electric dipole transition from $^2P_{1/2}$ to $^1S_{1/2}$ is possible by photon emission. Since the photon is a spin-1 particle, there is a shift from $P(L=1)$ to $S(L=0)$. Here the preservation of orbital angular momentum ($J = S + L$) and parity ($\pi = (-1)^L$) is guaranteed. The transition from the $^2S_{1/2}$ state to the $^1S_{1/2}$ state is very unlikely due to the long lifetime of the $^2S_{1/2}$ state (0.14 s), but still possible by a two-photon emission as demonstrated by Hänsch et al. [110]. Furthermore, the lifetime of the $^2P_{1/2}$ state is relatively short with 10^{-9} s due to the dipole transition. Even when an electric dipole transition from the $^2S_{1/2}$ substates into the corresponding $^2P_{1/2}$ substates is possible, a natural decay is not observed due to the extremely small energy difference in between [108, 111–113].

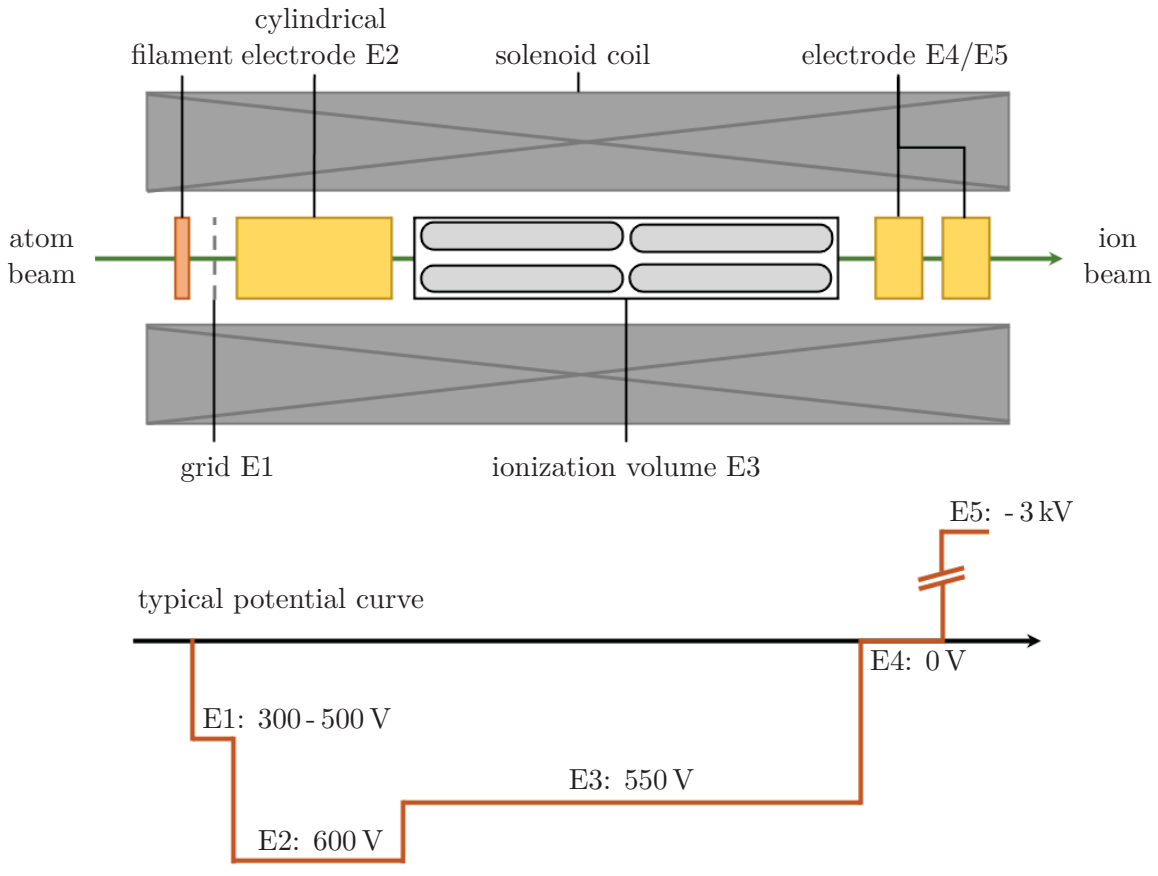

Figure 4.6: Working principle of the Glavish-type electron-collision ionizer, adapted from Ref. [108].

The functionality of the individual components is described below [108, 111–113].

Glavish ionizer The first component of the LSP is an electron-impact ionizer of the Glavish type as depicted in Fig. 4.6 [114]. It ionizes the hydrogen in its strong magnetic field to preserve the nuclear polarization. The ionizer consists first of a filament, from which electrons are emitted and accelerated in the direction of the first grid (E1), which is at a positive potential, into the strong magnetic field of a solenoid coil. By the cylinder electrode E2 the electrons are focused into the ionization volume E3 that is set from 500 V to 3000 V to define the potential energy of the ions. The filament and the electrode E4 form a potential trap for the emitted electrons, since their potentials are each at 0 V. Thus, the highest possible electron density can be achieved. Furthermore, the applied external magnetic field forces the electrons onto a spiral track, so that a large number of the hydrogen's sheath electrons can be stripped off by collisions with the free electrons in the potential trap: $e + {}^1\mathrm{H} \rightarrow 2e + \mathrm{H}^+$. In parallel, the magnetic field serves to decouple the nuclear spins of the electrons from the shell spins of the protons so that the polarization is not destroyed by the electron collisions. The ions produced at the potential E3 can escape only in the direction of E4, since the potential E2 has a repulsive effect on them. Hence, the negative potential on the electrode E5 serves as an accelerating lens attracting the protons and accelerating them to velocities of about $4.4{\cdot}10^5$ m/s on the one side, while they are decelerated on the other side. In sum, the beam energy is not changed, but the beam is better focused on the axis. The proton beam generated in this way has a relatively sharp energy, but is still divergent, which is compensated by an additional electrostatic lens behind the ionizer. Even though the efficiency of the Glavish ionizer is with 10^{-4} to 10^{-3} one to two orders of magnitude lower than other types, it offers the opportunity to distinguish individual hyperfine substates with the same nuclear spin by varying the strong magnetic field, i.e., the measured polarization of the pure state. For example, $\alpha 1$ does not depend on the magnetic field, but on the corresponding state $\beta 4 = \sqrt{a+1}\,|\,-1/2, +1/2\,\rangle - \sqrt{a-1}\,|\,+1/2, -1/2\,\rangle$ it does. The ionizer can also be operated in the so-called plasma mode, so that a burning plasma is created between E1 and E3. Although this has the advantage of an increasing efficiency, the operation is much more unstable and the beam energy is not as well defined as in this mode it decreases from $E_{\mathrm{beam}} \approx \mathrm{E3}$ to $E_{\mathrm{beam}} \lesssim \mathrm{E3}$.

Wien filter After leaving the ionizer, the now ionized proton beam enters the Wien filter. Its purpose is to separate atomic and molecular ions in the beam according to their masses using a combination of a static electric $\mathbf{E}$ and a magnetic field $\mathbf{B}$, arranged perpendicular to each other and both perpendicular to the beam direction [115]. Thus, the hydrogen ions with charge q and velocity v experience an electrostatic force $\mathbf{F}_{\mathrm{el}}$ and an opposing Lorentz force $\mathbf{F}_{\mathrm{L}}$ so that only ions in the force equilibrium are transmitted through the Wien filter

$$\mathbf{F}_{\mathrm{el}} = \mathbf{F}_{\mathrm{L}} \Longleftrightarrow q\mathbf{E} = q\mathbf{v} \times \mathbf{B} \tag{4.40}$$

with

$$v = \frac{|\mathbf{E}|}{|\mathbf{B}|} \ . \tag{4.41}$$

In this way, all other ions are removed from the beam and the background is lowered. As all hydrogen ions, e.g., H^+ and H_2^+, are accelerated by the same electric potential E3, they gain

identical kinetic energies and their velocities vary by a factor of $\sqrt{2}$. Like that they can be clearly identified when the intensity of the through-going ion beam is measured with help of a Faraday cup and an oscilloscope as function of the electric field in the Wien filter. Beside the mass separation, the Wien filter also has the purpose of rotating the polarization angle in the vertical plane perpendicular to the magnetic field, so that the projection of the proton polarization to the beam axis can be controlled later. When entering the magnetic field with (anti-)parallel spin orientation compared to the beam direction, the ions begin to precess around the magnetic field direction with the Larmor frequency ω_{Larmor}

$$\omega_{\mathrm{Larmor}} = \frac{2\mu_{\mathrm{p}}\mathbf{B}}{\hbar} \ , \tag{4.42}$$

where μ_{p} is the magnetic moment of the proton. Only the projection of the nuclear polarization on the beam axis $P_{\mathrm{z}} = \sin(a) \cdot P_0 = \sin(\omega_{\mathrm{Larmor}} \cdot t) \cdot P_0$ can be determined with the spin filter, which depends now on the time-of-flight t and the transverse magnetic field B. In normal operation the magnetic field B is chosen to rotate the spin by $a = 180°$ and, thus, the measured polarization P_{z} must be inverted to get the beam polarization P_0. Behind the Wien filter there is another electric lens to focus the beam on the axis.

Caesium cell In the caesium cell, the transmitted ions are transformed into metastable atoms in the $2S_{1/2}$ state by capturing an electron from the caesium vapor known as charge-exchange reaction: $\mathrm{Cs} + \mathrm{H}^+ \rightarrow \mathrm{Cs}^+ + \mathrm{H}_{2\mathrm{S}_{1/2}}$. This process produces metastable $\mathrm{H}_{2\mathrm{S}_{1/2}}$ atoms with an efficiency of up to 30 %, being most profitable for proton energies of 0.5 keV and an areal number density of $1.2{\cdot}10^{14}$ Cs atoms/cm^2 [116]. Technically, the caesium cell consists of a stainless steel container and a caesium ampoule enclosed into it. Before the experiment is started, it is mechanically cracked from the outside so that the liquid caesium enters the container. As the top of the container is heated to about 60 °C and its bottom to 160 °C, caesium vapor is formed, which is crossed by the ion beam on axis, condenses again at the top and drips into the container so that it can be reused. Additionally, the cell is equipped with two coils forming a longitudinal holding field of up to about 50 mT. Consequently, more than 99 % of the initial polarization is maintained in the metastable atoms [113].

Spin filter The spin filter separates metastable atoms in the Zeeman states $\alpha 1$ and $\alpha 2$ by means of a static magnetic field, a static electric field and a RF field of 1.60975 GHz. In total, the spin filter consists of seven coils whose homogeneity is important for the transmission of the individual Zeeman components. Inside the solenoid is a cylindrical cavity with a length and diameter adapted to the high frequency field. As explained above, this setup only transmits the metastable atoms in the hyperfine substate $\alpha 1$ at a magnetic field of 53.5 mT, and the substate $\alpha 2$ at 60.5 mT. All other states are quenched to the ground state [117].

Quench chamber The last component of the LSP is the quench chamber with a Faraday cup. By using a strong electric field of an electric lens of several 100 V/cm all residual metastable atoms are quenched into the ground state under the emission of a Lyman-α photon with a wavelength of $\lambda = 121$ nm (10.2 eV). This process is also referred to as the Stark effect, which is analog to the Zeeman effect, but for electric fields. These photons are selectively detected by a

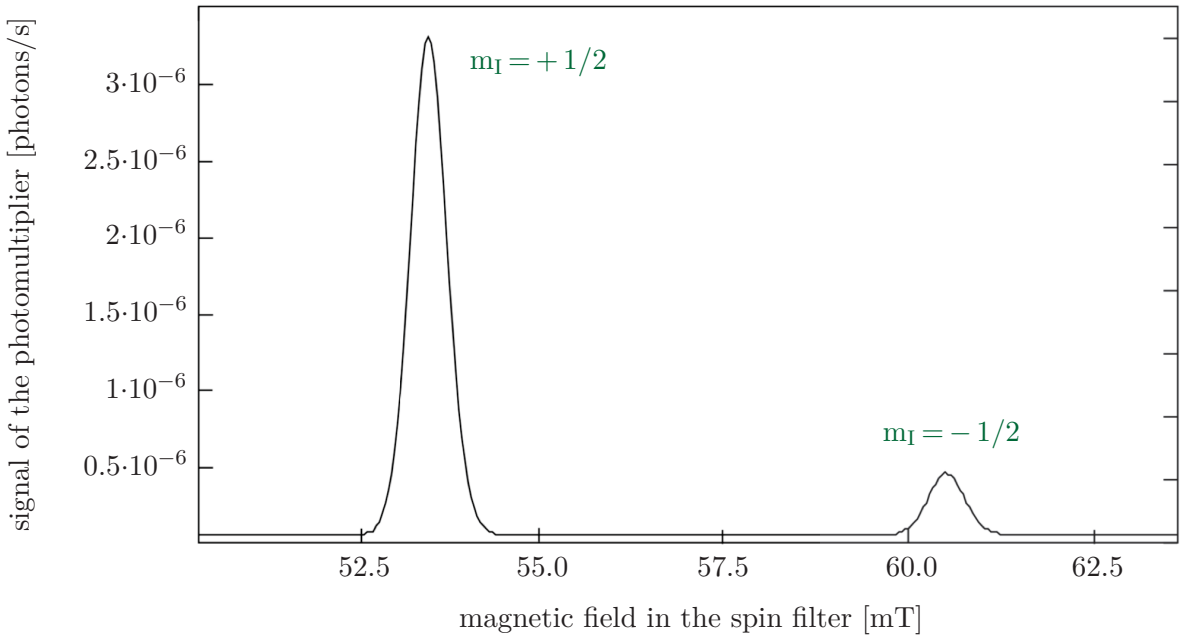

Figure 4.7: Typical Lyman spectrum of a polarized hydrogen beam of atoms mostly in the Zeeman state $\alpha 1$ of the $^1S_{1/2}$ state entering the ionizer. The ratio of peak height to linear background in this example is about 70:1. The ratio of the two peak heights for the state $m_I = +1/2$ and $m_I = -1/2$ is equivalent to the summed intensities, i.e., the areas under the two peaks, and corresponds here to 8.1:1. Using Eq. 4.35, the degree of polarization can be determined as $P_{Ly}(1) = 0.780$, adapted from Ref. [108].

photomultiplier with a photocathode made from KBr and an entrance window made by MgFl to define the sensitivity range from 115 nm to 165 nm. Its signal as function of the magnetic field in the spin filter leads to a spectrum with separated peaks for the hyperfine substates transmitted by the spin filter as shown in Fig. 4.7.

The sensitivity of the LSP is sufficient to measure the polarization at limited beam intensities. For example, an incoming beam of 10^{12} atoms/s generates a proton beam of 10^9 particles/s and an amount of metastable atoms behind the caesium cell of about 10^8 per second. Thus, for an unpolarized beam about 10^7 residual metastable atoms/s leave the spin filter and are quenched to get the same amount of Lyman-α photons. The efficiency of the photomultiplier of 10^{-3} allows then to register 10^4 Lyman-α photons/s, which is not difficult to observe with an oscilloscope. Compared to other polarimeters, the LSP has three decisive advantages.

- Depending on the intensity of the incoming atomic beam the polarization can be measured very quickly, within a few seconds. This allows to monitor modifications in the experimental parameters in time and, therefore, simplifies the handling of the complete experiment.

- This method of polarization measurement is very descriptive: the vector (spin-1/2 and spin-1 particles) and tensor (spin-1 particles) polarization can be read directly from the ratio of the peak contents in the Lyman spectrum, which clearly reduces errors in the analysis of the results (cf. Fig. 4.7).

- When measuring the full atomic beam of an Atomic Beam Source (ABS) like the one for the ANKE/COSY experiment of about $3{\cdot}10^{16}$ particles/s, the statistical error can be neglected after only a few seconds of measurement time. The systematic error is in the range of 1 % and, thus, dominant.

Using the LSP the polarization of many atomic hydrogen and deuterium ensembles has been measured in several experiments during the last years. Just two examples are highlighted in the following.

- The LSP has been applied to measure the spin dependence of many nuclear reactions produced in a polarized internal gas target developed for the ANKE spectrometer at COSY. The target consists of an ABS providing nuclear-polarized hydrogen or deuterium, a vacuum target chamber, and the LSP. With this setup the transition units could be tuned and the polarization of the ABS beam could be controlled. It was found to be stable within 5 % during one week of operation [118].

- The nuclear polarization of hydrogen or deuterium molecules has also been measured by ionizing the molecules and injecting the H_2^+ or D_2^+ ions into the LSP. With this technique the H_2^+ ions have been separated from the protons in 1 keV beams by the Wien filter and the nuclear polarization of both components has been experimentally determined with a precision of 2 % or better [113].

4.5 Status quo of experiments on laser-accelerated spin-polarized protons

Experimental data on the degree of polarization of laser-accelerated particles are very sparse. The first and up to now only published experimental results are from our group and have been obtained at the ARCTURUS laser system at HHUD using an unpolarized foil target. In Fig. 4.8 the experimental setup is schematically depicted.

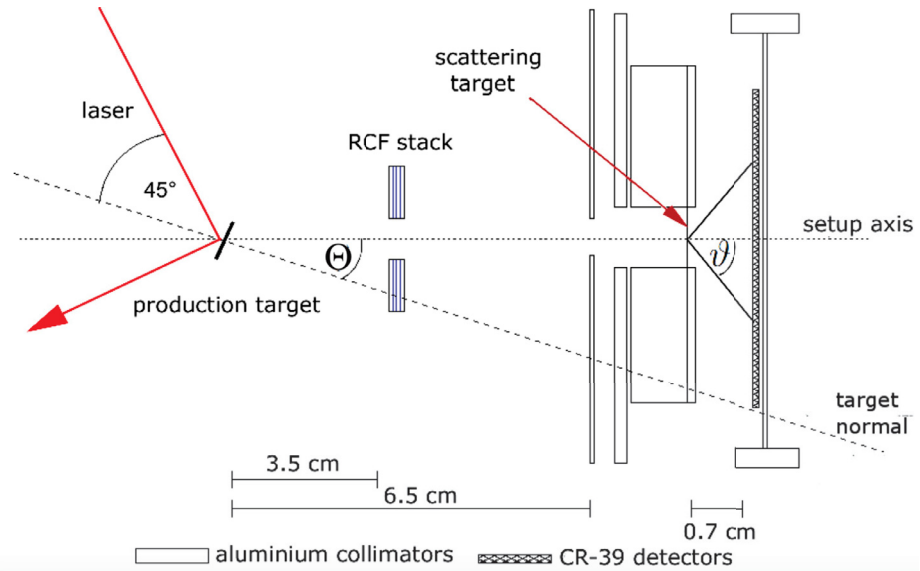

Figure 4.8: Schematic view of the setup for the first proton polarization measurement performed at HHUD. For illustration purposes, the angle Θ is drawn larger than in reality [34].

For the measurements the 100 TW Ti:Sa laser system with a typical pulse duration of 25 fs and a repetition rate of 10 Hz was used producing an intensity of several $10^{20}\,\mathrm{Wcm}^{-2}$ when being focused on the target. Impinging the laser pulse in a 45° angle on an unpolarized gold foil of 3 μm thickness, protons with an energy of typically a few MeV are produced. They are accelerated according to the TNSA mechanism (cf. Sec. 3.2.1) towards a stack of three RCF detectors, where the number of protons is measured. In a Silicon target with a thickness of 24 μm elastic scattering takes place. Behind this scattering target, CR-39 detectors are placed, covering scattering angles ϑ of up to 68° as well as the complete azimuthal range ϕ. Hence, the number of protons impinging on the Silicon target is analysed shot-by-shot from the dose on the calibrated RCF detectors.

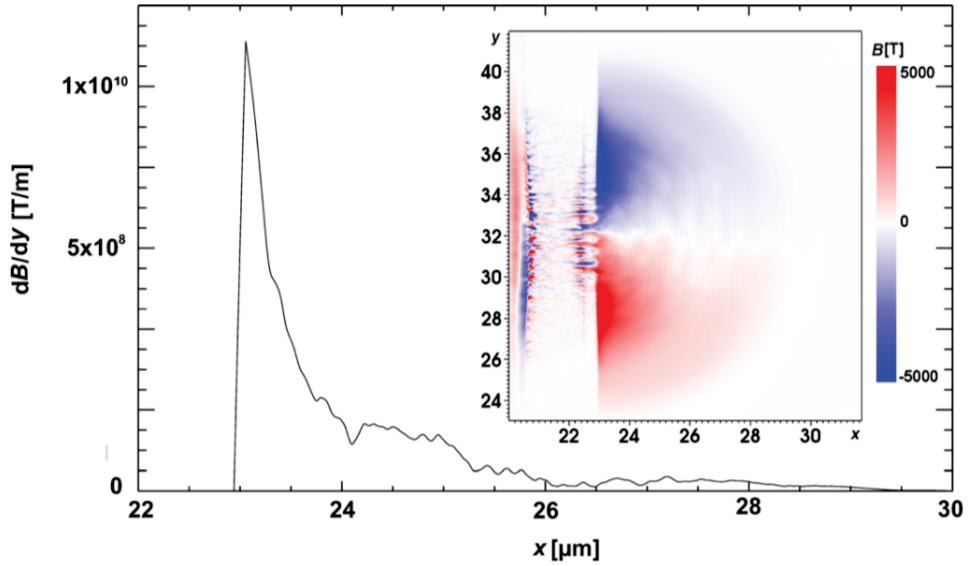

Figure 4.9: 2D simulation of the magnitude of polarizing magnetic fields acting on the laser-accelerated protons [34].

To estimate the magnitude of possible polarizing magnetic fields acting on the laser-accelerated protons in the experiment, PIC simulations have been carried out with the fully relativistic 2D code EPOCH [34, 119]. The simulation was performed for a normally incident laser fitting to the parameters mentioned above on a Au foil (2.5 μm thickness, $6 \cdot 10^{22}\,\mathrm{cm}^{-3}$ density, charge state 6^+) with a proton layer (0.5 μm, $2{\cdot}10^{23}\,\mathrm{cm}^{-3}$). A B-field strength of $\sim 10^4$ T and gradients of 10^{10} T/m are expected from the simulation. Although these values are rather high, they are yet too small to align the proton spins and do not yield of measurable proton polarization (cf. Fig. 4.9).

The authors of Ref. [34] conclude that for measuring a proton polarization $P \neq 0$ both, a stronger laser pulse with an intensity of about $10^{23}\,\mathrm{Wcm}^{-2}$ and an extended gas instead of a thin foil target, are needed. Such a scenario has been theoretically considered in a paper by Shen et al. (cf. Sec. 3.2.2) [72].

5 Identification of the Relevant Processes for Polarized Proton Acceleration

As already outlined in Secs. 3 and 4, the acceleration of polarized particles in strong laser and plasma fields promises an attractive opportunity to obtain polarized beams in the MeV or even GeV range. In conventional linear accelerators a reduction of the beam polarization is negligible due to the very short interaction time between accelerating fields and particle bunches. To overcome depolarizing spin resonances in circular accelerators, the polarization is maintained by applying complex correction techniques. For laser-plasma driven accelerators, the depolarization time for relativistic particles is not yet known, although it is of crucial importance to build the next generation of highly compact and cost-optimized accelerator facilities.

Based on the theoretical background summarized in Sec. 4.3, in this section the feasibility of polarized proton acceleration in strong fields without destroying an initial polarization is evaluated. Possible polarization losses caused by spin precessions described by the T-BMT equation, the Sokolov-Ternov effect and the SG effect are studied and corresponding scaling laws for the (de-)polarization times are formulated. For this, two relevant subprocesses have been identified: i) the injection of low energetic ($\gamma \approx 1$) particles into accelerating fields; ii) the subsequent acceleration of already relativistic ($\gamma \gg 1$) particles. In this section the focus is put on the detailed description of phase ii). The mechanisms taking place in phase i) have been scrutinized in the work of Yitong Wu, ..., Anna Hützen et al. [120] and Meng Wen et al. [121]. Finally, the analytic formulas are compared to test-particle simulations. The following discussion is part of the publication by Johannes Thomas, Anna Hützen et al. [30]. An equivalent discussion about the (de-)polarization of electrons can be found in the same reference.

5.1 T-BMT

First, a scaling law for the minimum depolarization time for protons in strong fields considering the T-BMT equation (cf. Eq. 4.26) is derived. Thereto, the system variables are normalized to the elementary charge e, electron mass m_e, speed of light c, momentum $m_\mathrm{e}c$, energy $m_\mathrm{e}c^2$, spin $\hbar/2$, the time $\omega_\mathrm{L} = \sqrt{4\pi e^2 n_\mathrm{c}/m_\mathrm{e}}$ with the critical plasma density n_c, the length k_L^{-1} and the laser field strength $E_0 = m_\mathrm{e}c\omega_\mathrm{L}/e$. For a rather asymmetric field configuration, a clear conclusion about the conservation of a given polarization $\mathbf{P}$ is difficult. This is why for a conclusive analysis Eq. 4.26 needs to be solved for every particle. The maximum action angle α_max (cf. Eq. 4.5) between the initial polarization $\mathbf{P}_0$ and the final spin vectors $\mathbf{s}_\mathrm{i,f} = \mathbf{s}_\mathrm{i}(t)$ during the time t has to be estimated analytically. Assuming that the individual spin precessions are incoherent, their absolute values would be reduced to $P(t) = P_0 - \sin(\alpha_\mathrm{max})$. Thus, if α_max is of the order of $\pi/2$, a complete depolarization of the N-particle ensemble is expected and the corresponding time is referred to as minimum depolarization time t_D.

For a more precise estimation of t_D, a relativistic ($|\mathbf{v}| \approx c$) ensemble, in which all particles have almost the same energy but move in various directions, is considered. Thus, the single spin precession axes are not aligned. Moreover, the rotation around the ω-axis can be interpreted as a superposition of the precessions around the $\mathbf{B}$-, $\mathbf{v}$- and $\mathbf{v} \times \mathbf{E}$-axis. A suitable assumption for

the absolute value of the precision frequency is given by

$$|\mathbf{\Omega}| \leq \frac{m_\mathrm{e}}{m_\mathrm{p}}\Big(\Omega_\mathrm{B}|\mathbf{B}| + \Omega_\mathrm{v}|\mathbf{B}| + \Omega_\mathrm{E}|\mathbf{E}|\Big) \ , \tag{5.1}$$

where the equal sign applies if all precession axes are aligned and Ω_B, Ω_v and Ω_E correspond to the definition in Eq. 4.30.

Aiming at calculating a lower limit for t_D, an upper limit of $|\mathbf{\Omega}|$ has to be derived. Considering that, the dominant field strength $F = \max(\mathbf{E}, \mathbf{B})$ is substituted for $|\mathbf{B}|$ and $|\mathbf{E}|$, so that

$$\begin{aligned} |\mathbf{\Omega}| &< \frac{m_\mathrm{e}}{m_\mathrm{p}}\Big(\Omega_\mathrm{B} + \Omega_\mathrm{v} + \Omega_\mathrm{E}\Big) \cdot F \\ &< \frac{m_\mathrm{e}}{m_\mathrm{p}}\left(a_\mathrm{p} + \frac{1}{\gamma} + \frac{a_\mathrm{p}\gamma}{\gamma+1} + a_\mathrm{p} + \frac{1}{1+\gamma}\right) \cdot F \\ &< \underbrace{3a_\mathrm{e}F}_{\Omega_{\mathrm{p,\,TeV}}} + \frac{m_\mathrm{e}}{m_\mathrm{p}} \underbrace{\left(\frac{1}{\gamma} - a_\mathrm{p} - \frac{a_\mathrm{p}\gamma}{\gamma+1} + \frac{1}{1+\gamma}\right)}_{\frac{1}{\gamma}+\frac{1-a_\mathrm{p}}{1+\gamma}} \cdot F \ , \end{aligned} \tag{5.2}$$

using $m_\mathrm{e}/m_\mathrm{p} = a_\mathrm{e}/a_\mathrm{p}$, where $a_\mathrm{e} = \alpha/2\pi \approx 10^{-3}$ is the anomalous magnetic moment of the electron and α is the fine-structure constant and $a_\mathrm{p} \approx 1.8$ is the anomalous magnetic moment of the proton.

For relativistic ($\gamma \gg 1$) protons carrying an energy of a few hundred GeV, the second term in Eq. 5.2 is negligible due to the large anomalous magnetic moment $a_\mathrm{p} > 1$. Under consideration of $\gamma \gg 1/a_\mathrm{e}$ for electrons of more than 10 GeV energy, it applies that the (near) TeV proton-spin motion is equivalent to that of a GeV electron if the external fields show a certain asymmetry.

For protons with energy in the few GeV range, γ is close to unity but still $|\mathbf{v}| \approx 1$. Coming back to Eq. 5.2, the precession frequency then reads as

$$\begin{aligned} \Omega_{\mathrm{p,\,GeV}} &\approx \Omega_{\mathrm{p,\,TeV}} + \frac{m_\mathrm{e}}{m_\mathrm{p}}\left(\frac{1}{\gamma} + \frac{1-a_\mathrm{p}}{1+\gamma}\right) \cdot F \\ &\approx a_\mathrm{e}F\left(3 + \frac{0.6}{a_\mathrm{p}}\right) \\ &\approx 3.3a_\mathrm{e}F \ . \end{aligned} \tag{5.3}$$

For ions with smaller anomalous magnetic moment than a_p the precession frequency in Eq. 5.3 is much less than $3.3a_\mathrm{e}F$. This is why Eq. 5.3 is interpreted as the relevant limit for the work presented within the scope of this thesis. Hence, the minimum depolarization time for protons is

$$t_\mathrm{D,p} = \frac{\pi}{2\Omega_{\mathrm{p,\,GeV}}} = \frac{\pi}{6.6a_\mathrm{e}F} \ , \tag{5.4}$$

being independent of the particles' energy.

As the focus is put on particle acceleration in strong fields, the dominant field strength F has to be in the same range compared to that of laser-plasma accelerators. To do so, the laser field strength E_0 is interpreted as the relevant laser field and F is expected to be in the order of unity given that the particle beam is separated by the laser pulse itself. Usually, the corresponding plasma fields are $\epsilon = \omega_\mathrm{p}/\omega_\mathrm{L}$ times smaller than E_0 [122]. In order to conserve the proton polarization in fields as strong as those in a plasma wakefield, $F \equiv \epsilon$ is set. When substituting $F = 1$,

for relativistic ions, the minimum depolarization time is $t_{\mathrm{D,L}} \approx 520\,\omega_{\mathrm{L}}^{-1}$. Considering a wakefield, the lower limit is in the order of $t_{\mathrm{D,W}} \approx 520\,\omega_{\mathrm{L}}^{-1}\epsilon^{-1} \gg t_{\mathrm{D,L}}$. For experimentally reasonable values, $t_{\mathrm{D,L}}$ is in the range of picoseconds. Compared to the interaction with a passing laser pulse in the range of a few femtoseconds, like the 10 PW laser system at SULF (cf. Tab. 1), this time span is long enough to guarantee polarization conservation. Considering wakefield acceleration in underdense plasma, the given time is in accordance with an acceleration length of a few mm [30].

5.2 Sokolov-Ternov

In the next step, the polarization buildup due to slightly varying probabilities for a spin flip from down to up $\mathcal{P}^{\uparrow}$ compared to an up-down flip $\mathcal{P}^{\downarrow}$ during the emission of synchrotron radiation, known as the Sokolov-Ternov effect (cf. Sec. 4.3.2), is investigated. This section examines the question whether spontaneous self-polarization, as is the case for accelerated or stored particle bunches in conventional accelerators, can also occur in laser-plasma accelerators. For this, the characteristic polarization time from protons in laser- and plasma fields is calculated by firstly introducing a Lagrangian describing the complete Sokolov-Ternov effect

$$L_{\mathrm{tot}} = L_{\mathrm{EM}} + L_{\mathrm{SG}} + L_{\mathrm{RAD}} + L_{\mathrm{ST}} \ . \tag{5.5}$$

In this equation the Lagrangian

$$L_{\mathrm{EM}} = -\frac{mc^2}{\gamma} + \frac{q}{c}\mathbf{v}\cdot\mathbf{A}_{\mathrm{EM}} - q\varphi_{\mathrm{EM}} \tag{5.6}$$

characterizes the motion of the particle in an external electromagnetic field with $\mathbf{E} = -\nabla\varphi - 1/c\cdot\partial\mathbf{A}_{\mathrm{EM}}/\partial t$ with the generic field φ and $\mathbf{B} = \nabla\times\mathbf{A}_{\mathrm{EM}}$. The spin interaction Lagrangian reads as

$$L_{\mathrm{SG}} = -\boldsymbol{\Omega}_{\mathrm{spin}}\cdot\mathbf{s} \ . \tag{5.7}$$

Accordingly, the Lagrangian modifying the emitted back radiation acting on the particle trajectories

$$L_{\mathrm{RAD}} = \frac{q}{c}\mathbf{v}\cdot\mathbf{A}_{\mathrm{rad}} - q\varphi_{\mathrm{rad}} \tag{5.8}$$

and the one describing a direct coupling between radiation and spin due to $\boldsymbol{\Omega}_{\mathrm{rad}} = \boldsymbol{\Omega}(\mathbf{E}_{\mathrm{rad}}, \mathbf{B}_{\mathrm{rad}})$

$$L_{\mathrm{ST}} = -\boldsymbol{\Omega}_{\mathrm{rad}}\cdot\mathbf{s} \ . \tag{5.9}$$

is defined. Aiming at quantizing the system and finding the transition probabilities, the corresponding Hamiltonian can be found in literature [123, 124]

$$H_{\mathrm{tot}} = H_{\mathrm{EM}} + H_{\mathrm{SG}} + H_{\mathrm{RAD}} + H_{\mathrm{ST}} \ , \tag{5.10}$$

where

$$H_{\mathrm{EM}} = \gamma mc^2 + q\varphi_{\mathrm{EM}} \ , \qquad H_{\mathrm{SG}} = \boldsymbol{\Omega}_{\mathrm{spin}}\cdot\mathbf{s} \ , \tag{5.11}$$

$$H_{\mathrm{RAD}} = q\varphi_{\mathrm{rad}} - \frac{q}{c}\mathbf{v}\cdot\mathbf{A}_{\mathrm{rad}} \ , \qquad H_{\mathrm{ST}} = \boldsymbol{\Omega}_{\mathrm{rad}}\cdot\mathbf{s} \ . \tag{5.12}$$

Using Eqs. 4.31, 4.34, and 4.35 the average transition rates are approximated as [125, 126]

$$\alpha\pm = \frac{1}{4}\int_{\mathbb{R}} \mathrm{d}\tau' \langle 0|\overline{[(\omega\cdot\eta)_{\mathrm{t}+\tau/2}(\omega\cdot\eta^*)_{\mathrm{t}-\tau/2}]_\pm}|0\rangle \ , \tag{5.13}$$

with

$$\alpha\pm = p_+ \pm p_- \tag{5.14}$$

making the connection between the transition rates and the corresponding spin-flip probabilities.

Taking into account the latest relations, the T-BMT equation can be reformulated

$$\dot{s}_\mathrm{n} = \hbar^{-1}\alpha_-(s^2 - s_\mathrm{n}^2) - \alpha_+ s_\mathrm{n} \ , \qquad\qquad s_\mathrm{n} = \mathbf{s}\cdot\mathbf{n} \ , \tag{5.15}$$

where $\mathbf{n}$ denotes the equilibrium polarization axis. It has be be mentioned that $\alpha_+ s_\mathrm{n}$ is of pure quantum origin and, thus, a non-local function of the trajectory. If concentrating on the relevant case, the laser-plasma acceleration, where the motion is assumed to be ultra-relativistic, the change of the acceleration is very short compared to the length $\propto|\gamma\dot{\mathbf{v}}|^{-1}$, in which the radiation is shaped. That is why the integral in α_+ must be considered only in the region $|\tau|\propto|\gamma\dot{\mathbf{v}}|^{-1}$. With the help of Refs. [123] and [127] the region of importance is estimated as

$$\mathbf{r}(r+\tau) \approx \mathbf{r}(t) + \mathbf{v}(t)\tau + \dot{\mathbf{v}}(t)\frac{\tau^2}{2} + \ddot{\mathbf{v}}(t)\frac{\tau^3}{6} \ . \tag{5.16}$$

As at $\gamma \gg 1$ the radiation is emitted into a cone with opening angle $\propto\gamma^{-1}$ about the velocity, in Ref. [123] the average transition rates are quantified under the assumption that the particles move across the field lines in a homogeneous field

$$\alpha_- \approx -\frac{q^2\hbar\gamma^5|\dot{\mathbf{v}}|^3}{m^2c^8}\left(1 + \frac{14}{3}a + 8a^2 + \frac{23}{3}a^3 + \frac{10}{3}a^4 + \frac{2}{3}a^5\right) \ , \tag{5.17}$$

and

$$\alpha_+ \approx -\alpha_-\frac{|a|}{a} + R(a) \ , \tag{5.18}$$

where a is the anomalous magnetic moment and the rest term R reads as

$$\begin{aligned} R = \frac{q^2\hbar\gamma^5|\dot{\mathbf{v}}|^3}{\exp\left(\sqrt{12}a\right)m^2c^8}\Bigg[\Bigg(-1 - \frac{11}{12}a + \frac{17}{12}a^2 + \frac{13}{24}a^3 - a^4\Bigg)\frac{|a|}{a} \\ + \frac{1}{\sqrt{3}}\left(\frac{15}{8} + \frac{41}{24}a - \frac{115}{48}a^2 - a^3 + \frac{7}{4}a^4\right)\Bigg] \ . \end{aligned} \tag{5.19}$$

The above three equations are exact if the radiation is assumed to be quasi-classical. In addition, the polarization time $t_\mathrm{pol} = 1/\alpha_+(x)$ for particles with spin $\hbar/2$ and the equilibrium polarization P_eq is defined as $P_\mathrm{eq} = \alpha_-/\alpha_+$.

For the particular case of protons with a moderate anomalous magnetic moment $a_\mathrm{p} \approx 1.8$, the R term is suppressed, such that

$$\alpha_-(1.8) \approx -128\cdot\frac{e^2\hbar\gamma^5|\dot{\mathbf{v}}|^3}{m^2c^8} \ , \tag{5.20}$$

and

$$R(1.8) \approx 0.0004 \cdot \frac{e^2\hbar\gamma^5|\dot{\mathbf{v}}|^3}{m^2c^8} \quad . \tag{5.21}$$

From that it follows that

$$t_{\mathrm{pol}}^{-1} = \alpha_+(1.8) \approx 128 \cdot \frac{e^2\hbar\gamma^5|\dot{\mathbf{v}}|^3}{m^2c^8} \ll t_{\mathrm{min}}^{-1} \quad . \tag{5.22}$$

To find a more intuitive description of the polarization time, it is set as a function of the kinetic energy T and the maximum field strength F, known from the previous section, so

$$\frac{|\dot{\mathbf{v}}|}{c} = \frac{eF}{\gamma mc} \quad . \tag{5.23}$$

Inserting Eq. 5.23 into Eq. 5.22 and using $e^2 = \alpha\hbar c$ and $\gamma_{\mathrm{p}} = T/(mc^2)$, results in a term for the characteristic polarization time

$$t_{\mathrm{pol}} = \frac{(mc^2)^7}{128\alpha(\hbar c)^2(eF)^3T^2c} \quad . \tag{5.24}$$

For high energetic protons with $T = 100\,\mathrm{GeV}$, moving in a field with the strength $F = 10^{17}\,\mathrm{V/m}$ (corresponding to a laser with peak intensity $10^{24}\,\mathrm{Wcm^{-2}}$) and accordingly $eF = 10^8\,\mathrm{GeV/m}$ and $mc^2 = 1\,\mathrm{GeV}$, it can be approximated that $t_{\mathrm{pol}} \approx 10^{-5}\,\mathrm{s}$. Taking this result, the final scaling law can be derived

$$t_{\mathrm{pol}} = \frac{10^{14}\,\mathrm{s}}{T[\mathrm{GeV}]^2 \cdot F[\mathrm{TV/m}]^3} \quad . \tag{5.25}$$

Substituting values known from conventional circular accelerators, i.e., $F \approx 10^{-4}\,\mathrm{TV/m}$, yields polarization times of the order of million years for TeV protons. This is in line with the well-known fact that protons in storage rings cannot be spin polarized via the SG effect. For laser-plasma accelerators, the field strength is a thousand times higher, but the acceleration distance is in the range of decimeters or smaller, which corresponds to about one nanosecond particle-field interaction. But since, as shown, the polarization time is several orders of magnitude higher, the Sokolov-Ternov effect and, thus, the self-polarization in laser-plasma accelerators can be neglected. Furthermore, this effect does not need to be implemented in corresponding numerical simulation studies on polarized laser-driven proton acceleration, such as PIC codes.

It should be mentioned that for electrons further theoretical investigations have been reported. Geng et al. discussed polarization effects within the quantum radiation-reaction regime stating that a collision of an initially unpolarized electron beam with an ultra-intense laser pulse leads to a significant polarization [128, 129]. In other approaches, the Sokolov-Ternov effect is not included, but rather different QED effects like the strongly nonlinear Compton scattering [130, 131] or the Breit-Wheeler process [132] predicting an electron-spin polarization during the interaction with strong fields from laser-induced QED plasmas [133–135]. Despite that Kotkin et al. disagree on a polarization buildup resulting from a collision between an electron bunch and a single circularly polarized laser pulse [136].

5.3 Stern-Gerlach

Finally, the possibility of polarization losses induced by the Stern-Gerlach (SG) force is investigated. In more detail, the spin-back action on the particle trajectory for fast ($|\mathbf{v}| \approx c$) and charged spin 1/2-particles with uncorrelated movement is estimated. Before doing so, it has to be pointed out that the applied semi-classical approach causes a continuous spread of the particle beam (cf. Fig. 4.1). However, in the context of the SG force, the phrase "split" will be used in the following, as it seems to be a more adequate description of this effect.

Already more than 60 years ago, a potential separation of spin states of charged particles has attracted the attention of N. Bohr [137] who held the opinion that quantum effects would destroy the separated trajectories in a SG like setup. He argued that the spatial uncertainty of the particles along the direction of the magnetic gradient would result in an uncertainty in the Lorentz force in a similar scale compared to the force that separates the spin states [34]. About 40 years later, Garraway and Stenholm deemed that a spatial splitting in the momentum space is sufficient and a spatial separation in the interaction region is not required. In a suitable scheme for practical implementation they presented a SG type of experiment, in which this splitting is predicted for particle beams of small diameter in the field region and at sufficiently long propagation times. These requirements seem achievable in laser-plasma experiments as the size of the field region matches the focal diameter of the laser pulse [33, 34, 138].

In order to quantify the SG force in dependence of the spin precession, again the Lagrange formalism is used [139]

$$L_{\mathrm{tot}} = L_{\mathrm{EM}} + L_{\mathrm{SG}} \ . \tag{5.26}$$

L_{EM} and L_{SG} are defined similarly as in the Sokolov-Ternov section, Eqs. 5.6 and 5.7.

Taking this ansatz, in the next step the canonical momentum $\mathbf{P}$ is determined

$$\mathbf{P} = \gamma m \mathbf{v} + \frac{q}{c}\mathbf{A} + \mathbf{P}_{\mathrm{SG}} \ , \tag{5.27}$$

where $\mathbf{P}_{\mathrm{SG}} = \nabla_{\mathrm{v}} L_{\mathrm{SG}}$. From the Lagrange equation of motion

$$\frac{\mathrm{d}(\gamma m \mathbf{v})}{\mathrm{d}t} = \frac{\mathrm{d}\mathbf{p}_{\mathrm{kin}}}{\mathrm{d}t} = \mathbf{F}_{\mathrm{tot}} = \mathbf{F}_{\mathrm{EM}} + \mathbf{F}_{\mathrm{SG}} \tag{5.28}$$

the Lorentz force

$$\mathbf{F}_{\mathrm{EM}} = q\mathbf{E} + \frac{q}{c}\mathbf{v} \times \mathbf{B} \tag{5.29}$$

and the Stern-Gerlach force

$$\mathbf{F}_{\mathrm{SG}} = \left(\nabla - \frac{\mathrm{d}}{\mathrm{d}t}\nabla_{\mathrm{v}}\right)(\boldsymbol{\Omega} \cdot \mathbf{s}) \tag{5.30}$$

are determined. Including a spin normalization of $\hbar/2$ and making again use of the same normalization as in the beginning of Sec. 5.1, Eq. 5.30 becomes

$$\mathbf{F}_{\mathrm{SG}} = \Lambda_{\mathrm{SG}}\left(\nabla - \frac{\mathrm{d}}{\mathrm{d}t}\nabla_{\mathrm{v}}\right)(\boldsymbol{\Omega} \cdot \mathbf{s}) \ , \tag{5.31}$$

with

$$\Lambda_{\mathrm{SG}} = \frac{\hbar\omega_{\mathrm{L}}}{2m_{\mathrm{e}}c^2} \approx 1.2 \cdot 10^{-6}\lambda_{\mathrm{L}}[\mu\mathrm{m}]^{-1} \ , \tag{5.32}$$

where the counter specifies the energy of a photon with wavelength λ_L and the denominator the electron rest energy, $\mathbf{\Omega}$ is know from Eq. 4.29 and $s=1$. For fields being in the same order as wakefields, Λ_SG is about 10^{-7} to 10^{-8}, while for laser fields with a few tens of nm wavelength Λ_SG is in the range of 10^{-4} to 10^{-5}.

The next goal is to analytically estimate if the SG force can change the total polarization of the relativistic proton ensemble. Like in the last chapter, all field symmetries are neglected while only considering a dominant field strength $\mathbf{F}=\max(\mathbf{E},\mathbf{B})$ and the corresponding dominant field gradient $\partial F=\max_{\mathrm{i,j}}(|\partial_{\mathrm{x_i}}F_\mathrm{j}|)$. Following that approach, an upper limit for $|\mathbf{F}_\mathrm{SG}|$ is quantified resulting in a discussion of the possibility to separate two particles of opposite spin leading to a certain polarization of an initially unpolarized system by the SG force.

The coordinate $\mathbf{r}$, the canonical momentum $\mathbf{P}$ and the spin $\mathbf{s}$ are treated as independent variables, respectively. In the case of relativistic particles, the correction in $\mathbf{F}_\mathrm{SG}$ consists of the $\mathrm{d}/\,\mathrm{d}t\cdot\nabla_\mathrm{v}$ term (cf. Eq. 5.31) and additionally of contributions from $\Omega_\mathrm{v}\nabla$ and $\Omega_\mathrm{E}\nabla$ (cf. Eq. 4.29). As can be seen from Eq. 4.29, the coefficients Ω_B, Ω_v and Ω_E just depend on $|\mathbf{v}|$, hence the gradient only acts on the fields: $\nabla(\mathbf{B}\cdot\mathbf{s})$, $\nabla(\mathbf{B}\cdot\mathbf{v})$ and $\nabla(\mathbf{E}\times\mathbf{v})$. For $\gamma\gg1$, the contribution of the spatial gradient to $\mathbf{F}_\mathrm{SG}$ is bounded by

$$F_\nabla=\Lambda_\mathrm{SG}\frac{qm_\mathrm{e}}{m}\left(3a+\frac{2}{\gamma}\right)3\sqrt{3}\partial F\ , \tag{5.33}$$

where

$$|\mathbf{\Omega}\times\mathbf{s}|=\Big(|\Omega_\mathrm{B}|+|\Omega_\mathrm{E}|+|\Omega_\mathrm{v}|\Big)\cdot F\leq\left(a+\frac{1}{\gamma}+a+\frac{1}{\gamma}+a\right)\cdot F=\left(3a+\frac{2}{\gamma}\right)\cdot F\ , \tag{5.34}$$

and the norm of the normalized spin is $3\sqrt{3}\partial F$ since

$$\begin{aligned}
|\nabla(\mathbf{F}\cdot\mathbf{a})| &= \sqrt{\left(\frac{\partial(Fa)}{\partial x}\right)^2+\left(\frac{\partial(Fa)}{\partial y}\right)^2+\left(\frac{\partial(Fa)}{\partial z}\right)^2}\\
&\leq \sqrt{\partial F\big(a_\mathrm{x}+a_\mathrm{y}+a_\mathrm{z}\big)^2\cdot3}\\
&= |a|\sqrt{\partial F^2\left(\frac{|F_\mathrm{x}|}{|F|}+\frac{|F_\mathrm{y}|}{|F|}+\frac{|F_\mathrm{z}|}{|F|}\right)\cdot3}\\
&= \sqrt{3}|a|\frac{\partial F}{|F|}\Big(|F_\mathrm{x}|+|F_\mathrm{y}|+|F_\mathrm{z}|\Big)\\
&= 3\sqrt{3}|a|\partial F\ .
\end{aligned} \tag{5.35}$$

Thus, Eq. 5.33 is related to the spatial gradient. For relativistic protons with $\gamma\gg1$ there are three more basic proportionalities, which have to be taken into consideration. The second relation is due to the spin-change rate. In order to estimate its contribution, the second term in Eq. 5.31 is relevant. It influences the trajectory of the accelerated proton because of temporal and spatial field variations, the energy-changing rate and the change in direction. Using the T-BMT equation (cf. Eq. 4.26), the k-th component in Eq. 5.31 is

$$\frac{\mathrm{d}}{\mathrm{d}t}\frac{\partial}{\partial v_\mathrm{k}}(\mathbf{\Omega}\cdot\mathbf{s})=\frac{\mathrm{d}}{\mathrm{d}t}\frac{\partial\mathbf{\Omega}}{\partial v_\mathrm{k}}\cdot\mathbf{s}-\frac{\partial\mathbf{\Omega}}{\partial v_\mathrm{k}}(\mathbf{\Omega}\times\mathbf{s})\ . \tag{5.36}$$

Applying Eq. 5.34 and the relation

$$\left(\left|\frac{\mathrm{d}\Omega_\mathrm{B}}{\mathrm{d}\gamma}\right|F+\left|\frac{\mathrm{d}\Omega_\mathrm{v}}{\mathrm{d}\gamma}\right|F+\left|\frac{\mathrm{d}\Omega_\mathrm{E}}{\mathrm{d}\gamma}\right|F\right)\gamma^3 \leq \left(\frac{1}{\gamma^2}+\frac{a}{\gamma^2}+\frac{1}{\gamma^2}\right)F\gamma^3 = (2+a)F\gamma \ , \tag{5.37}$$

and $\partial\gamma/\partial v_\mathrm{k} = \gamma^3 v_\mathrm{k}$, a limit, which applies to the spin-change rate, is given by

$$\left|\frac{\partial\mathbf{\Omega}}{\partial v_\mathrm{k}}\right|(\mathbf{\Omega}\times\mathbf{s}) \leq \frac{m_\mathrm{e}^2}{m^2}(2+a)(2+3a\gamma)F^2 \ . \tag{5.38}$$

Finally, the proportionality, which is related to the spin-change rate F_s, can be noted

$$F_\mathrm{s} \propto \Lambda_\mathrm{SG}\frac{m_\mathrm{e}^2}{m^2}(2+3a\gamma)F^2 \ . \tag{5.39}$$

Accordingly, a proportionality for the energy-changing rate or the change in direction

$$F_\mathrm{EV} \propto \Lambda_\mathrm{SG}\frac{m_\mathrm{e}}{m}F^2 \ , \tag{5.40}$$

and for the temporal and spatial field variations

$$F_\mathrm{T} \propto \Lambda_\mathrm{SG}\frac{m_\mathrm{e}}{m}\gamma\partial F \ , \tag{5.41}$$

can be defined.

Analysing Eqs. 5.33, 5.39, 5.40, and 5.41 for moderate relativistic ($1/a_\mathrm{e} \gg \gamma \gg 1$) protons with mass ratio $m_\mathrm{e}/m_\mathrm{p} = a_\mathrm{e}/a_\mathrm{p} \ll 1$ and energy in the lower GeV regime yields that $F_\mathrm{EV} \gg F_\mathrm{s}$. Thus, for $\partial F = 0$, the T-BMT rotation is overcompensated by the spin-acceleration coupling. In the case of $\partial F \gg F^2/\gamma$, the temporal and/or spatial field variations dominate over all other forces. For protons with energies in the TeV ($\gamma \gg 1/a_\mathrm{e}$) range, $F_\mathrm{s} \gg F_\mathrm{EV}$ for $\partial F = 0$. Consequently, the change of the particle trajectory induced by the coupling of the spin to the acceleration is always negligible against the alternation traced back to the T-BMT rotation. This assessment perfectly matches the experience gained at conventional accelerator facilities [85]. If $\partial F \gg a_\mathrm{e}F^2$, the field variations are supposed to be the relevant mechanism. Based on the above calculation it can be summarized that for high-energetic ($\gamma \gg 1/a_\mathrm{e}$) protons the T-BMT rotation dominates over perturbations due to energy- or velocity-changing rates. Moreover, it could be shown that ions sensitively react on the field gradients such that the F_T part (cf. Eq. 5.41) of the SG force outdoes the other three effects, even for small field variations. Since for $\lambda_\mathrm{SG}\gamma\partial F \ll F$, the electromagnetic force is much stronger than the SG force. Significant trajectory perturbations induced by the latter one are extraneous for $\gamma \approx (\lambda_\mathrm{SG}\partial F)^{-1}$ in the gradient field, assuming a field strength of about $F = 1$. That corresponds to kinetic energies in the range of 200 TeV and, hence, the SG force is negligible for laser-induced proton acceleration.

In order to confirm the last statement, the spatial beam separation caused by the SG force of an initially unpolarized relativistic particle beam while being accelerated in a strong electromagnetic field is estimated. Following the same scheme as in the last section, E_0 is interpreted as a laser field since the focus is put on laser-induced proton acceleration. Setting again $\epsilon = \omega_\mathrm{p}/\omega_\mathrm{L}$, $F \equiv \epsilon$ and $\partial F \equiv \epsilon/R_\mathrm{L}$ with the laser focal spot radius $R_\mathrm{L} = 2\pi/\epsilon$ (cf. Sec. 5.1) [122], a polarization in fields being comparable strong as those in pure plasma is selected. Thus, considering that

the SG force constantly acts in one direction, which is perpendicular to that one of the particle beam, the proton energy is assumed to be maintained and two copropagating polarized beams with a spatial distance of

$$\Delta = \frac{m_\mathrm{e}}{m}|\mathbf{F}_\mathrm{SG}|T_\mathrm{acc}^2\gamma^{-1} \ , \tag{5.42}$$

emerge, where t_acc is the acceleration time of the proton beam. In the previous section it has been calculated that the minimum depolarization time t_D is always shorter than t_acc (cf. Sec. 5.1). That is why for the maximum proton separation distance Δ_p, $t_\mathrm{acc} = t_\mathrm{D} \propto 500$ is chosen for a field strength comparable to that from lasers ($F = 1$) and $t_\mathrm{acc} \propto 500\epsilon^{-1}$ if it is equivalent to that from wakefields ($F = \epsilon$). Assuming a specific field homogeneity ($\partial F = 0$) for protons with an energy in the GeV range in a tailored plasma channel, the F_EV term has to be taken into account as a primary source for the SG force as already stated above. With Eqs. 5.40 and 5.42 the maximum proton separation yields

$$\Delta_\mathrm{p}(\partial F = 0) \propto \frac{m_\mathrm{e}}{m}F_\mathrm{EV}T_\mathrm{acc}^2\gamma^{-1} \propto \Lambda_\mathrm{SG}T_\mathrm{acc}^2\left(\frac{m_\mathrm{e}}{m}\right)^2\gamma^{-1} \propto 0.3\left(\frac{m_\mathrm{e}}{m}\right)^2\lambda_\mathrm{L}[\mu\mathrm{m}]^{-1}\gamma^{-1} \ , \tag{5.43}$$

which is in the sum pm range.

In the case of $\partial F \gg F^2/\gamma \propto \epsilon^2/\gamma$, an additional field gradient has to be considered and the F_T part (cf. Eq. 5.41) determines the maximum separation, so that

$$\Delta_\mathrm{p} \propto \frac{m_\mathrm{e}}{m}F_\mathrm{T}T_\mathrm{acc}^2\gamma^{-1} \propto \Lambda_\mathrm{SG}T_\mathrm{acc}^2\left(\frac{m_\mathrm{e}}{m}\right)^2\partial F \propto 0.05\left(\frac{m_\mathrm{e}}{m}\right)^2\lambda_\mathrm{L}[\mu\mathrm{m}]^{-1} \ . \tag{5.44}$$

For the 10 PW laser at SULF supplying a wavelength of 0.8 μm, the maximum separation distance caused by the SG force would be about 20 fm. This value is well below the laser focus diameter and much too small to be observed, even with state-of-the-art detectors. In summary, there is no chance to build up a particular polarization due to beam separation by the SG force for protons. The same holds for protons in the limit $\gamma \to 1$ so that $|\mathbf{v}| \approx 1$. Hence, the SG force is negligible in almost all computational studies on laser-plasma acceleration and, in particular, does not have to be implemented in PIC codes [30].

For the sake of completeness it has to be mentioned that there exists a related theoretically investigated mechanism on the polarization of an also initially unpolarized electron beam in combination with a ultra-intense, elliptically polarized laser pulse ($I_0 \approx 1.38{\cdot}10^{22}$ Wcm^{-2}) leading to a separation into two oppositely transversely polarized fractions due to the spin-dependent radiation reaction [30, 87].

6 Modelling of Particle-Spin Effects in Plasmas

Numerical computer simulations are an essential tool to gain an insight into the physics of laser-plasma interactions. However, at the beginning of this PhD thesis there existed PIC code, a very commonly used method to simulate the trajectory of charged particles in self-consistent electromagnetic and/or electrostatic fields, into which the spin characteristics were implemented. Within this work the particle-spin tracking has been integrated into the fully 3D PIC code VLPL in a cooperation between HHUD and FZJ. First, the basics of PIC algorithms and the VLPL code in particular are introduced. Then, it is explained how to implement the additional option to simulate spin dynamics into this code and first tests are presented.

6.1 Particle-in-cell algorithms

Computational simulations have had a fundamental impact on the design and understanding of past and present laser-plasma based acceleration experiments [52, 140, 141]. The accurate modelling of the formation of a wakefield structure, the capture of the protons or electrons and their acceleration requires trustworthy fully kinetic methods. The Particle-In-Cell (PIC) method has proven itself as such over years. However, these codes require large resources due to the wide range of time and space scales involved as the laser beam itself and the acceleration structure, which often is orders of magnitude larger than the beam, need to be resolved. Apart from that, PIC simulations pave the way towards the layout and development of next class laser-based accelerators with the aim of reducing development cost significantly. With this in mind, large-scale simulations will be driven forward to be a key component for an in-depth insight of the complex, interrelated physical phenomena.

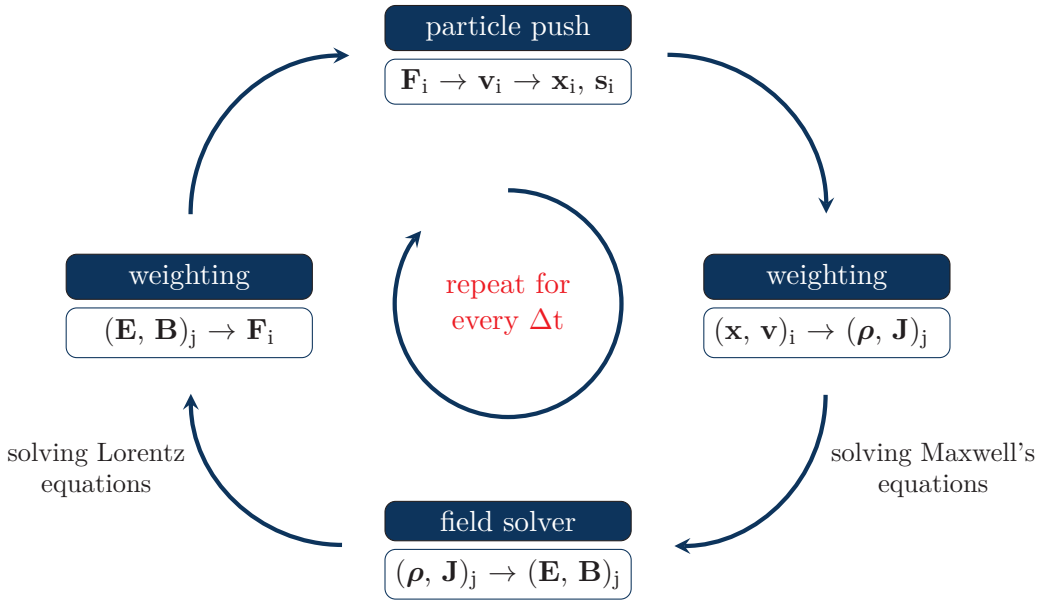

Figure 6.1: Flow chart of the working principle of the PIC algorithm including spin dynamics for one discrete time step Δt.

The principle of the PIC technique is to represent samples of physical particles by a smaller number of discrete macro-particles with the same properties and charge-to-mass ratio as the real plasma electrons and ions. Under the influence of electromagnetic fields, the particles are

mapped on a grid, defining the charge density $\rho(r)$ and the current $\mathbf{J}(r)$ on each grid point. While performing a simulation, the basic PIC algorithm contains four operations in each time step (cf. Fig. 6.1).

- Evolution of position and velocity of the macro-particles according to the Newton-Lorentz equation.
- Deposition of the current and/or the charge densities onto the simulation grid by interpolation from the particle distributions.
- Evolution of Maxwell's wave equations on the grid.
- Interpolation of the fields from the grid onto the particle positions according to the Lorentz equation as preparation for the next particle push.

Between these core operations, additional "add-on" operations are inserted to include additional physics such as absorption/emission of particles or numerical effects like smoothing/filtering of the charge/current densities [141].

Within the problems investigated in this thesis, collective electromagnetic phenomena are dominant. The considered densities are too low for quantum effects to be relevant. Therefore, the germane physical laws are the dimensional Maxwell equations [142]

$$\frac{\partial \mathbf{E}}{\partial t} = c\nabla \times \mathbf{B} - 4\pi \mathbf{J} \ , \tag{6.1}$$

$$\frac{\partial \mathbf{B}}{\partial t} = -c\nabla \times \mathbf{E} \ , \tag{6.2}$$

$$\nabla \cdot \mathbf{E} = 4\pi\rho \ , \tag{6.3}$$

$$\nabla \cdot \mathbf{B} = 0 \ , \tag{6.4}$$

where cgs units are used and c is the speed of light in vacuum.

Particle push The position $\mathbf{x}$ and momentum $\mathbf{p}$ of the simulated particles are given by the non-relativistic Newton's equations of motion

$$\frac{\partial}{\partial t}\mathbf{x}_\mathrm{n} = \frac{\mathbf{p}_\mathrm{n}}{m_\mathrm{j}\sqrt{1+\frac{\mathbf{p}_\mathrm{n}^2}{m^2c^2}}} \ , \tag{6.5}$$

$$\frac{\partial}{\partial t}\mathbf{p}_\mathrm{n} = \frac{q_\mathrm{j}}{m_\mathrm{j}}\Big(\mathbf{E} + \mathbf{v}_\mathrm{n} \times \mathbf{B}\Big) \ , \tag{6.6}$$

where m and q are the varying mass and the charge of a macro-particle n belonging to species j, while $\mathbf{E}$ is the given electric and $\mathbf{B}$ the magnetic field at position $\mathbf{x}$. Since in a typical PIC simulation 10^8 - 10^9 particles are substituted by one single macro-particle (several 10 millions in the 3D simulations performed within this thesis), the integration of their corresponding equation of motion will take a significant amount of the total Central Processing Unit (CPU) time. Moreover, the total memory consumption is occupied to a large extent by such high numbers of simulated particles.

One commonly used algorithm for advancing the particles in time and numerically integrate Eqs. 6.5 and 6.6 is the so-called Boris scheme given as [143]

$$\frac{\mathbf{p}_1 - \mathbf{p}_0}{\tau} = e\left(E + \frac{1}{c}\frac{\mathbf{p}_1 + \mathbf{p}_0}{2\gamma_{1/2}} \times \mathbf{B}\right) \ , \tag{6.7}$$

with the initial and final particle momenta $\mathbf{p}_0$ and $\mathbf{p}_1$ and $\gamma_{1/2}$ the γ-factor taken at the middle of the time step τ.

Since the Boris mover is a leapfrog algorithm, both, position and momentum, of the simulated particles are computed each discrete time step $(m-1/2)\Delta t$ but shifted with respect to the time of the position $m\Delta t$, assuming $(\mathbf{x}_\mathrm{n}^\mathrm{m}, \mathbf{p}_\mathrm{n}^{\mathrm{m}-1/2})$ are the phase-space coordinates at time $m\Delta t$. This scheme is depicted in Fig. 6.2 and works as follows:

1. Linear interpolation of $\mathbf{E}^\mathrm{m}$ and $\mathbf{B}^\mathrm{m}$ onto the particle's center of mass.
2. Pushing $\mathbf{p}_\mathrm{n}^{\mathrm{m}-1/2} \rightarrow \mathbf{p}_\mathrm{n}^{\mathrm{m}+1/2}$ by using the interpolated fields $\mathbf{E}_\mathrm{int}^\mathrm{m}$ and $\mathbf{B}_\mathrm{int}^\mathrm{m}$.

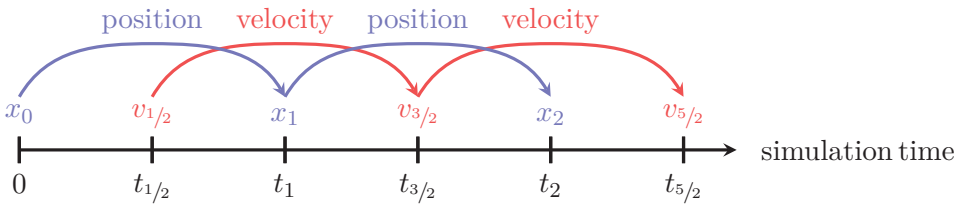

Figure 6.2: Principle of the leapfrog algorithm.

Since the second step is not trivial, this process is further subdivided again taking advantage of the splitting o the electric Lorentz force:

1. $\mathbf{p}_\mathrm{n}^- = \mathbf{p}_\mathrm{n}^{\mathrm{m}-1/2} + \frac{\Delta t}{2}\frac{q_\mathrm{j}}{m_\mathrm{j}}\mathbf{E}_\mathrm{int}^\mathrm{m}$.
2. $\mathbf{p}_\mathrm{n}^- \rightarrow \mathbf{p}_\mathrm{n}^+$.
3. $\mathbf{p}_\mathrm{n}^{\mathrm{m}+1/2} = \mathbf{p}_\mathrm{n}^+ + \frac{\Delta t}{2}\frac{q_\mathrm{j}}{m_\mathrm{j}}\mathbf{E}_\mathrm{int}^\mathrm{m}$.

However, the non-symmetric integration needed to solve this intermediate push causes unphysical numerical heating. In order to overcome this unwanted side-effect the so-called Boris method is applied, which basically computes a rotation induced by the $\mathbf{v}_\mathrm{n} \times \mathbf{B}_\mathrm{int}^\mathrm{m}$ term [144]. Thus, the momentum push for a particle n is given by:

1. Linear interpolation of $\mathbf{E}^\mathrm{m}$ and $\mathbf{B}^\mathrm{m}$ onto the particle's center of mass,
2. $\mathbf{p}_\mathrm{n}^- = \mathbf{p}_\mathrm{n}^{\mathrm{m}-1/2} + \frac{\Delta t}{2}\frac{q_\mathrm{j}}{m_\mathrm{j}}\mathbf{E}_\mathrm{int}^\mathrm{m}$ and $\mathbf{v}^- := \frac{\mathbf{p}_\mathrm{n}^-}{m_\mathrm{j}}$,
3. $\mathbf{v}' := \mathbf{v}^- + \mathbf{v}^- \times \mathbf{t}$ with $\mathbf{t} := \frac{q\mathbf{B}_\mathrm{int}^\mathrm{m}}{m}\frac{\Delta t}{2}$, $\mathbf{t} \in \mathbb{R}^3$,
4. $\mathbf{v}^+ = \mathbf{v}^- + \mathbf{v}' \times \frac{2\mathbf{t}}{1+t^2}$ and $\mathbf{p}_\mathrm{n}^{\mathrm{m}+1/2} := m_\mathrm{j}\mathbf{v}^+$,
5. $\mathbf{p}_\mathrm{n}^{\mathrm{m}+1/2} = \mathbf{p}_\mathrm{n}^+ + \frac{\Delta t}{2}\frac{q_\mathrm{j}}{m_\mathrm{j}}\mathbf{E}_\mathrm{int}^\mathrm{m}$,

where $\mathbf{v}^-$ is the initial and $\mathbf{v}^+$ is the rotated velocity and this schema is also valid for the relativistic case. Still making use of the leapfrog approach, from the new particle momenta

$\left(\mathbf{p}_n^{m+1/2}\right)_{m=1}^{N}$ the pushed particle positions $\mathbf{x}_n^{m+1}$ can be derived

$$\mathbf{x}_n^{m+1} = \mathbf{x}_n^m + \Delta t \frac{\mathbf{p}_n^{m+1/2}}{\sqrt{1 + \left(\mathbf{p}_n^{m+1/2}\right)^2}} \ . \tag{6.8}$$

Finally, taking into account the changed position of the macro-particle, the related new charge density $\rho_{i,j,k}^{m+1}$ can be calculated [143, 145, 146].

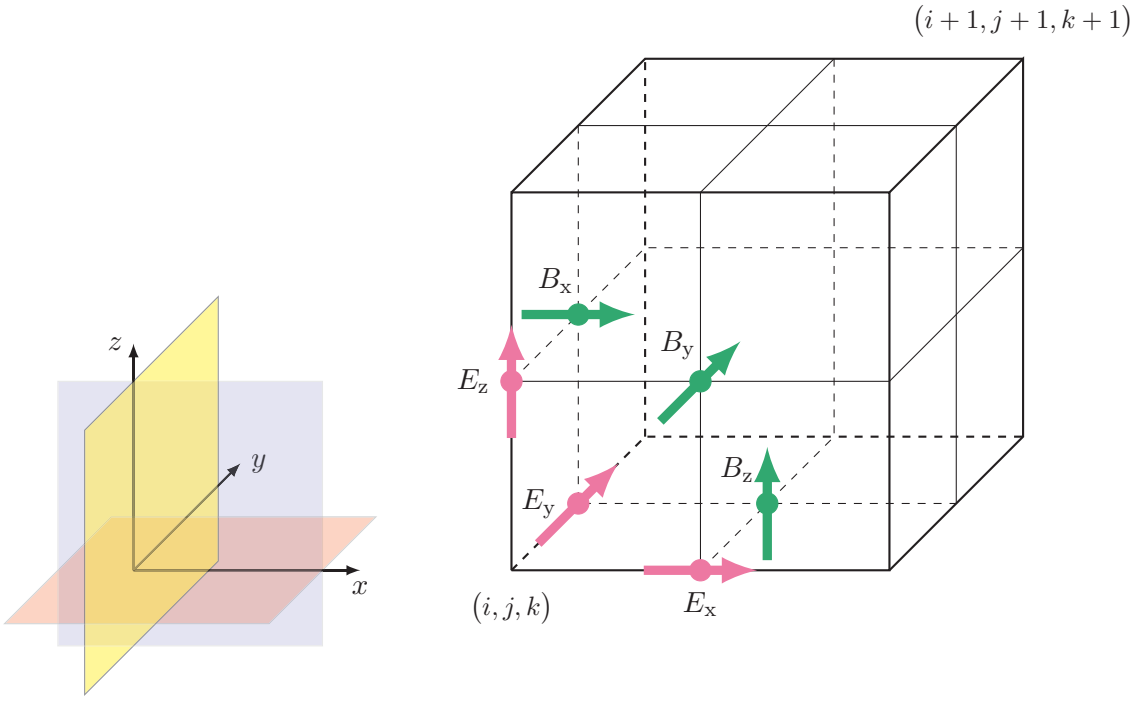

Figure 6.3: Arrangement of the **E** and **B** field components in the unit cell of the 3D Yee-scheme.

In order to calculate the mentioned particles' properties, often a so-called staggered or Yee lattice is used [147]. It is a mapping of Maxwell's equations in Cartesian coordinates to discrete space, resulting in a regular, orthogonal and three-dimensional grid. The components of the electric field are calculated at the edge centers, while those of the magnetic field at the surface centers of the unit cell. To quantify this, the following two assumptions are made as illustrated in Fig. 6.3:

- Electric field vectors are parallel to and constant along the edges of the lattice.
- Magnetic field vectors are normal to and constant on each side of the grid.

This arrangement ensures that the rotation formation occurring in the Maxwell's equations can be approximated by calculating central differences. In addition to this spatial nesting of the two fields, such a nesting is also performed with respect to time, since the time derivative of one field depends on the rotation of the other field and is again approximated as a central difference. The electric field strengths are therefore always calculated at the times $m\Delta t$, the magnetic field components at the times $(m + 1/2)\Delta t$.

Weighting One of the key features of a PIC algorithm is to control the smoothness of the solution. This is done by the weighting function, which links the assumed composition of the particle cloud to the formed macro-particle. Here, the numerical particles mark the distribution function $f(\mathbf{x}, \mathbf{p})$ given by a set of Finite Phase-Fluid Elements (FPFEs) such that the plasma is represented by macro-particles statistically populating the phase space with a finite number of elements

$$f_{\mathrm{j}}(\mathbf{x}, \mathbf{p}) = \sum_{\mathrm{n}=1}^{\mathrm{N_j}} W_{\mathrm{n}}^{\mathrm{ph}} S^{\mathrm{ph}}(\mathbf{x} - \mathbf{x}_{\mathrm{n}}, \mathbf{p} - \mathbf{p}_{\mathrm{n}}) \ . \tag{6.9}$$

N_{j} represents the number of numerical particles of the species j, $W_{\mathrm{n}}^{\mathrm{ph}}$ is the weighting coefficient of the n-th FPFE, S^{ph} the shape function of a macro-particle and $(\mathbf{x}_{\mathrm{n}}, \mathbf{p}_{\mathrm{n}})$ specifies the position of the center of the n-th FPFE.

For the commonly used cloud-in-cell, S^{ph} is set to

$$S^{\mathrm{ph}}(\mathbf{x}, \mathbf{p}) := \delta(\mathbf{p}) \begin{cases} 1 & , \quad |x_\alpha| < \frac{\Delta x_\alpha}{2}, |p_\alpha| < \frac{\Delta p_\alpha}{2} \text{ for } \alpha = x, y, z \ , \\ 0 & , \quad \text{otherwise} \ , \end{cases} \tag{6.10}$$

where Δx_α is the size of a FPFE along the j-axis, while Δp_α is the size of a FPFE along the p_α-axis in the momentum space. Within the PIC algorithm the weighting is performed twice (cf. Fig. 6.1). First, for interpolation of the electromagnetic fields to the position of the macro-particle. Second, having updated the current, the new properties are transferred onto the discrete grid [143].

Field solver The electric and magnetic fields involved are self-consistently described in the field solver as a feature of full electromagnetic PIC codes. One way of calculating both quantities is the so-called Finite Difference Time Domain (FDTD) method. Here, partial differential equations are transferred into algebraic equations since the derivatives are approximated as differences between contiguous points of the Yee grid. Using the leapfrog algorithm again, for Maxwell's equation (cf. Eq. 6.2) one obtains for the magnetic field

$$\mathbf{B}^{\mathrm{n}+1/2} = \mathbf{B}^{\mathrm{n}} - \frac{1}{2}\Delta t \tilde{\nabla} \times \mathbf{E}^{\mathrm{n}} \ . \tag{6.11}$$

Likewise, the electric field is determined by (cf. Eq. 6.1)

$$\mathbf{E}^{\mathrm{n}+1} = \mathbf{E}^{\mathrm{n}} + \Delta t \tilde{\nabla} \times \mathbf{B}^{\mathrm{n}+1/2} - \Delta t \mathbf{J}^{\mathrm{n}+1/2} \ . \tag{6.12}$$

By interpolating the electric and magnetic field onto the macro-particles' center of mass and, thus, updating $\mathbf{p}_{\mathrm{n}}$ (cf. Eq. 6.6), the numerical particle is pushed to a new position while inducing a current density given by

$$\mathbf{J}_{\mathrm{n}} = \int_{\Gamma_{\mathrm{x}}} q_{\mathrm{j}} W_{\mathrm{n}}^{\mathrm{ph}} S^{\mathrm{ph}}(\mathbf{x} - \mathbf{x}_{\mathrm{n}}(t) - \mathbf{p} - \mathbf{p}_{\mathrm{n}}(t)) \ , \tag{6.13}$$

where Γ_{x} denotes the spacial part of the vector space. This so-called Maxwell solver is one of the most widely used FDTD electromagnetic field solvers and also used as a field solver in the PIC code VLPL [143].

6.2 Implementation of particle spins into the VLPL code

Particle-spin effects have been implemented as an additional feature into the 3D PIC simulation code VLPL in a joint collaboration between HHUD and FZJ. Being able to simulate the acceleration process for our dynamically polarized gas target and to study the (de-)polarization effects of the involved particles, the VLPL code includes radiation reaction effects as well as the spin dynamics characterized by the T-BMT equation (cf. Eq. 4.26). From a technical point of view, this is realized by calculating not only the position and velocity during the particle push, but also the spin of each macro-particle during each time step Δt as can be seen in Fig. 6.1. As the particle trajectories are not affected by the spin effects, this implementation is quite straight forward. The three dimensional spin vector is additionally stored in the generated Hierarchical Data Format (HDF) particles file. An example is given in Fig. 6.4. Information about the involved fields are accordingly saved in a HDF5 fields file.

After having implemented the spin properties into the PIC code, test simulations have been carried out for code commissioning. The spin motion of a single PIC particle, representing an electron, with initial spin $\mathbf{s}_0 = \mathbf{e}_\mathrm{y} + \mathbf{e}_\mathrm{z}$ pointing into y-/z-direction, e.g., under a 45° angle, in a homogeneous magnetic field showing into z-direction, $\mathbf{B} = B_0 \mathbf{e}_\mathrm{z}$ and $B_0 = mc\omega/e$ with ω being the angular frequency, is simulated. Additionally, the following three conditions are defined as:

1. energy conservation $\longrightarrow \gamma \rightarrow \gamma_0$.
2. no electric field $\longrightarrow \left(a_\mathrm{e} + \frac{1}{1+\gamma_0}\right)\frac{\mathbf{v}}{c} \times \mathbf{E} = 0$.
3. movement perpendicular to magnetic field $\longrightarrow \frac{a_\mathrm{e}\gamma_0}{\gamma_0+1}\left(\frac{\mathbf{v}}{c} \cdot \mathbf{B}\right)\frac{\mathbf{v}}{c} = 0$.

This results in a reduction of the T-BMT equation (cf. Eq. 4.26) to

$$\frac{\mathrm{d}\mathbf{s}}{\mathrm{d}t} = \left(a_\mathrm{e} + \frac{1}{\gamma_0}\right)\mathbf{s} \times \mathbf{B} \ , \tag{6.14}$$

where a_e is the anomalous magnetic moment of the electron, γ_0 is the initial Lorentz factor and the spin $\mathbf{s} = (\langle s_\mathrm{x}\rangle, \langle s_\mathrm{y}\rangle, \langle s_\mathrm{z}\rangle)$ is given in the semi-classical limit. An excerpt from the corresponding HDF5 particles file is shown in Fig. 6.4. As expected, the simulation contains only one macro-particle and the spin is initially set in y-/z-direction.

Plotting the positions x, y, and z of the macro-particle at the different time steps in Fig. 6.5, it is confirmed that the particle moves according to the Lorentz equation on an orbit with radius $\mathbf{r}$

$$\mathbf{r} = \frac{p_0}{2\pi}\begin{pmatrix} \sin\left(\frac{2\pi t}{\gamma_0}\right) \\ 1 - \cos\left(\frac{2\pi t}{\gamma_0}\right) \\ 0 \end{pmatrix} \ . \tag{6.15}$$

	Mark	x	y	z	px	py	pz	sx	sy	sz	weight	q2m
0	1	1.970142...	0.500093...	2.000000...	9.998240...	-0.18758...	-4.92128...	0.031240...	0.706416...	0.707106...	1.000000...	1.0

Figure 6.4: Example of a HDF5 particles file of particle 0 containing information about the position, momentum, spin, particle's weight and charge.

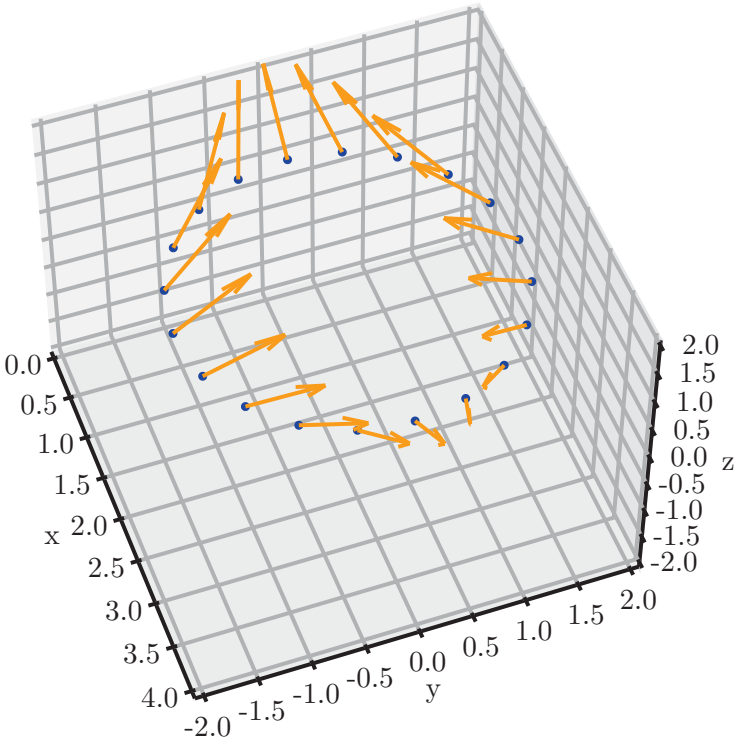

Figure 6.5: Test particle simulation of one macro-particle with Landé factor $g = -2$, i.e., equal Larmor and spin precession frequencies, initially polarized in y-/z-direction. The particle moves according to the Lorentz equation on an orbit with radius $\mathbf{r}$. The spin motion, indicated by the orange arrows, corresponds to the prediction by the T-BMT equation.

The particle momentum $\mathbf{p}$ is given by

$$\mathbf{p} = p_0 \begin{pmatrix} \cos\left(\frac{2\pi t}{\gamma_0}\right) \\ \sin\left(\frac{2\pi t}{\gamma_0}\right) \\ 0 \end{pmatrix} , \tag{6.16}$$

where p_0 is initial particle momentum.

As expected, the spin motion, represented by the orange arrows, is according to the T-BMT equation (cf. Fig. 6.5) and the spin $\mathbf{s}$ reads as follows

$$\mathbf{s} = \begin{pmatrix} \sin\left(2\pi\omega_\mathrm{s} t\right) \\ \cos\left(2\pi\omega_\mathrm{s} t\right) \\ 1 \end{pmatrix} , \tag{6.17}$$

where $\omega_\mathrm{s} = a_\mathrm{e} + 1/\gamma_0$ represents the Larmor frequency.

This test simulation shows that by implementing the spin dynamics according to the T-BMT equation the spin motion in laser-plasma simulations is correctly described with the VLPL code.

However, when interpreting the results, it is important to note that the continuous spin vector of a macro-particle represents the polarization of the particles it substitutes or the temporal mean value of a single particle depending on the particle's weight. When simulating more than just one PIC particle, the sum of spin vectors of the different macro-particles within a certain volume (polarization cell) corresponds to the local polarization of the ensemble.

7 Simulation of Polarized Proton Beams from Laser-Plasma Accelerators

This section focuses on simulation results on polarized laser-plasma induced proton acceleration, which serve as essential preparation for the experiments at SULF. All presented simulations aim at the investigation of the polarization characteristics and possible depolarization effects as well as acceleration mechanisms in the respective simulation geometry and are performed in 3D. Since such extensive simulation series cannot be carried out on conventional desktop PCs, the computing power of supercomputers is required. For the simulations mostly the Jülich supercomputers are used, which are introduced first (cf. Sec. 7.1) and on which a computing time of several million core-h was granted for this project. In the following, an outline of the general structure of a simulation file in VLPL including input parameters is provided (cf. Sec. 7.2). An overview over all simulations performed within this thesis is given in Tab. 2.

Table 2: Overview over all simulations performed within this thesis.

simul. particle	target	laser	computer	code	leading group	Sec.	Ref.
proton	pol. foil	ARCTURUS	JURECA	VLPL	FZJ/HHUD	7.3	[26, 27]
proton	pol. H/T & HCl gas	$a_0 = 200$	JURECA	VLPL	FZJ/HHUD	7.4	[28]
proton	pol. HCl gas	$a_0 = 25,\ 50,\ 75,\ 100$	China	EPOCH	Wuhan Univ.	7.5	[32]
proton	pol. HCl gas	SULF	JURECA	VLPL	FZJ/HHUD	7.6	in prep.
proton	pol. HCl gas	$a_0 = 316/\sqrt{2}$	JUWELS	VLPL	HHUD	7.6	[148]
proton	pol. H/T gas	$a_0 = 25$	JURECA	EPOCH	FZJ	7.4	[149]
electron	pol. HCl gas	vortex LG, $a_0 = 2$	China	VLPL	SIOM	10.2.2	[120]
electron	pol. HCl gas	PWFA	China	VLPL	SIOM	10.2.2	[150]
electron	pol. HCl gas	$a_0 = 2.5$	China	VLPL	SIOM	10.2.2	[151]

7.1 The Jülich supercomputers

The Jülich Supercomputing Centre (JSC) at FZJ has been operating the first German supercomputing center since 1987 and continues the long tradition of scientific computing in Jülich. It provides researchers in Germany and Europe with computing time of the highest performance level via an independent peer review process. Currently, with the JURECA and the JUWELS systems it operates two of the most powerful computers in Europe [152].

In the framework of this thesis, laser-plasma simulations mainly were performed on JURECA, a petaflop-scale modular supercomputer, which consists of two separate, but tightly integrated, compute modules, the Cluster and the Booster module. Being on rank 65 of today's most powerful computer systems, the JURECA Cluster module is equipped with 1872 compute nodes, of which 1733 are T-Platform V-Class V210S compute nodes and 75 are GPU-accelerated V210F blades housed in a V5050 enclosure. In addition, 64 Supermicro F618R2-RT+ twin blade servers (512 GiB storage nodes) and 12 Supermicro 1028GR-TR visualization nodes are accessible. Apart from that, the JURECA Booster module comprises 1640 compute nodes of type Dell PowerEdge C6320P.

Once, computing time on the supercomputers has been granted to both modules, one can connect via the same Secure Shell Protocol (SSH) connection. As needed for our simulation

tool, both, the Intel and ParTec ParaStation Message Passing Interface (MPI) implementations, are supported. In order to start a job on the JURECA system, users have to submit a batch application (usually bash scripts) in the *scratch* directory. Multiple *srun* calls can be placed in a single batch script such as information about the nodes, ntasks, ntasks-per-node and wallclock time or special modules like Intel, ParaStationMPI and HDF5 to be loaded. For the majority of our simulations 32 nodes with 48 ntasks-per-node resulting in 1536 ntasks were used. Due to its architecture, the Cluster module runs about four times faster for our VLPL simulations compared to the Booster module [152].

7.2 Structure of a simulation file in VLPL and input parameters

As earlier discussed in Sec. 4.5, both a strong laser pulse with an intensity in the range of $10^{23}\,\mathrm{Wcm}^{-2}$ and an extended gas instead of a thin foil target are needed to successfully perform laser-plasma based polarized proton acceleration. These requirements are realized step by step in the following simulations up to an experimentally feasible geometry. In most simulations, the VLPL code is used, while one simulation is carried out with the EPOCH code [119] (cf. Tab. 2).

For the VLPL simulations, first all input parameters are defined in the so-called "v.ini" file in a *namelist* format. Each namelist begins with the symbol "&" followed by the namelist name and ends with a slash. The most important namelists, from a physical point of view, for the simulations are the &`Domain`, the &`PulseN`, the &`Electrons`, the &`SpecieN` and the &`Boundary` namelists. The &`Domain` namelist contains general information about the simulation domain. In the &`PulseN` namelist the laser pulse is characterized by, among other things, the dimensionless laser amplitude $\mathtt{a}_0$, the pulse length and its width. With the &`Electrons` and the &`SpecieN` namelists the electron distribution and particle species are defined, exemplary by density measured in critical densities, the plasma profile or the number of particles per cell for each species. The parameters $\mathtt{S}_\mathrm{x}$, $\mathtt{S}_\mathrm{y}$ and $\mathtt{S}_\mathrm{z}$ determine the initial polarization of the PIC particles for the corresponding particle type in all three dimensions. For example, in the last simulation series (cf. Sec. 7.6) the polarization for hydrogen in &`Specie1` is specified to be $\mathtt{P}_\mathrm{y} = 1$, thus, 100 % polarization in y-direction. In the &`Boundary` namelists the boundary conditions for the lower and upper boundaries in all three dimensions are individually determined. In addition, input parameters for the computational realization are necessary, e.g., the controls for the parallel partition in the &`MPP_partition` namelist, or general controls like saving times or stop time in the &`Controls` namelist. A complete "v.ini" file with all parameters for simulation set 3 from Sec. 7.6 can be found in App. B.

7.3 Simulation of the ARCTURUS experiment with a polarized foil target

As a starting point, 3D simulations with the PIC code VLPL have been carried out for the experiment at the ARCTURUS laser facility presented in Sec. 4.5 [34] but including spin tracking. While for the experiment an unpolarized foil target was available, in the simulation a proton layer with 100 % initial polarization ($P_\mathrm{z} = +1$) is assumed for benchmarking purposes. The simulations were performed for a focused laser pulse of Gaussian shape with wavelength $\lambda_\mathrm{L} = 800\,\mathrm{nm}$, a normalized laser amplitude $a_0 = 12$, a pulse duration of 25 fs and a $1/\exp(2)$ focal spot size of $5\,\mu\mathrm{m}$. The results shown below were published in the two papers by Anna Hützen et al. [26] and Markus Büscher, Anna Hützen et al. [27].

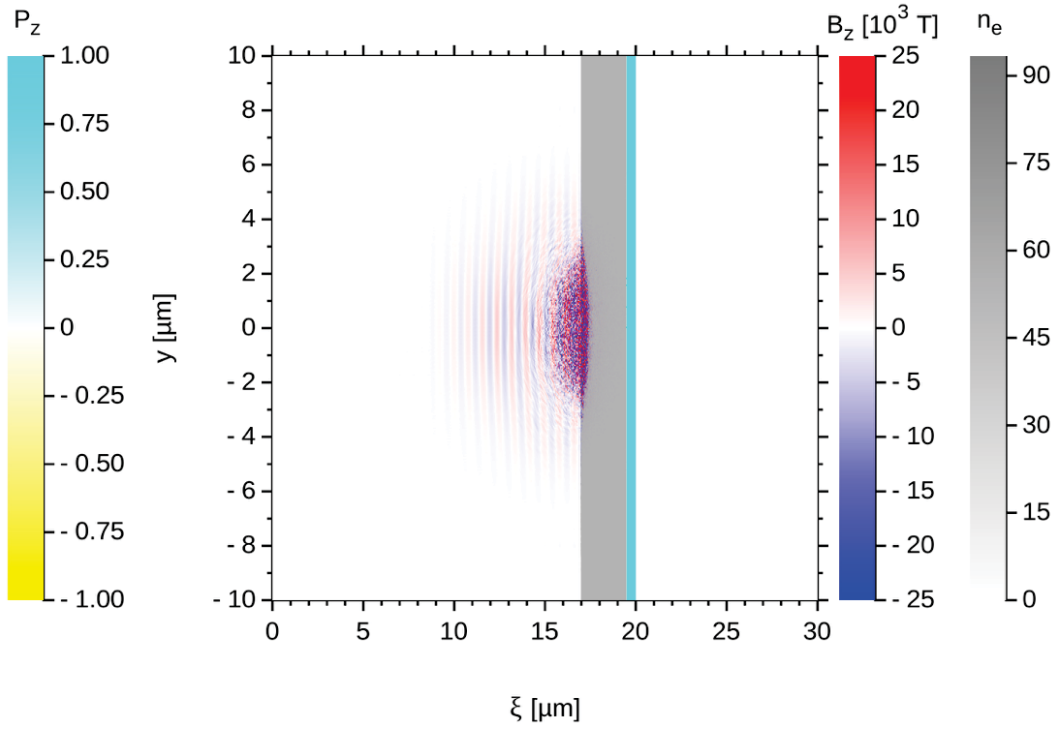

(a) Aluminum foil target (2.5 μm, 35 n_{cr}) covered with a fully polarized proton layer (0.5 μm, 117 n_{cr}) at simulation time 32.5 fs. n_e represents the electron density, B_z the magnetic field and P_z the polarization, both in z-direction [26].

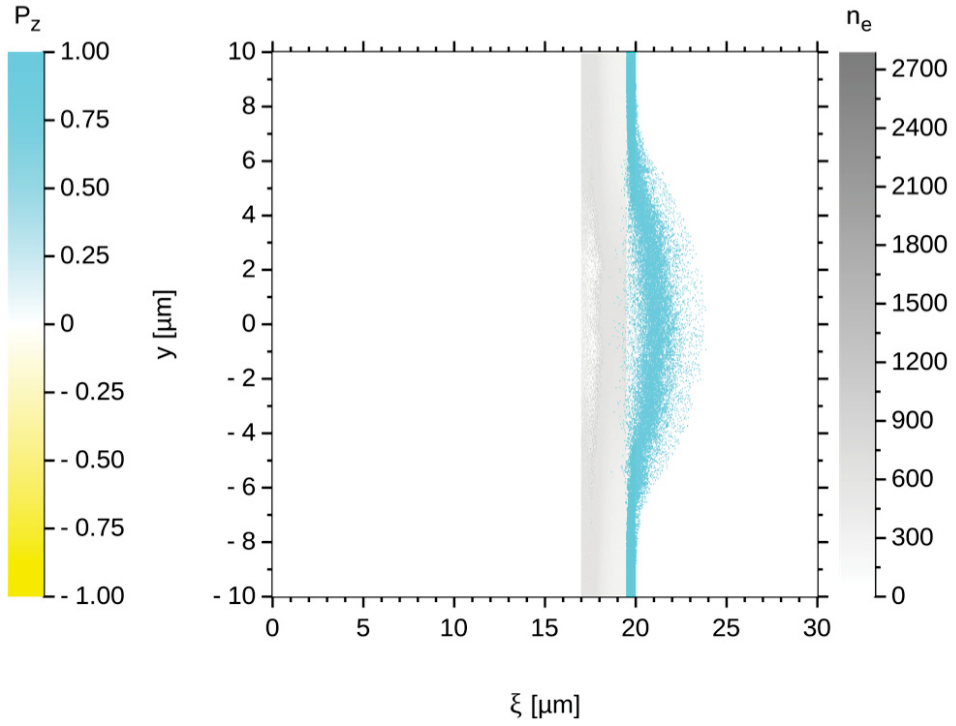

(b) Same as a) at simulation time 130 fs. The proton polarization is preserved both within the interaction process and within the acceleration process [26].

Figure 7.1: First simulation showing the conservation of proton polarization after interaction with a laser pulse ($\lambda_L = 800$ nm, normalized laser amplitude $a_0 = 12$, 25 fs duration, 5 μm focal spot size) impinging from the left side of the simulation box from 3D VLPL simulations. At the beginning, the laser pulse is centered at $\xi = 8\,\mu$m [26].

In Fig. 7.1 the laser, which is centered around $y = 0\,\mu$m, impinges on an Aluminum foil target covered with a proton layer fully polarized in the z-component. A grid cell size $h_\mathrm{x} = 0.025\,\mu$m and $h_\mathrm{y} = h_\mathrm{z} = 0.05\,\mu$m is used. For such kind of foils an acceleration according to the TNSA mechanism (cf. Sec. 3.2.1) is expected. The upper picture, taken at a simulation time of 32.5 fs, shows the laser pulse interacting with the foil target. On its left surface, the fields are particularly high. Electrons are, due to their lighter mass, partially separated from the ions by the presence of the laser field resulting in a very strong electric field between the moving electron cloud and the ion layer at the rear side of the target. The lower picture (Fig. 7.1b) is for an interaction time of 130 fs when the reflected laser pulse has already left the simulation box. The electron density in the target, given in units of the critical density n_cr, has increased significantly, where the interaction with the laser pulse has taken place, which is due to a compression of the foil by the laser. At the rear surface electrons leave the target and the fully polarized protons, being accelerated by the quasi-static electric field, follow this electron layer. Because of the extremely high generated field strengths the polarized protons are accelerated to energies of a few MeV over sub-mm distances. This fact corresponds to an acceleration of the protons due to the TNSA mechanism (cf. Sec. 3.2.1). As can be seen in the figure, the initial polarization of the protons in the z-direction is maintained to a large extent also during the acceleration process. Following Eq. 4.4, for the analysis for P_z, the polarization vector P is given by the weighted sum of all spin vectors $\mathbf{s}_\mathrm{i}$, where i represents direction of the polarization, i.e., z. The polarization is most strongly conserved at the upper and lower edge of the target, since barely any protons are accelerated here. In contrast, in the region around the $y = 0\,\mu$m axis the polarization is maintained to a smaller degree. Here, due to the interaction with the laser pulse, the strongest interaction and acceleration occurs. Furthermore, the fields that interact in the target are comparatively static and a proton polarization preservation for at least 0.18 ps is expected from the simulations [26].

In the next step it must be investigated whether the time, in which the direction of the spin is maintained, is longer than the simulation time t_sim. Since the spin precession vector $\mathbf{\Omega}$ always has a component perpendicular to the spin vector $\mathbf{s}$, the single spins in a polarized particle ensemble precess with the angular frequency $\omega_\mathrm{s} = |\mathbf{\Omega} \times \mathbf{S}| < |\mathbf{\Omega}|$. For protons with an energy in the range of a few GeV, $\gamma \approx 1$ and $1 \gtrsim v/c$, it follows that

$$\begin{aligned} \omega_\mathrm{s} &< \frac{e}{m_\mathrm{p} c} \sqrt{(a_\mathrm{p}+1)^2\,\mathbf{B}^2 + \left(\frac{a_\mathrm{p}}{2}\right)^2 \mathbf{B}^2 + \left(a_\mathrm{p} + \frac{1}{2}\right)^2 \mathbf{E}^2} \\ &= \frac{e}{m_\mathrm{p} c} \sqrt{\frac{5}{4} a_\mathrm{p}^2 \mathbf{B}^2 + 2 a_\mathrm{p} \mathbf{B}^2 + \mathbf{B}^2 + a_\mathrm{p}^2 \mathbf{E}^2 + a_\mathrm{p} \mathbf{E} + \frac{1}{4}\mathbf{E}^2} \ . \end{aligned} \tag{7.1}$$

Under the assumption $|\mathbf{B}| \approx |\mathbf{E}| \approx F$, where F is the field strength, this simplifies to

$$\omega_\mathrm{s} < \frac{e}{m_\mathrm{p} c} F \sqrt{\frac{9}{4}\, a_\mathrm{p}^2 + 3\, a_\mathrm{p} + \frac{5}{4}} \ . \tag{7.2}$$

Thus, for protons with anomalous magnetic moment $a_\mathrm{p} = 1.8$, a conservation of the polarization is expected for times

$$t \ll \frac{2\pi}{\omega_\mathrm{s}} \approx \frac{2\pi}{3.7 \frac{e}{m_\mathrm{p} c} F} \ . \tag{7.3}$$

For typical field strengths in the above presented simulations of $F = 5.11 \cdot 10^{12}\,\mathrm{V/m} = 17.0 \cdot 10^{3}\,\mathrm{T}$ the conservation of the spin directions is estimated for times $t < 1\,\mathrm{ps}$. This time is sufficiently long taking into account that the simulation time is $t_{\mathrm{sim}} = 0.18\,\mathrm{ps} \ll 1\,\mathrm{ps}$. Consequently, the polarization is maintained during the entire simulation and, thus, also during the acceleration process [26].

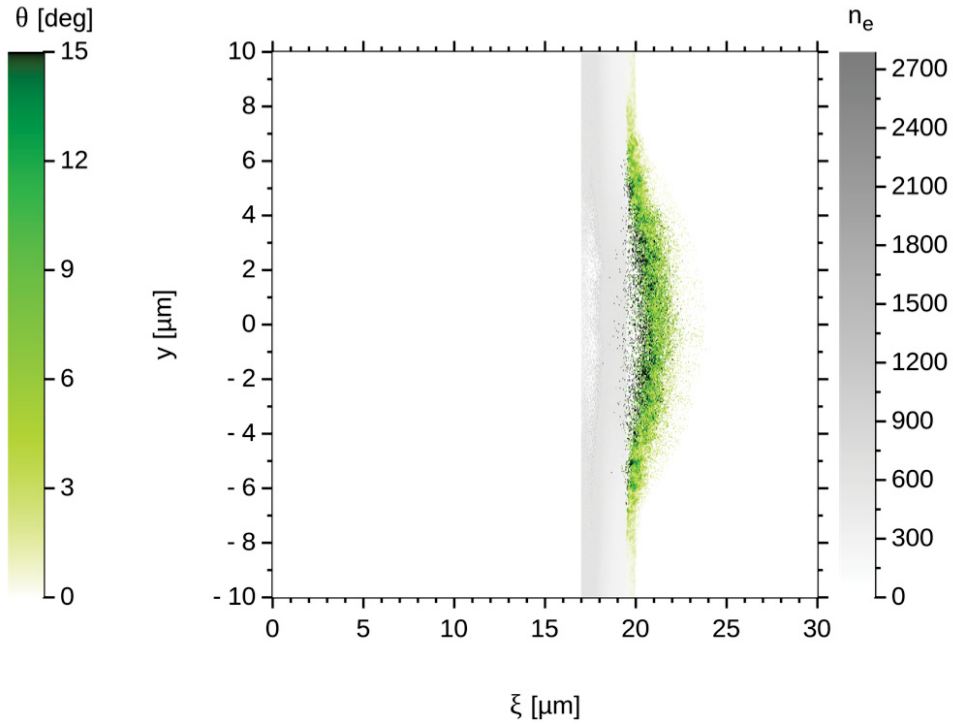

Figure 7.2: 3D VLPL simulation with the same parameters as depicted in Fig. 7.1 at simulation time 130 fs. Instead of the polarization P_{z} (cf. Fig. 7.1b), the spin rotation angle Θ relative to the initial value $\sigma = (0,\, 0,\, 1)$ is visualized here [27].

To gain a more complete understanding of the behavior of the spin during the acceleration process, also the spin rotation angles Θ have been calculated. This provides an understanding of possible changes of the polarization in the x- and y-direction. The spin rotation angle relative to the initial value $\sigma = (0,\, 0,\, 1)$ is depicted in Fig. 7.2. Θ is calculated as

$$\Theta = \arccos\left(\frac{\mathbf{p}_{\mathrm{ini}} \cdot \mathbf{p}_{\mathrm{end}}}{|\mathbf{p}_{\mathrm{ini}}| \cdot |\mathbf{p}_{\mathrm{end}}|}\right) , \tag{7.4}$$

where $\mathbf{p}_{\mathrm{ini}} = \sigma$ is the initial polarization and $\mathbf{p}_{\mathrm{end}}$ is the polarization vector at the end of the simulation. As can be seen in the figure, there is a maximum rotation of the spin rotation angle of 15° for most PIC particles. In agreement with the analysis of Fig. 7.1b, the largest angles are observed in the area around $y = 0$, where also the strongest acceleration is observed. It is evident the angles at the rear side of the target are comparatively large since the largest B-fields occur here. Thus, there is no strong spin precession and no significant depolarization seen in the simulation. Further depolarization effects in the ballistic phase between target and detector are not investigated since it is assumed that the electromagnetic fields are negligible small there and, thus, no spin rotation according to the T-BMT equation is to be expected [26, 27].

The conservation of the polarization is the most important result of this simulation. Overall, the conservation of polarization during the acceleration process is demonstrated for the first time in a PIC simulation for laser-induced particle acceleration. This simulation series thus not only is the basis for further studies regarding target material, laser parameters and acceleration mechanisms, but also makes the starting point for the further planning of our experiment on the laser-based acceleration of spin-polarized protons (cf. Sec. 8).

7.4 Comparison with gas-target simulations from literature

After demonstrating for the first time the conservation of polarization for a pre-polarized foil target with PIC simulations, a set of simulations for more realistic target parameters is has been prepared in the following. As explained in Sec. 8.1, pre-polarized foil targets are not available yet and their realization is extremely challenging, whereas gas targets are. In a paper by Shen et al. [72] 3D PIC simulations show the trapping and acceleration of *unpolarized* protons in an electron bubble-channel structure, for which both, a high-intensity laser pulse and a gas target with atoms possessing a large A/Z ratio, are required (cf. Sec. 3.2.2).

Since such target properties are remarkably similar to those of our polarized gas target, the work by Shen et al. serves as inspiration for the following simulations, where a similar setup *including the spin dynamics* of pre-polarized protons is used. The first simulation set follows Ref. [72] by choosing a hydrogen-tritium plasma with a hydrogen density of $n_\mathrm{H} = 1{\cdot}10^{20}\,\mathrm{cm}^{-3}$ and a tritium density of $n_\mathrm{T} = 1.4{\cdot}10^{21}\,\mathrm{cm}^{-3}$. In the second series a hydrogen-chloride gas with a hydrogen density of $n_\mathrm{H} = 8.5{\cdot}10^{19}\,\mathrm{cm}^{-3}$ and an equal chloride density is assumed. The additional simulations for HCl are already performed to get a first appraisal for the final experiments at the 10 PW laser system at SULF, aiming the observation of a polarized particle beam. In both simulations the electron density of $n_\mathrm{e} = 1.5{\cdot}10^{21}\,\mathrm{cm}^{-3}$ is near-critical. The plasma distribution is rectangular with sharp edges at the front (80 μm) and the rear (800 μm). Initially all protons are spin-aligned in y-direction ($P_\mathrm{y} = +1$) at the beginning of the simulation to study whether the proton polarization is conserved. The evolution of particle spins is simulated based on the T-BMT equation as described in Sec. 6.2. In both simulations, the laser pulse is circularly polarized, has a wavelength of 800 nm, a normalized laser amplitude of $a_0 = 200$, a length of 10 μm and a 1/exp(2) focal spot size of 16 μm. It enters the simulation box from the left in the $\xi = x\text{-}ct$-direction and propagated in a co-moving frame of size $80\,\mu\mathrm{m} \cdot 80\,\mu\mathrm{m} \cdot 80\,\mu\mathrm{m}$. There are $2500 \cdot 100 \cdot 100$ cells in the simulation volume and two PIC particles per species per cell. The results of these two simulation series were published in the paper by Anna Hützen et al. [28], on which the subsequent analysis is also based on.

In the following four figures the proton densities (Fig. 7.3), the p_x-ξ phase space for the x-component of the kinetic momentum $\mathbf{p}$ (Fig. 7.4), the energy spectra (Fig. 7.5) and the polarization distributions (Fig. 7.6) are presented at three different times $t_1 = 800$ fs (first column), $t_2 = 1600$ fs (second column) and $t_3 = 2000$ fs (third column), comparing hydrogen-tritium (first line) and hydrogen-chloride plasma (second line) in each figure. These times correspond to the propagation distances of 240 μm, 480 μm and 600 μm of the moving frame.

Figure 7.3 depicts the proton densities for H/T and HCl plasma in the described simulation window in units of the critical densities. At time t_1 in Figs. 7.3a and 7.3d a channel with a diameter larger than 40 μm shortly after its formation is identified. The laser peak amplitude is

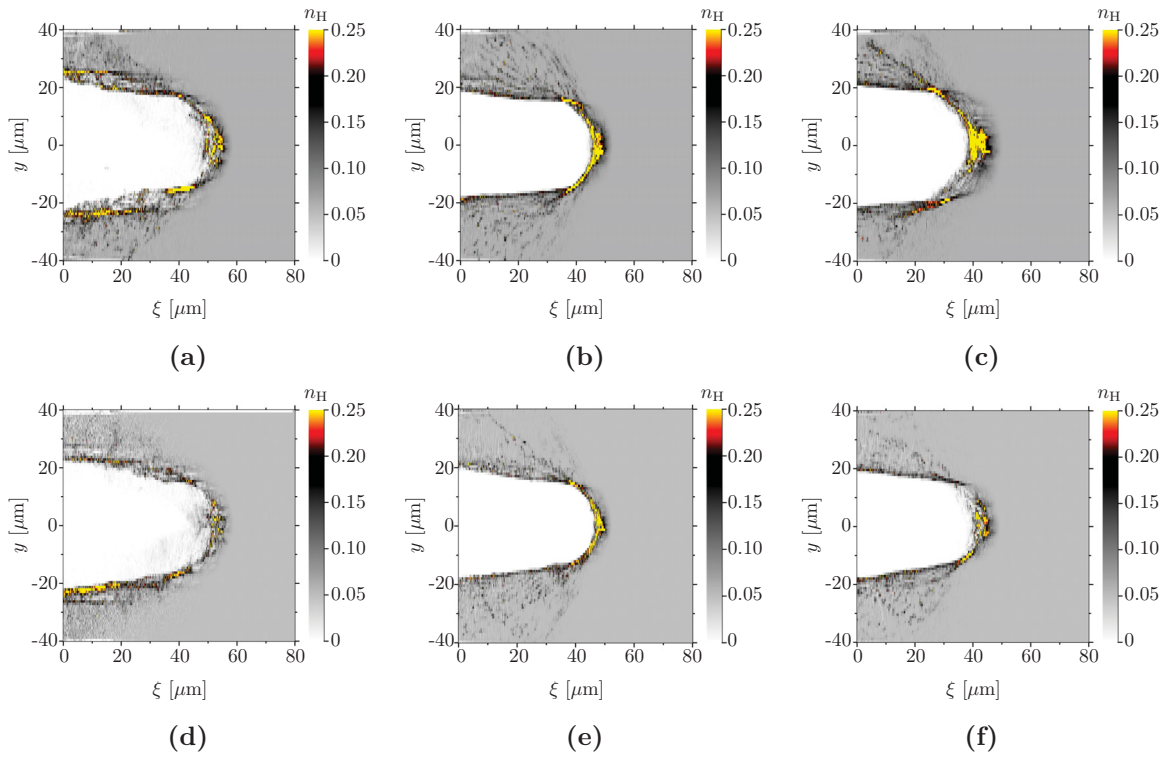

Figure 7.3: Proton densities for a H/T (upper plots) and a HCl (lower) plasma at the time $t_1 = 800$ fs (Figs. 7.3a, 7.3d), $t_2 = 1600$ fs (Figs. 7.3b, 7.3e) and $t_3 = 2000$ fs (Figs. 7.3c, 7.3f) from 3D VLPL simulations [28].

located at $\xi = 57.5\,\mu$m in both simulations. After a stabilization phase, the channel structures in Figs. 7.3b and 7.3e look very similar at time t_2. An additional accumulation of protons, especially in the H/T case, can be observed at the front right end of the bubble structure. Since the simulation window moves with c and, thus, faster than the channel, the laser peak amplitude shifts slightly to the left of the simulation box: it is situated at $\xi = 50.5\,\mu$m in the H/T and at $\xi = 50\,\mu$m in the HCl simulation. The slightly larger proton density and the vanishing channel structure at time t_3 in Figs. 7.3c and 7.3f indicate that the laser has started to deplete in both plasmas. Both, the channel structure and the peak amplitude, continue to shift to the left end of the box: the peak amplitude is located at $\xi = 49.5\,\mu$m in the H/T and at $\xi = 48\,\mu$m in the HCl case. At this advanced time the hydrogen density in the front of the channel structure in H/T plasma is visibly further enhanced, particularly around the $y = 0\,\mu$m axis, compared to the HCl simulation case.

The p_x-ξ phase spaces for the x-component of the momentum $\mathbf{p}$ at time t_1 in Figs. 7.4a for H/T and 7.4d for HCl look almost identical with a maximum of 2.5 GeV/c at $\xi = 50\,\mu$m. A comparison to the proton densities in Figs. 7.3a and 7.3d portends that the dense (yellow) spots at the channel edges are rather cold ($E \leq 1$ GeV) protons, which are not further accelerated. At time t_2 in Figs. 7.4b and 7.4e the phase-space distributions are very similar in shape and height for both cases. However, in the HCl simulation a slightly higher proton density around 6 GeV/c is visible. An increased peak level of more than 10 GeV/c in both diagrams corresponds to a mean acceleration force in the range of 30 TeV/m. A comparison of the positions of those protons with large momentum with the density plots (cf. Figs. 7.3b and 7.3e) emphasises that this field strength is reached in front of the channel. The phase-space plots at time t_3 for H/T

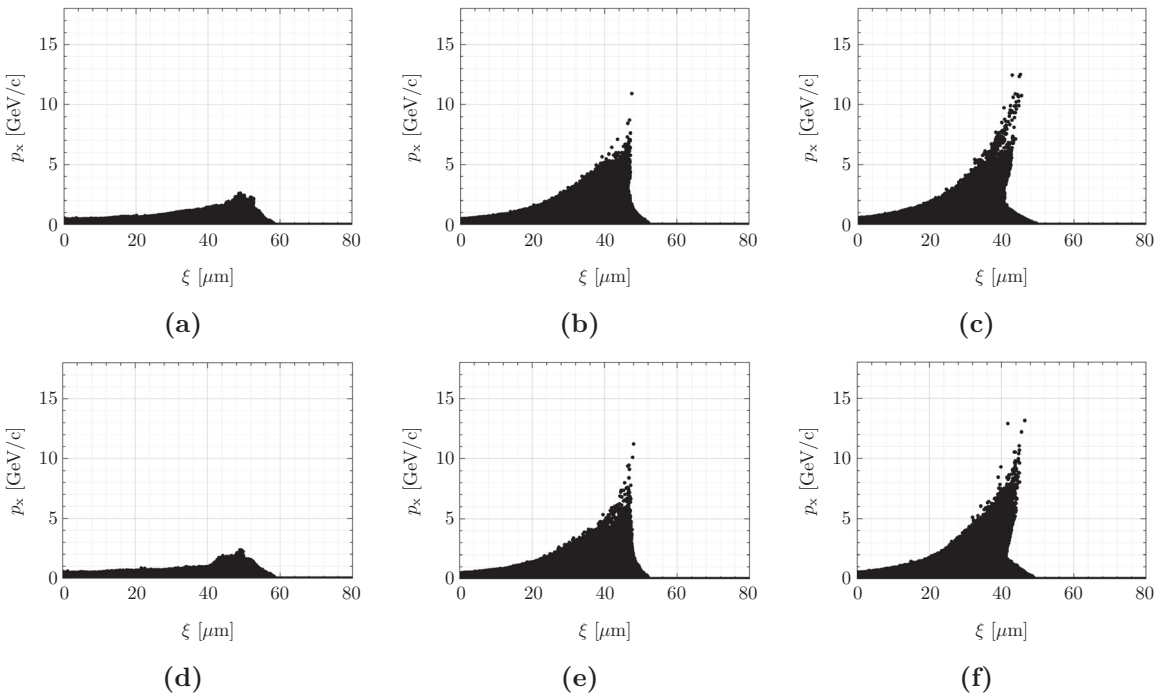

Figure 7.4: The p_x-ξ phase-spaces for a H/T (upper plots) and a HCl (lower) plasma at the time $t_1 = 800\,\text{fs}$ (Figs. 7.4a, 7.4d), $t_2 = 1600\,\text{fs}$ (Figs. 7.4b, 7.4e) and $t_3 = 2000\,\text{fs}$ (Figs. 7.4c, 7.4f) from 3D VLPL simulations [28].

and for HCl show similar characteristics. Shortly before the laser depletes, the highest momenta are reached in both simulations. At this time the maximum momentum in Figs. 7.4c and 7.4f is about 14 GeV/c. Certainly, only a small fraction of protons gain a momentum higher than 10 GeV/c. Although the phase-space density between 2.5 GeV/c and 10 GeV/c is much larger than at the previous times, most protons still have momenta smaller than 2.5 GeV/c. The maximal momentum for HCl is a bit higher, nevertheless the corresponding protons with large momentum are represented by single PIC particles only. This artifact can be explained by the strongly limited number of particles per cell. However, each series of simulations with a volume of over 110.000 core-h is already very complex and can only be handled by supercomputers (cf. Sec.7.1).

Figure 7.5 presents the energy histograms at the three different time steps for a H/T and a HCl plasma, while in Fig. 7.6 the corresponding polarization distributions are depicted. Equivalent to the analysis of the density and the phase-space plots, only minor differences are observable in the energy histograms and the polarization distributions at t_1 in Figs. 7.5a and 7.6a. In Fig. 7.5b $\mathrm{d}N/\mathrm{d}E$ linearly decreases for the H/T plasma, whereas the HCl histogram features a higher particle number at lower ($E \approx 1\,\text{GeV}$) and higher ($E > 5\,\text{GeV}$) energies (Fig. 7.5e). The single bars both, in the H/T and the HCl polarization spectrum in Figs. 7.6b and 7.6e, result from the same artefact as in the phase-space plots and indicate that only single PIC particles carry the highest energies. For lower energies around 5 GeV the polarization distribution for H/T indicates that at least 50 % of the initial polarization is preserved. In contrast, the distribution in Fig. 7.6e demonstrates that protons at even higher energies do not lose more than 30 % of their initial polarization when being accelerated in a HCl plasma. This should be interpreted with caution due to the poor statistics. In the energy histograms at time t_3 in

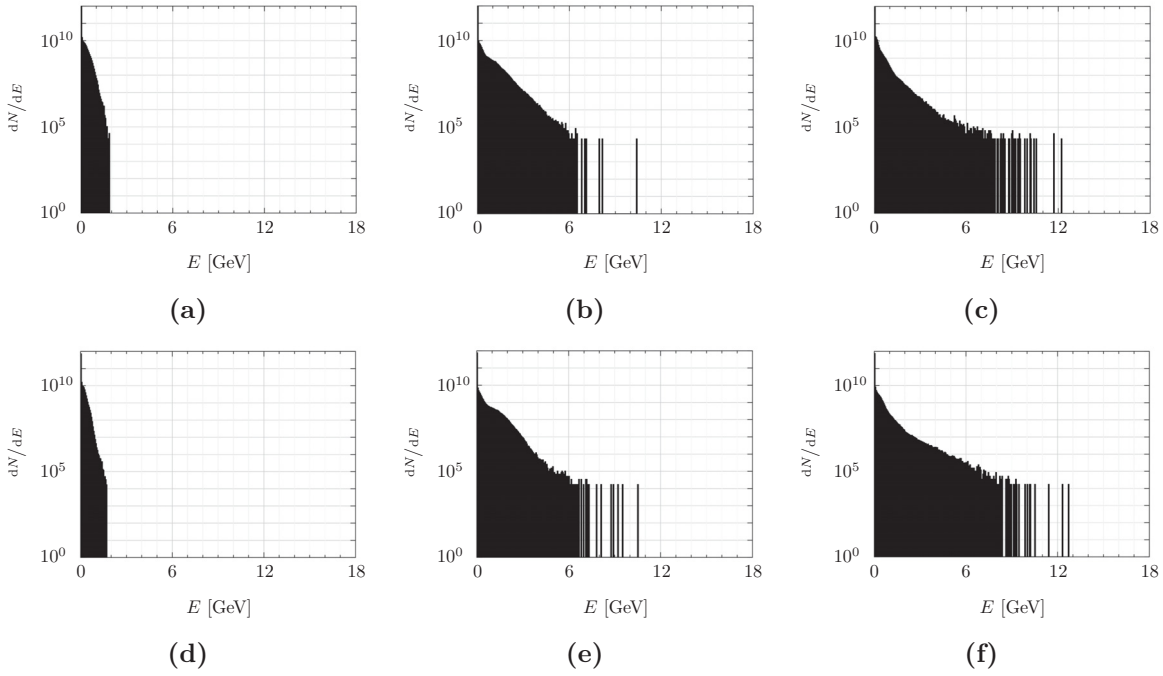

Figure 7.5: Energy histograms for a H/T (upper plots) and a HCl (lower) plasma at the time $t_1 = 800\,\text{fs}$ (Figs. 7.5a, 7.5d), $t_2 = 1600\,\text{fs}$ (Figs. 7.5b, 7.5e) and $t_3 = 2000\,\text{fs}$ (Figs. 7.5c, 7.5f) from 3D VLPL simulations [28].

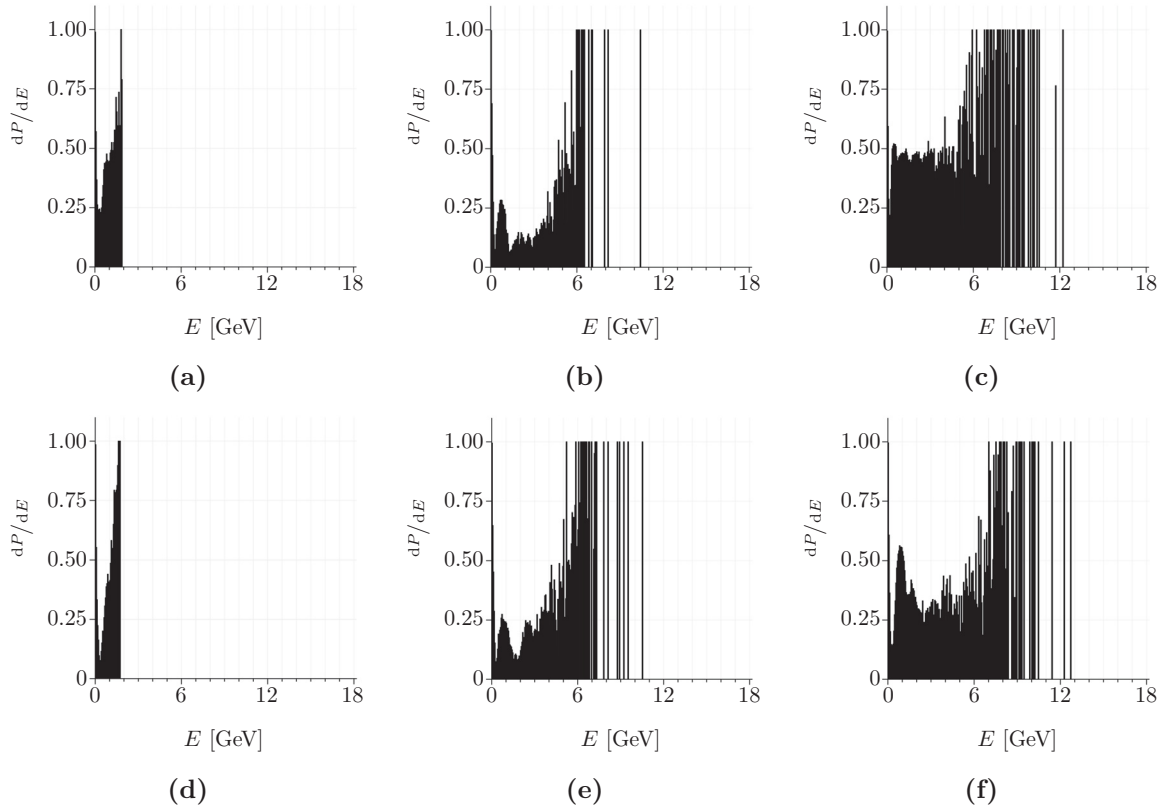

Figure 7.6: Polarization distributions for a H/T (upper plots) and a HCl (lower) plasma at the time $t_1 = 800\,\text{fs}$ (Figs. 7.6a, 7.6d), $t_2 = 1600\,\text{fs}$ (Figs. 7.6b, 7.6e) and $t_3 = 2000\,\text{fs}$ (Figs. 7.6c, 7.6f) from 3D VLPL simulations [28].

Figs. 7.5c and 7.5f the distribution decreases equally fast between 0 GeV and 2 GeV. Then, in the range between 2 GeV and 5 GeV, the spectra show minor differences as for H/T the drop is still linearly but with a smaller gradient, while in the histogram for HCl a significantly shallower slope appears. In both cases, $\mathrm{d}N/\mathrm{d}E$ is nearly constant between 5 GeV and 8 GeV. For higher energies ($E > 8\,\mathrm{GeV}$) there are only a few PIC particles present, as already mentioned. The maximum energy is slightly higher for HCl, which is in accordance with the observations for the corresponding phase-space plots. Additionally, there are small amplitude fluctuations around $\mathrm{d}P/\mathrm{d}E = 0.5$ for energies up to 6 GeV in the H/T polarization distribution (Fig. 7.6c). In comparison, the HCl distribution in the same energy range is less stable and drops to much smaller values (Fig. 7.6f). Both spectra characterize strong noise in the high-energy level well above 6 GeV.

The simulation for H/T is in good agreement with the results from Ref. [72], which is to be expected since the input parameters are very similar and this gives confidence in the robustness of our VLPL code. The analysis of the two simulation sets indicates that polarized HCl gas seems to be the better target choice compared to a H/T gas because slightly higher energies and momenta are observable. These are very satisfying results, since in the framework of this thesis a gas target based on HCl is built. A more detailed discussion of the effect on the acceleration of polarized protons with an ultra-intense laser in near-critical density H/T plasma can be found in our publication by Xiaofeng Li, Paul Gibbon, Anna Hützen et al. [149].

To investigate the polarization of protons with higher energies in detail, a larger number of PIC particles per cell is required. In order to simulate the experimental conditions as they will be given at SULF, the focus is directed towards two aspects: first, more realistic laser parameters, especially a smaller normalized laser amplitude a_0, so that a maximum power of 10 PW is considered. Secondly, a more realistic gas profile at best based on a profile of a gas jet that has already been measured experimentally. In the following, simulations are presented, which address these two improvements.

7.5 Acceleration mechanisms at moderate laser power

Starting from the results of the two simulation series outlined in Secs. 7.3 and 7.4, a 3D simulation for a HCl gas-jet target at moderate laser powers $a_0 \geq 25$ has been carried out. The subsequent discussion of these simulations can be found in our publication by Luling Jin, ..., Anna Hützen et al. [32]. The setup chosen in the simulation is already very similar to the layout of the final polarized proton-acceleration experiment planned at SULF. Thus, the simulation is intended to clarify two important questions: first, to what degree is the polarization maintained during the acceleration with moderate laser power and do the high-energy protons carry the highest degree of polarization. Second, which mechanisms contribute to the acceleration of the protons at the highest energies.

For this study, a simulation with a moving box of size $80\,\mu\mathrm{m} \cdot 64\,\mu\mathrm{m} \cdot 64\,\mu\mathrm{m}$ represented by a $1000 \cdot 400 \cdot 400$ grid at the speed of light c and a total macro-particle number of $8 \cdot 10^8$ is performed. The laser pulse has a bi-Gaussian envelope with $\mathbf{a} = \mathbf{e}_\mathrm{x} a_0 \exp[-(t - z/c + z_0/c)^2/\tau_0^2 - r^2/\omega_0^2]$, with the normalized laser amplitude $a_0 = 25$, focal radius $\omega_0 = 8\,\mu\mathrm{m}$, temporal duration $\tau_0 = 10\lambda/c$ and wavelength $\lambda = 800\,\mathrm{nm}$. The focal position z_0 propagates along the z-axis. To reach a high acceleration efficiency, the laser pulse is focused to the left boundary of the gas

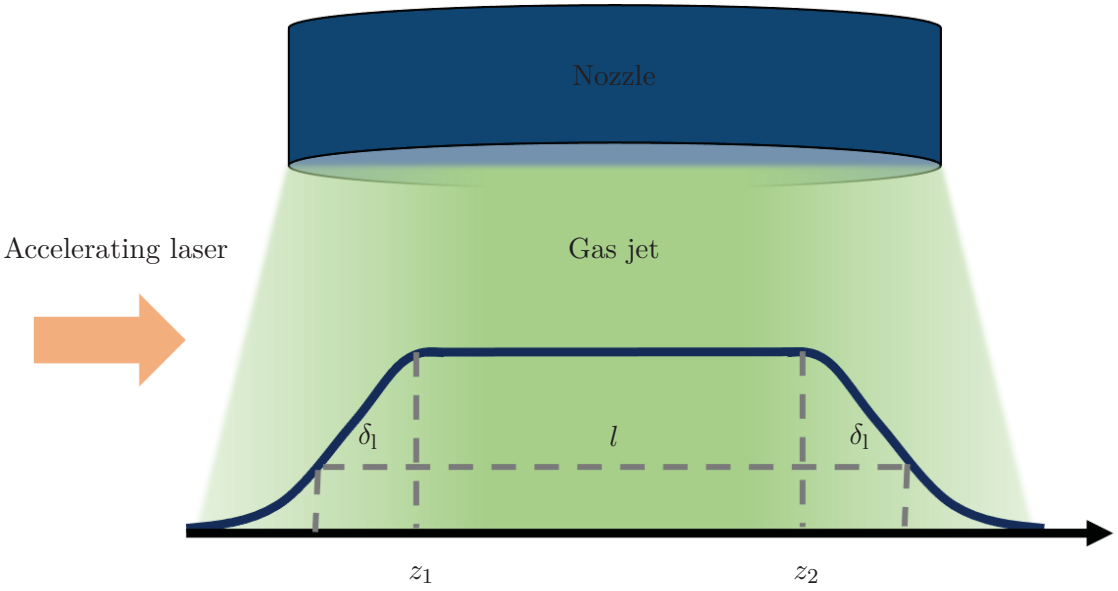

Figure 7.7: Density distribution of the HCl gas-jet target for 3D EPOCH simulations on polarized proton beam generation, adapted from Ref. [32].

target at $z_0 = z_1 = 40\,\mu$m. Similar to the simulation from Sec. 7.4, the target is assumed to be a fully ionized plasma of HCl gas. All protons are initially polarized along the z-axis ($P_z = +1$). Its density profile forms a uniform plateau with steep edges and the length of the target is $l = z_2 - z_1 = 200\lambda = 160\,\mu$m as sketched in Fig. 7.7. The density gradient at the edge follows the equation $n = n_0 \exp[-(z - zi)^2/\delta_l^2]$. Here, $\delta_l = 5\lambda = 4\,\mu$m refers to the length of the up and down ramp of the density profile, with $i \in \{1, 2\}$ corresponding to the left and right boundaries of the target. For the gas jet an electron density of $n_0 = 0.36 n_c$ is simulated, where n_c is the critical plasma density. The proton density is $n_p = n_0/(Z_H + Z_{Cl}) \approx 3.48 \cdot 10^{19}\,\mathrm{cm}^{-3}$, with charge numbers of hydrogen $Z_H = 1$ and chlorine $Z_{Cl} = 17$, and, thus, lower than the plasma density.

The acceleration of protons as well as the spin precession takes place within the plasma channel driven by the intense laser pulse. This plasma channel is created due to the interaction between the laser itself and the particles resulting in a ponderomotive expulsion of charges on the laser propagation axis. It is known as a relativistic self-focusing effect in high-power laser-plasma interactions and occurs if the laser power exceeds the critical value of $P_c = 17 n_c/n_0\,\mathrm{GW}$. Considering a laser pulse with even higher power P_L propagating in an underdense plasma, an additional central electron filament is enclosed in the evacuated channel, when fulfilling the condition $P_L = 21.49\, a_0^2 \omega_0^2/\lambda^2\,\mathrm{GW} \gg P_c$ [153, 154]. Due to the subsequent displacement of the electrons, both, a radial electric field E_r and an azimuthal magnetic field B_ϕ around the channel axis, are generated in the plasma channel. The magnetic field B_ϕ represented by B_x in the zy-plane at time $t = 250\,\lambda/c$, where the laser still propagates in the plateau, is shown in Fig. 7.8a.

Moreover, ions are attracted into the filament along the channel axis as an effect of the space-charge field E_r [155]. Due to the small charge-to-mass ratio of the ions, they converge towards the center on a much longer timescale as compared to the electrons. That is why an electron filament forms inside the laser fields, while the proton filament appears behind the laser pulse but in front of the chlorine nuclei filament. Fig. 7.8d depicts the proton density at $t = 290\,\lambda/c$. The proton filament can be identified around $240 \leq z/\lambda \leq 260$. Due to different

responses of particles, longitudinal and radial space-charge fields are induced within the plasma channel resulting in an acceleration of protons in forward and transverse directions under the actions of the electrons in front and the chlorine nuclei behind.

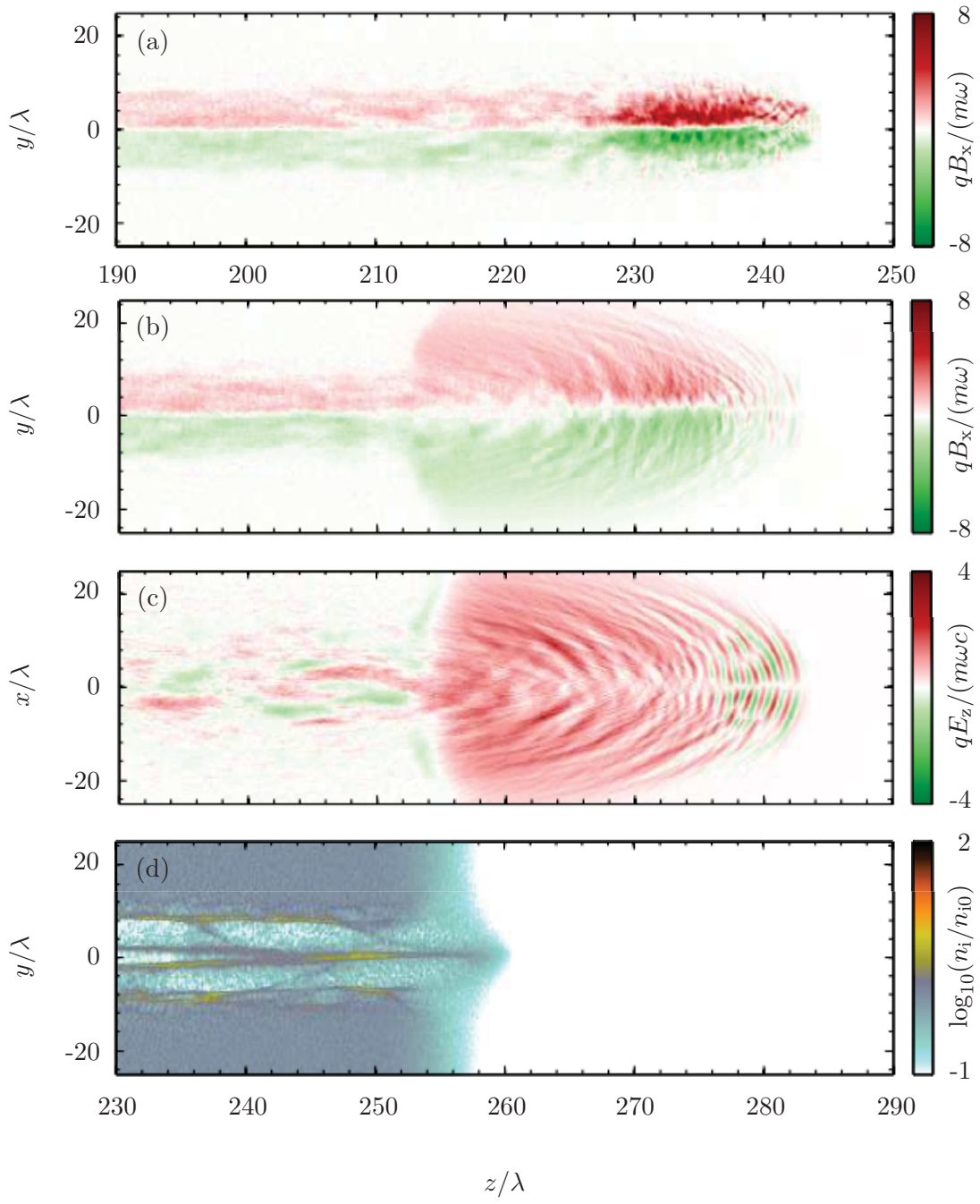

Figure 7.8: Proton beam generation from a HCl gas-jet target from 3D EPOCH simulations using a multi petawatt laser: (a) azimuthal magnetic field at $t = 250\,\lambda/c$, (b) azimuthal magnetic field, (c) longitudinal electric field, (d) proton density at $t = 290\,\lambda/c$ [32].

After this first-stage acceleration in the plasma channel, a second effect is observed at the rear end of the gas jet, which enhances the proton energies even more significantly. As the electrons driven by the laser pulse pass through the plasma down ramp at the rear target boundary, the azimuthal magnetic field expands into the vacuum under large angles generating a strong longitudinal field according to Faraday's law. This scenario is presented in Figs. 7.8b, c for the

azimuthal magnetic and the longitudinal electric field at $t = 290\,\lambda/c$. Thus, the focused protons in the filament near the rear boundary are then accelerated strongly. This secondary acceleration effect has been explained by the authors as MVA (cf. Sec. 3.2.3).

Figures 7.9a, b show the effects of the proton acceleration in the plasma channel for $z < z_2$ and the spin distribution of energetic protons in density plots at $t = 250\lambda/c$, respectively. At this time, many energetic protons start to converge to the front of the proton filament around $z_\mathrm{f} = 230\lambda = 184\,\mu$m. The energy of these front protons is less than 10 MeV. Compared to that, the tail protons are accelerated to energies exceeding the 10 MeV range, but are located far behind the driving laser with $z < z_\mathrm{f}$. As a result of the cylindrical symmetry of the azimuthal magnetic field in the plasma channel, the transverse spin components, s_x and s_y spread symmetrically. Hence, the polarization of the proton ensemble is specified by the longitudinal spin component $P = \langle s_\mathrm{z} \rangle$. As discussed in Sec. 5, depolarization effects by the direct proton-spin precession according to the T-BMT equation are dominant in laser-plasma based accelerators [30]. Then, the spin of the protons in the filament can be approximated as $s_\mathrm{z} \approx 1 - \int_0^\tau \mathrm{d}t (q/m)(G+1)B_\phi$ with the proton mass m, the anomalous magnetic moment of the proton $G \approx 1.79$ and the time duration τ for proton to move towards the axis under the influence of the radial electric field E_r.

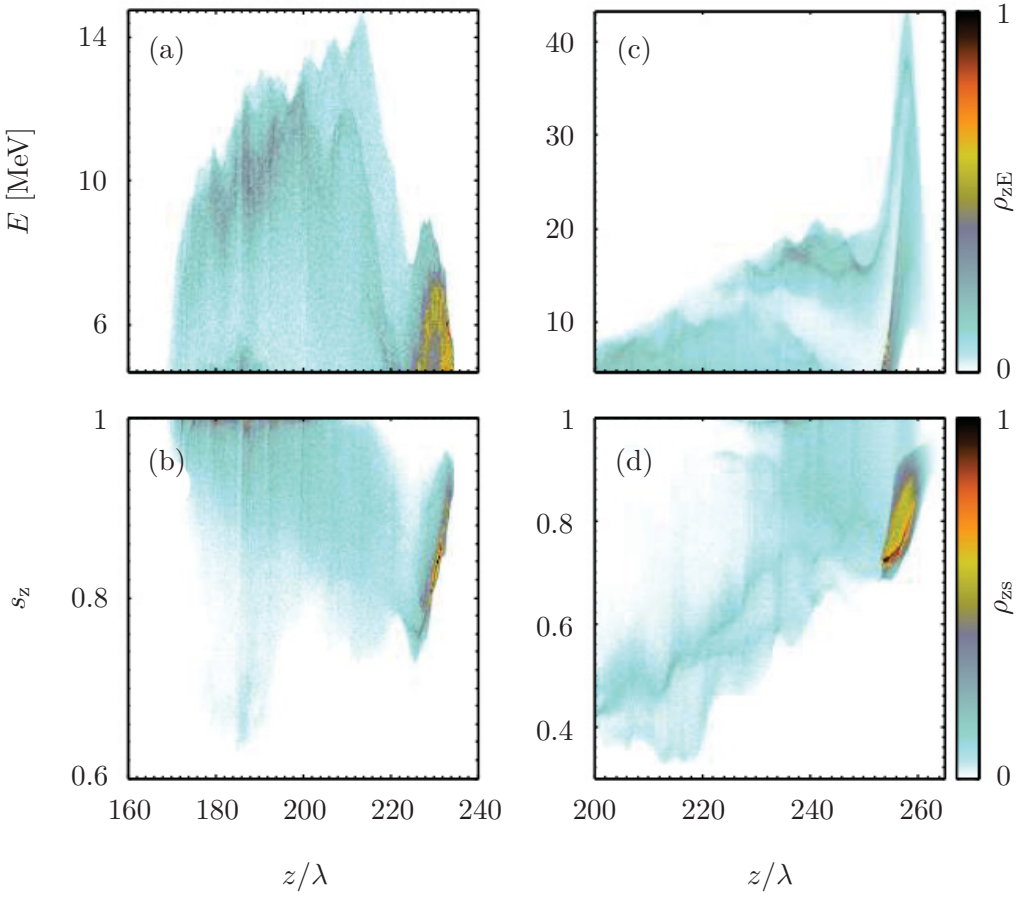

Figure 7.9: Density plots of energetic protons (with $E \geq 5$ MeV) in a HCl plasma from 3D EPOCH simulations in (a), (c) phase space and (b), (d) space with spin component s_z and z-axis. Panels (a), (b) correspond to density plots at t = 250 λ/c and (c), (d) to t = 290 λ/c, respectively [32].

Thus, a significant spin precession in the simulation results can be attributed to the following three reasons: first, the precession time τ in the magnetic fields is comparatively long due to the small proton velocity. Second, the anomalous magnetic moment G for the proton is larger than that of the electron. Third, the spin precession is directly influenced by both, the trajectory and the field structure, where also the dominant azimuthal magnetic field $B_\phi \sim 8m\omega/q$ in the plasma channel has a strong effect.

For the many but low-energy front protons, which are focused to the axis, the longitudinal spin component around $z = z_\mathrm{f}$ decreases to $s_\mathrm{z} \approx 80\,\%$ as illustrated in Fig. 7.9b. This indicates that the magnetic field is strong enough to partially depolarize the accelerated beam protons. In the channel driven by lasers with $a_0 = 25$, mostly more than 80 % of the initial polarization is maintained. The tail protons carrying the higher energies are further accelerated in the channel $z < z_\mathrm{f}$ (cf. Fig. 7.9a). Their momentum is largely conserved as they are radially repulsed after crossing the laser axis leading to a change of the direction of B_ϕ. Figure 7.9b shows larger s_z of these tail protons, concluding a realignment towards their initial direction along z.

In the second-stage acceleration, the front protons are accelerated at the rear boundary of the gas jet to energies exceeding the 40 MeV range (cf. Fig. 7.9c), which is attributed by the authors to MVA. At the same time, the spin vector of these protons precesses roughly at the same rate ($\approx 80\,\%$) compared to those front protons in the plasma channel (cf. Fig. 7.9d). However, the more energetic tail protons in the channel do not experience this acceleration effect since the magnetic-vortex-induced electric field becomes too weak. Furthermore, the longitudinal spin component s_z reduces to values below 40 %. Thus, the tail protons neither contribute to the final accelerated proton beam nor to the beam polarization.

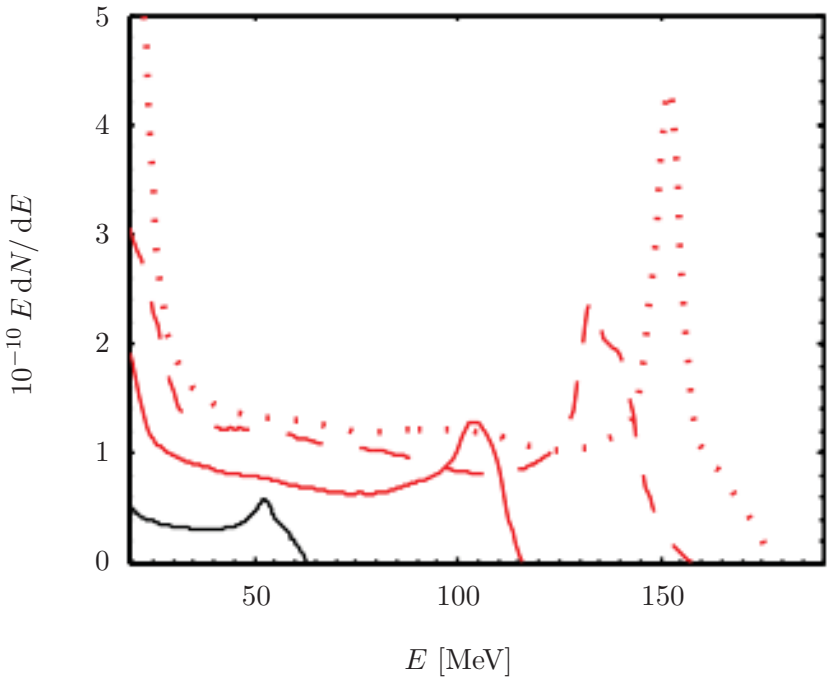

Figure 7.10: Energy spectra for protons in a HCl plasma with $E \geq 20$ MeV from 3D EPOCH simulations, with $a_0 = 25$, 50, 75, and 100, which are presented with solid-black, solid-red, dashed-red, and dotted-red curves, respectively [32].

After the second acceleration phase in the down ramp of the plasma density, the electromagnetic fields around the laser propagating axis quickly decay and finally become too weak to have an impact on the protons after $t = 330\lambda/c$. After this time, both, the energy and polarization of the proton beam, stay constant. The energy spectrum of the final accelerated proton beam with $E \geq 20\,\mathrm{MeV}$ is presented as a solid black line in Fig. 7.10. For a comparable, state-of-the-art laser system with a power of 1.3 PW, the protons are accelerated to tens of MeV with a peak at 53 MeV, while the polarization of $P = 82\,\%$ is conserved. For a further investigation of the maximum energy gain of the accelerated protons and the properties of the polarization, the simulation series is performed with the same target geometry, but for higher laser powers of $a_0 = 50$, 75, 100. The energy spectra are also plotted in Fig. 7.10. Table 3 gives an additional overview of the corresponding laser powers P_L, the peak proton energies E_p and degree of polarization P for these a_0 values.

Table 3: Characteristics of polarized beams accelerated by PW lasers with different normalized laser amplitudes a_0. P_L denotes the laser power, E_p the peak proton energy, and P is the beam polarization [32].

a_0	P_L [PW]	E_p [MeV]	P [%]
25	1.34	53	82
50	5.37	105	65
75	12.1	133	57
100	21.5	152	56

In general it can be stated that the energy of the accelerated protons increases with larger a_0 and, thus, also with higher laser power. For reasons already described, the polarization decreases with increasing laser power and is still 56 % for a laser with a power of 21.5 PW, for example. It can also be concluded that both, the beam energy as well as the proton depolarization, do not linearly depend on the laser power. It should be noted that both, Eqs. 3.13 and 3.14, cannot be applied to this simulation, since here an underdense plasma configuration with a density gradient is chosen. The simulation series for $a_0 = 75$ and a laser power of 12.1 PW matches the parameters for the 10 PW system at SULF best. A maximum proton energy of 133 MeV and a degree of polarization of at least 57 % can be expected [32].

The simulation results presented here for a pre-polarized HCl gas target and moderate laser powers contribute significantly to the understanding of how protons can be accelerated in such a geometry. By analyzing the magnetic and electric fields, two acceleration mechanisms can be distinguished: first, the acceleration in the plasma channel and second, an effect at the rear end of the gas jet known as MVA mechanism, which mainly boosts the energy of the front protons. The polarization is largely preserved, which is an important feature for the long-term goal of building a competitive laser-plasma based accelerator.

In order to simulate even more realistic experimental conditions, the width of the gas target should be enlarged, so that the gas can be injected into the interaction chamber through a standard nozzle. Such simulations for a nozzle, for which the formation of the gas jet was measured using Michelson interferometry, are discussed below.

7.6 Simulations for the acceleration at SULF

In this section, 3D simulations with experimentally practical parameters are presented as a basis for the planned experiments at SULF. Already in the simulations from the last Sec. 7.5, the laser power was adjusted to 10 PW systems, of which several worldwide are currently in the commissioning phase and are expected to be available for external users soon. The simulations shown here assume a significantly broader gas-jet target comprising a nozzle that has been characterized with Michelson interferometry and is available for experiments [156]. Other than that, the simulation setup is very similar to the simulations already shown for pre-polarized HCl gas targets including the spin dynamics. Thus, they can serve as a further benchmarking between VLPL and EPOCH.

In these PIC simulations, a HCl gas with a hydrogen density of $n_\mathrm{H} = 0.0122\, n_\mathrm{cr} = 2.1{\cdot}10^{19}\,\mathrm{cm}^{-3}$ with the critical density of $n_\mathrm{cr} = 1.74{\cdot}10^{21}\,\mathrm{cm}^{-3}$ and an equal chloride density is chosen. The electron density then is $n_\mathrm{e} = 0.22\, n_\mathrm{cr} = 3.8{\cdot}10^{20}\,\mathrm{cm}^{-3}$. As shown in Fig. 7.11, the plasma profile has a trapezoidal shape with a total length of 600 μm in agreement with the measured values. The up and down ramps each stretch over 200 μm. Similarly, the plasma volume with the highest density covers a length of 200 μm. To investigate whether an initial proton polarization is conserved, all protons are spin-aligned in y-direction ($P_\mathrm{y} = +1$) at the beginning of the simulation. The laser pulse is circularly polarized, has a wavelength of 800 nm and a normalized laser amplitude of $a_0 = 50$, a length of 10 μm and a 1/exp(2) focal spot size of 5.36 μm. This corresponds to a laser power of 4.8 PW. The simulation box is a co-moving frame, which is entered by the pulse from the left-hand side in the $\xi = x$-ct-direction. Every cell is initially filled with two PIC particles of each species.

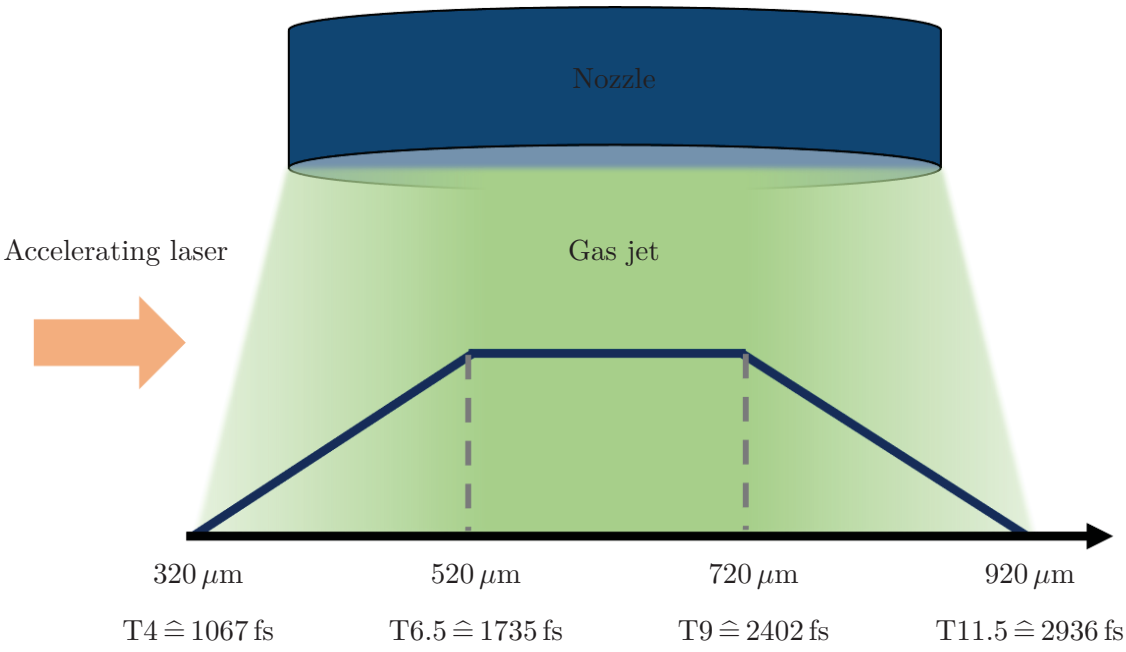

Figure 7.11: Sketch of the density distribution of the gas-jet target used for the simulations in Sec. 7.6. The profile results from the measurement of a standard gas nozzle with the Michelson interferometry method and, thus, corresponds to an experimentally realizable geometry for laser-plasma acceleration [156].

The data analysis revealed that the choice of boundary conditions is of crucial importance for the results, especially with respect to the maximum energy that the particles can gain during the acceleration process. The boundary conditions must be set at each boundary for the particles and fields and are applied to the electromagnetic fields after Maxwell's equations have been solved (cf. Fig. 6.1). The VLPL code offers two different options for the boundary conditions: either the particle boundaries can be periodic such that the particles loop around the box or they are set to be open meaning that particles reaching a boundary are removed from the simulation box. Either option can be set for any pair of boundaries separately. The same applies to the field boundary conditions. In the case of an open boundary, the electromagnetic waves are absorbed; periodic boundary conditions correspond to applying the fields from the opposite boundary. Both conditions have been used for numerical modelling and show limited applicability. Therefore, three simulation sets are presented below, which differ in the choice of boundary conditions and the size of the simulation box, as follows:

- Set 1: All boundaries are open for particles and fields. The simulation box is of size $320\,\mu\text{m} \cdot 48\,\mu\text{m} \cdot 48\,\mu\text{m}$ and there are $10000 \cdot 60 \cdot 60$ cells in the simulation window.
- Set 2: The boundary conditions for fields and particles at the left and right box edges in the x-dimension are open. In the other two dimensions, the boundaries for the fields are periodic, while all of them are open for the particles. All other parameters are the same as in set 1.
- Set 3: All boundary conditions correspond to those in set 2. The simulation box is enlarged to a size of $320\,\mu\text{m} \cdot 80\,\mu\text{m} \cdot 80\,\mu\text{m}$ in the y- and z-directions. There are $10000 \cdot 80 \cdot 80$ cells in the simulation window (cf. App. B).

In the following, the simulations of set 3 are analyzed in detail and then compared with sets 1 and 2. Generally, it can be stated that these simulations have remarkable similarities with the one presented in Sec. 7.5, especially with respect to the acceleration mechanisms. Figure 7.12 shows the hydrogen density at the simulation times T8 $\widehat{=}$ 2135 fs and T11 $\widehat{=}$ 2936 fs. At T8, i.e., the laser has reached the plasma plateau with very high density (cf. Fig. 7.11), the formation of a plasma channel along the $y = 0$ axis is clearly seen and has a diameter of about $40\,\mu\text{m}$. It is generated due to the interaction between the laser itself and the particles resulting in a ponderomotive expulsion of charges on the laser propagation axis. A very high proton density in the range of about $0.02\,n_{\text{cr}}$ appears in front of the bubble structure as a central spot around $\xi = 240\,\mu\text{m}$ along the entire laser propagation axis and at the edges of the bubble. In the lower image of Fig. 7.12 at time T11, i.e., already in the plasma down ramp, the plasma becomes correspondingly thinner and the bubble structure slowly dissolves. As expected, the high proton densities are still located at the left front channel edge and on the $y = 0\,\mu\text{m}$ axis.

For the electron density in Fig. 7.13 a similar structure can be recognized. The upper plot depicts the electron filament formed inside the laser fields. In front of the long filament, which can also be found in the hydrogen density distribution, an additional roundish bubble forms between ξ =240 μm and ξ =270 μm. The highest electron densities are observed on the central laser propagation axis and at the bubble edges. At the later simulation time T11 in the plasma down ramp, the electron density again decreases significantly, and only few particles between $\xi = 0\,\mu\text{m}$ and $\xi = 80\,\mu\text{m}$ as well as around $\xi = 220\,\mu\text{m}$ are visible.

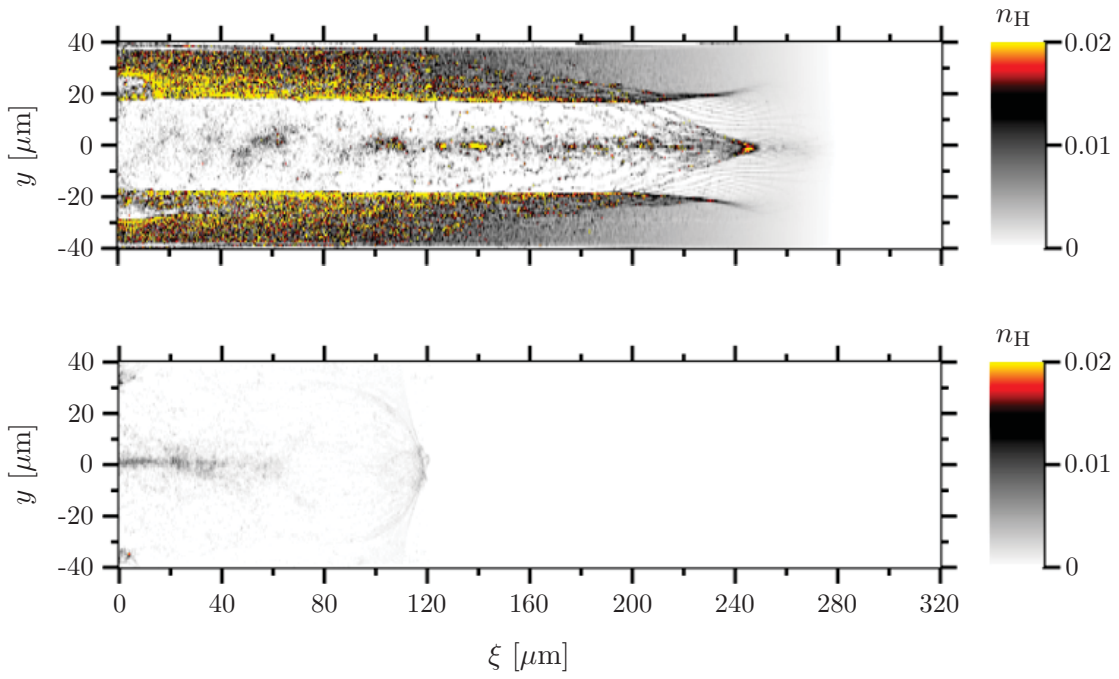

Figure 7.12: Hydrogen density in units of the critical density in a HCl plasma from 3D VLPL simulations at simulation time T8 $\widehat{=}$ 2135 fs (upper) and T11 $\widehat{=}$ 2936 fs (lower).

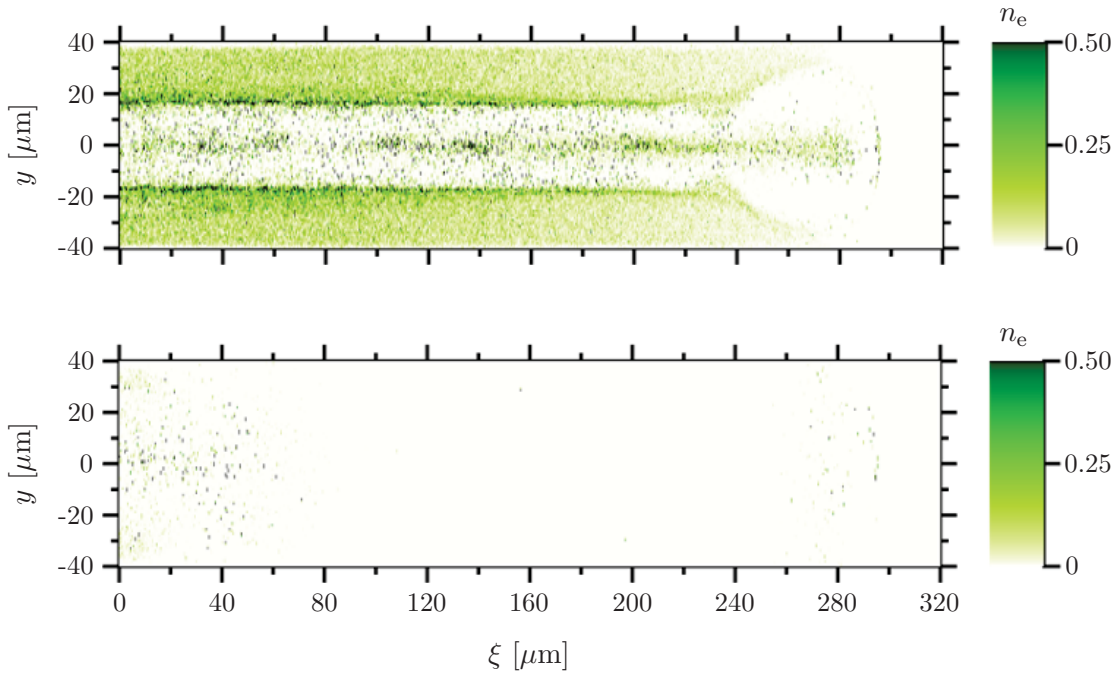

Figure 7.13: Electron density in units of the critical density in a HCl plasma from 3D VLPL simulations at simulation time T8 $\widehat{=}$ 2135 fs (upper) and T11 $\widehat{=}$ 2936 fs (lower).

A central question with respect to the proton acceleration is whether the high-energy protons are located at the areas of high hydrogen density. In this context, Fig. 7.14 shows the average energy per pixel for protons in the HCl plasma at the same simulation times as in Figs. 7.12 and 7.13. At the earlier simulation time, a well-defined band of high energetic protons along the $y = 0\,\mu$m axis of a few micrometers diameter is identified between $\xi = 220\,\mu$m and $\xi = 260\,\mu$m. From about $\xi = 240\,\mu$m the band starts to fade out and the energy on the central laser prop-

agation axis decreases. A comparison with the hydrogen density in the upper plot of Fig. 7.12 shows that the high proton density is located exactly, where the high energies are observed. The expansion of the bubble at $\xi = 240\,\mu$m is consistent with the fading out in the energy heat-map. For the high proton densities at the outer edges of the filament structure, especially between $\xi = 0\,\mu$m and $\xi = 160\,\mu$m in Fig. 7.12, the energy distribution does not indicate high energetic protons. Thus, the high proton energies are found on the central laser propagation axis. Only these protons are significantly accelerated and not those at the filament edges. Already here, the mechanism described in the previous section as first-stage acceleration in the plasma channel (Sec. 7.5) is recognized. The lower plot of Fig. 7.14 at the later simulation time T11, i.e., almost at the end of the down ramp, indicates a clear change in the distribution of the high-energy protons. Instead of the narrow band in y-direction, now a disk structure between $\xi = 100\,\mu$m and $\xi = 120\,\mu$m appears in y-direction between $y = \pm 40\,\mu$m. The position of this disk coincides exactly with the front edge of the filament in the proton density plot and has a very similar shape (cf. Fig. 7.12). The highest proton energies are still found around the laser propagation axis and are about two orders of magnitude higher compared to the average energy per pixel in the upper plot. This altered structure and the higher energies indicate a second acceleration mechanism, most likely MVA (cf. Sec. 3.2.3) identified in the previous section at the rear end of the gas jet, and, thus boosting the proton energies.

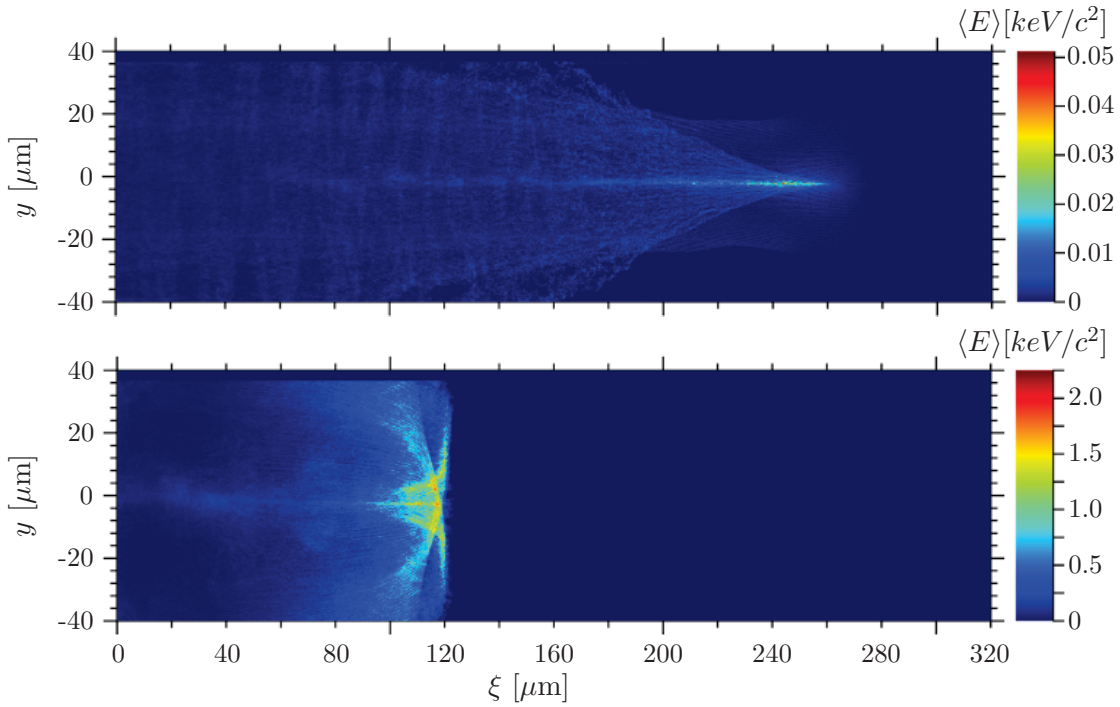

Figure 7.14: Average energy per pixel for protons in a HCl plasma from 3D VLPL simulations at simulation time T8 ≙ 2135 fs (upper) and T11 ≙ 2936 fs (lower).

To further elucidate the acceleration mechanisms, the magnetic fields in the z-direction (Fig. 7.15) and the electric fields in the x-direction (Fig. 7.16) are now considered, also at times T8 ≙ 2135 fs and T11 ≙ 2936 fs. The structures in the upper plots of Figs. 7.15 and 7.16 exactly correspond to the one in the electron density plot. Both are generated in the plasma channel due to the displacement of electrons as can be seen in the upper plot of Fig. 7.13. Furthermore, the protons are attracted into the filament along the channel axis as an effect of the radial space-

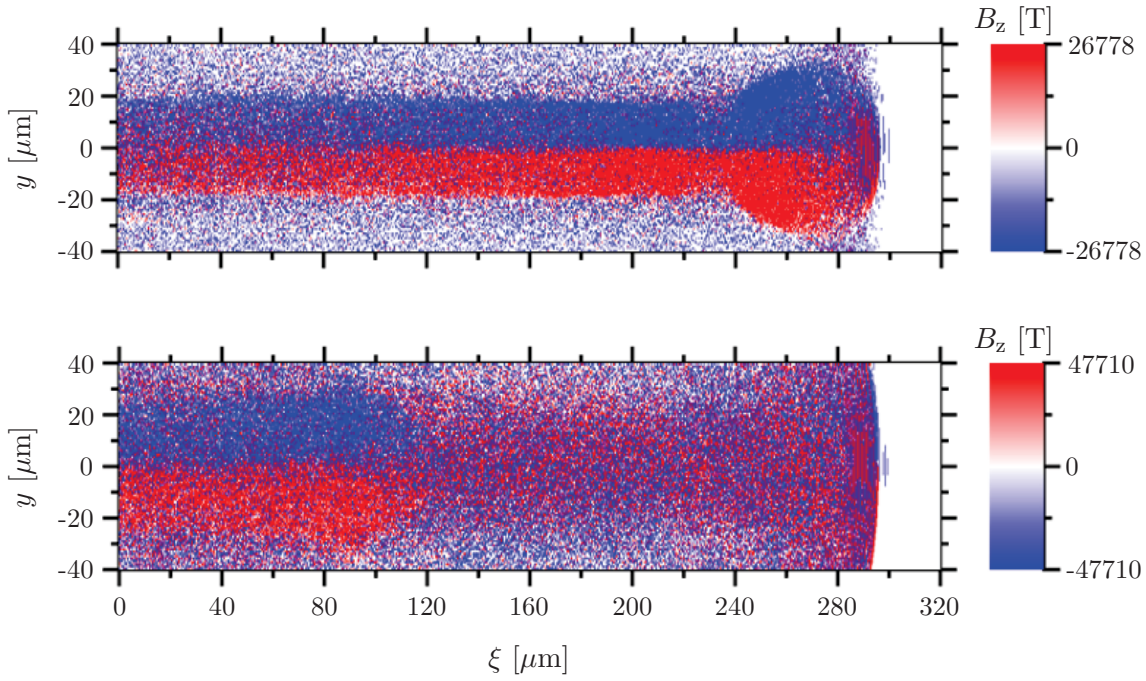

Figure 7.15: Magnetic field in z-direction in a HCl plasma from 3D VLPL simulations at simulation time T8 $\widehat{=}$ 2135 fs (upper) and T11 $\widehat{=}$ 2936 fs (lower).

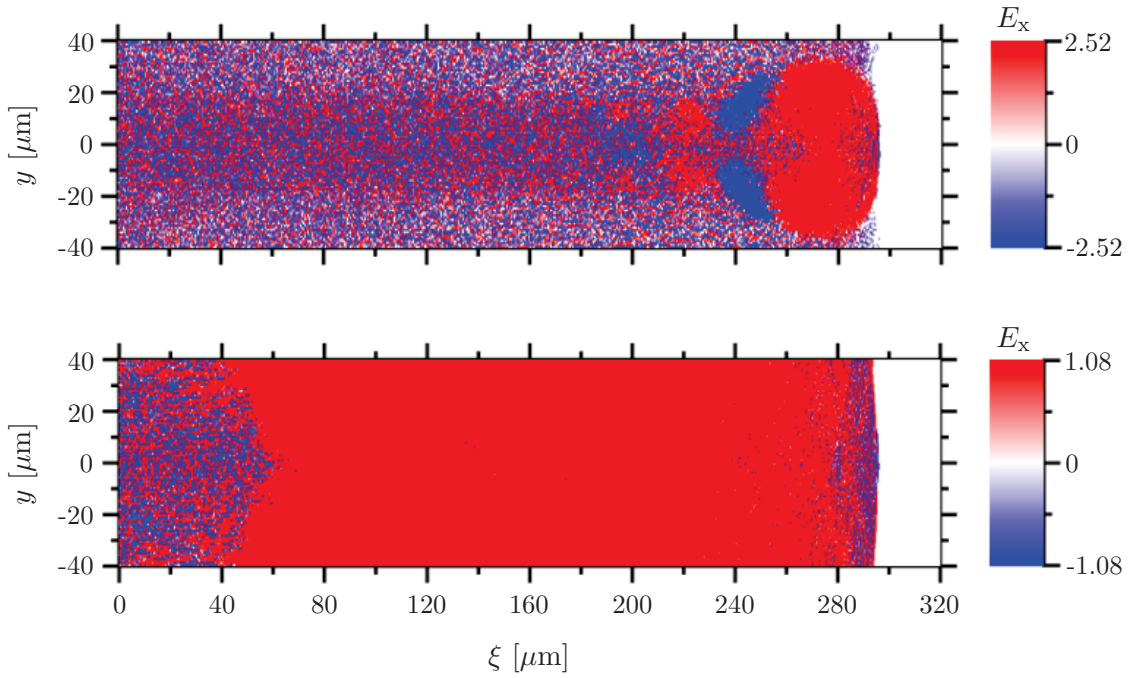

Figure 7.16: Electric field in x-direction in multiples of $mc\omega_0/e$ with the frequency $\omega_0 = 2\pi c/\lambda$ in a HCl plasma from 3D VLPL simulations at simulation time T8 $\widehat{=}$ 2135 fs (upper) and T11 $\widehat{=}$ 2936 fs (lower).

charge field. Caused by the comparably small charge-to-mass ratio of the ions, they converge towards the center on a much longer timescale than the electrons. Thus, the proton filament appears behind the laser pulse at around $\xi = 240\,\mu$m in the hydrogen density plot (cf. Fig. 7.12), while the electron filament forms inside the laser fields between $\xi = 240\,\mu$m and $\xi = 300\,\mu$m as visible in the electron density plot (cf. Fig. 7.13), as well as in the plots for the magnetic

and electric fields. As a further consequence of the longitudinal and radial space-charge fields within the plasma channel, an acceleration of higher energetic protons in forward and transverse directions results (cf. Fig. 7.14).

An investigation of the electric and magnetic fields at the later time T11 confirms the change of the acceleration mechanism. As the electrons driven by the laser pulse traverse the plasma down ramp at the rear target boundary starting from T9 (cf. Fig. 7.11), the azimuthal magnetic field expands into the vacuum under large angles creating a strong longitudinal electric field according to Faraday's law. This causes a strong secondary acceleration of protons at the rear boundary. Since this observation agrees with the results from Sec. 7.5, the mechanism is also referred to here as MVA. However, due to the decreasing plasma density in the down ramp, the electromagnetic fields around the laser propagating axis should quickly decay and finally become too weak to have a further impact on the acceleration of the protons. That effect, though, does not occur in the simulations; instead, a steadily growing energy is evident. This may result from the choice of boundary conditions in combination with a possibly too small simulation box. Thereby, non-physically high electromagnetic fields can develop, which would lead to a too strong acceleration. An enlargement of the size of the simulation box would result in a significant increase in simulation time. The simulation time for the presented simulation series, however, was well over 400000 core-h, which precludes a simulation with different parameters. Instead, the overestimate in the acceleration energies is analytically investigated in the following.

For this, a closer look is taken at the lower plot of Fig. 7.16 at simulation time T11, i.e., in the plasma down ramp. At this point, a kind of coulomb explosion has already occurred at the edge of the plasma down ramp at T9 (cf. Fig. 7.11), so that the shape of the high-energy proton bunch changes from a band-like structure to a disk (cf. Fig. 7.14). Due to this explosion, the electrons are accelerated away from the central propagation axis forming an electron cloud with high velocity along the y-direction by the strong electromagnetic field of the laser beam. These electrons then hit the vertical simulation box boundaries. As the Coulomb force acts on the electric charges a strong electric field is induced. Because of the choice of box boundaries in y-direction, which are open for particles but periodic for fields in set 2 and set 3, the charges at the boundaries cannot escape and accumulate as comparable with a plate capacitor in a non-physical way. Thus, the electron cloud does not propagate in the shape of a half-sphere at the plasma down ramp at time T9, as would be expected under experimental conditions. It is rather the case in the PIC simulations that the electron cloud spreads out in the shape of a compressed half-sphere, i.e., a cylinder, as illustrated in Fig. 7.17.

Due to the unrealistically strong electric field E_{x}, the proton acceleration in the PIC simulations of sets 2 and 3 is overestimated, resulting in too high proton energies. Other than that, the proton energies for simulation set 1 are underestimated as a consequence of the open boundaries for fields and particles. Due to the numerical implementation in the VLPL code, too many PIC particles are removed from the simulation box and the electromagnetic fields are unphysically strongly absorbed. Both leads to the assumption that the proton energies for set 1 are too small.

In Fig. 7.18 the energy spectra for all three sets for the simulation times T8 $\widehat{=}$ 2135 fs and T11 $\widehat{=}$ 2936 fs are provided. The crucial question now is how large the over- or underestimation of the proton energies due to the expansion of the electron cloud in the cylinder structure scales. In this context, an analytical estimate is made, for which the volume of the experimentally expected

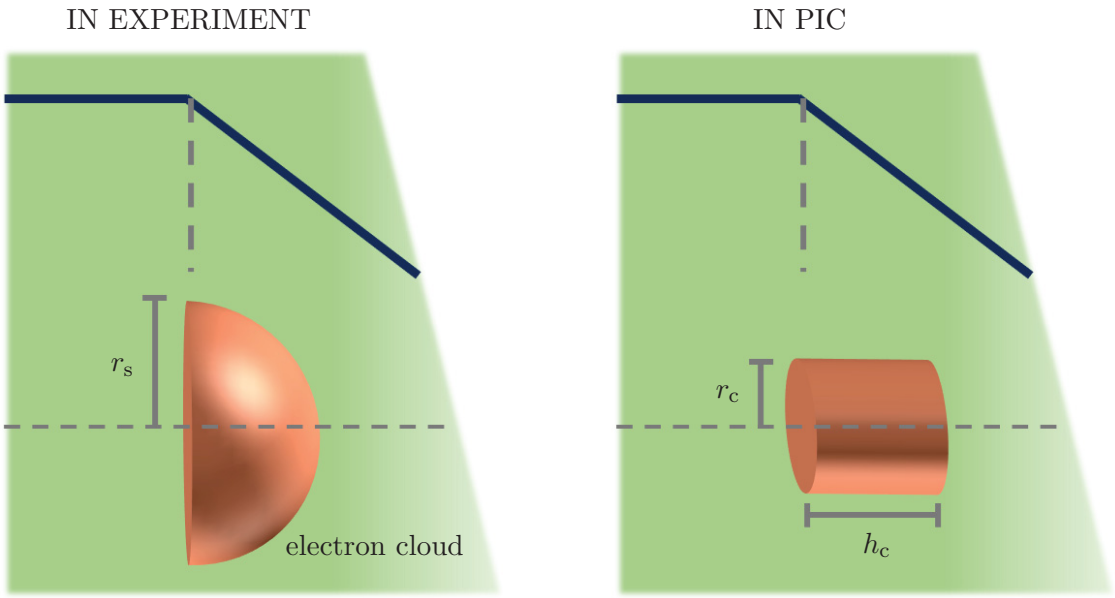

Figure 7.17: Expansion of the electron cloud during the transition from the density plateau to the plasma down ramp at time T9 (cf. Fig. 7.11). Left: Scenario as expected experimentally as a hemisphere-shaped propagation due to a Coulomb explosion. Right: Observation in the PIC simulations with open simulation boundaries in y-direction for particles and periodic for fields in sets 2 and 3 as expansion. The electron forms a narrow cylinder due to the unphysical accumulation of charges.

expansion of the electron cloud as a half-sphere is related to the expansion as a cylinder structure observed in the PIC simulations. Hereinafter, this is exemplarily demonstrated for set 3, the results for the other two sets are only listed in Tab. 4.

First, the radius of the half-sphere r_s is determined using the expansion of the overestimated positive longitudinal electric field E_x at simulation time T11. This amounts to $280\,\mu\text{m} - 40\,\mu\text{m} = 240\,\mu\text{m}$, from which the volume of the half-sphere V_s can be calculated. Similarly, the volume of the cylinder V_c is estimated as an approximation of the expanding electron cloud. It must be noted that the height of the cylinder h_s corresponds to the extension of the electric field E_x, while its radius r_c is limited by half the length of the simulation box in y-direction. The ratio of the two

Table 4: Comparison of the analytically estimated proton energies due to post-acceleration, which can be expected experimentally, with the under- or overestimated energies from the PIC simulations for the three simulation sets.

	set 1	set 2	set 3
radius half-sphere r_s	$45\,\mu$m	$200\,\mu$m	$240\,\mu$m
volume half-sphere V_s	$1.9{\cdot}10^5\,\mu\text{m}^3$	$1.7{\cdot}10^7\,\mu\text{m}^3$	$2.9{\cdot}10^7\,\mu\text{m}^3$
radius cylinder r_c	$24\,\mu$m	$24\,\mu$m	$40\,\mu$m
height cylinder h_c	$45\,\mu$m	$200\,\mu$m	$240\,\mu$m
volume cylinder V_c	$8.1{\cdot}10^4\,\mu\text{m}^3$	$3.6{\cdot}10^5\,\mu\text{m}^3$	$1.2{\cdot}10^6\,\mu\text{m}^3$
ratio of volumes $\Delta V = V_s/V_c$	2.3	47.2	24.2
energy gain btw. T8 & T11 in simulation ΔE_s	-15 MeV	300 MeV	180 MeV
analyt. calc. energy gain btw. T8 & T11 ΔE_a	6.5 MeV	6.4 MeV	7.4 MeV

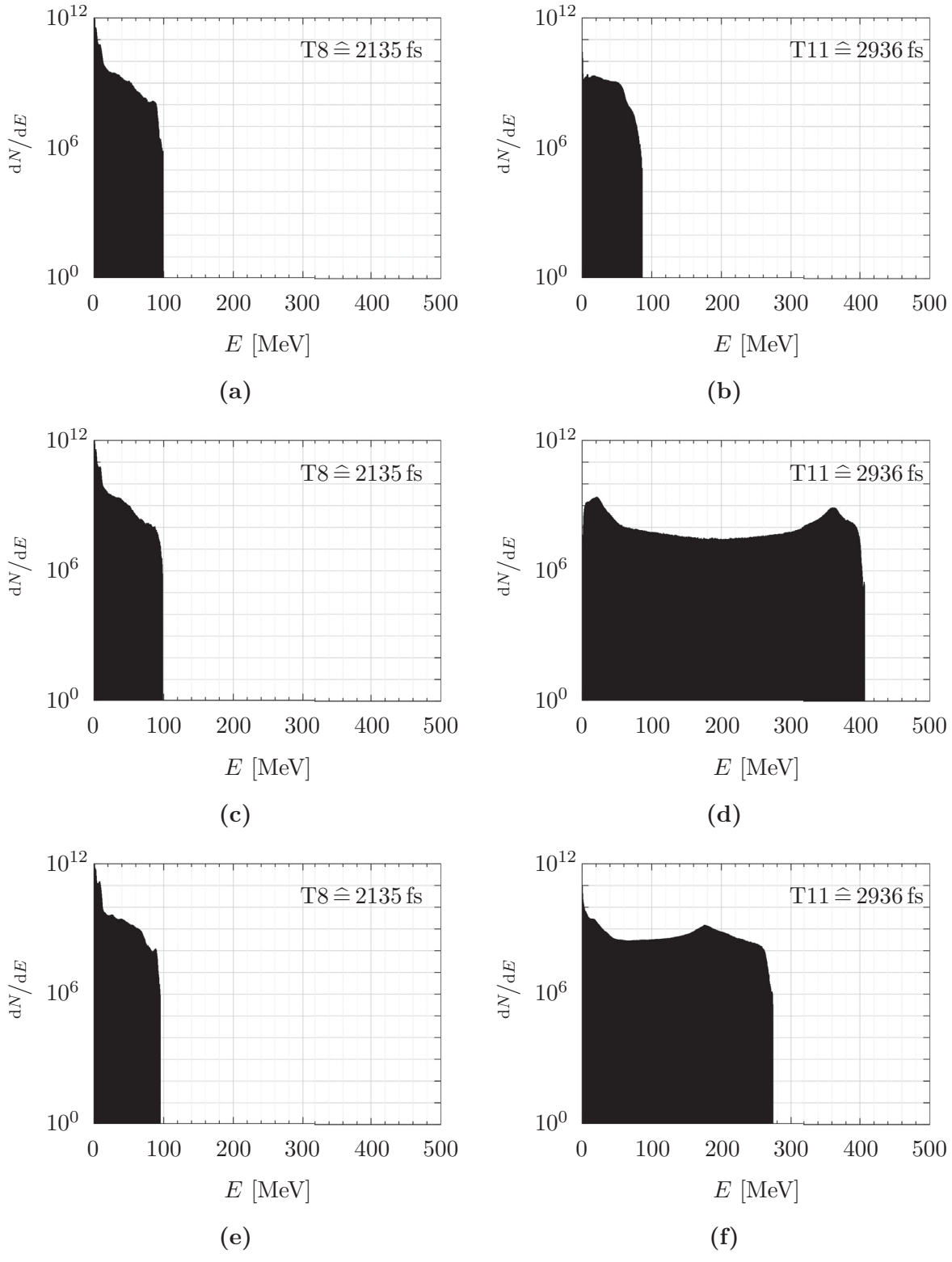

Figure 7.18: Energy spectra for protons in a HCl plasma from 3D VLPL simulations at two different times. First row: set 1, second row: set 2, third row: set 3.

volumes $\Delta V = V_\mathrm{s}/V_\mathrm{c}$ can be approximated as the correction factor for the proton energies. For simulation set 3, a ΔV of 24.2 is determined analytically. From the PIC simulations, an energy of nearly 100 MeV at simulation time T8 in the plasma plateau and of almost 280 MeV at T11 in the plasma down ramp is obtained from the spectra in Figs. 7.18e and 7.18f. This yields an

energy gain ΔE_s of 180 MeV between these two times. Thus, from the volume factor, the energy to be expected in the experiment due to the post-acceleration is only about $\Delta E_\mathrm{a} = 7.4\,\mathrm{MeV}$. Consequently, the analytical estimation confirms the assumption that the simulation box size and the choice of boundary conditions result in an artefact in the proton energies.

Compared to the simulations presented in Sec. 7.5 the influence of post-acceleration by the MVA mechanism turns out to be significantly smaller. However, this can be explained by the significantly wider target extent, which is adapted to experimental conditions here, leading to an earlier absorption of the laser pulse in the target. For simulation set 2, the result is similar, but more significant. Due to the smaller simulation box in y- und z-direction, the longitudinal electric field E_x is further compressed and the cylinder structure comparatively expands even further, so that the volume factor $\Delta V = 47.2$ becomes even larger. The simulated energy gain of about $\Delta E_\mathrm{s} = 300\,\mathrm{MeV}$ (cf. Figs. 7.18c and 7.18d) is reduced to only $\Delta E_\mathrm{a} = 6.4\,\mathrm{MeV}$ by the analytical estimation. In set 1 even a decrease of the proton energy from about 100 MeV at T8 to about 85 MeV at T11 (cf. Figs. 7.18a and 7.18b) can be found. The MVA mechanism, therefore, has no effect here and a post-acceleration at the plasma down ramp does not take place. This can be attributed to the choice of open boundaries for fields and particles in all three spatial directions, since otherwise all parameters are identical to set 2. Unlike observed for sets 2 and 3, no overestimated E_x field is formed here, which makes the estimation of the radius of the half-sphere for the electron cloud more difficult. Based on this, $r_\mathrm{s} = 45\,\mu\mathrm{m}$ is applied. Then, ΔV equals 2.3 and the proton energy is only overestimated by a factor of 2.3 so that in total an energy gain of $\Delta E_\mathrm{a} = 6.5\,\mathrm{MeV}$ can be expected in the experiment. Here it becomes apparent that $r_\mathrm{s} = 45\,\mu\mathrm{m}$ is a reasonable choice because the analytical calculations for the energy gain for sets 1 and 2 yield the same result. Finally, it can be concluded that the post-acceleration in all three cases only has a minor influence on the proton energies and that the energy is clearly overestimated, when using periodic boundaries. In all cases, a maximum proton energy of about 100 MeV can be expected.

In the last step, it must be investigated whether the unphysically strong electric fields lead to a depolarization of the protons initially fully polarized in y-direction. First of all, it is not expected that there will be an enhancement effect for the magnetic fields due to the Coulomb explosion. The polarized protons are located only inside the target and, thus, there should be no influence on the polarization. Figure 7.19 shows the average polarization in y-direction for high-energy protons in the cutout between $\xi = 90\,\mu\mathrm{m}$ and $\xi = 120\,\mu\mathrm{m}$ and $y = \pm 10\,\mu\mathrm{m}$ related to the lower plot in Fig. 7.14 at time T11. At this point, the final proton polarization can already be well estimated, since the protons have almost completely left the target. While the average polarization at the rear part of the disk (cf. Fig. 7.14) between $\xi = 90\,\mu\mathrm{m}$ and $\xi = 110\,\mu\mathrm{m}$ is mostly above 90 %, there are stronger depolarization effects in the front part. Here, the average polarization drops to about 48 %, which is a bit lower compared to the values in Tab. 3. This can be explained by the fact that the magnetic fields at the front of the filament are less stable (cf. Fig. 7.15) and a rotation of the proton spin according to the T-BMT equation is more likely. Thus, no further correction factors need to be considered for the magnetic fields and the proton spins. A more comprehensive discussion of the effects on the polarization of protons in the plasma down ramp can be found in our publication by Lars Reichhwein, Anna Hützen et al. [148].

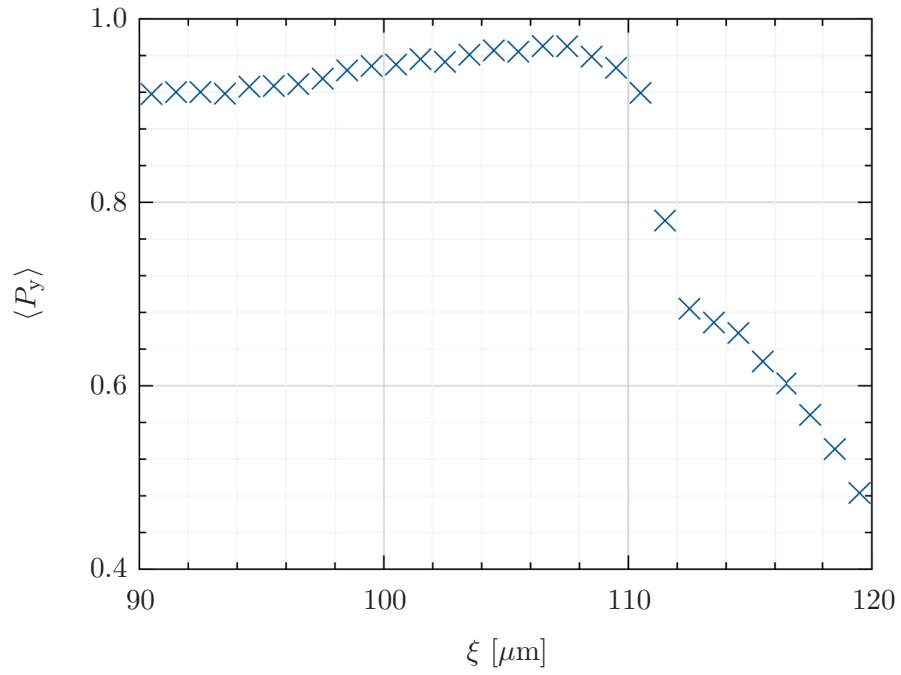

Figure 7.19: Average polarization in y-direction for high-energy protons in the cutout between $\xi = 90\,\mu$m and $\xi = 120\,\mu$m and $y = \pm 10\,\mu$m related to the lower plot in Fig. 7.14 at time T11.

To confirm the analytical estimate of the expected proton energy of about 100 MeV after acceleration (cf. Fig. 7.18 and Tab. 4) and to verify the average proton polarization (cf. Fig. 7.19), another 3D VLPL simulation is in preparation. For this purpose, the simulation box should be enlarged in y- and z-direction by at least a factor of two. As a result, the simulation will require at least four times more resources, i.e., about 1.6 Mcore-h. This is slightly more than half of our budget this year on the JURECA Cluster module.

8 Layout of the Polarized Gas Target

A key task of this PhD thesis is the design of an experiment for the generation of polarized proton beams, as well as the identification of a suitable measuring tool for polarimetry, which can be integrated into the setup. For the experimental realization of this new concept for a dynamically polarized proton source, three components are required: a dedicated laser system, a vacuum interaction chamber including a gas jet and a polarimeter. Figure 8.1 depicts the schematic view of the setup, which has already been described in several publications of our group [26, 27, 29, 31, 32]. The selection of the laser system with optical elements for beam guiding, as well as the complete design of the interaction chamber including the choice of a suitable method for the generation of a gas jet is part of this work. In the following sections, the setup is described in detail, starting with the method to realize a dynamically polarized gas target (cf. Sec. 8.1). Based on this, the target, which acts as a polarized proton source (cf. Sec. 8.2), and the layout of the interaction chamber are presented (cf. Sec. 8.3). Subsequently, the *Ju*SPARC_Mira laser system and the beam optics are characterized (cf. Sec. 8.4). The LSP was already introduced in Sec. 4.4 and has been in use for more than ten years in various experiments [108, 111–113].

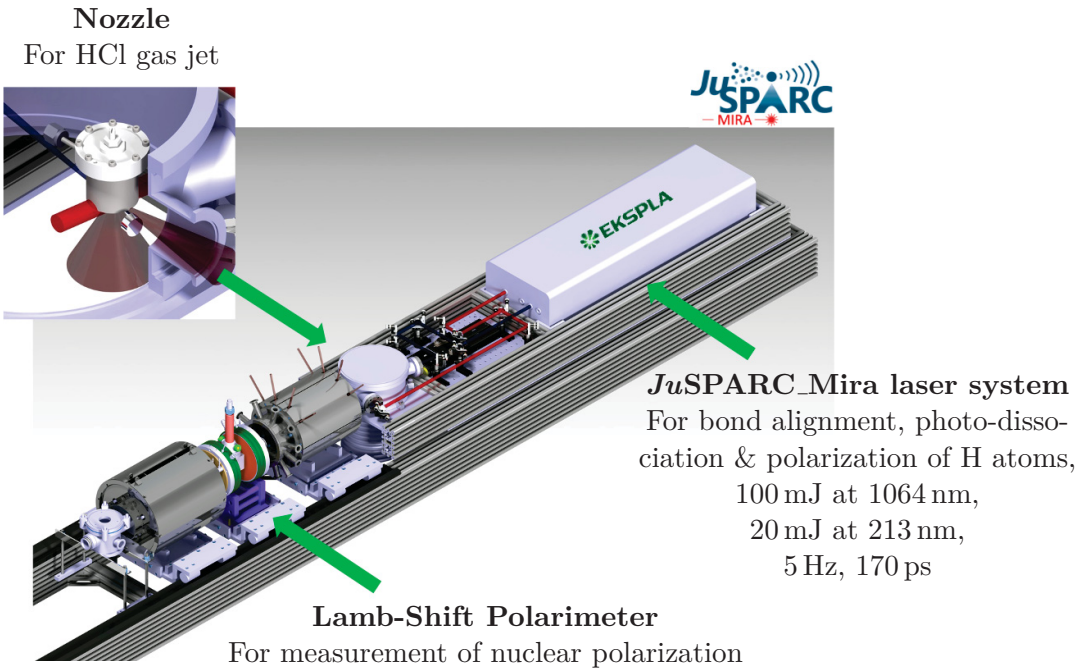

Figure 8.1: Schematic view of the setup for the proton polarization measurement using a polarized hydrogen gas target [26].

8.1 Polarized gas jets as laser target

As learned from the simulation results in Sec. 7, a compact target is needed for laser-induced particle acceleration, in which the nuclear spins are already aligned at the time of irradiation with the accelerating laser. For proton acceleration and, to a large extent, also for electron acceleration, plasma depolarization effects are mostly independent of the target material and negligible, as shown in Sec. 5. In principle, two possible geometries of polarized targets for laser-induced particle acceleration are distinguished: solid and gas targets, as shown in Fig. 8.2.

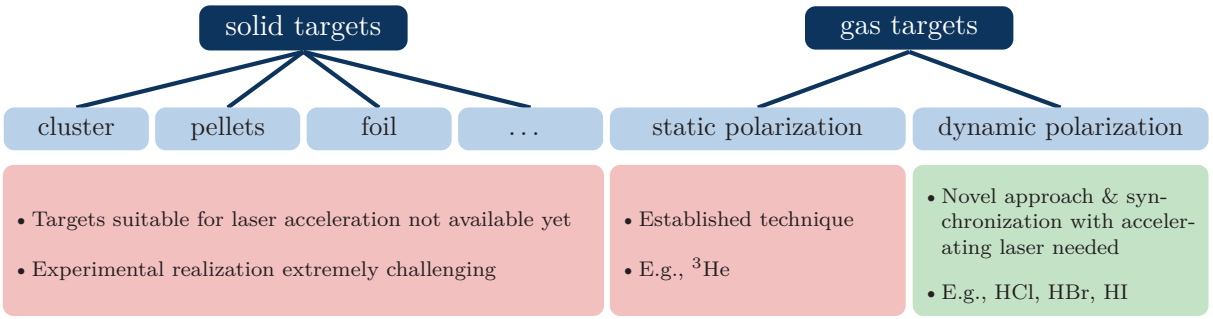

Figure 8.2: Possible realizations of polarized targets for laser-induced particle acceleration.

At conventional accelerators, such as COSY, so-called Atomic Beam Sources (ABSs) are used to generate polarized beams. The selection of certain nuclear-spin states in an ABS is based on the Stern-Gerlach (SG) principle: an atomic beam of unpolarized hydrogen atoms passes through an inhomogeneous magnetic field resulting in a separation of the atoms with spin-up and spin-down electrons into separate beams due to the deflection force induced by the magnetic field. However, the typical density of an ABS beam ($\rho \approx \mathcal{O}(10^{12}\,\mathrm{cm}^{-3})$) is far below the requested value for laser-acceleration experiments, which typically amounts to $10^{19}\,\mathrm{cm}^{-3}$.

Currently, three kinds of nuclear-polarized targets are conceivable for laser-plasma acceleration:

- Alignment of spins in strong magnetic fields (several T) at low temperatures (mK), also known as “brute-force polarization”, since the energy difference between two spin states $\Delta E = g \cdot {}^{e\hbar}/_{2m} \cdot B$ is larger than the average thermal energy E_{thermal}, e.g., $\Delta E(\mathrm{proton}) = 1.76{\cdot}10^{-7}\,\mathrm{eV/T}$ compared to $E_{\mathrm{thermal}} \approx 1/40\,\mathrm{eV}$ at room temperature. An example are so-called frozen-spin targets, which have the disadvantage that the maximum achievable polarization is limited to approximately 0.25 [157]. The use of such targets in context of laser-plasma acceleration would be extremely challenging.

- Polarization transfer with optical methods and minimization of (depolarizing) interactions in “hyper-polarized targets”, e.g., a ^{3}He gas-jet target [158, 159]. Such a laser-driven spin-polarized ^{3}He-ion beam source is brought into operation by our research group. The essential components of such a target are permanent external magnetic fields in order to hold the spins during the experiment, and a non-magnetic valve for providing the desired gas-jet target. However, this target concept is very limited in view of the target material, since only atoms of noble gases, ^{3}He and ^{129}Xe, can be polarized. A possibility for polarizing protons may be offered by cryogenic foil targets. However, their realization is extremely challenging as low temperatures and permanent magnetic holding fields are needed similar to frozen-spin targets. Nevertheless, there are efforts in our group to build a hyper-polarized foil target by freezing hydrogen molecules initially polarized in an ABS [160]. This option promises the possibility of a more effective acceleration, i.e., according to the TNSA mechanism (cf. Sec. 3.2.1), due to the higher particle density compared to a gas target.

- A dynamically polarized hydrogen gas target, in which the nuclear spins are already aligned when irradiated with the accelerating laser. The only, so far known method to realize such a target is based on hydrogen halides. This method has already been studied by the group of T. P. Rakitzis from the University of Crete [161–166] and can be used for both, proton [26, 27, 29, 32] and electron polarization [29, 120]. A schematic overview of this principle is shown in Fig. 8.3 and will be further described in the following.

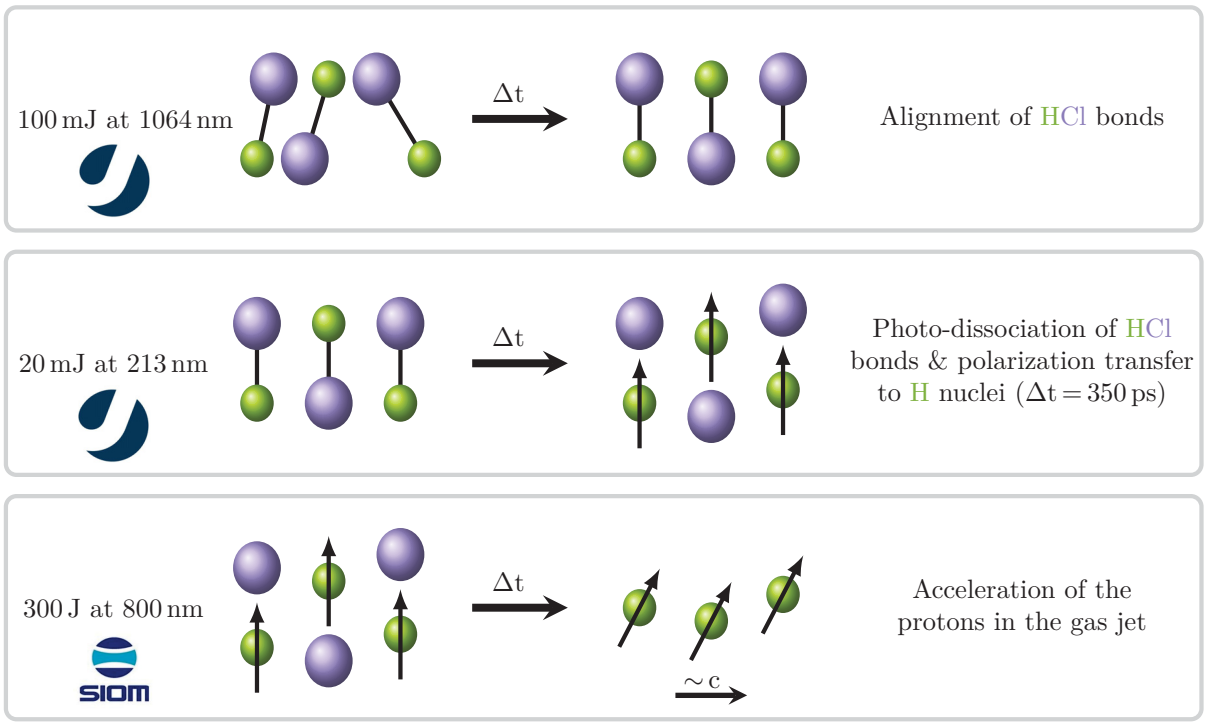

Figure 8.3: Schematic overview of the production of laser-driven polarized proton beams. The HCl bonds are first aligned with an IR laser beam. This is an optional process to increase cross section of the photo-dissociation and, thus, to increase the final signal. The 213 nm UV laser with 20 mJ energy photo-dissociates the HCl molecules and consequently the electron polarization is transfered into nuclear polarization due to hyperfine-structure oscillations. Finally, the protons polarized in this way are accelerated to high energies with a high-intensity laser pulse, e.g., the SULF laser, while maintaining their polarization (cf. Sec.7).

8.2 Spin-polarized HCl/HBr as polarized proton source

A very promising approach to realize a polarized target with an average degree of polarization of about 70 % relies on the principle of photo-dissociation of hydrogen halides. Hydrogen halides are chemical diatomic inorganic compounds, which are formed from the corresponding halogens, such as fluorine (F), chlorine (Cl), bromine (Br), iodine (I), or astatine (At), with hydrogen. At, being a radioactive element with a lifetime of only a few hours, is not considered in the following. For our experiments HCl and HBr have been used. Here, the hydrogen atom and the halogen atom are connected by a polar covalent bond as the halogen atom is much more electronegative than the hydrogen atom, which makes this bond polar. Thus, the molecule has a large dipole moment with a positive partial charge at the hydrogen atom and a negative partial charge at the halogen atom.

8.2.1 Spin-selective photo-dissociation

In photo-dissociation, the absorption of electromagnetic radiation in the visible, ultraviolet or even shorter wavelength spectrum leads to a bond splitting. The wavelength of the absorbed light must be more energetic than the binding energy, and the overlap of the ground-state and excited-state wavefunctions of the allowed transition must be significant. Compared to the mentioned conventional production method by an ABS, in the photo-dissociation process the densities and timescales are at least seven orders of magnitude higher or faster [164, 166].

Spin-polarized atoms can be produced from the adiabatic photo-dissociation of hydrogen halides with circularly polarized light [162, 167, 168], since the photo-dissociation is prompt (leading to axial recoil). The total electronic angular-momentum projection Ω along the bond of a particular molecular state adiabatically correlates with the sum of the m-states of the separated atoms, e.g., $\Omega = m_\mathrm{H} + m_\mathrm{Cl}$ [169, 170]. This process is schematically depicted for the photo-dissociation of HCl in Fig. 8.4.

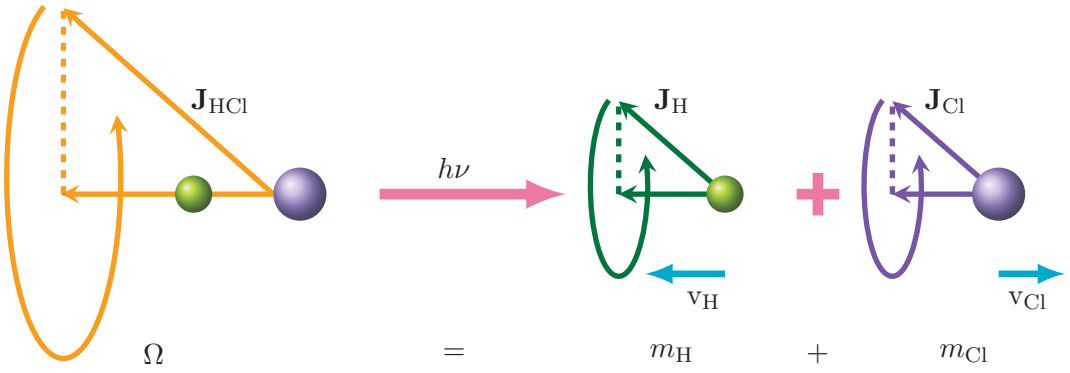

Figure 8.4: The photo-dissociation process using the example of HCl: the total electronic angular-momentum projection Ω is conserved during the photo-dissociation process, and is equal to the sum of the product m-states. The flight directions of the H and the Cl are opposite and the H atom gains the larger momentum due to its smaller mass. The precession of the angular momentum about the quantization axis is indicated by the rotating arrows, adapted from Ref. [164].

Using a photo-dissociation laser of 213 nm wavelength, like *Ju*SPARC_Mira (cf. Sec. 8.4), and circularly polarized light, the HCl molecules are photo-dissociated by UV excitation via the $A^1\Pi_1$ state, which has a total electronic angular-momentum projection of $\Omega = +1$ along the bond axis. The resulting H and Cl($^2\mathrm{P}_{3/2}$) photofragments conserve this $+1$ projection of the laser photons, producing H and Cl($^2\mathrm{P}_{3/2}$) atoms each with the projections of approximately $m_\mathrm{s} = +1/2$ (so that they sum to $+1$), where m_s is the spin quantum number. Thus, the H atom electron spin is approximately $m_\mathrm{s} = +1/2$ [164].

In a weak magnetic field (Zeeman region), all H atoms are in a coherent superposition of the total angular momentum states $|F, m_\mathrm{F}\rangle$ with the coupling $\mathbf{F} = \mathbf{s} + \mathbf{I}$ of the electron spin $\mathbf{s}$ and the nuclear spin $\mathbf{I}$ (cf. Fig. 4.5). Since the electron spin is fixed due to the polarization of the incident laser pulse, e.g., $m_\mathrm{s} = +1/2$, only the spin combinations $|m_\mathrm{s} = +1/2,\ m_\mathrm{I} = +1/2\rangle$ and $|+1/2, -1/2\rangle$ are allowed in free hydrogen atoms. As the hyperfine state $|+1/2, +1/2\rangle = |F = 1,\ m_\mathrm{F} = +1\rangle$ is an eigenstate, it will stay unchanged in time (cf. Eq. 4.37). The states $|-1/2, +1/2\rangle$ and $|+1/2, -1/2\rangle$ are not eigenstates and, thus, are defined as linear combinations of the

eigenstates $|F=1,\ m_F=0\rangle$ and $|F=0, m_F=0\rangle$, having different energies (cf. Eq. 4.37). This is why atoms, which are produced in the $|+1/2,-1/2\rangle$ state, oscillate to the $|-1/2,+1/2\rangle$ state and back. If now the electron-polarized hydrogen atoms are generated during a very short time, i.e., $t<1$ ns, they will oscillate in phase. Hence, after 0.35 ns only the spin combinations $|+1/2,+1/2\rangle$ and $|-1/2,+1/2\rangle$ are observed, as illustrated in Fig. 8.5. This means that the electron polarization of the hydrogen atoms, produced by the incident circularly polarized UV laser beam, is transferred into a nuclear polarization due to hyperfine-structure oscillations.

The process described applies not only to HCl, but to all hydrogen halides. However, it should be noted that the dissociation enthalpies of the H-X bond increase, while the bond lengths are reduced with decreasing atomic numbers. Thus, the laser wavelength must be adjusted accordingly for the relevant photo-dissociation process [161–166, 171, 172]. If, in the second stage, the hydrogen atoms are ionized and accelerated, the out-coming protons will remain polarized, even if they undergo spin precession according to the T-BMT equation (cf. Sec. 5) [26, 30].

It should be noted that if an additional external magnetic field $B > B_c = 50.7$ mT is applied, the hyperfine-structure oscillations are suppressed, since the spin combination $|m_s=+1/2,\ m_I=-1/2\rangle$ is now fixed as $|F=1,\ m_F=0\rangle$. For one half of the atoms $m_I=+1/2$, for the other half $m_I=-1/2$, so that finally no polarization is measurable.

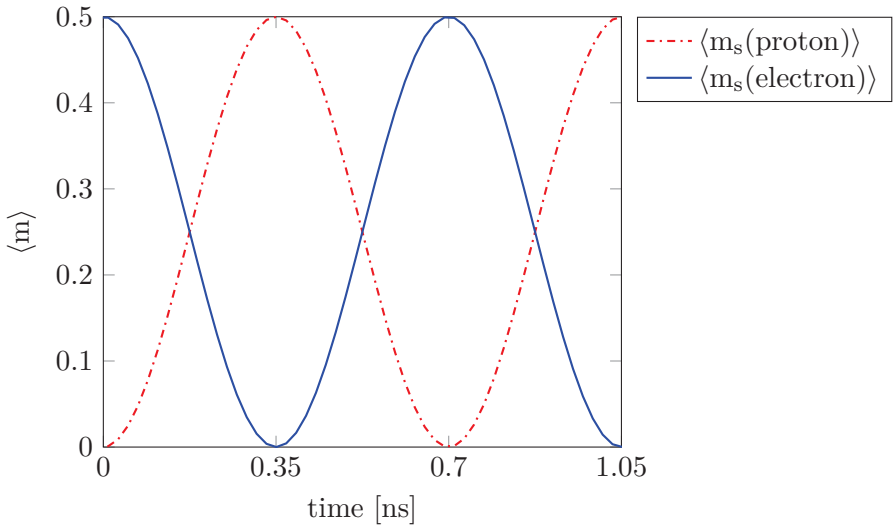

Figure 8.5: After 0.35 ns the electron polarization of the hydrogen atoms, produced by the circularly polarized UV laser beam, is transferred into a nuclear polarization due to hyperfine-structure oscillations.

There are two key advantages for the production of spin-polarized hydrogen from the photo-dissociation of HCl that are particularly important, when designing a polarized target [164]:

- Since the density of the photo-dissociation fragments (H and Cl) can be equivalent to the initial density of the parent molecules, the intensity of the polarized atomic beam can be that high to measure the degree of polarization directly with the LSP.
- The photo-dissociating light of the laser, which can be set both, temporally and spatially, as suitable, controls the polarization of the resulting fragments. This opens up further freedom in the performance of experiments.

8.2.2 Increase of the photo-dissociation cross section by bond alignment

Furthermore, there is the option to increase the average polarization by a prior alignment of the bonds. This requires another laser beam, which is linearly polarized, has a wavelength of 1064 nm and interacts before the 213 nm pulse with the HCl gas, shifted by 90°. By this, when the laser field is on, a dipole moment is induced into the molecules that is even larger than typical permanent electric dipole moments of polar molecules. This induced electric dipole moment μ is then aligned by the laser field, and the bond with it. Here, the laser alignment occurs for molecules that have different polarizabilities parallel and perpendicular to the bond. μ is induced along the bond, and it oscillates, positively or negatively but not perpendicularly. As it adjusts with the electric field of the light, the bond is always parallel to the electric field of the light: when the electric field is positive, μ is positive and vice versa. Thus, the electrons oscillate up and down, with the oscillating electric field. Because that oscillation is basically parallel to the bond, the bond is forced to be parallel to the electric field. However, the permanent electric dipole moment of HCl, which decides whether H is up or down, is not oscillating. Hence, by irradiation the bonds with IR light, only alignment occurs meaning that the bonds are aligned but it cannot be distinguished between a parallel or an antiparallel orientation.

By this process, the cross section of the photo-dissociation and, thus, also the final signal intensity is increased. The polarizability interaction for the bond alignment is governed by a $\cos^2\theta$ potential with the angle θ between the molecular axis and the electric field distribution. Using the equations by Friedrich et al., the amplification factor x is calculated to be $x \approx 2$ assuming an interaction parameter of $\Delta\omega = 49$ and, thus, $\ll \cos^2\theta \gg = 6/7$ [26, 173, 174]. Finally, with the alignment of the bonds in the designed experiment a doubling of the signal intensity can be achieved. Overall, an average degree of polarization of about 70 % can be reached for HCl as well as for HBr gas, using both lasers. This polarization scheme has been applied at gas densities up to $10^{19}\,\mathrm{cm}^{-3}$, which is in the useful range for laser-plasma acceleration [164, 166].

8.3 Interaction chamber and piezo valve

The injection of the gas into the interaction chamber is not only a relevant issue in terms of safety, to which special importance must be attached during the planning of the entire experiment, but also the reproducible performance of the polarization process. For this purpose, it is primarily important to select a gas valve that can deliver small quantities of the gas in defined, very short pulses. The corrosion-resistant piezo valve *S/N 17522* from *Innovative Research Solutions GmbH* has been selected. A schematic drawing can be found in App. D. The valve is 59 mm long and 33.8 mm wide and consists of a stainless steel valve body and cover, which are connected by the valve base. On the valve body there is a connection, to which a Teflon tube is attached as a gas supply line. Using a vacuum feed-through, this is connected to the gas line in the lab. In addition, there are two electrical cables on the valve, one for the signal and one for grounding, which allow the valve to be controlled externally with a *piezo valve controller*. By applying a high voltage, a plunger in the valve is moved by two piezo crystals, allowing gas to flow through the cylindrical opening with 1.5 mm in diameter into the interaction chamber. To perform most experiments a voltage of -800 V is used, the opening time of the valve is 30 μs at 5 Hz repetition rate. With similar test parameters for H_2 gas at 8 bar backing pressure, the company guarantees a formation of the gas jet after about 150 μs at a distance of 200 mm from the valve opening.

As a further option for gas-jet shaping, a de Laval nozzle is available, which can be fixed to the piezo valve with two screws. The jet is formed by the special geometry of the nozzle: first the cross section narrows from 1.0 mm to 0.5 mm and then widens again to 2.2 mm in diameter, with a continuous transition from one part to the other. The cross-sectional area is circular at each point. This allows the through-flowing gas to be accelerated to supersonic velocity as a result of the relative density change. The out-flowing gas has a velocity parallel to the axis, so that a directed thin gas jet with high particle densities is formed.

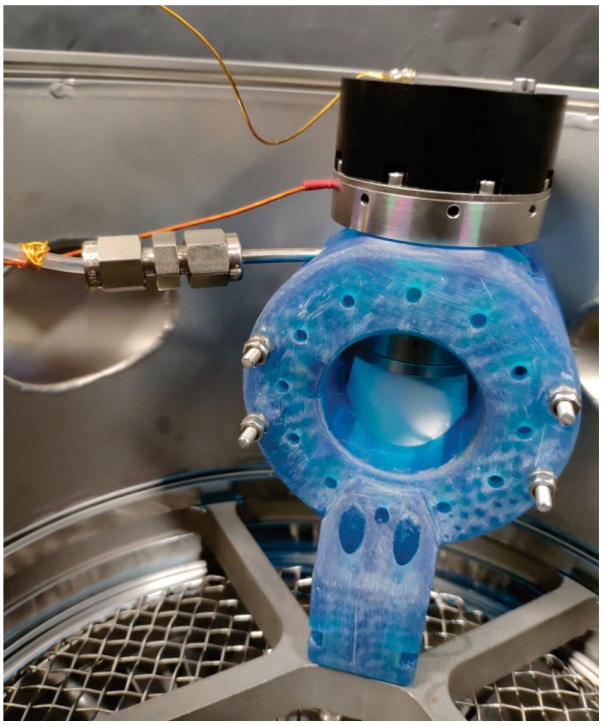

Figure 8.6: View into the interaction chamber with the 3D-printed acid resistant holder and the piezo valve connected to the gas line (white Teflon tube) and electricity. In the center of the cylindrical opening the interaction between the laser beams and the gas takes place.

To achieve a defined interaction point of gas and laser beams, the valve must have a fixed position in the interaction chamber. This is obtained with the help of a specially designed holder, which is shown in Fig. 8.6 including the valve and the supply lines. The holder is manufactured using a 3D-printing process and consists of a synthetic resin that is both, vacuum and corrosion resistant. It is screwed to the interaction chamber using an auxiliary X-shaped construction so that it can only be mounted in one position. Moreover, this structure ensures the alignment with the vacuum chamber, which in turn is adjusted to the LSP. An important point to note is that the holder is not mounted in the center of the interaction chamber, but as close as possible to the first component of the LSP, the ionizer. This is to maximize the signal of the polarized protons. Additionally, the positioning of the valve is also firmly defined by a precisely fitting opening, a recess for the gas supply line, and M3 threaded rods that connect the two main parts of the holder and are kept together with nuts. Besides, there is a cylindrical opening in the holder, in which the valve is positioned so that it is centrally located in the holder. The two laser beams can also pass through this opening and interact with the gas. The geometry of the holder is also designed in such way that the interaction point is located just a few millimeters below the valve opening. As an additional option, a strong magnetic field $B > B_c = 50.7\,\mathrm{mT}$ can

be generated with the installation of permanent magnets around the interaction point, which then suppresses the hyperfine-structure oscillations (cf. Sec. 8.2.1). Consequently, unpolarized atoms can be observed in the LSP.

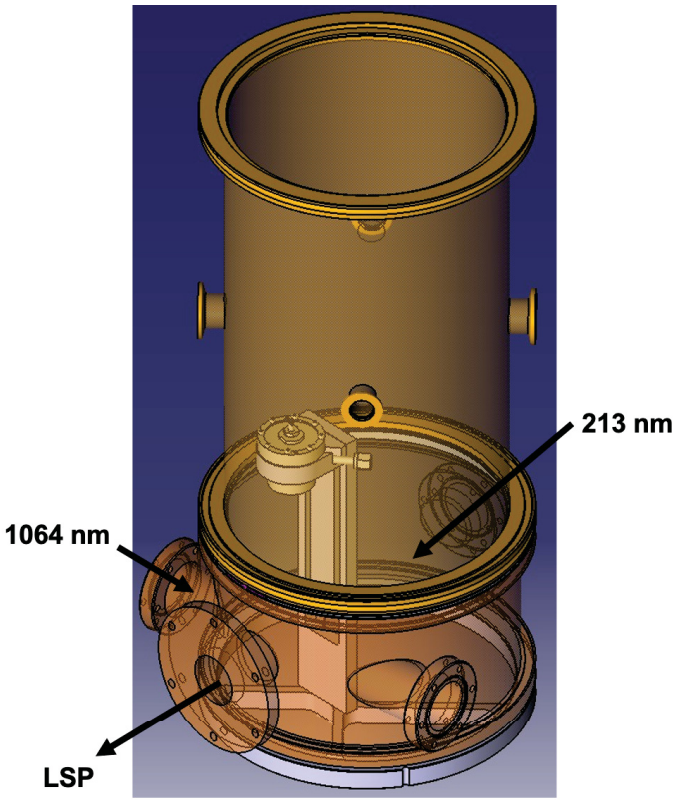

Figure 8.7: Schematic view of the new designed interaction chamber with an holder for variable adjustment of the height of the piezo gas valve.

The cylindrical interaction chamber is based on the ISO-K standard, has a diameter of 213 mm and a height of 130 mm. On three sides of the chamber there are ISO-CF40 flanges with windows made of fused quartz on each side, so that laser radiation from infrared to ultraviolet radiation can be transmitted but the generated radiation cannot escape (cf. Fig. 8.7). The fourth side is equipped with a flange for connection to the LSP. Two pumps are used to create the vacuum in the interaction chamber: an oilfree *SCROLLVAC SC 15 D* backing pump and a *MAG integra* turbo molecular pump, both from *Leybold*. The backing pump is mounted to the chamber with a bellow, while the turbo pump is installed just below the chamber, so that the gas can be pumped off directly after the interaction. Thus, a pressure of about 10^{-8} mbar can be achieved in the chamber, which is primarily useful to suppress the background in the ionizer of the LSP to achieve a higher sensitivity of the measurements. The pressure can be read out using a pressure gauge attached to the chamber. A grid directly above the turbo pump ensures that no small components can accidentally fall into the pump (cf. Fig. 8.6).

During commissioning of the setup and the first experiments it turns out that it is necessary to vary the distance between valve and interaction point (cf. Sec. 9). Thus, a new valve holder has been developed, which is adjustable in height, but still has a defined position in the other two spatial directions. Figure 8.7 shows the final design. The holder can be connected to the interaction chamber at the same position as the old holder by using the auxiliary construction.

Two guide rails allow the position of the holder to be varied in height over a length of 135 mm and at the same time prevent the device from tilting. The installation of the height-adjustable holder also entails an enlargement of the interaction chamber in vertical direction. For this purpose, another ISO-K chamber with a height of 356 mm is assembled onto the existing chamber. The four flanges with ISO-K16 and ISO-K25 dimensions are initially unneeded.

To ensure the overlap of gas jet and laser pulses not only in space but also in time, the digital pulse delay generator *STDG645-EU* from *Stanford Research Systems* with a maximum resolution of 5 ps is utilized. By connecting the laser system and the valve with the pulse generator, the laser pulse can be emitted in such a way that it shoots into the gas when the gas jet is fully formed, thus generating the largest amount of polarized protons. The *RTP044 digital oscilloscope* from *Rohde & Schwarz GmbH & Co. KG* is used for signal readout, which has the special feature of resolving the short pulses of the laser system with a duration of 170 ps.

8.4 The *Ju*SPARC_Mira laser system and beam optics

The peculiarity of the *SLL334-5 Ju*SPARC_Mira system, belonging to the *EKSPLA SL330 series*, is the simultaneous output of the fundamental wavelength at 1064 nm and the fifth harmonic at 213 nm provided by a Nd:YAG crystal serving as active medium (cf. App. C) [175]. In Tab. 5 the most important features of the *Ju*SPARC_Mira system are summarized.

Table 5: Main parameters of the *Ju*SPARC_Mira laser system [175].

Manufacturer:	EKSPLA
Repetition rate	5 Hz
Pulse duration	170 ps
Pulse energy	100 mJ @ 1064 nm, 20 mJ @ 213 nm
Average power	0.5 W
Up-converted Radiation	532 nm, 266 nm, 213 nm
Conversion principle	Built-in 2nd, 4th, 5th harmonic generator
Experimental technique	Control of nuclear spins via photo-dissociation

Operating at a repetition rate of 5 Hz, the pulse duration of 170 ps is realized by compressing the pulse during Backward-stimulated Brillouin Scattering (SBS). SBS is a non-linear process occurring in optical fibers at input power levels much lower than that required for stimulated Raman scattering [176]. Once the Brillouin threshold is reached, it appears by the generation of a backward propagating Stokes wave, which carries most of the input power. Thus, this is a very useful technique in the fabrication of lasers and amplifiers. The pulse compression itself takes place in the dedicated SBS cell such that tunable pulses with duration in the $170 - 1500$ ps range can be achieved. After SBS compression, the fundamental pulse is guided to a multi-pass power amplifier system, where amplification of up to 500 mJ energy is foreseen. In order to produce pulses with a smooth temporal envelope, an electro-optically Q-switched Single Longitudinal Mode (SLM) nanosecond generator in combination with a Fabry-Perrot etalon and a laser cavity is implemented. Before the beam is coupled out, up to three temperature controlled harmonics generators, based on Potassium Dihydrogen Phosphate (KDP) crystals, are used to provide the second, fourth or fifth harmonic. Since frequency doubling is a non-linear optical phenomenon, phase-matching conditions have to be taken into consideration. The phase-matching angle is

also dependent on the crystal temperature. The harmonic crystals are mounted in temperature-controlled heaters and kept at a stable temperature. Thus, before every operation, the crystals are angle-tuned from outside the housing to achieve stable conditions. Harmonic separation optics direct each of the four producible wavelengths to its separate output port. With a half-wave plate (HWP1) in front of the crystals it can be adjusted, which fraction goes into the fundamental beam and into the harmonic generation. Figure 8.8 schematically depicts the described optical scheme of the harmonic generation inside the SLL334-5 laser system.

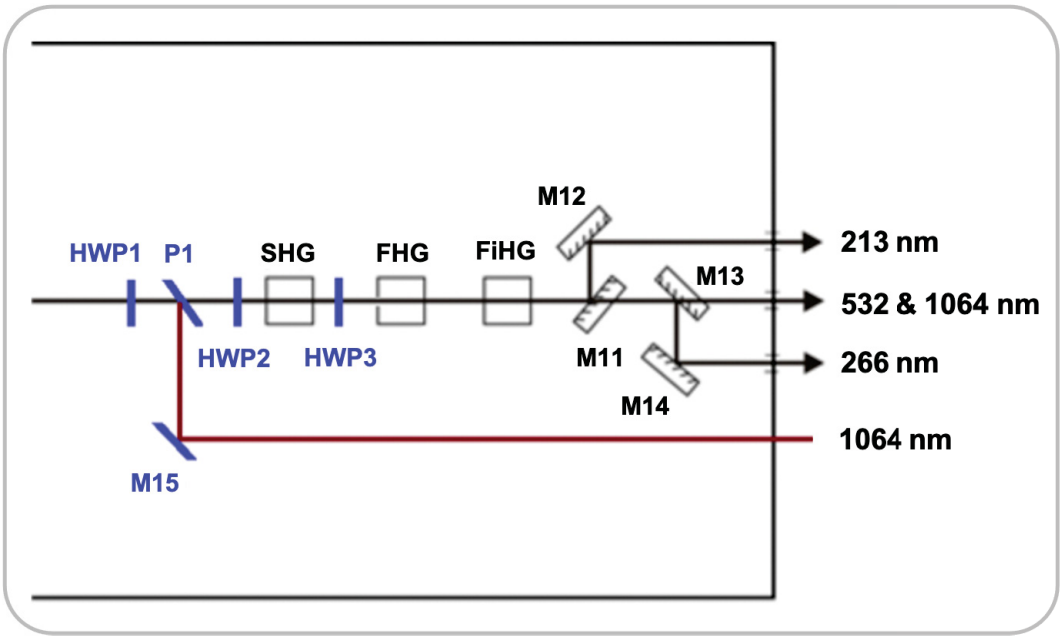

Figure 8.8: Optical scheme of the harmonic generation part inside the SLL334-5 laser system. HWP: half-wave plate, P: polarizer, M: mirror, SHG: second harmonic crystal, FHG: forth harmonic crystal, FiHF: fifth harmonic crystal.

For our purpose, this half-wave plate is set such that the linear polarized fundamental beam is focused with a pulse energy of 100 mJ into the gas jet to increase the polarization signal. At the same time, but under an angle of 90°, the circularly polarized fifth harmonic beam containing an intensity of $\sim 10^{12}\,\mathrm{Wcm}^{-2}$ is also directed into the vacuum chamber. The interaction with the already aligned HCl or HBr molecules leads to a photo-dissociation process by UV excitation and, thus, the polarization of the hydrogen nuclei via hyperfine-spin beating with a period of about 350 ps (cf. Sec. 8.2.1). The polarization of the atomic hydrogen ensemble can be optimized and detected with the LSP (cf. Sec. 4.4) [111, 112]. All laser parameters are easily configurable via a remote control keypad. Using the pyroelectric detector head *J-50MB-LE: ENERGYMAX SENSOR* in combination with a *LabMax-TO Laser Power Meter* from *COHERENT* the correct setting of the laser energy is ensured [29, 31, 175].

Figure 8.9 shows the optical beam paths for the 213 nm beam (green) and the 1064 nm beam (red), which is described in detail below. The fifth harmonic beam having a diameter of 12 mm is guided by customized optics. Since an important requirement is to let as much of the generated laser energy interact with the gas as possible, the mirrors should have the highest possible light reflectance. This is realized by an optical coating technology, the so-called ion beam sputtering provided by *LAYERTEC GmbH*. It promises a very strong mechanical stability, a high coating accuracy as well as very little light scattering (reflectively $> 98\,\%$ at 45° incidence angle). Slightly

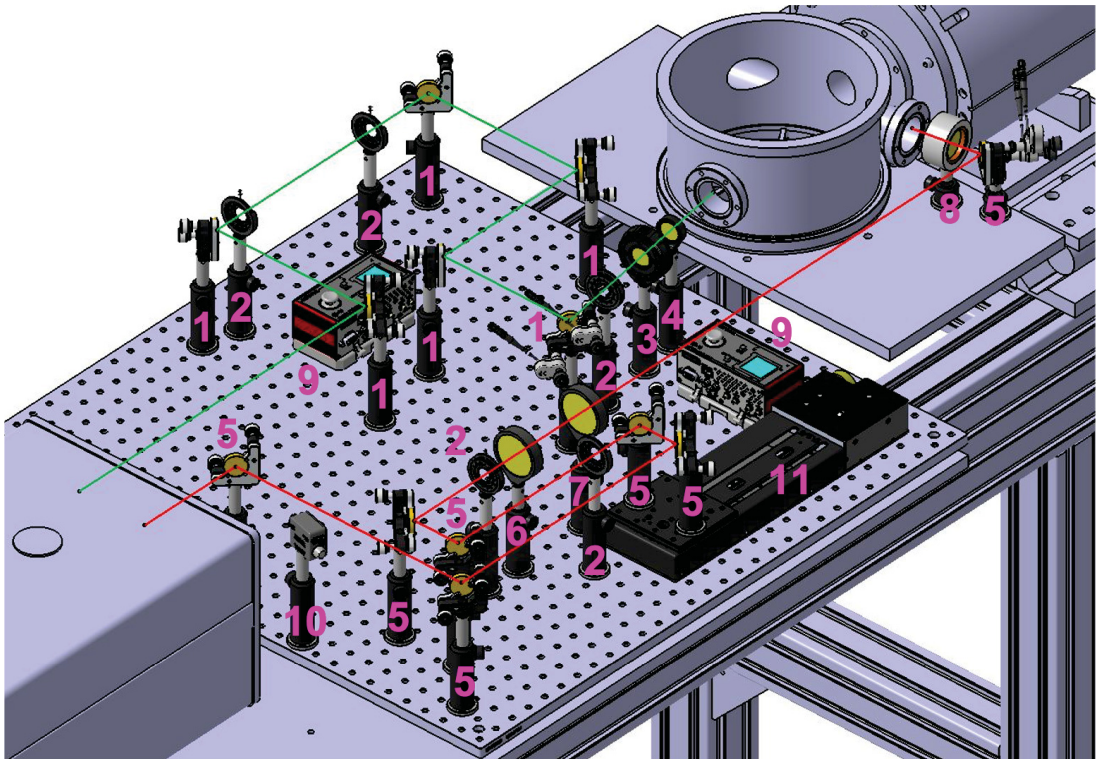

Figure 8.9: Schematic view of the optical beam paths, green: 213 nm and red: 1064 nm. 1: mirror for 213 nm, 2: iris diaphragm, 3: quarter-wave plate, 4: plano-convex lens, 5: mirror for 1064 nm, 6: plano-concave lens, 7: plano-convex lens, 8: plano-convex lens, 9: piezo controller, 10: photodiode, 11: 150 mm linear translation stage.

lower values could be confirmed in our experiment. Beside the mirrors mounted on the optical table, a quartz quarter-wave plate with two-sided anti-reflection coating from *EKSMA Optics* is used for converting the initially linearly polarized laser beam into circular polarization. By using a polarizer, it can be determined in three steps whether the polarization of the laser light has changed from linear to circular when the wave plate is mounted:

1. Verify the linear polarization of the laser light: Put the polarizer into the beam path and detect the transmitted light with the power meter. If the transmitted light fully disappears at a certain angle when rotating the polarizer, the laser light is linearly polarized.

2. Achieve circular polarization: First an iris is implemented to reduce the beam size, followed by the polarizer, the wave plate and finally a slightly tilted mirror. The polarizer has to be set at maximum transmission. By rotating the wave plate the back reflection is minimized. With this setting of the wave plate the light polarization is circular.

3. Verify circular polarization: The wave plate, the polarizer and the power meter are placed behind each other in the beam path. By rotating the polarizer, the light should not be extinguished. With the power meter it can be checked that the *s* polarized (deflected) and the *p* polarized (undeflected) light have more or less the same intensities at all positions.

Behind the quarter wave plate and right in front of the interaction chamber, a plano-convex lens with a focal length of 213.75 mm from *Laser 2000 GmbH* finally focuses the UV beam below the piezo valve inside the vacuum interaction chamber. With a *DT - 30OBG UV converter card*

from *Laser Components GmbH*, the fifth harmonic can be made visible to our eyes in red color, making it easier to align the optical components. The fundamental beam at 1064 nm is guided by standard mirrors with dielectric Nd:YAG coatings providing high damage thresholds and offering high reflectivity for *p*- and *s*-polarized light at the same time. To spatially overlap the two laser beams in the interaction point just below the gas valve, a 150 mm long linear translation stage is integrated in the beam path. In front of the vacuum chamber, the beam is first expanded by a plano-concave and a plano-convex lens, aligned in reverse Galilean arrangement and, thus, directed to another lens in order to focus the fundamental wavelength to an intensity of $\sim 5{\cdot}10^{13}\,\mathrm{Wcm}^{-2}$ into the HCl or HBr gas. The last mirror for both wavelengths before beam focusing can be controlled by a piezo controller. A photodiode, also placed onto the optical table, guarantees the control of the temporal overlap of the two beams by detecting the scattered light of both pulses [29, 31].

9 Measurements with the *Ju*SPARC_Mira Setup

In this dissertation, the layout of a pre-polarized target described in the last section has been implemented and measurements with the piezo valve, the laser system and the LSP are performed, aiming at generating and observing spin-polarized atomic hydrogen from the photo-dissociation of HCl and HBr gases. Figure 9.1 shows a photo of the complete *Ju*SPARC_Mira experiment as it was approved by the safety department and, thus, is ready for operation. Within this section, calculations of the expected processes and signals are made with experimental parameters as well as measurements with the LSP are presented. First, the photo-dissociation process resulting from the interaction of the gas with the 213 nm laser pulse is investigated in order to estimate how many polarized hydrogen atoms are produced. Then, the ionization efficiency, yielding polarized protons, and the flight time to the Faraday cup behind the Wien filter is studied (cf. Sec. 9.1). The expected signal is estimated and related measurements with HCl and HBr gases are shown (cf. Sec 9.2). Future measurements with a photomultiplier are motivated (cf. Sec. 9.3). Finally, the safety concept for the use of this setup is outlined, since it has strong impact on the experimental operation on a daily basis (cf. Sec. 9.4).

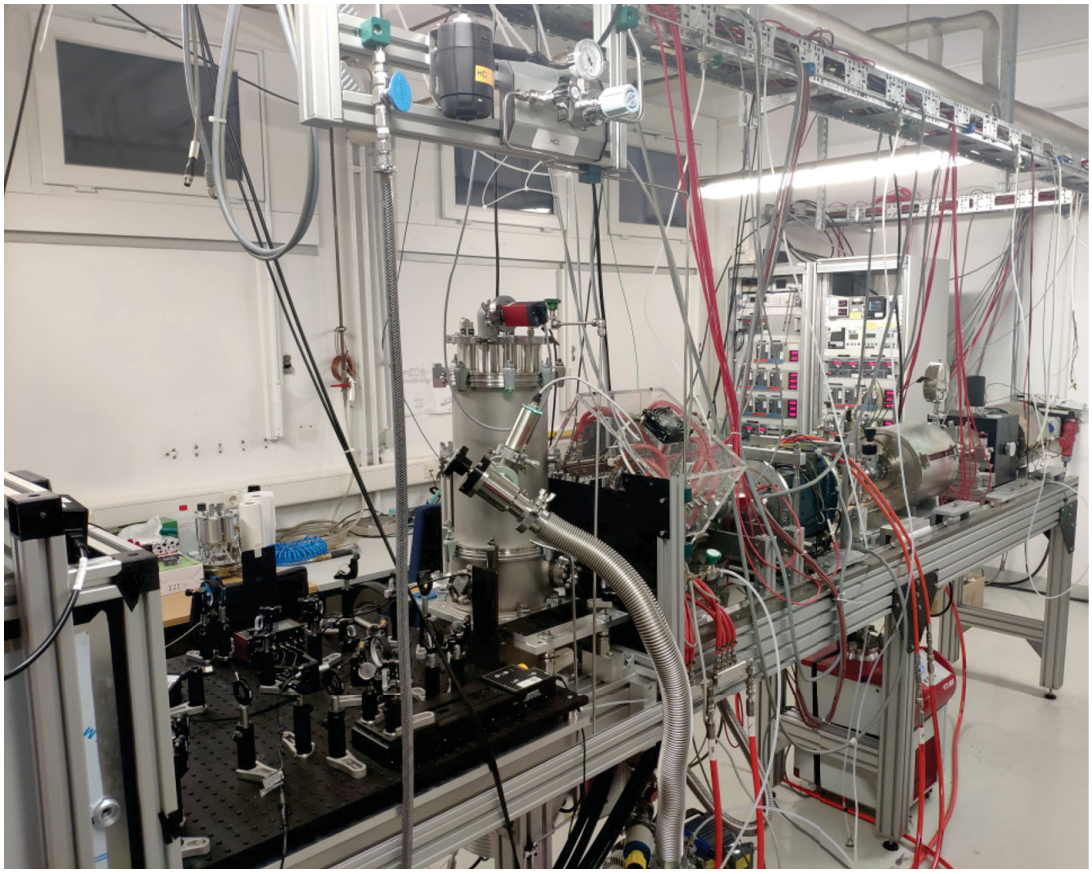

Figure 9.1: Photo of the complete *Ju*SPARC_Mira experiment. From left to right: *Ju*SPARC_Mira laser system in the open shielding box, beam guiding optics for the 213 nm and the 1064 nm pulse, above: exhaust line, gas detector sensitive to HBr and HCl gas for leak detection and gas fitting for setting the backing pressure, interaction chamber including the piezo valve, LSP.

9.1 Study of the photo-dissociation process

In order to make qualitative statements about the number of polarized particles, it is essential to first evaluate the polarization process, i.e., the photo-dissociation, with consideration of the experimental parameters. Here, both the formation of the gas jet and the interaction with the laser pulse of 213 nm wavelength must be taken into account. The objective is to calculate the number of expected polarized hydrogen atoms in the ionizer and protons that are detected by the Faraday cup behind the Wien filter as well as the time, after which the protons are expected to hit the cup (cf. Sec. 4.4). In the following estimation HBr gas is considered, since the absorption cross section for HBr gas is more than two orders of magnitude larger compared to HCl. As shown in Fig. 9.2, the absorption cross section for HBr is $\approx 6{\cdot}10^{-19}\,\mathrm{cm}^2\,\mathrm{molecule}^{-1}$ at room temperature and for 213 nm laser wavelength. In comparison, it is $\approx 1.5{\cdot}10^{-21}\,\mathrm{cm}^2\,\mathrm{molecule}^{-1}$ for HCl for the same parameters. Both gases are available for the experiment, but a higher number of polarized protons can be expected for HBr as a consequence of the higher absorption cross section.

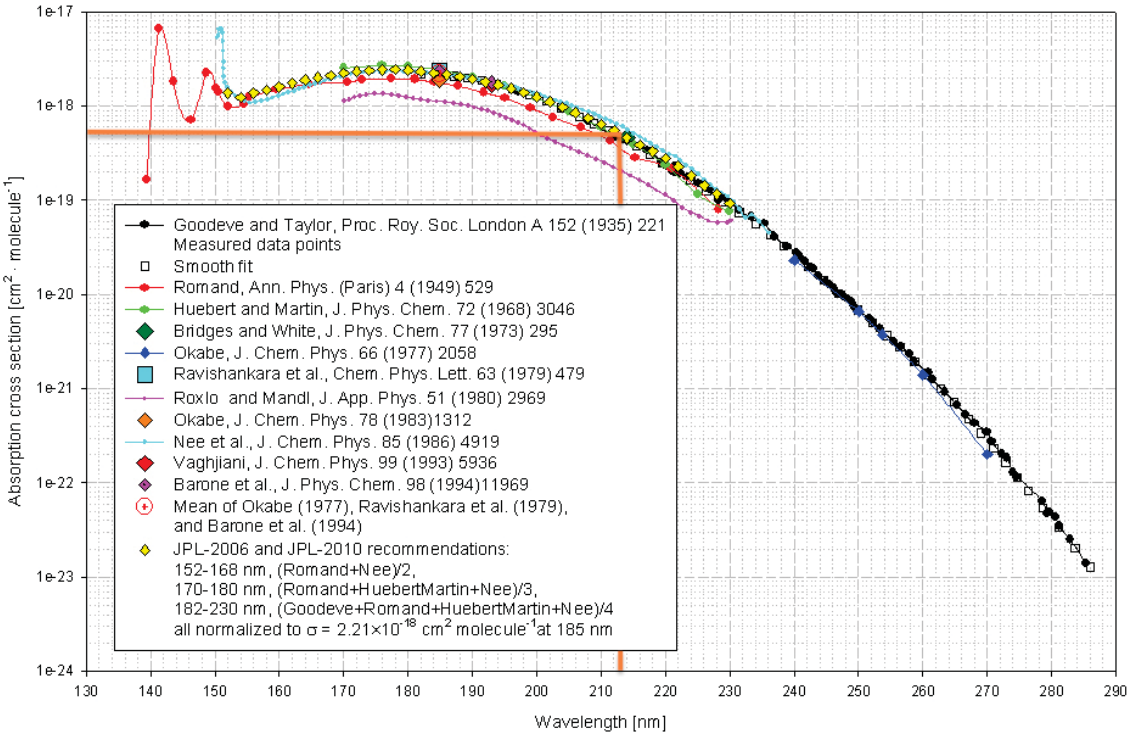

Figure 9.2: Photo-absorption cross sections of HBr at room temperature for different wavelengths [177, 178].

First, the expansion of the gas into the interaction chamber is investigated. After reviewing the literature, it is assumed that the gas jet exits the valve with a diameter of 1.5 mm as a supersonic beam due to the steep pressure gradient between the backing pressure and the pressure in the chamber. Considering that, the speed of sound is defined as the distance travelled by a sound wave as it propagates through an elastic medium, such as gas. For ideal gas the speed of sound α is given by [179]

$$\alpha = \alpha(t) = \sqrt{\frac{\gamma RT}{M_{\mathrm{mol}}}} \quad . \tag{9.1}$$

$\gamma = C_\mathrm{P}/C_\mathrm{V}$ is the heat capacity ratio with the heat capacity at constant pressure C_P and constant volume C_V, R is the ideal gas constant defined as product of the Avogadro constant $N_\mathrm{A} = 6.022 \cdot 10^{23}\,\mathrm{mol}^{-1}$ and the Boltzmann constant $k_\mathrm{B} = 1.381 \cdot 10^{-23}\,\mathrm{J/K}$, such that $R = k_\mathrm{B} N_\mathrm{A} = 8.316\,\mathrm{JK}^{-1}\mathrm{mol}^{-1}$, T is the temperature in Kelvin and M_mol is the molar mass of the gas.

Assuming that the gas expands ideally and neglecting effects of viscosity and heat transfer, an adabatic, isentropic expansion can be expected for the gas flow. Thus, by considering adiabaticity, the sum of the enthalpy and the kinetic energy of mass flow as the gas expands is conserved [180]

$$H(x) + \frac{1}{2} m v^2(x) = H_0 = \text{const.} \tag{9.2}$$

$H(x)$ is the enthalpy of the gas at position x from the point of expansion, $v(x)$ the average flow velocity at this position, m the mass of the gas, and H_0 the stagnation enthalpy. As all streamlines originate at the stagnation source, where $H(x=0) = H_0$, the constant is the same throughout the expansion yielding

$$v^2(x) = \frac{2}{m}\Big(H(x) - H_0\Big) \ . \tag{9.3}$$

Moreover, $\mathrm{d}H/\,\mathrm{d}t = C_\mathrm{P}$, which is also constant in ideal gases, it turns out that

$$v^2(x) = \frac{2}{m} \int_{T_\mathrm{x}}^{T_0} C_\mathrm{P}\,\mathrm{d}T \ , \tag{9.4}$$

with T_x defined as the temperature at position x from the point of expansion and T_0 the temperature in the stagnation source. Using Mayer's relation $C_\mathrm{P} - C_\mathrm{V} = nR$, where n is the amount of substance of gas, i.e., the number of moles

$$C_\mathrm{P} = \frac{\gamma}{\gamma - 1} nR \Leftrightarrow \frac{C_\mathrm{P}}{m} = \frac{\gamma}{\gamma - 1} \frac{R}{M_\mathrm{mol}} \ , \tag{9.5}$$

the average flow velocity at position x_1 can be obtained

$$v_1 = \sqrt{\frac{2\gamma}{\gamma - 1} \frac{R}{M_\mathrm{mol}} \Big(T_0 - T_1\Big)} \ . \tag{9.6}$$

Due to Eq. 9.6 the maximum velocity v is limited to the value

$$v_\mathrm{max} = \sqrt{\frac{2\gamma}{\gamma - 1} \frac{RT_0}{M_\mathrm{mol}}} \ . \tag{9.7}$$

Substituting $\gamma = 1.38$ and $M_\mathrm{mol} = 80.91\,\mathrm{g/mol}$ for the HBr gas at $T_0 = 295.15\,\mathrm{K}$, the maximum sonic speed, at which the gas expands, is $v_\mathrm{max} \approx 469\,\mathrm{m/s}$.

In our experiment the average flow velocity is larger than the speed of sound, $v > \alpha$ (supersonic flow). Thus, there is no propagation of sound at all in the upstream direction. This can be demonstrated by considering the propagation of a disturbance at a given point in space within a uniform gas flow. The disturbance takes place at the time $t_0 = 0$ and propagates with sonic speed as a spherical wave, while its center moves with the flow velocity. Because $v > \alpha$, all spherical waves are confined to a given cone, the so-called Mach cone and the space outside the

cone is completely free of disturbances, as depicted in Fig. 9.3. As a result, the conical separating surface forms a wave front, which is known as Mach wave. The half-angle Θ of the cone can be evaluated from [181]

$$\sin(\Theta) = \frac{\alpha}{v} = \frac{1}{M} \ , \tag{9.8}$$

and is referred to as Mach angle. The quotient of flow velocity α and local sonic speed v is defined as Mach number M.

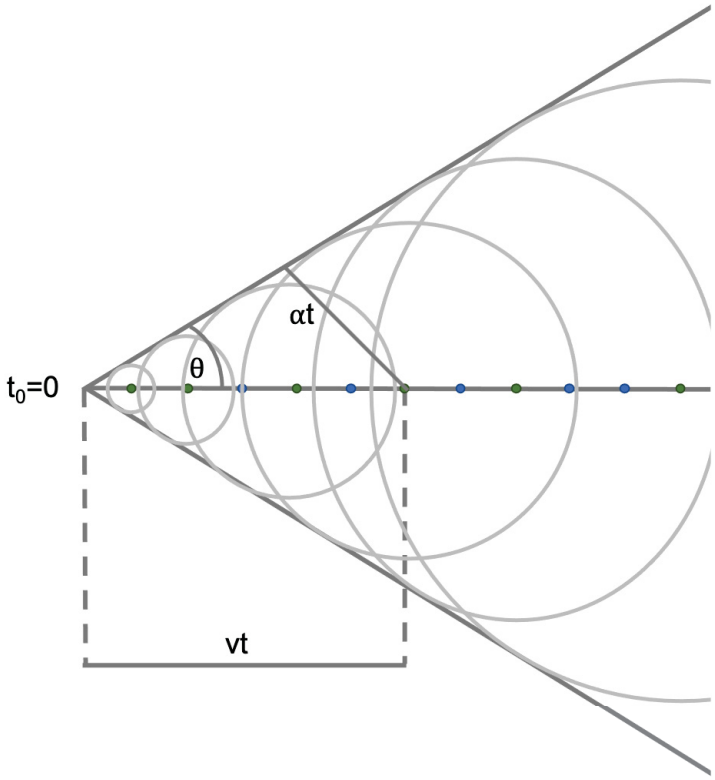

Figure 9.3: Propagation of a disturbance in a flowing medium for $v > \alpha$. The different wave fronts are enveloped by the Mach cone, adapted from Ref. [181].

Apparently, the Mach number depends on the downstream distance x. It has been calculated using the method of characteristics [182] and can be fitted by the analytical formula [183]

$$M(x) = A\left(\frac{x - x_0}{d}\right)^{\gamma-1} - \frac{1}{2}\frac{\frac{\gamma+1}{\gamma-1}}{A\left(\frac{x-x_0}{d}\right)^{\gamma-1}} \ . \tag{9.9}$$

Here, d is the opening diameter of the valve, and x_0/d and the constant A both depend on γ (cf. Tab. I, p. 24 of [180]). The heat capacity ratio γ is equal to 5/3 for mono-atomic gases, 7/5 for diatomic gases ignoring vibrations, and 9/7 for diatomic gases at high temperatures, where the vibrations contribute to the heat capacity. Since $\gamma_{\mathrm{HBr}} = 1.38$ and the corresponding values of the aforementioned constants are not known, the values of $A = 3.65$ and $x_0/d = 0.40$ for $\gamma = 1.4$ are employed in the following formulae because they seem to be reasonable due to a literature

research. Thus, $v/\alpha = M$ is substituted into Eq. 9.6 and rearranged to

$$\frac{T(x)}{T_0} = \left(1 + \frac{\gamma - 1}{2} M^2(x)\right)^{-1} , \tag{9.10}$$

and

$$v(x) = M(x)\sqrt{\frac{\gamma R T_0}{M_{\mathrm{mol}}}}\left(1 + \frac{\gamma - 1}{2} M^2(x)\right)^{-1/2} . \tag{9.11}$$

For $\gamma = C_{\mathrm{P}}/C_{\mathrm{V}} = -\,\mathrm{d}P/\,\mathrm{d}V \cdot P/V$ or when integrating both, $PV^{\gamma} = \text{const.}$ and the ideal gas law $PV = nRT \Leftrightarrow P = \rho RT$, it can be shown that $TV^{\gamma-1} = \text{const.}$ or $P^{\gamma-1}/T^{\gamma} = \text{const.}$, with n being the amount of substance and ρ the density. Hence, the following relations for the rest of the thermodynamic parameters apply

$$\frac{P(x)}{P_0} = \left(\frac{T(x)}{T_0}\right)^{\gamma/(\gamma-1)} = \left(1 + \frac{\gamma - 1}{2} M^2(x)\right)^{-\gamma/(\gamma-1)} , \tag{9.12}$$

and

$$\frac{\rho(x)}{\rho_0} = \frac{n(x)}{n_0} = \left(\frac{T(x)}{T_0}\right)^{1/(\gamma-1)} = \left(1 + \frac{\gamma - 1}{2} M^2(x)\right)^{-1/(\gamma-1)} . \tag{9.13}$$

For the production of polarized hydrogen atoms pulsed laser beams are used (cf. Sec. 8.4), which also makes a pulsed gas expansion convenient for such an application. A question arising in the implementation of a pulsed valve is how long it has to remain open for a supersonic expansion to fully develop. According to Ref. [180], a rule of thumb is that the pulsed valve should release gas for times $\Delta t \geq 4\mathrm{d}/\alpha(T_0)$ [184]. Substituting the values for the HBr experiment, which are $d = 1.5\,\mathrm{mm}$ and $T_0 = 295.15\,\mathrm{K}$ so that $\alpha(T_0) = 206.08\,\mathrm{m/s}$, yields to $\Delta t \geq 29\,\mu\mathrm{s}$. For all of the performed experiments a value of $30\,\mu\mathrm{s}$ is set into the digital pulse delay generator as opening time.

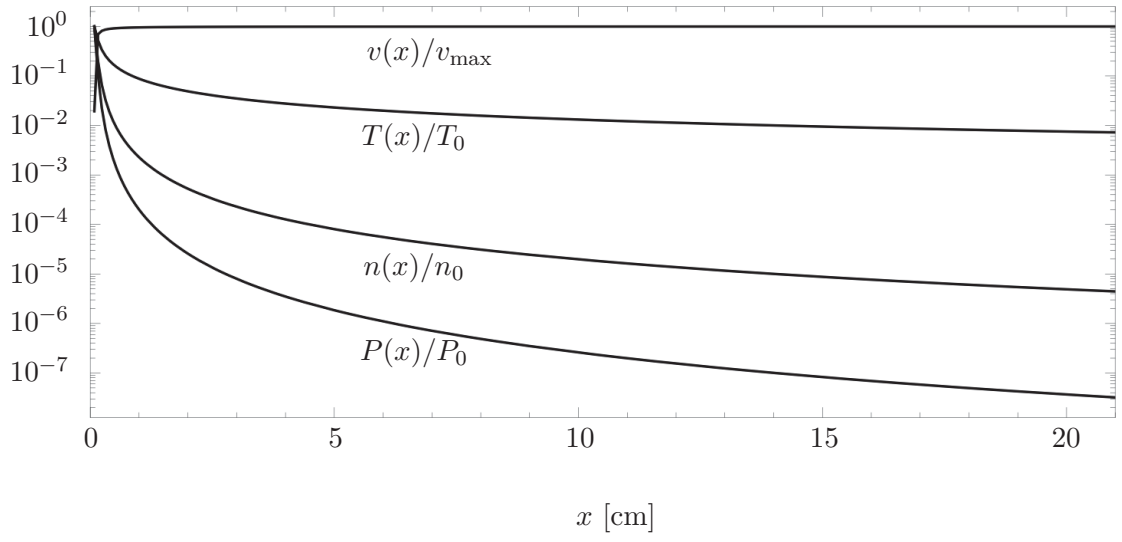

Figure 9.4: Thermodynamic parameters according to Eqs. 9.12 – 9.14 for different values of distance from the valve. The calculations were performed for a diatomic gas without vibrations ($\gamma = 1.4$).

For a more quantitative analysis it is assumed that the flow velocity is maximized throughout the expansion. Thus, the half-angle Θ of the Mach cone for $\gamma = 1.4$ is approximated by

$$\sin(\Theta) = \frac{\alpha(T_0)}{v_{\max}} = \sqrt{\frac{\gamma - 1}{2}} = \sqrt{0.2} \Leftrightarrow \Theta = 26.57^\circ \ . \tag{9.14}$$

Now a distance between the valve opening and the point of interaction must be determined, where the gas jet has already fully expanded, but the density is not too high, so that particles can escape from the gas jet. Figure 9.4 shows the thermodynamic parameters according to Eqs. 9.12 – 9.14 for different values of distance from the valve. While the ratio between $v(x)/v_{\max}$ is basically constant, $T(x)/T_0$, $n(x)/n_0$ and $P(x)/P_0$ decrease with distance. Assuming that the ratio $P(x)/P_0$ is about 10^{-7}, a distance of $x = 10\,\text{cm}$ between the valve and the interaction point is considered for the following calculation. To be able to set a variable distance between the valve and the point of interaction, a height-adjustable valve holder is required (cf. Sec. 8.3). For simplicity, the diameter of the laser beam is neglected and the length l of the laser-beam path along the gas jet is calculated according to $l = 2x\tan(\Theta) = x = 10\,\text{cm}$. This value seems quite large, however, it must be taken into account that the gas density decreases sharply towards the outside [185]. The complete layout is schematically presented in Fig. 9.5.

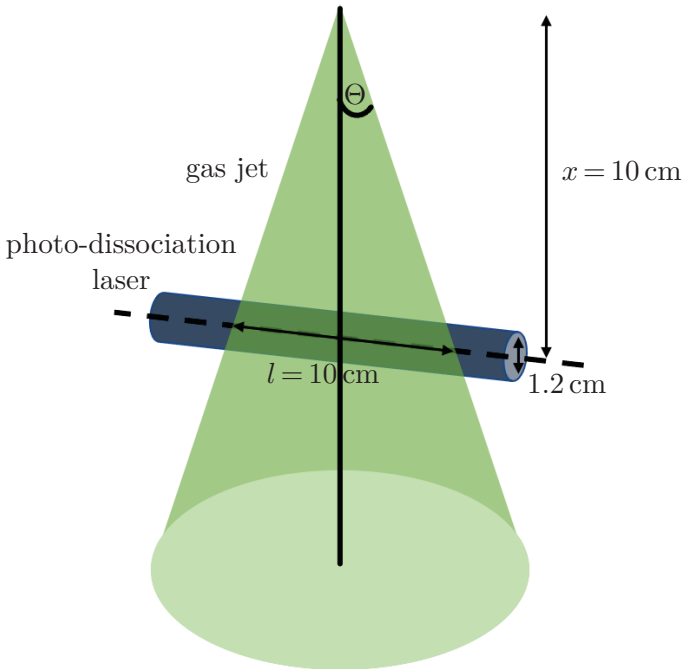

Figure 9.5: Propagation of photo-dissociation laser beam through the gas expansion.

The amount of the photons transmitted through the gas jet of length l, is then given by the Lambert–Beer law

$$N_\text{t} = N_0 \exp\left(-\sigma n l\right) \ . \tag{9.15}$$

In this equation, N_0 is the initial photon number and σ the the photo-dissociation cross section (cf. Fig. 9.2). The initial number of photons in a laser pulse is given by $N_0 = E\lambda/(hc)$, where E is the energy of the laser pulse, h the Planck constant, c the speed of light, and λ the laser wavelength. For the 213 nm beam with an energy of 20 mJ there are $2.15{\cdot}10^{16}$ photons in the

beam. From that, the number of absorbed photons, which photo-dissociate the molecular gas, is

$$N_{\mathrm{a}} = N_0\Big(1 - \exp\left(-\sigma n l\right)\Big) \ . \tag{9.16}$$

Another important parameter, which has to be taken into account, is the mean free path characterized as the average distance between collisions for a gas molecule. It is given by

$$l_{\mathrm{mfp}} = \frac{1}{\sqrt{2} n \pi \delta^2} \ , \tag{9.17}$$

where n is the particle density and δ the molecular bond length, which is $\delta = 0.141\,\mathrm{nm}$ for photomultiplierhe HBr molecule. To have as few collisions as possible, $l < l_{\mathrm{mfp}}$ is required. This leads to a particle density of $n(x = 10\,\mathrm{cm}) < 1/(\sqrt{2} l \pi \delta^2) \approx 1.13{\cdot}10^{14}$ molecules/cm^3. Thus, the amount of the absorbed photons is smaller than $\approx 6.77{\cdot}10^{-4}\, N_0$ or $\approx 1.46{\cdot}10^{13}$ photons at 20 mJ pulse energy employing the cross section at room temperature. The actual temperature of the sample is given in Fig. 9.4 and is smaller, yielding a larger absorption cross section. So, the presented calculation underestimates the number of the absorbed photons. Furthermore, using Eq. 9.13, $n(x = 10\,\mathrm{cm}) \approx 2{\cdot}10^{-5}\, n_0$. Therefore, $n_0 < 6{\cdot}10^{24}$ molecules/m^3 or $\mathrm{P}_0 < 0.73\,\mathrm{bar}$.

Given that the gas expands at a velocity $v_{\mathrm{max}} = 469\,\mathrm{m/s}$ from the valve at an opening time of $30\,\mu\mathrm{s}$, it travels a distance of 1.4 cm downstream. If the gas volume covered in this way is approximated to that of a cone with diameter $l = 10\,\mathrm{cm}$ and height 1.4 cm, this corresponds to $36.65\,\mathrm{cm}^3$. Using the already calculated particle density $n(x = 10\,\mathrm{cm})$, there are about $4.15 \cdot 10^{15}$ molecules/shot in this volume.

Finally, the time the protons need to reach the Faraday cup is calculated. According to Ref. [186], the velocity of hydrogen atoms from HBr photo-dissociation at 213 nm is $v \approx 20\,\mathrm{km/s}$. Thus, it takes about $10\,\mu\mathrm{s}$ assuming a distance of 0.2 m between the interaction point and the ionizer (cf. Sec. 4.4). From the ionizer to the Faraday cup it is another meter. Considering an accelerating voltage of $U = 1\,\mathrm{kV}$, the velocity is determined to be $v = \sqrt{2Uq/m} = 437695\,\mathrm{m/s}$ yielding to a time of about $2.3\,\mu\mathrm{s}$ to the Faraday cup. Hence, it takes about $10\,\mu\mathrm{s}$ to $15\,\mu\mathrm{s}$ for protons to reach the Faraday cup behind the Wien filter (cf. Sec. 4.4) after photo-dissociation.

9.2 Detection with the Faraday cup of the LSP

For the very first measurements HCl gas was used, which is injected into the interaction chamber with a standard piezo valve (cf. Sec. 8.3). Without using the laser system and, thus, without producing polarized protons, the signal produced from the diffusive gas is measured on a Faraday cup. This is positioned behind the ionization chamber and the Wien filter of the LSP (cf. Sec. 4.4). Figure 9.6 shows the HCl diffusion signal without mass separation for various values of the backing pressure between 0.5 bar and 5.0 bar.

This measurement was primarily intended to test the operation of the Glavish ionizer with a pulsed gas flow, to investigate the background without mass separation and to calibrate the gas flow with respect to the maximum current at different backing pressures. Looking at the graphs, it can be generally stated that the ionizer ionizes the gas and a signal can be detected in the cup for all employed backing pressures. Furthermore, it can be observed that the higher the backing pressure, i.e., the more gas flows into the interaction chamber, the more gas enters the ionizer, which causes a higher current on the cup (cf. Tab. 6). The dependence here is not

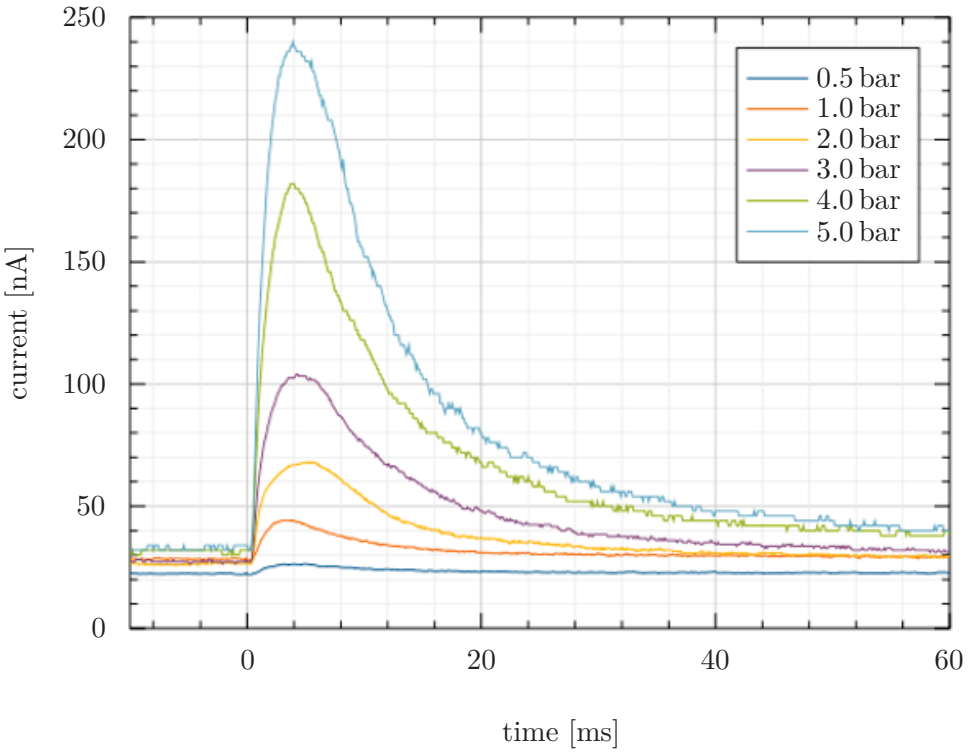

Figure 9.6: HCl diffusion signal of all masses for various values of backing pressures measured by a Faraday cup in order to test the operation conditions of the Glavish ionizer, to investigate the background signal and to calibrate the gas flux.

completely linear, since the backing pressure is adjusted via a manual valve and, thus, inaccuracies in the adjustment are to be expected. Moreover, the background and the ionization process, both depend on additional factors, for example, in the latter case, at higher pressures, secondary collision processes and additional wall collisions occur. All curves also show a typical behavior: first a fast rise to the maximum current, then a shallower fall with a life-time of tens of ms to the value of the background depending on the backing pressure. The maximum current is reached after 2 ms to 6 ms after the trigger signal. This is in good agreement with the theoretically calculated value considering a thermal velocity $v_{\mathrm{th}} = \sqrt{2k_{\mathrm{B}}T/m} = 371\,\mathrm{m/s}$ for bromine atoms with a mass of $m = 5.88{\cdot}10^{-26}\,\mathrm{kg}$ at room temperature and the Boltzmann constant k_{B}. Then, taking into account a distance s of 1.2 m for all heavy masses to reach the cup, a time of $t = s/v_{\mathrm{th}} = 3.2\,\mathrm{ms}$ is expected. The time that is needed for this distance can be larger compared to the calculated one, because the diffusive gas does not move on a straight line. The assumption $s = 1.2\,\mathrm{m}$ is based on the estimate that the molecules in the vacuum chamber have to undergo a few wall collisions before they reach the ionizer. As the diameter of the chamber is 21.3 cm, at least six collisions are expected.

Table 6: Calibration of the gas flow using the Faraday cup by detecting the maximum current at different backing pressures without mass separation for the measurement depicted in Fig. 9.6.

pressure [bar]	0.5	1.0	2.0	3.0	4.0	5.0
I_{max} [nA]	26.3	44.2	68.0	104.0	182.0	240.0

The next step is to analyze at which time and with which height the signal of the spin-polarized hydrogen is expected to be detected. First, it is tested whether the mass selection with the Wien filter works and, thus, to record a spectrum for H^+ and H_2^+ ions on the Faraday cup (cf. Fig. 9.7). Here, again, the laser is still switched off so that no spin-polarized hydrogen is likely to appear in the spectrum. For this measurement the gas is changed from HCl to HBr, since the latter has a larger absorption cross section and, thus, a higher signal can be expected for the spin-polarized hydrogen. Before the measurement the pressure in the interaction chamber with the valve is $9.2{\cdot}10^{-7}$ mbar and in the interaction chamber of the ionizer $1.1{\cdot}10^{-7}$ mbar. The valve is mounted on the adjustable holder so that the distance to the point of interaction with the laser is about 10 cm. To operate the valve, a voltage of -846 V is applied in the controller and the opening frequency is set to 1 Hz. The backing pressure of the HBr gas is about 3 bar. Thus, when opening the valve, an increase in pressure in the interaction chamber in the range of 10^{-7} mbar can be observed in the pressure gauge. The opening frequency is set to 1 Hz and not 5 Hz (repetition rate of the laser system) to reduce the residual gas pressure further. If the pressure in the ionization chamber rises above 10^{-6} mbar, a clear signal can no longer be acquired by the Faraday cup and displayed in the oscilloscope. The ionizer and the Wien filter are operated in such a way that the highest possible and at the same time a pure signal can be visualized in the oscilloscope. Optimal values for this measurement are listed in Tab. 7 and correspond to the definitions in Fig. 4.6. For mass selection, a current and two voltages must be applied in the Wien filter, one negative and one positive in the plate capacitor. For example, it is possible to differentiate between H^+ and H_2^+ ions, as for the latter the root of the sum of the modulus is smaller by a factor of $\sqrt{2}$, as the velocities for H^+ and H_2^+ ions vary by a factor of $\sqrt{2}$ (cf. Sec. 4.4).

Table 7: Typical settings in the LSP for operating ionizer and Wien filter (cf. Fig. 4.6).

ionizer: coil currents	$3 \cdot 112$ A
ionizer: filament current	7.31 A
ionizer: E_1 voltage	1.705 kV
ionizer: E_2 voltage	514 V
ionizer: E_3 voltage	1500 V
ionizer: E_4 voltage	-196 V
ionizer: E_5 voltage	-5.504 kV
Wien filter: current	3.000 A
Wien filter: voltage for H ions	96 V, -312 V

First of all it can be stated that both, the Glavish ionizer and the Wien filter, work properly, since in Fig. 9.7 different spectra for H^+ and H_2^+ ions can be identified, which show additional characteristics to the graphs in Fig. 9.6. The graph for the H^+ ions shows the usual fast rise to the maximum current. The decrease is then generally less steep and two time constants can be identified in the graph. First a steeper drop to a time of about 10 ms, which can be attributed to the pumped HBr gas. Then a shallower decay follows, which results from secondary processes, i.e., the protons now stem mostly from H_2 molecules. In the signal of the H_2^+ ions, a slower increase up to the maximum current, which is reached after about 20 ms, can generally be noticed, as well as a smoother decrease. This can be attributed to the fact that H_2 has two

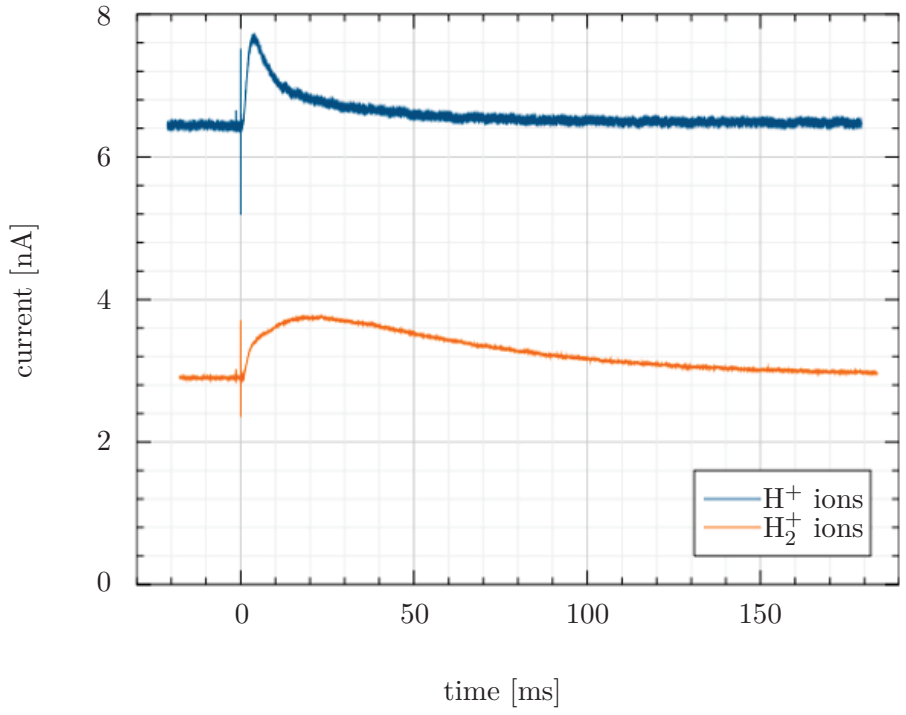

Figure 9.7: HBr diffusion signal of H^+ and H_2^+ ions at a backing pressure of 3 bar measured by a Faraday cup. The laser is not operated, so no signal from spin-polarized hydrogen is expected in the spectrum.

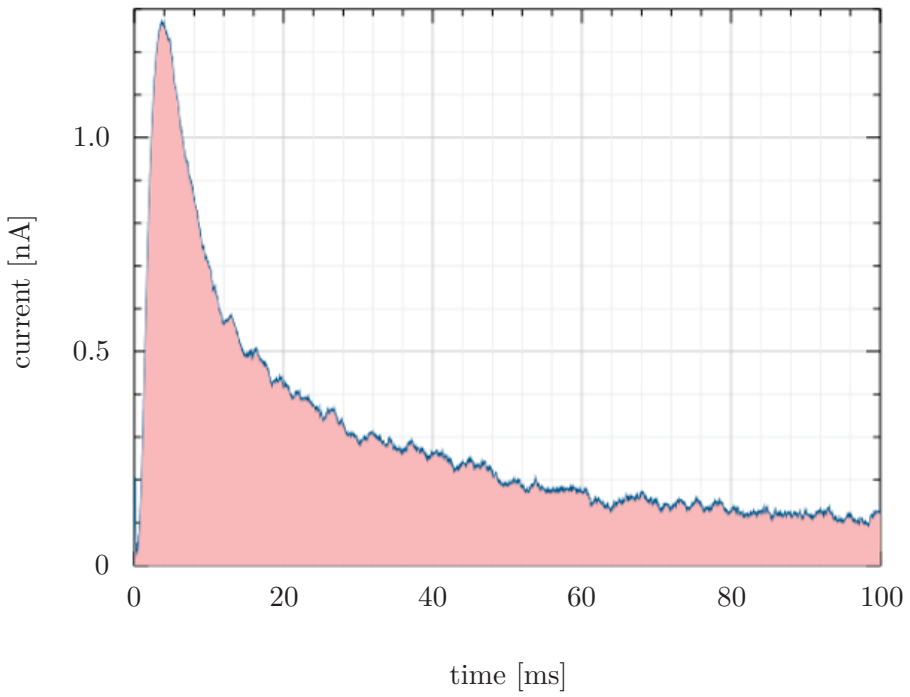

Figure 9.8: Zoom in on the spectrum of the HBr diffusion signal of H^+ ions from Fig. 9.7, normalized to the $y = 0$ nA axis and scaled down for the first 100 ms after the trigger pulse. After this time the signal has decreased almost completely to the background value and by integrating the area under the graph, colored in rose pink, the number of protons/shot in the Faraday cup can be determined.

sources: first, it is injected directly with the gas into the interaction chamber, and second, it is generated in the chamber from the decay of HBr during wall collisions. The first part of the rise is as steep as for the H, then the rise becomes flatter and the newly produced molecules predominate. Additionally, the delayed rise can be explained by the fact that the mass of the H_2^+ ions is twice as large as that of the H^+ ions and a consequently lower velocity and later detection in the Faraday cup. In the downward slope, the graph is rather constant and softer, because H_2 has to be produced first in recombination processes and by wall collisions and only then it is detected. Both signals have a lifetime of several tens of milliseconds. Generally speaking, the signal of the H^+ ions is higher due to the larger number of protons compared to H_2^+ ions. Both carry the same charge ($+e$), so higher current means larger number of ions and also higher background.

Based on the above analysis of the spectra for H^+ and H_2^+ ions, the expected spectrum for spin-polarized hydrogen can now be studied. In Sec. 9.1 it has been estimated that about $1.5{\cdot}10^{13}$ absorbed photons and, thus, the same amount of H atoms are produced by each laser shot of 20 mJ energy. Assuming that the velocity v of the hydrogen atoms from HBr photo-dissociation at 213 nm laser wavelength is ≈ 20 km/s and the atoms are ionized over a length of $\Delta a = 10$ cm in the ionizer, the time span Δt between the first and last polarized atom in each shot is $\Delta t = \Delta a / v = 5\,\mu$s. Considering that a peak height of $\Delta I = 0.1$ nA can still be easily resolved with the oscilloscope, the minimum number of protons/shot that can be detected with the Faraday cup and, thus, its resolution is determined via the charge Q: $Q = \Delta I \cdot \Delta t = 0.1\,\text{nA} \cdot 5\,\mu\text{s} = 5{\cdot}10^{-16}$ C. Dividing by the elementary charge e leads to a sensitivity of about $3{\cdot}10^3$ protons/shot, which can be reached with the photo-dissociation fragments in the presence of the residual gas. This number is comparatively low and the detection with the Faraday cup is therefore quite sensitive.

In the next step, this value is compared with the number of expected protons/shot, since the amount of $1.5{\cdot}10^{13}$ H atoms/shot is reduced due to the geometry of the experiment and by taking into account the efficiency of the Glavish-type electron-collision ionizer. Since the diameter of the entrance opening into the ionizer is about a hundred times smaller than the diameter of the opening size of the turbo pump, it can be assumed that the maximum number of H atoms/shot entering the ionizer is reduced by four orders of magnitude. The efficiency of the ionizer is given as 10^{-3}, which lowers the number of protons/shot on the Faraday cup due to laser-induced photo-dissociation in total by seven orders to about $1.5{\cdot}10^6$.

Finally, this estimate is compared with the actual and experimentally calculated number of protons/shot detected on the Faraday cup. For this evaluation, Fig. 9.8 is used, which shows a zoom in on the spectrum of the HBr diffusion signal of H^+ ions from Fig. 9.7, normalized to the $y = 0$ nA axis and scaled down for the first 100 ms after the trigger pulse. Determining the area below the graph, colored in rose pink, by calculating the integral again yields a charge, so that the division by the elementary charge e gives the intended result. The integral amounts to 29.30 nA·ms and, thus, about $2{\cdot}10^8$ protons/shot are experimentally observed.

An analytical estimate of $4.2{\cdot}\,10^{15}$ molecules/shot was already made above. This value fits very well with the estimated amount of protons. Thus, if $4.2{\cdot}\,10^{15}$ molecules/shot are injected into the interaction chamber, the fraction that entered the ionizer is reduced by four orders of magnitude. Another fraction of 10^{-3} is be ionized to produce protons. Therefore, a maximum of $4.2{\cdot}\,10^8$ protons/shot is expected due to diffusive flux. Consequently, only half as many

protons/shot are observed experimentally as theoretically possible. This can be explained by the fact that a large fraction of the molecules leaving the valve are pumped off directly by the turbo pump, are not registered by the pressure gauge and also have no chance of entering the ionizer.

The amount of experimentally detected protons/shot should be related to the number of particles/shot being pumped out by the turbo-pump below the interaction chamber. Using a pumping speed of 1000 l/s and the relation that 1 mole of gas fills a volume of 22.4 l at a pressure of about 1.0 bar, the ideal gas equation estimates that $2.7{\cdot}10^{15}$ particles/s are pumped out after one shot with a pressure increase in the interaction chamber of 10^{-7} mbar. Since the pumping process does not last for 1 s but about 50 ms and this process is not linear but can be approximated as a triangular shape, about $6.7{\cdot}10^{13}$ molecules/shot are pumped off. Thus, the number of particles/shot that are pumped out is reduced even by a factor of about 60 because again the majority of molecules is pumped directly by the turbo pump and a still smaller fraction of molecules can be detected by the pressure gauge.

From the above calculations and estimations two aspects can thus be summarized: i) although the number of expected produced spin-polarized protons per shot is reduced by seven orders of magnitude from $1.5{\cdot}10^{13}$ to about $1.5{\cdot}10^{6}$ behind the Wien filter, the estimated sensitivity of about $3{\cdot}10^{3}$ protons/shot on the Faraday cup is sufficient to detect them. ii) With a number of $2{\cdot}10^{8}$ about 30 times more protons/shot are recorded in the Faraday cup than estimated. One possible reason is that the ionization efficiency to get protons from electron impact on HBr is larger than to produce protons from hydrogen atoms that was known to be 10^{-3}.

The last step is to quantify the height of the signal of the spin-polarized hydrogen. As discussed above, the number of protons expected in the Faraday cup is $1.5{\cdot}10^{6}$ per shot, assuming that $1.5{\cdot}10^{13}$ H atoms/shot are generated by the photo-dissociation process. From this the current I on the Faraday cup can be derived, which is $2.4{\cdot}10^{-13}\,\mathrm{A/s} \approx 0.24\,\mathrm{pA/s}$ integrated over one second. But the expected signal has only a width of 5 μs, so the average current is about 48 nA. Considering that the signal has not a rectangular shape, as assumed so far, but a triangular one in first approximation, the value increases by a factor of two, so that finally a signal height of 96 nA is predicted, resulting in a peak of about 100 mV at an input resistance of 1 MΩ in the oscilloscope. In summary, the additional signal from spin-polarized hydrogen is therefore assumed about 10 μs to 15 μs after the trigger signal with a width of 5 μs and in the ideal case an approximate height of 96 nA in the Faraday cup.

In Fig. 9.9 the signal of heavy masses from HBr gas at a backing pressure of 5 bar measured by a Faraday cup is presented. The measurement is performed both without laser (blue graph) and with switched on photo-dissociation laser (orange). In the LSP the settings for the ionizers and the Wien filter are comparable to those in Tab. 7, but must be readjusted and optimized daily. The two voltages in the Wien filter for selecting all masses are, for example, 0 V and -22 V for the given measurement. To operate the valve and, thus, to ensure the gas flow into the interaction chamber, a voltage of -810 V is applied in the controller and the opening frequency is set to 5 Hz to synchronize the opening of the valve with the laser frequency. Furthermore, the gas valve and laser are synchronized in time with each other by using the digital pulse delay generator, as shown in Fig. 9.11. This ensures that the laser shoots into the interaction volume exactly when gas has reached the interaction point. For example, the laser needs a start signal

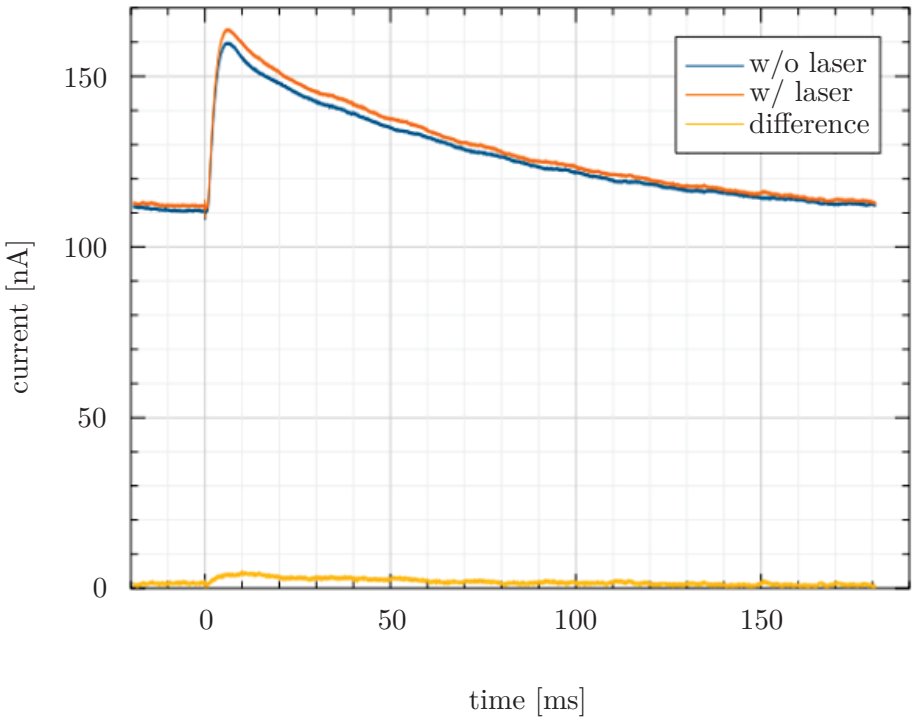

Figure 9.9: Signal of heavy masses from HBr gas at a backing pressure of 5 bar measured by a Faraday cup. The graphs are recorded without laser (blue) and with the photo-dissociation laser switched on (orange). In the yellow graph the difference between those two signals is depicted.

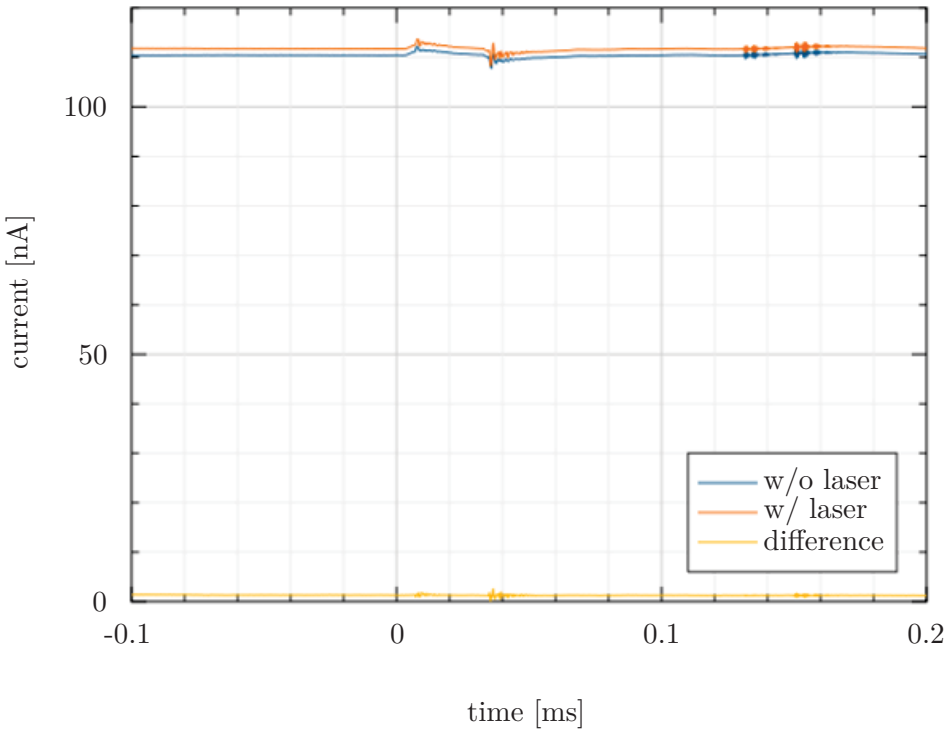

Figure 9.10: Zoom in on the spectrum of the HBr signal of heavy ions from Fig. 9.9 scaled down for the first 200 μs after the trigger pulse. An additional signal of the spin-polarized hydrogen during operation of the photo-dissociation laser should be visible during this time period.

1.5 ms before emitting the pulse. To reach the interaction chamber, the laser pulse is guided about 1.2 m via the beam optics into the interaction chamber. Since the pulse moves at the speed of light, the 4 ns flight time are negligible in the considered time scales and, therefore, it can be assumed that the laser pulse reaches the interaction volume within 1.5 ms after the start signal is provided. Considering a velocity $v \approx 210\,\mathrm{m/s}$ for the supersonic expansion of bromine atoms, the interaction point 10 cm distanced from the valve opening is reached after about 476 μs. Since the valve is opened for 30 μs, the start pulse of the valve is sent 994 μs later than the start pulse for the laser. However, the last value is varied during the experiment to identify the additional signal of the polarized protons in the oscilloscope. As already analyzed above, the signal of spin-polarized hydrogen is expected to appear about 10 μs to 15 μs after interaction, while the diffusion signal starts to increase after about 1 ms.

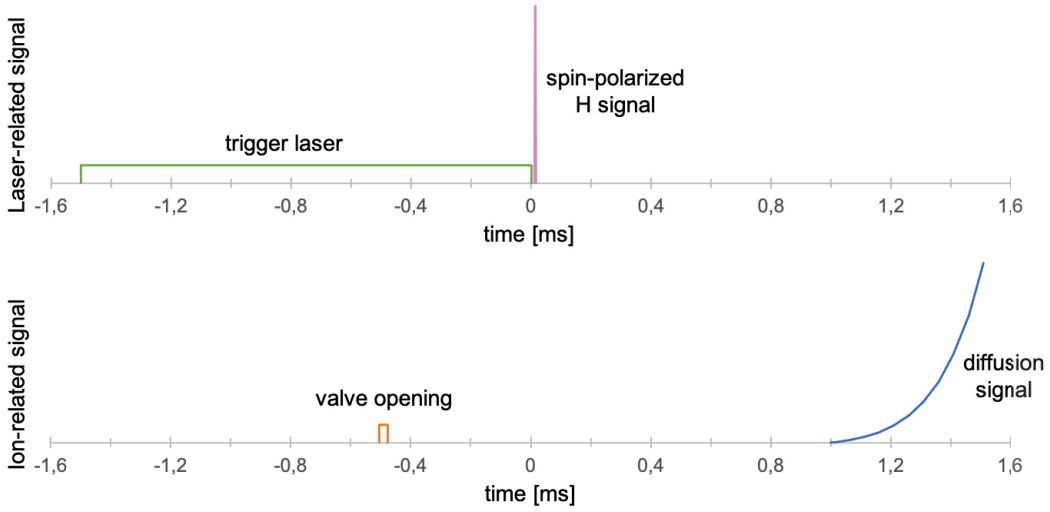

Figure 9.11: Schematic view of the synchronization between valve and laser pulse using the digital pulse delay generator. In the upper row the laser-related signal with the start pulse of the laser and the expected spin-polarized hydrogen signal resulting from the interaction of the photo-dissociation laser with the HBr gas is illustrated. The lower row shows, in the similar time scale, the pulse inducing the opening and closing of the valve as well as the diffusion signal.

First of all it can be stated that the diffusion signal for the heavy masses looks as expected: while the background is at about 110 nA due to residual gases like N_2, O_2 or water and the corresponding heavy ions (N_2^+, O_2^+, ...), the maximum signal is registered in the Faraday cup about 5 ms after the trigger pulse. Afterwards the signal drops, first faster due to the contribution of the fast recombination from HBr gas, then slower, because secondary processes take place. The signal has a lifetime of several tens of ms. Additionally, in both signals, the opening and closing of the valve for 30 μs can be identified. Not visible in the spectrum in Fig. 9.9, however, is the additional signal of the spin-polarized protons. It is also not observed in any of the further measurements. The difference of the two signals without and with laser operation (yellow graph), in which the additional contribution should be even more clearly visible, shows only a minimal increase in the first 60 ms after the trigger signal. This is because the measurement with laser operation shows a slightly higher signal and can be explained by small experimental variations in the time between the two measurements. In Fig. 9.10 a zoom in on the spectrum of the HBr signal of heavy ions from Fig. 9.9 scaled down for the first 200 μs

after the trigger pulse is displayed. The small signal contributions are due to electrical noise. Nevertheless, the additional signal of the polarized protons after about 10 μs to 15 μs after the trigger pulse should be clearly visible in this enlarged time scale. But, this is not the case even after varying the timing between laser and valve, although the above calculations confirm the detection of the additional contribution by the polarized protons with high probability.

Assuming that the gas is properly released from the valve opening, that a supersonic beam as described in Sec. 9.1 is formed and that photo-dissociation results from the interaction with the 213 nm laser pulse, it must be concluded that polarized protons are produced in the experiment. The fact that no signal contribution is registered on the Faraday cup must be explained by the – for this experiment – faulty or insufficient ionization process. The ionization cross section efficiency of 10^{-3} in the above calculations is assumed for thermal gases passing through the ionizer due to former measurements at the COSY ABS and can be even estimated due to the background current in the Faraday cup as function of the residual gas pressure. For the spin-polarized proton signal the ionizer needs to ionize hydrogen atoms moving with velocity $v = 20\,\mathrm{km/s}$ through the ionization volume. Thus, the ionization efficiency might drop much faster when those atoms pass through the ionizer compared to the diffusive gas, since the hydrogen atoms have thermal velocity and they are more likely to collide with an electron and get ionized. Assuming that the ionization efficiency correlates with the time of flight of the gas in the ionization volume, the 100 times faster hydrogen atoms have an ionization efficiency of 10^{-5} instead of 10^{-3}. In addition, most of the fast hydrogen atoms are moving parallel through the axis of the ionization volume after photo-dissociation, while the diffusive gas might hit the wall and, therefore, will stay longer inside this volume. An insufficient function of the ionizer for these experiments was not foreseeable in advance since there exists no absolute ionization efficiency measurements for such fast atoms or molecules [187].

In most experiments, the valve was used without the de Laval nozzle because the initial focus was on the laser-gas overlap with the widest possible jet, rather than forming a narrow directed beam. However, given that there has not been an overlap after all, and, therefore, no atoms were produced in the first place, an improved method of finding the correct timing is required. This can be remedied by a compression tube, for which a device for installation on the valve holder near the laser-gas interaction point has already been designed. Thus, the atomic hydrogen intensity after each laser shot can be measured and the pressure increase as a result of the photo-dissociation process is read out with a pressure gauge. In the first experiments, however, after a few minutes of operation of the value with HBr gas, no more gas-jet formation was detectable. This phenomenon occurred even faster when the de Laval nozzle was used. It was evident from the fact that no pressure increase in the interaction chamber was observable in the gauge. As this behavior has not changed even after checking the functionality of the valve by the manufacturer, it must be assumed that the valve is actually functional. Therefore, it is likely that the valve opening becomes blocked during operation, probably by clustering of HBr gas due to the cold temperatures during the injection process. Thus, for future experiments, the valve will be heated.

As a side aspect, it should be mentioned that during the experiments with HBr gas, a decisively larger fraction of pulsed H_2^+ compared to H^+ is registered as contribution produced from the diffusive gas in correlation to the HBr gas jet. However, in the diffusive and the

residual gas are mostly gases that should allow the production of protons, e.g., from H_2O or HBr/HCl. Only a constant contribution of H_2 molecules from residual gas should appear. Further investigation reveals that HBr already undergoes a decay during the storage in the gas bottle: $2\,HBr \rightarrow H_2 + Br_2$. Thus, the pulsed signal can also be explained, since the H_2 is directly fed into the interaction chamber via the pulsed piezo valve.

The generation of H^+ during the ionization of the pulsed gas jet can result from the following two processes: i) by ionizing HBr directly. However, in the experiment, H^+ is only detected in a ratio of about 1:30 heavy ions. For the heavy ions the Wien filter is not able to distinguish between HBr^+ and Br^+. This ratio agrees very well with measured values for the cross sections from the literature and, therefore, supports again the observation of the high resolution of the LSP [187]. ii) By ionizing H_2. This becomes H_2^+ and H^+ in a ratio of 10:1 and, thus, explains the significantly large fraction of H_2^+ compared to H^+ in addition.

9.3 Detection with the photomultiplier of the LSP

If the method of ionization is improved and the signal from the spin-polarized hydrogen on the Faraday cup can be recorded in the oscilloscope, it is necessary to ensure that the number of polarized protons/shot is sufficient to determine the degree of polarization at the end of the LSP by detecting the Lyman-α emission (cf. Fig. 4.4). Already in Sec. 9.1 it has been estimated that about $1.5{\cdot}10^{13}$ absorbed photons and, thus, the same amount of hydrogen atoms should be produced by each laser shot of 20 mJ energy. After passing through the Glavish-type electron-collision ionizer, this number decreases to about $1.5{\cdot}10^{6}$. This value is taken as the starting value to make an evolution of the number of particles passing through the LSP up to the detection with the photomultiplier as shown in Fig. 9.12.

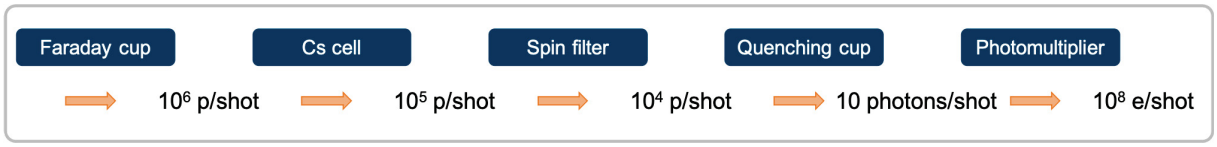

Figure 9.12: Evolution of the number of particles passing through the LSP up to the detection with the photomultiplier.

In the caesium cell, metastable atoms are produced from H^+ ions with an efficiency of about 10 % to 15 %, so the number of protons per shot is reduced by an order of magnitude to 10^5 metastable hydrogen atoms. Also, in the spin filter, where only the metastable atoms are partially quenched into the ground state, the number of metastable atoms in one single hyperfine substate/shot is reduced by another order of magnitude due to the efficiency of the process. During the selective detection of metastable hydrogen atoms by Lyman-α emission using Stark-effect quenching, the number of particles is further reduced to 10 photons/shot. Compared to the dark current of about 1 photon/s, this number is still large enough to be detectable. Finally, the photons are amplified by a factor of 10^7 in the subsequent photomultiplier, so that in the end a number of about 10^8 electrons/shot can be expected. Since the pulse of the polarized protons has a width of 5 μs, as already explained, a signal corresponding to $2{\cdot}10^{13}$ electrons/s is eventually recorded. This corresponds to a current of about 3 μA, which, when using a resistor of 1 MΩ, delivers a voltage of 3 V. A signal with a level of 3 V can be visualized in the oscilloscope

without any difficulty and, thus, the number of $1.5{\cdot}10^6$ protons/shot leaving the Wien filter is sufficient. In addition, this signal can be well triggered to average out statistical fluctuation and to get a reproducible and stable signal.

A typical Lyman spectrum of a polarized hydrogen beam of atoms to determine the degree of polarization is already presented in Fig. 4.7. Supposing that out of 1000 H^+ ions, 750 are in the $\alpha 1 = |m_J = +1/2,\, m_I = +1/2\rangle$ state and 250 are in the $\alpha 2 = |m_J = +1/2,\, m_I = -1/2\rangle$ state, the polarization is $P_{Ly} = 0.5 \pm 0.06$ (cf. Eq. 4.3). Theoretically, even a signal with a level of only 1 mV would be adequate to be visualized due to averaging. Hence, about 300 protons/shot on the Faraday cup would be sufficient to be finally amplified in the photomultiplier. However, this would require averaging over many shots to acquire a reasonably low-noise signal. Nevertheless, this small number underlines the high sensitivity of the LSP.

9.4 Security concept for Laser operation and gas composed of hydrogen halides

Before the above described experiments could be performed, the available lab, in which the LSP had already been set up, had to be made safe. This includes firstly the modification of the already existing lab into a laser lab according to current safety standards and secondly the installation of a gas supply and exhaust system for HCl and HBr with all safety precautions.

By inspecting the *Ju*SPARC_Mira laser specifications (cf. Tab. 5), it is apparent that the system is designed to emit infrared and ultraviolet light – both wavelengths invisible to the human eye. The UV-C radiation of 213 nm does not penetrate very deeply into the skin due to the increasing scattering with shorter wavelengths, but skin contact can cause DNA damages, which can inhibit replication or may result in mutations. In the case of mistreated use, the strong near-infrared laser radiation of 1064 nm and 100 mJ may be hazardous to the eyes, resulting in damage or at worst blindness to the user. Therefore, it is indispensable and comfortable to wear laser safety goggles, which are especially suitable for Nd:YAG lasers and possess full protection level for both wavelengths within the range of 180 nm up to 1100 nm, e.g., the goggle *F18.P1L12.1003* from *UVEX*. The goggles are stored in a case in a separate cabinet right at the entrance door to the lab, so that they are ready to hand when entering the lab and the surface of the goggles is protected from external damage. During normal laser operation, i.e., when no adjustment of the optics is required, the shielding box should be closed (cf. Fig. 9.1). A laser warning light is installed so that it is clearly visible from the outside of the lab and is switched on when the laser is in operation.

The second risk factor in the lab is the HCl or HBr gas. Both, HCl and HBr, are colorless and pungently smelling gases that very easily dissolve in water. Due to acid formation in water, both gases have an irritating effect on the eyes and the respiratory tract and are also toxic in high concentrations. For this reason, it is only under very limited circumstances that these gases can be commercially purchased in Germany, one being for scientific research. Due to safety precautions, it is stored outside the lab in the open air in a lockable gas bottle cabinet. Replacement of the gas bottle must be carried out by trained personnel wearing heavy respiratory protection and safety suits under the supervision of the fire department. The gas is fed into the lab via stainless steel pipes. Above the interaction chamber a gas fitting for setting the backing pressure is mounted, as can be seen in Fig. 9.1. In the same place there is also a gas warning

sensor from *Dräger*, which emits a warning tone in the event of a leak. From there, the gas is directed into the interaction chamber, where it can be retained by shut-off valves. This also serves to easily pump the setup after venting. The gas is then first sucked away via a turbo pump and a backing pump and conveyed outside via an exhaust line. As a further safety feature, a control box is installed in the lab that allows gas to flow out of the gas bottle, controlled by a valve, only when the turbo pump is switched on and the gas sensor is operational.

During the experiments, it became apparent that an initially used gas washer after the backing pump is not necessary, since the quantities of gas blown out are extremely small. After a few months of operation, however, it has been noticed that, primarily in summer, vapor water forms in the exhaust line due to the temperature difference between the air-conditioned lab and the outside temperature. This not only damages the gas line, but also causes the water to flow through the line towards the backing pump. Due to the fact that both gases are extremely attractive to water and a small amount remains on the surface of the lines and inside the pump, a reaction occurs here. This results in the formation of a brownish red, crumbly and toxic solid, similar to rust, which was found in the exhaust line upstream of the backing pump. The liquid in the gas washer even originally favored this scenario. To eliminate the problem, a low flow of argon or nitrogen gas is now continuously fed through the backing pump and the exhaust line, so that the remaining HCl or HBr gas is flushed to the outside. In the future, it should also be ensured that the entire gas supply line is sloped until it reaches the gas fitting, thus preventing water from collecting in the line. It is also recommended to use the more resistant Teflon instead of stainless steel for the pipes.

10 Concluding Remarks and Outlook

In this section, the most relevant results from this dissertation, both, from the PIC simulations and the experiments, are summarized (cf. Sec. 10.1). Then, an outlook is presented on how the research work of this thesis can be carried on (cf. Sec. 10.2). In this respect, a distinction is made between the short-term goal, which is to measure the degree of polarization of protons with the LSP (cf. Sec. 10.2.1), and the long-term perspectives. The latter is the realization of an electron-positron collider, for which a concept for polarized electron acceleration has also been developed (cf. Sec. 10.2.2).

10.1 Laser-based polarized proton acceleration from HCl and HBr gas targets

Within the scope of this thesis, preparatory investigations for the measurement of spin-polarized laser-accelerated protons from a pre-polarized HCl or HBr gas-jet target, based on extensive 3D PIC simulations including spin dynamics, at the 10 PW laser at SULF were conducted.

The key issue of this thesis was to develop a scheme for the spin-polarized laser-driven proton acceleration. To do so, this thesis is divided into two main subjects: first, extensive 3D PIC simulations to study the acceleration mechanisms and possible depolarization effects for polarized protons. Second, the question of how to realize a device, in which the nuclear spins are already aligned before the acceleration phase, as well as the setup and commissioning of such a gas target, and first measurements on the degree of nuclear polarization with an appropriate tool for polarimetry.

The 3D PIC simulations were performed to model the acceleration process of polarized protons, based on previous studies by our group indicating that the generation of polarized proton beams requires a target, in which the spins are already aligned prior to acceleration. Aiming to produce and observe for the first time a polarized, laser-accelerated proton beam of $10-100$ MeV energy, the 10 PW laser system at SULF (cf. Sec. 2.2.1) was assessed as a suitable facility. To make more accurate predictions for these experimental surveys, especially at such new laser systems, PIC simulations are a proven and helpful tool. At the beginning of this work, however, there was no PIC simulation software, into which spin dynamics were implemented. Thus, a central task was to determine the mechanisms that could lead to polarization or depolarization of a particle beam. Here, the following three mechanisms were identified: i) the spin precession as described by the T-BMT equation, ii) the Sokolov-Ternov effect, and iii) the Stern-Gerlach (SG) effect (cf. Sec. 4). In the second step, it was analytically specified, which of these effects, originally known from classical accelerator physics, are also relevant for laser-based proton acceleration (cf. Sec. 5). To do so, scaling laws for the (de-)polarization time of high energetic particle beams moving in strong fields have been derived. For initially polarized proton beams, the minimum depolarization time $t_{\mathrm{D,L}} \approx 520\,\omega_{\mathrm{L}}^{-1}$ has been calculated from the T-BMT equation assuming that all particle spins precess incoherently. It was found that this time is long enough to ensure the conservation of proton polarization. In contrast, the Sokolov-Ternov effect, for which too long times for the polarization to build up have been estimated, and the SG effect, for which the maximum separation distance would be only about 20 fm at SULF, both have negligible influence and, hence, do not need to be considered further.

In the next step, the only mechanism identified as relevant, the spin precession according to the T-BMT equation, has been implemented in the fully 3D PIC code VLPL in a collaboration between HHUD and FZJ (cf. Sec. 6). The first PIC simulations with particle polarization had the goal to gradually simulate a realistic scenario for the experiments at the 10 PW laser at SULF (cf. Sec. 7). For this purpose, in addition to laser and target parameters, the relevant acceleration mechanisms must be investigated. Most simulation series were carried out with the VLPL code, and one with EPOCH, into which spin tracking has been included by Chinese collaboration partners. All VLPL simulations were performed on the Jülich supercomputers JURECA and JUWELS (cf. Tab 2). First, the functionality of the code was retested by carrying out a simulation for the experiment at the ARCTURUS laser facility. As an additional feature, the target consisted of a fully polarized proton layer, so that the simulated polarization effects become more obvious. The conservation of the polarization in this simulation is to be regarded as the most important result. Thus, this simulation series not only formed the basis for further studies regarding target material, laser parameters and acceleration mechanisms, but also the starting point for the further planning of the experiment on the laser-based acceleration of spin-polarized protons.

For further analysis, the first simulation series with a polarized gas target was prepared. Following the work by Shen et al. [72], a similar simulation setup but including spin dynamics with a H/T mixture and, in addition, a HCl gas target, which is used in our experiments, is simulated. As expected, the simulation for H/T is in good agreement with the results from Ref. [72], since the input parameters are very similar and this gives confidence in the robustness of our VLPL code. Polarized HCl gas seems to be the better target choice compared to H/T because slightly higher energies and momenta are predicted. Furthermore, for the first time a polarization conservation in a polarized gas target could be demonstrated, which amounts to at least 50 % of the initial polarization. In the following two simulations, the focus was directed to the simulation of more realistic parameters both, for the target dimensions as well as for the laser. The latter was addressed in the next simulation and, by analyzing the electromagnetic fields involved. It led to the conclusion that two mechanisms cause the acceleration of protons to high energies: first, a direct acceleration in the plasma channel, and second, an additional effect at the rear end of the gas target, referred to as MVA mechanism. This effect only boosts the energy of the front protons, but not that of the higher-energy tail protons in the channel. The last simulation series corresponds to the most realistic experimental conditions. In addition to the previous one, the target parameters were adjusted to simulate a gas nozzle previously characterized with Michelson interferometry. Due to the extended target and the choice of boundary conditions in the simulation, the electric fields turned out to be unphysically high. Thus, the proton energies are overestimated, as shown by the comparison of three sets with different parameters and an analytical investigation based on these findings. The analytical analysis showed that a maximum proton energy of about 100 MeV can be expected for an accelerating laser of 4.8 PW power. Moreover, it has been found that the magnetic fields are not affected by this overestimation, and, hence, the polarization is preserved up to a degree of 50 %, which is in good agreement with the previous findings. If these numerical results could be demonstrated even partially experimentally, it would be a huge success for the entire laser-plasma accelerator community.

Meanwhile, a device has been developed, which allows the generation of polarized proton beams in a feasible experiment (cf. Sec. 8). It turns out that the most promising method for generating spin-polarized protons is a novel pre-polarized hydrogen target based on a photo-dissociation of hydrogen halides, such as HCl or HBr, in which the nuclear spins are already aligned before acceleration with a high-intensity laser. Through the photo-dissociation process, a dissociative excited state of the molecule can be accessed optically, and each such state adiabatically correlates, for a prompt dissociation, to the two photo-fragments in specific quantum and spin states. First, the electrons are polarized by the photo-dissociation laser. Then, the polarization is subsequently transferred to the proton by the hyperfine-structure oscillations in a time span of about 350 ps. The experimental setup was designed accordingly, consisting of the *SLL334-5 Ju*SPARC_Mira laser system, the beam optics, the interaction chamber with a piezo valve and the gas feed line, as well as the LSP for detection of the polarization. Most important for this setup is the laser system, which provides the wavelength of 213 nm, because the photo-dissociation cross section is particularly high in this range.

Now that the setup was completely designed and the components were assembled and individually tested, the entire experiment could be put into operation and first measurements were performed in strict compliance with the approved safety concept (cf. Sec. 9). Thereby, the synchronization of the laser with the piezo valve using a digital pulse delay generator ensures the overlap of the gas jet with the laser pulse in the interaction point on the horizontal beam axis of the LSP. HCl and HBr gases at different backing pressures between 0 bar and 5 bar were used. For the latter the photo-dissociation cross section is about two orders higher, assuming that both gases expand as a supersonic beam when exiting the valve. Calculations have shown that the gas jet, which opens for 30 μs, must not be too dense, and, thus, the mean free path, i.e., the average distance traveled by a moving particle between successive collisions, must not be too small, so that the polarized protons can escape from the jet. Furthermore, a distance between the gas valve and the interaction point of 10 cm was assumed to be optimal, whereby the distance can be adjusted with a holder that is variable in height. Thus, a number of about $1.5{\cdot}10^{13}$ photons at 20 mJ laser pulse energy are expected employing the cross section at room temperature. Their signal is estimated to arrive between 10 μs and 15 μs after the photo-dissociation on the Faraday cup behind the Glavish ionizer and Wien filter. First, measurements for diffusive gas of H^+ and H_2^+ ions without laser operation have shown that both, the Glavish ionizer and the Wien filter, work properly. In further experiments, the laser was switched on, so that spin-polarized protons should be generated and the signal be detected on the Faraday cup. However, an additional contribution in the signal originating from the spin-polarized protons could not be observed, neither for all heavy masses nor at that of the H^+ ions. This observation is not in line with the expectations: the total number of about $1.5{\cdot}10^6$ protons per laser shot should be detected in the Faraday cup due to the efficiency of the ionizer, assuming that $1.5{\cdot}10^{13}$ H atoms/shot are generated by the photo-dissociation process. Hence, a signal height of about 100 nA with a width of 5 μs of the spin-polarized hydrogen is predicted in the Faraday cup, resulting in a peak of about 100 mV in the oscilloscope, which would have been clearly identifiable. The fact that no signal contribution is registered on the Faraday cup can be attributed to two reasons: first, the gas jet is not hit by the photo-dissociation laser, so that consequently no photo-dissociation process takes place and no polarized protons are

produced, which can be observed with the LSP. To verify the correct timing between gas jet and laser pulse, a compression tube has already been installed near the interaction point. In this way, the detection of the pressure increase in the interaction chamber as a result of the photo-dissociation process is about 100 times more sensitive in future experiments. Second, the laser-gas overlap takes place and polarized protons are produced, which enter the ionizer. Then, the ionization efficiency in the ionizer must be much smaller than expected for fast atoms and significantly smaller than known from previous experiments for thermal gas or slow atom beams ($\sim 1000\,\mathrm{m/s}$) from an ABS. This could be solved by ionizing the spin-polarised hydrogen atoms with an additional laser pulse (cf. Sec. 10.2.1). For the planned experiments with the polarized target at SULF this is anyway obsolete, since no polarimetry with the LSP will be performed here. However, further estimations have shown that the number of $1.5{\cdot}10^6$ protons/shot in the Faraday cup would be sufficient to observe a voltage of possibly up to 3 V at the end of the LSP using a photomultiplier. Thus, if the ionization process works properly, the experiment is tested to be successful and a detection of spin-polarized protons becomes straightforward. Then, the target can be combined with the 10 PW laser, where proton energies in the 100 MeV range are expected.

10.2 Future work

Since the experimental as well as the simulated results within this doctoral studies demonstrate the feasibility of polarized laser-driven proton acceleration, the further work aiming at the production and observation of a polarized laser-accelerated proton beam of about 100 MeV energy for the first time will be continued. The future work can be classified by two objectives: first, a short-term goal, in which nuclear proton polarization using a HCl or a HBr gas target is detected with the LSP, thus demonstrating the proper operation of the polarized proton source. Second, the long-term and overall goal of realizing an electron-positron collider, for which first studies on polarized electron polarization have been carried out within this dissertation.

10.2.1 Modification of the existing setup

The experiments with a compression tube should enable an optimal laser-gas jet overlap and can be used to proof the expected photo-dissociation of the hydrogen halides by measuring the atomic hydrogen intensity after each laser shot. If this is optimized and still there are no polarized protons produced within the ionizer, then the missing ionization efficiency is the next problem to overcome. Therefore, it would be expedient to ionize the hydrogen atoms before entering the LSP. A promising option is ionization with a laser still in the interaction chamber, as shown in Fig. 10.1. A new laser systems is needed for this new approach: as usual, the HCl or HBr bonds are aligned with the fundamental wavelength of Nd:YAG at 1064 nm and an energy of about 100 mJ. This is followed by the photo-dissociation of HCl or HBr and the polarization transfer to the H nucleus. This can still be accomplished with the existing *Ju*SPARC_Mira laser. However, the new laser system can already be used here, which is operated at a wavelength of 205 nm and also at an energy of 20 mJ. This would have the advantage that the photo-dissociation cross section for HCl and HBr is somewhat larger at this slightly smaller wavelength. The new laser is then needed in any case to induce a (2+1)-photon ionization of the spin-polarized hydrogen atoms at 205 nm.

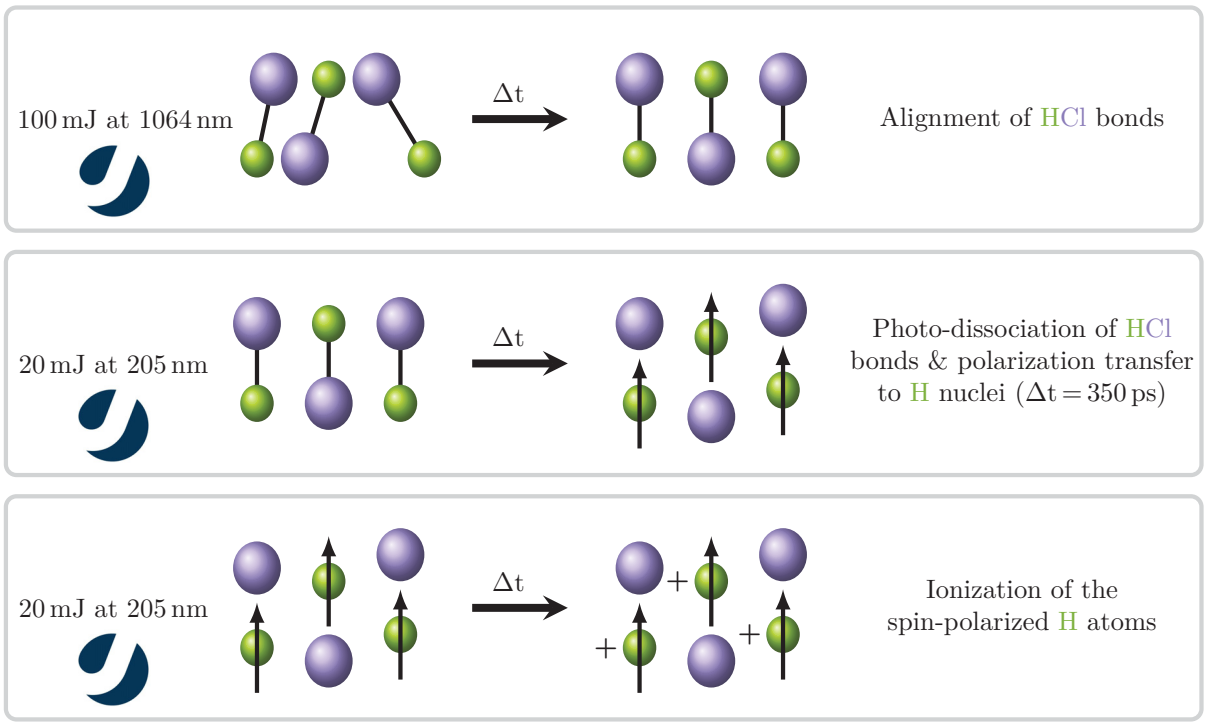

Figure 10.1: New approach for the detection of polarized proton beams by ionizing the spin-polarized hydrogen atoms after the photo-dissociation process using a laser of wavelength 205 nm and an energy of 20 mJ. The ionization process thus no longer takes place in the LSP. The photo-dissociation can be performed with the same laser, with the advantage that the photo-dissociation cross-section is slightly larger at this wavelength. But the second laser pulse at 205 nm for ionizing the H atoms has to interact with the gas 350 ps after the photo-dissociation process took place, so that the polarization can be completely transferred to the protons by the hyperfine-structure oscillations.

Technically, this could be realized with a combined YAG-pumped dye-laser system from *Sirah Lasertechnik GmbH*, as depicted in App. E. Using the *Cobra-Stretch Tunable Dye Laser* in combination with a Frequency Conversion Unit (FCU), the initial laser beam is amplified and the corresponding harmonics are generated implementing doubling crystals for 206 nm – 380 nm with high absolute wavelength accuracy [188]. The frequency is doubled by a Beta Barium Borate (BBO) crystal followed by a compensator. Behind, the *Boston 500* is connected in series or parallel. It is a compact and versatile Nd:YAG laser based on an efficient single rod, oscillator only, design [189]. The main parameters of the *Boston 500* Nd:YAG laser system are given in Tab. 8.

Table 8: Main parameters of the *Boston 500* Nd:YAG laser system [189].

Manufacturer	Sirah Lasertechnik GmbH
Repetition rate	± 10% in 0.1 μHz steps down to 0.1 Hz
Pulse duration	5 – 8 ns
Pulse energy	100 mJ @ 1064 nm, 20 mJ @ 205 nm
Beam diameter	< 8 mm
Up-converted radiation	532 nm, 355 nm, 205 nm
Conversion principle	Built-in harmonic generator
Experimental technique	Control of nuclear spins & ionization of H atoms

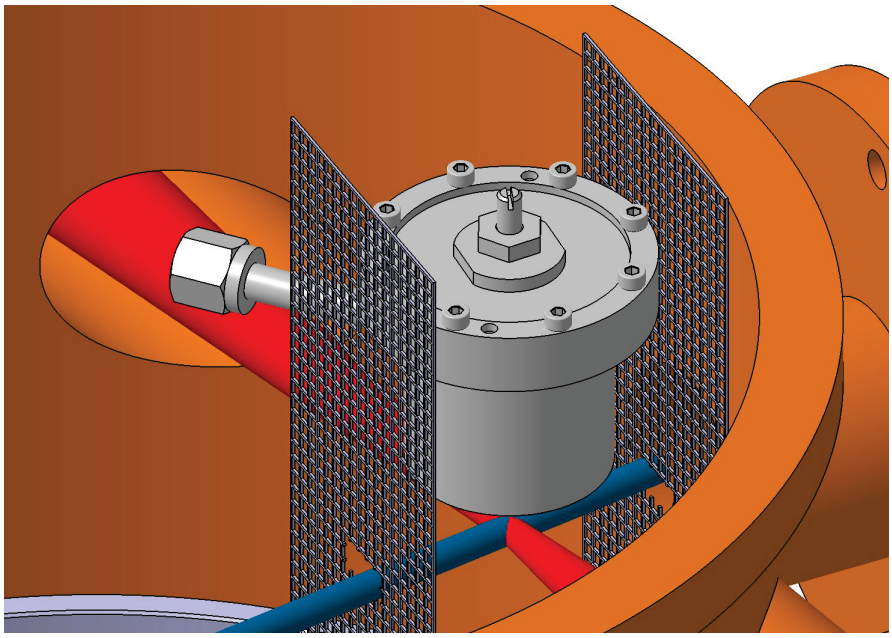

Figure 10.2: Design of the future interaction chamber with two gratings between the piezo valve for acceleration of polarized and ionized hydrogen atoms into the LSP.

After the hydrogen is polarized and ionized with the new laser system, it is necessary to guide the protons into the LSP. Electric fields can be used for this by applying an electric voltage to two gratings as shown in Fig. 10.2. It is important that the voltage on the grid facing the LSP is lower, so that the protons are accelerated in this direction. These modifications can be implemented without rebuilding the existing interaction chamber. Due to the use of the laser for the ionization process instead of the Glavish ionizer, the signal in the LSP will be increased by about four orders of magnitude. Thus, there are no losses resulting from the geometry of the expanding sphere of spin-polarized protons and the small acceptance angle of the detector. Consequently, a detection of the degree of polarization becomes much more likely.

10.2.2 Towards polarized electron acceleration

One long-term goal of the laser-plasma physics community is the realization of an electron-positron collider, as it is stated in the *2020 Roadmap on Plasma Accelerators* [16]. Thus, another aim of this thesis was the conceptual design of a polarized target for laser-induced electron acceleration based on the already developed target for polarized protons. Several challenges must be overcome: i) since significant polarization transfer to electrons from an initially unpolarized target does not occur during laser acceleration, the use of a gas target, in which the electron spins are already aligned prior to laser acceleration is required. ii) Polarization losses during the injection of electrons into a bubble structure, and iii) subsequent acceleration in the wakefield must be controlled and optimized [120]. Considering positrons, experimental investigations of acceleration concepts in a plasma is even more ambitious due to the difficulty of providing an injector of adequate quality that can be synchronised with the positron-accelerating region of a wakefield.

Figure 10.3 shows the scheme for polarized laser-induced electron acceleration based on the polarized gas target for protons. The following descriptions are based on the publication by Yitong Wu, ..., Anna Hützen et al. [120]. The first two steps, in which the HCl bonds are aligned using the 1064 nm laser as well as the photo-dissociation and polarization of the electrons takes place by either a 205 nm laser or a pulse of 213 nm wavelength, is already known from the polarized proton target (cf. Fig. 8.3). Applying 234.62 nm UV light the Cl atoms are ionized. Due to thermal expansion of the electrons a large Coulomb field is induced, which expels the Cl^+ ions. Subsequently, the remaining spin-polarized electrons from the hydrogen are accelerated with a high-intensity laser, while maintaining their polarization to a large degree.

Based on 3D PIC simulations implementing this new target scheme Yitong Wu, ..., Anna Hützen et al. [120] predict larger electron beam currents via vortex Laguerre-Gaussian (LG) laser-driven wakefield acceleration compared to Gaussian laser-driven acceleration. The topology of the vortex wakefield resolves the depolarization issue of the injected electrons and due to the LG

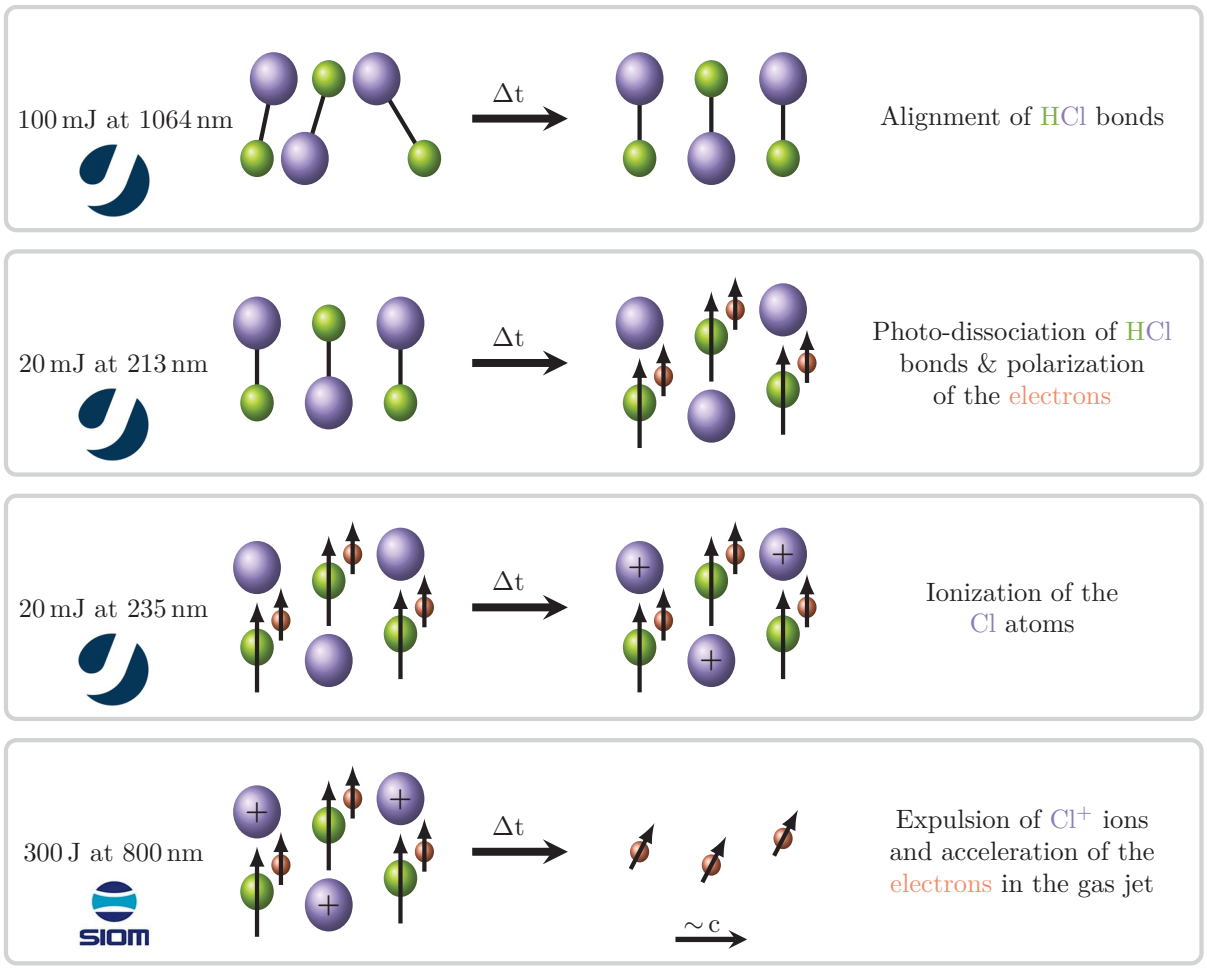

Figure 10.3: Schematic overview of the production of laser-driven polarized electron beams. The HCl bonds are first aligned with an IR laser beam. This is an optional process to increase the degree of polarization of the photo-fragments and, thus, the final signal. The 213 nm UV laser propagates with 20 mJ beam energy along the z-axis to photo-dissociate the HCl molecules and consequently transfer the polarization to the electrons. After the Cl atoms are ionized by another UV light of 235 nm wavelength, they can be removed by either an external electric field or thermal expansion. Finally, the spin-polarized electrons are accelerated to high energies with a high-intensity laser pulse, e.g. the SULF laser, while maintaining their polarization.

laser a conservation of the electron-spin polarization by more than 80 % is expected as presented in Fig. 10.4. This method releases the limit on beam flux for polarized electron acceleration and assures a boost in the peak flux by more than one order of magnitude as compared to Gaussian beams [29, 120].

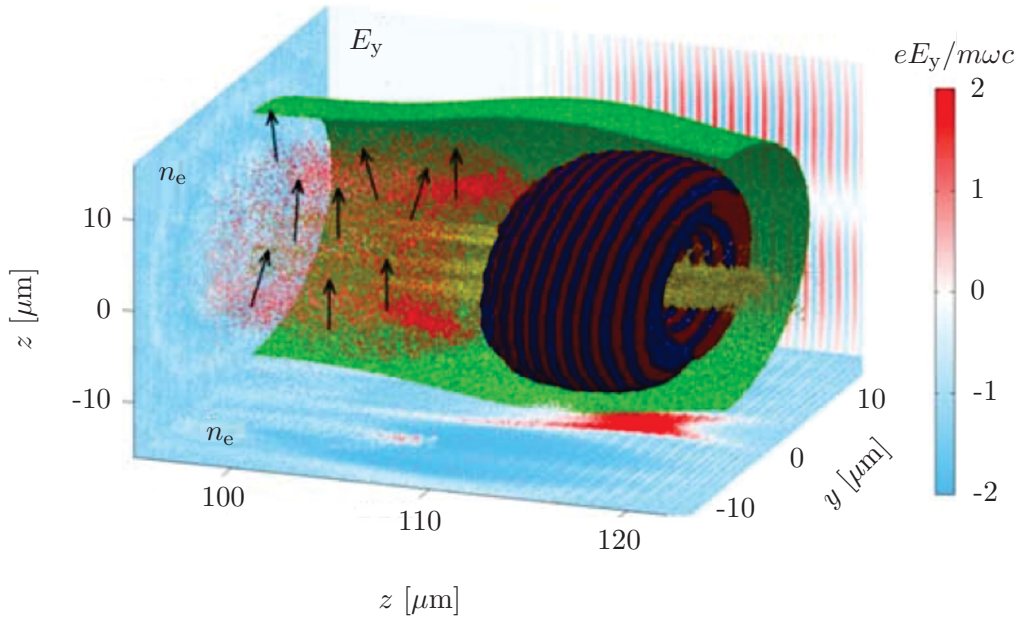

Figure 10.4: Polarized electron acceleration driven by vortex laser pulses: the picture shows the electron density and laser field distributions (iso-surface) for the LG laser as well as the electron spin directions according to the T-BMT equation indicated by the black arrows. The laser electric field is projected onto the x–z plane (at $y = 0$), while the electron density is projected onto the x–y (at $z = 0$) and y–z planes [120].

In a subsequent paper Yitong Wu, ..., Anna Hützen et al. [150] apply the scheme presented in Fig. 10.3 to plasma wakefield acceleration driven by a particle beams (PWFA) to investigate the precession of electron spins based on density down ramp injection using 3D PIC simulations incorporating the spin dynamics. The unpolarized electron driver beam, which is free of the prepulse issue associated with a laser driver, is produced by the well-known LWFA. Thus, possible depolarization effects of the polarized gas are eliminated, which may be caused by an ionization induced by a prepulse. As a result, electron beams with high polarization by controlling the driving-beam parameters and plasma densities at different initial spin directions are obtained [29, 150].

Further investigations of electron beam polarization by means of 3D PIC simulations and a theoretical analysis in the scope of a quasi-static model published by Yitong Wu, ..., Anna Hützen et al. [151] indicate a dependence on the azimuthal angle in plasma wakefields as a consequence of the symmetric bubble field. Accordingly, an X-shaped slit as a kind of spin filter is recommended to be placed immediately behind the plasma accelerator to significantly enhance the beam polarization of the accelerated electrons. By filtering out the low-polarization population implementing the suggested slit, a beam polarization of about 80 % is achieved, while the initial polarization is only about 35 % [29, 151].

With this preliminary work, the realization of a polarized electron accelerator is certainly getting a bit closer.

List of Publications

In this section, I list my publications and publications with my co-authorship that were published in the context of this PhD thesis. These publications are referred to in the sections indicated. My own contribution to the content of each publication is outlined.

Polarized proton beams from laser-induced plasmas (Ref. [26])
A. Hützen, J. Thomas, J. Böker, R. Engels, R. Gebel, A. Lehrach, A. Pukhov, T. P. Rakitzis, D. Sofikitis, and M. Büscher
High Power Laser Sci. Eng., 7(E16), 2019

- First author with all responsibilities

Polarized electron-beam acceleration driven by vortex laser pulses (Ref. [120])
Y. Wu, L. Ji, X. Geng, Q. Yu, N. Wang, B. Feng, Z. Guo, W. Wang, C. Qin, X. Yan, L. Zhang, J. Thomas, A. Hützen, M. Büscher, T. P. Rakitzis, A. Pukhov, B. Shen, and R. Li
New J. Phys., 21(073052), 2019

- Joint development of the new concept for laser-driven electron acceleration described in the paper in one of our in-person collaboration meetings
- Check of the calculations on the spin dynamics
- Discussion of the results

Polarized electron acceleration in beam-driven plasma wakefield based on density down-ramp injection (Ref. [150])
Y. Wu, L. Ji, X. Geng, Q. Yu, N. Wang, B. Feng, Z. Guo, W. Wang, C. Qin, X. Yan, L. Zhang, J. Thomas, A. Hützen, A. Pukhov, M. Büscher, B. Shen, and R. Li
Phys. Rev. E, 100(043202), 2019

- Code benchmarking
- Discussion of the simulation setup and results

Polarized proton beams from a laser-plasma accelerator (Ref. [27])
M. Büscher, A. Hützen, I. Engin, J. Thomas, A. Pukhov, J. Böker, R. Gebel, A. Lehrach, R. Engels, T. P. Rakitzis, and D. Sofikitis
Int. J. Mod. Phys. A, 34(1942028), 2019

- Writing of the chapters "PARTICLE SPIN DYNAMICS", "PARTICLE-IN-CELL SIMULATIONS" including performance analysis of the presented 3D simulations and "EXPERIMENTAL REALIZATION" with supplying of the graphics

Simulation of Polarized Beams from Laser-Plasma Accelerators (Ref. [28])
A. Hützen, J. Thomas, A. Lehrach, T. P. Rakitzis, A. Pukhov, L. Ji, Y. Wu, R. Engels, and M. Büscher
J.Phys.: Conf. Ser., 1596(012013), 2020

- First author with all responsibilities

Spin Filter for Polarized Electron Acceleration in Plasma Wakefields (Ref. [151])
Y. Wu, L. Ji, X. Geng, J. Thomas, M. Büscher, A. Pukhov, A. Hützen, L. Zhang, B. Shen, and R. Li
Phys. Rev. Applied 13(044064), 2020

- Working out the simulation setup in an in-person meeting
- Joint development of a concept for experimental realization
- Discussion of the results

Scaling laws for the depolarization time of relativistic particle beams in strong fields (Ref. [30])
J. Thomas, A. Hützen, A. Lehrach, A. Pukhov, L. Ji, Y. Wu, X. Geng, and M. Büscher
Phys. Rev. Accel. Beams 23(064401), 2020

- Working closely with the first author in constituting the paper
- Joint development of a concept for experimental realization
- Elaborating the analytical concepts
- Checking the calculations
- Discussion of the results

Spin-polarized proton beam generation from gas-jet targets by intense laser pulses (Ref. [32])
L. Jin, M. Wen, X. Zhang, A. Hützen, J. Thomas, M. Büscher, and B. Shen
Phys.Rev. E, 102(011201(R)), 2020

- Performance of a comparable 3D simulation series with the VLPL code for benchmarking the EPOCH code, in which the spin dynamics has been newly implemented for the paper
- Evaluation and comparison of the simulations
- Discussion of the results

Generation of polarized particle beams at relativistic laser intensities (Ref. [29])
M. Büscher, A. Hützen, L. Ji, and A. Lehrach
High Power Laser Sci. Eng., 8(E36), 2020

- Review article with four equally contributing authors

On the robustness of spin polarization for magnetic vortex accelerated proton bunches in density down-ramps (Ref. [148])
L. Reichwein, A. Hützen, M. Büscher, and A. Pukhov
Plasma Phys. Control. Fusion, 63(085011), 2021

- Preparation of simulations
- Co-elaboration of the final simulation setup
- Discussion of the results

Polarized proton acceleration in ultraintense laser interaction with near-critical-density plasmas (Ref. [149])

X. Li, P. Gibbon, A. Hützen, M. Büscher, S. Weng, M. Chen, and Z. Sheng

Phys. Rev. E, Accepted 8 July 2021

- Preparation of simulations
- Discussion of the graphical visualization of the simulation results
- Discussion of the results

References

[1] D. Androić et al. (The Jefferson Lab Qweak Collaboration). Precision measurement of the weak charge of the proton. *Nature*, 557(207), 2018.

[2] J. Grange et al. (Muon g-2 Collaboration). Muon (g-2) Technical Design Report. arXiv:1501.06858 [physics.ins-det], 2015.

[3] F. Rathmann, A. Saleev, and N. N. Nikolaev (JEDI and srEDM collaborations). The search for electric dipole moments of light ions in storage rings. *J. Phys.: Conf. Ser.*, 447(012011), 2013.

[4] M. Burkardt, C. A. Miller, and W.-D. Nowak. Spin-polarized high-energy scattering of charged leptons on nucleons. *Rep. Prog. Phys.*, 73(016201), 2010.

[5] E. S. Ageev et al. (COMPASS Collaboration). Measurement of the spin structure of the deuteron in the DIS region. *Phys. Lett. B*, 612(154), 2015.

[6] C. Glashausser. Nuclear physics with polarized beams. *Ann. Rev. Nucl. Part. Sci.*, 29(33), 1979.

[7] R. L. Jaffe. Open questions in high energy spin physics. *Int. J. Mod. Phys. A*, 18(1141), 2002.

[8] H. Baer et al. The international linear collider technical design report - volume 2: Physics. arXiv:1306.6352 [hep-ph], 2013.

[9] P. Adlarson et al. (WASA-at-COSY Collaboration, SAID Data Analysis Center). Evidence for a New Resonance from Polarized Neutron-Proton Scattering. *Phys. Rev. Lett.*, 112(202301), 2014.

[10] T. J. Gay. *Advances In Atomic, Molecular, and Optical Physics*. ISBN: 978-0-12-374799-0. Academic Press, New York, 2009.

[11] B. Bederson and H. Walther. Advances in atomic, molecular, and optical physics. *Academic Press, New York*, 62(17), 2017.

[12] A. Lehrach, U. Bechstedt, J. Dietrich, R. Gebel, B. Lorentz, R. Maier, D. Prasuhn, A. Schnase, H. Schneider, R. Stassen, H. Stockhorst, and R. Tölle. Acceleration of Polarized Protons and Deuterons at COSY. *AIP Conference Proceedings*, 675(1), 2003.

[13] I. Alekseev et al. Polarized proton collider at RHIC, Nuclear Instruments & Methods in Physics Research. *Nucl. Instrum. Methods Phys. Res. A*, Section A 449(392), 2003.

[14] H. P. Schlenvoigt, O. Jäckel, S. M. Pfotenhauer, and M. C. Kaluza. Laser-based particle acceleration. In *Advances in Solid State Lasers*, chapter 24. IntechOpen, 2010.

[15] P. A. Walker et al. Horizon 2020 EuPRAXIA design study. *J. Phys.: Conf. Ser.*, 874(012029), 2017.

[16] F. Albert, M.-E. Couprie, A. D. Debus, M. Downer, J. Faure, A. Flacco, L. A. Gizzi, T. E. Grismayer, A. Huebl, C. Joshi, M. Labat, W. P. Leemans, A. Maier, S. Mangles, P. Mason, F. Mathieu, P. Muggli, M. Nishiuchi, J. Osterhoff, P. P. Rajeev, U. Schramm, J. Schreiber, A. G. R. Thomas, J.-L. Vay, M. Vranic, and K. Zeil. 2020 roadmap on plasma accelerators. *New J. Phys.*, 2020.

[17] A. J. Gonsalves, K. Nakamura, J. Daniels, C. Benedetti, C. Pieronek, T. C. H. de Raadt, S. Steinke, J. H. Bin, S. S. Bulanov, J. van Tilborg, C. G. R. Geddes, C. B. Schroeder, C. Tóth, E. Esarey, K. Swanson, L. Fan-Chiang, G. Bagdasarov, N. Bobrova, V. Gasilov, G. Korn, P. Sasorov, and W. P. Leemans. Petawatt Laser Guiding and Electron Beam Acceleration to 8 GeV in a Laser-Heated Capillary Discharge Waveguide. *Phys. Rev. Lett.*, 122(084801), 2019.

[18] I. J. Kim, K. H. Pae, I. W. Choi, C.-L. Lee, H. T. Kim, H. Singhal, J. H. Sung, S. K. Lee, H. W. Lee, P. V. Nickles, T. M. Jeong, C. M. Kim, and C. H. Nam. Radiation pressure acceleration of protons to 93 MeV with circularly polarized petawatt laser pulses. *Phys. Plasmas*, 23(070701), 2016.

[19] F. Wagner, O. Deppert, C. Brabetz, P. Fiala, A. Kleinschmidt, P. Poth, V. A. Schanz, A. Tebartz, B. Zielbauer, M. Roth, T. Stöhlker, and V. Bagnoud. Maximum Proton Energy above 85 MeV from the Relativistic Interaction of Laser Pulses with Micrometer Thick CH_2 Targets. *Phys. Rev. Lett.*, 116(205002), 2016.

[20] A. Higginson, R. J. Gray, M. King, R. J. Dance, S. D. R. Williamson, N. M. H. Butler, R. Wilson, R. Capdessus, C. Armstrong, J. S. Green, S. J. Hawkes, P. Martin, W. Q. Wei, S. R. Mirfayzi, X. H. Yuan, S. Kar, M. Borghesi, R. J. Clarke, D. Neely, and P. McKenna. Near-100 MeV protons via a laser-driven transparency-enhanced hybrid acceleration scheme. *Nat. Commun.*, 9(724), 2018.

[21] J. Park, S. S. Bulanov, J. Bin, Q. Ji, S. Steinke, J.-L. Vay, C. G. R. Geddes, C. B. Schroeder, W. P. Leemans, T. Schenkel, and E. Esarey. Ion acceleration in laser generated megatesla magnetic vortex. *Phys. Plasmas*, 26(103108), 2019.

[22] A. Pukhov and J. Meyer-ter Vehn. Laser wake field acceleration: the highly non-linear broken-wave regime. *Appl. Phys. B*, 74(355), 2002.

[23] J. van Tilborg, C. B. Schroeder, C. V. Filip, C. Tóth, C. G. R. Geddes, G. Fubiani, R. Huber, R. A. Kaindl, E. Esarey, and W. P. Leemans. Temporal Characterization of Femtosecond Laser-Plasma-Accelerated Electron Bunches Using Terahertz Radiation. *Phys. Rev. Lett.*, 96(014801), 2006.

[24] J. Fuchs, P. Antici, E. d'Humières, E. Lefebvre, M. Borghesi, E. Brambrink, C. A. Cecchetti, M. Kaluza, V. Malka, M. Manclossi, S. Meyroneinc, P. Mora, J. Schreiber, T. Toncian, H. Pépin, and P. Audebert. Laser-driven proton scaling laws and new paths towards energy increase. *Nat. Phys.*, 2(48), 2006.

[25] T. E. Cowan, J. Fuchs, H. Ruhl, A. Kemp, P. Audebert, M. Roth, R. Stephens, I. Barton, A. Blazevic, E. Brambrink, J. Cobble, J. Fernández, J.-C. Gauthier,

M. Geissel, M. Hegelich, J. Kaae, S. Karsch, G. P. Le Sage, S. Letzring, M. Manclossi, S. Meyroneinc, A. Newkirk, H. Pépin, and N. Renard-LeGalloudec. Ultralow Emittance, Multi-MeV Proton Beams from a Laser Virtual-Cathode Plasma Accelerator. *Phys. Rev. Lett.*, 92(204801), 2004.

[26] A. Hützen, J. Thomas, J. Böker, R. Engels, R. Gebel, A. Lehrach, A. Pukhov, T. P. Rakitzis, D. Sofikitis, and M. Büscher. Polarized proton beams from laser-induced plasmas. *High Power Laser Sci. Eng.*, 7(E16), 2019.

[27] M. Büscher, A. Hützen, I. Engin, J. Thomas, A. Pukhov, J. Böker, R. Gebel, A. Lehrach, R. Engels, T. P. Rakitzis, and D. Sofikitis. Polarized proton beams from a laser-plasma accelerator. *Int. J. Mod. Phys. A*, 34(1942028), 2019.

[28] A. Hützen, J. Thomas, A. Lehrach, T. P. Rakitzis, A. Pukhov, L. Ji, Y. Wu, R. Engels, and M. Büscher. Simulation of Polarized Beams from Laser-Plasma Accelerators. *J. Phys.: Conf. Ser.*, 1596(012013), 2020.

[29] M. Büscher, A. Hützen, L. Ji, and A. Lehrach. Generation of polarized particle beams at relativistic laser intensities. *High Power Laser Sci. Eng.*, 8(E36), 2020.

[30] J. Thomas, A. Hützen, A. Lehrach, A. Pukhov, L. Ji, Y. Wu, X. Geng, and M. Büscher. Scaling laws for the depolarization time of relativistic particle beams in strong fields. *Phys. Rev. Accel. Beams*, 23(064401), 2020.

[31] Peter Grünberg Institute (PGI-6) Forschungszentrum Jülich. JuSPARC — The Jülich Short-Pulsed Particle and Radiation Center. *JLSRF*, 6(A138), 2020.

[32] L. Jin, M. Wen, X. Zhang, A. Hützen, J. Thomas, M. Büscher, and B. Shen. Spin-polarized proton beam generation from gas-jet targets by intense laser pulses. *Phys. Rev. E*, 102(011201(R)), 2020.

[33] B. M. Garraway and S. Stenholm. Does a flying electron spin? *Contemp. Phys.*, 43(147), 2002.

[34] N. Raab, M. Büscher, M. Cerchez, R. Engels, I. Engin, P. Gibbon, P. Greven, A. Holler, A. Karmakar, A. Lehrach, R. Maier, M. Swantusch, M. Toncian, T. Toncian, and O. Willi. Polarization measurement of laser-accelerated protons. *Phys. Plasmas*, 21(023104), 2014.

[35] D. Strickland and M. Gerard. Compression of amplified chirped optical pulses. *Opt. Commun.*, 56(219), 1985.

[36] B. Struve. *Einführung in die Lasertechnik*. ISBN: 978-3-8007-2982-1. VDE Verlag GmbH, 2009.

[37] M. Eichhorn, E. Zscherpel, and F. Zocholl. *Laserphysik - Grundlagen und Anwendungen für Physiker, Maschinenbauer und Ingenieure*. ISBN: 978-3-642-32648-6. Springer-Verlag, 2012.

[38] F. K. Kneubühl and M. W. Sigrist. *Laser*. ISBN: 978-3-835-10145-6. Springer-Verlag, 2008.

[39] C. Danson, D. Hillier, N. Hopps, and D. Neely. Petawatt class lasers worldwide. *High Power Laser Sci. Eng.*, 3(E3), 2015.

[40] M. D. Perry, D. Pennington, B. C. Stuart, G. Tietbohl, J. A. Britten, C. Brown, S. Herman, B. Golick, M. Kartz, J. Miller, H. T. Powell, M. Vergino, and V. Yanovsky. Petawatt laser pulses. *Opt. Lett.*, 24(160), 1999.

[41] International Committee on Ultra-High Intensity Lasers. World map of ultrahigh intensity laser capabilities in 2020. *https://www.icuil.org/*, Accessed 03 November 2020.

[42] C. N. Danson, C. Haefner, J. Bromage, T. Butcher, J.-C. F. Chanteloup, E. A. Chowdhury, A. Galvanauskas, L. A. Gizzi, J. Hein, D. I. Hiller et al. Petawatt and exawatt class lasers worldwide. *High Power Laser Sci. Eng.*, 7(E54), 2019.

[43] M. Cerchez, R. Prasad, B. Aurand, A. L. Giesecke, S. Spickermann, S. Brauckmann, E. Aktan, M. Swantusch, M. Toncian, T. Toncian et al. ARCTURUS laser: a versatile high-contrast, high-power multi-beam laser system. *High Power Laser Sci. Eng.*, 7(E37), 2019.

[44] V. Bagnoud, B. Aurand, A. Blazevic, S. Borneis, C. Bruske, B. Ecker, U. Eisenbarth, J. Fils, A. Frank, E. Gaul, S. Goette, C. Haefner, T. Hahn, K. Harres, H. M. Heuck, D. Hochhaus, D. H. H. Hoffmann, D. Javorková, H. J. Kluge, T. Kuehl, S. Kunzer, M. Kreutz, T. Merz-Mantwill, P. Neumayer, E. Onkels, D. Reemts, O. Rosmej, M. Roth, T. Stoehlker, A. Tauschwitz, B. Zielbauer, D. Zimmer, and K. Witte. Commissioning and early experiments of the PHELIX facility. *Appl. Phys. B*, 100(137), 2010.

[45] F. Lureau, G. Matras, O. Chalus, C. Derycke, T. Morbieu, C. Radier, O. Casagrande, S. Laux, S. Ricaud, G. Rey et al. High-energy hybrid femtosecond laser system demonstrating 2×10 PW capability. *High Power Laser Sci. Eng.*, 8(E43), 2020.

[46] L. Yu, Y. Xu, S. Li, Y. Liu, J. Hu, F. Wu, X. Yang, Z. Zhang, Y. Wu, P. Bai, X. Wang, X. Lu, Y. Leng, R. Li, and Z. Xu. Investigation of the temporal contrast evolution in a 10-PW-level Ti:sapphire laser facility. *Opt. Express*, 27(8683), 2019.

[47] Z. Gan, L. Yu, S. Li, C. Wang, X. Liang, Y. Liu, S. Li, Z. Guo, Z. Fan, X. Yuan, L. Xu, Z. Liu, Y. Xu, J. Lu, H. Lu, D. Yin, Y. Leng, R. Li, and Z. Xu. 200 J high efficiency Ti:sapphire chirped pulse amplifier pumped by temporal dual-pulse. *Opt. Express*, 25(5169), 2017.

[48] W. Li, Z. Gan, L. Yu, C. Wang, Y. Liu, Z. Guo, L. Xu, M. Xu, Y. Hang, Y. Xu, J. Wang, P. Huang, H. Cao, B. Yao, X. Zhang, L. Chen, Y. Tang, S. Li, X. Liu, S. Li, M. He, D. Yin, X. Liang, Y. Leng, R. Li, and Z. Xu. 339 J high-energy Ti:sapphire chirped-pulse amplifier for 10 PW laser facility. *Opt. Lett.*, 43(5681), 2018.

[49] H. Zhang, B. Shen, W. Wang, S. Zhai, S. Li, X. Lu, J. Li, R. Xu, X. Wang, X. Liang, Y. Leng, R. Li, and Z. Xu. Collisionless Shock Acceleration of High-Flux Quasimonoenergetic Proton Beams Driven by Circularly Polarized Laser Pulses. *Phys. Rev. Lett.*, 119(164801), 2017.

[50] K. Nishikawa and M. Wakatani. *Basic Properties of Plasma*. Springer Berlin Heidelberg, ISBN: 978-3-662-04078-2, 2000.

[51] W. L. Kruer. *The physics of laser plasma interactions*. Westview Press, ISBN: 0813340837, 1988.

[52] P. Gibbon. *Short Pulse Laser Interactions with Matter: An Introduction*. Imperial College Press, ISBN: 978-1-86094-934-0, 2005.

[53] J. Meyer-ter Vehn, A. Pukhov, and Zh.-M. Sheng. *Relativistic Laser Plasma Interaction*. Springer US, ISBN: 978-1-4615-1351-3, 2001.

[54] T. Tajima and J. M. Dawson. Laser electron accelerator. *Phys. Rev. Lett.*, 43(267), 1979.

[55] J. Badziak. Laser-driven ion acceleration: methods, challenges and prospects. *J. Phys.: Conf. Ser.*, 959(012001), 2018.

[56] W. I. Linlor. Ion energies produced by laser giant pulse. *Appl. Phys. Lett.*, 3(210), 1963.

[57] D Lichtman and J. F. Ready. Laser beam induced electron emission. *Phys. Rev. Lett.*, 10(342), 1963.

[58] E. Clark, K. Krushelnick, J. Davies, M. Zepf, M. Tatarakis, F. Beg, A. Machacek, P. A. Norreys, M. I. K. Santala, I. I. Watts, and A. E. Dangor. Measurements of energetic proton transport through magnetized plasma from intense laser interactions with solids. *Phys. Rev. Lett.*, 84(670), 2000.

[59] A. Maksimchuk, S. Gu, K. Flippo, D. Umstadter, and V. Bychenkov. Forward ion acceleration in thin films driven by a high-intensity laser. *Phys. Rev. Lett.*, 84(4108), 2000.

[60] R. A. Snavely, M. Key, S. Hatchett, T. Cowan, M. Roth, T. Phillips, M. Stoyer, E. A. Henry, T. Sangster, M. Singh, S. Wilks, A. Mackinnon, A. Offenberger, D. Pennington, K. Yasuike, A. B. Langdon, B. Lasinski, J. Johnson, M. Perry, and M. Campbell. Intense high-energy proton beams from petawatt-laser irradiation of solids. *Phys. Rev. Lett.*, 85(2945), 2000.

[61] S. C. Wilks, A. B. Langdon, T. E. Cowan, M. Roth, M. Singh, S. Hatchett, M. H. Key, D. Pennington, A. MacKinnon, and R. A. Snavely. Energetic proton generation in ultra-intense laser–solid interactions. *Phys. Plasmas*, 8(542), 2001.

[62] J. Ferri, E. Siminos, and T. Fülöp. Enhanced target normal sheath acceleration using colliding laser pulses. *Commun. Phys.*, 2(40), 2019.

[63] P. Mora. Plasma expansion into a vacuum. *Phys. Rev. Lett.*, 90(185002), 2003.

[64] P. Mora. Collisionless expansion of a gaussian plasma into a vacuum. *Phys. Plasmas*, 12(112102), 2005.

[65] P. Mora. Thin-foil expansion into a vacuum. *Phys. Rev. E*, 72(056401), 2005.

[66] H. Schwoerer, S. Pfotenhauer, O. Jäckel, K.-U. Amthor, B. Liesfeld, W. Ziegler, R. Sauerbrey, K. W. D. Ledingham, and T. Esirkepov. Laser-plasma acceleration of quasi-monoenergetic protons from microstructured targets. *Nature*, 439(445), 2006.

[67] L. Willingale, S. P. D. Mangles, P. M. Nilson, R. J. Clarke, A. E. Dangor, M. C. Kaluza, S. Karsch, K. L. Lancaster, W. B. Mori, Z. Najmudin, J. Schreiber, A. G. R. Thomas, M. S. Wei, and K. Krushelnick. Collimated Multi-MeV Ion Beams from High-Intensity Laser Interactions with Underdense Plasma. *Phys. Rev. Lett.*, 96(245002), 2006.

[68] A. P. L. Robinson and P. Gibbon. Production of proton beams with narrow-band energy spectra from laser-irradiated ultrathin foils. *Phys. Rev. E*, 75(015401), 2007.

[69] P. McKenna, D. Neely, R. Bingham, and D. Jaroszynski. *Laser-Plasma Interactions and Applications*. Springer International Publishing, ISBN: 978-3-319-00037-4, 2013.

[70] I. Kostyukov, A. Pukhov, and S. Kiselev. Phenomenological theory of laser-plasma interaction in "bubble" regime. *Phys. Plasmas*, 11(5256), 2004.

[71] I. Kostyukov, E. Nerush, A. Pukhov, and V. Seredov. A multidimensional theory for electron trapping by a plasma wake generated in the bubble regime. *New J. Phys.*, 12(045009), 2010.

[72] B. Shen, Y. Li, M. Y. Yu, and J. Cary. Bubble regime for ion acceleration in a laser-driven plasma. *Phys. Rev. E*, 76(055402), 2007.

[73] B. Shen, X. Zhang, Z. Sheng, M. Y. Yu, and J. Cary. High-quality monoenergetic proton generation by sequential radiation pressure and bubble acceleration. *Phys. Rev. ST Accel. Beams*, 12(121301), 2009.

[74] S. V. Bulanov and T. Zh. Esirkepov. Comment on "Collimated Multi-MeV Ion Beams from High-Intensity Laser Interactions with Underdense Plasma". *Phys. Rev. Lett.*, 98(049503), 2007.

[75] T. Nakamura and K. Mima. Magnetic-Dipole Vortex Generation by Propagation of Ultraintense and Ultrashort Laser Pulses in Moderate-Density Plasmas. *Phys. Rev. Lett.*, 100(205006), 2008.

[76] A. Sharma. High energy electron and proton acceleration by circularly polarized laser pulse from near critical density hydrogen gas target. *Sci. Rep.*, 8(2191), 2018.

[77] T. Nakamura, S. V. Bulanov, T. Zh. Esirkepov, and M. Kando. High-energy ions from near-critical density plasmas via magnetic vortex acceleration. *Phys. Rev. Lett.*, 105(135002), 2010.

[78] S. V. Bulanov, D. V. Dylov, T. Zh. Esirkepov, F. F. Kamenets, and D. V. Sokolov. Ion acceleration in a dipole vortex in a laser plasma corona. *Plasma Phys. Rep.*, 31(369), 2005.

[79] W. Gerlach and O. Stern. Der experimentelle Nachweis der Richtungsquantelung im Magnetfeld. *Zeitschrift für Physik*, 9(349), 1922.

[80] S. Goudsmit and K. Uhlenbeck. Ersetzung der Hypothese vom unmechanischen Zwang durch eine Forderung bezüglich des inneren Verhaltens jedes einzelnen Elektrons. *Naturwiss.*, 54(593), 1925.

[81] C. Doran, D. Hestenes, F. Sommen, and N. Van Acker. Lie groups as spin groups. *J. Math. Phys.*, 34(3642), 1993.

[82] W. Pauli. Zur Quantenmechanik des magnetischen Elektrons. *Z. Physik*, 43(601), 1927.

[83] P. S. Farago. Electron spin polarization. *Rep. Prog. Phys.*, 34(1055), 1971.

[84] W. Nolting. *Grundkurs Theoretische Physik 5/2*. Springer Spektrum, ISBN: 978-3-662-44229-6, 2015.

[85] S. R. Mane, Yu M. Shatunov, and K. Yokoya. Spin-polarized charged particle beams in high-energy accelerators. *Rep. Prog. Phys.*, 68(1997), 2005.

[86] S. P. Flood and D. A. Burton. Stern-Gerlach surfing in laser wakefield accelerators. *Phys. Lett. A*, 379(1966), 2015.

[87] Y.-F. Li, R. Shaisultanov, K. Z. Hatsagortsyan, F. Wan, C. H. Keitel, and J.-X. Li. Ultrarelativistic electron-beam polarization in single-shot interaction with an ultraintense laser pulse. *Phys. Rev. Lett.*, 122(154801), 2019.

[88] L. H. Thomas. The kinematics of an electron with an axis. *The London, Edinburgh, and Dublin Philosophical Magazine and Journal of Science*, 3(13), 1927.

[89] L. L. Foldy and S. A. Wouthuysen. On the Dirac Theory of Spin 1/2 Particles and Its Non-Relativistic Limit. *Phys. Rev.*, 78(29), 1950.

[90] S. I. Rubinow and J. B. Keller. Asymptotic Solution of the Dirac Equation. *Phys. Rev.*, 131(2789), 1963.

[91] V. N. Baier and V. M. Katkov. Processes involved in the motion of high energy particles in a magnetic field. *J. Exp. Theor. Phys.*, 26(4), 1968.

[92] P. Ehrenfest. Bemerkung über die angenäherte Gültigkeit der klassischen Mechanik innerhalb der Quantenmechanik. *Z. Physik*, 45(455), 1927.

[93] F. Bloch. Nuclear induction. *Phys. Rev.*, 70(460), 1946.

[94] V. Bargmann, L. Michel, and V. L. Telegdi. Precession of the polarization of particles moving in a homogeneous electromagnetic field. *Phys. Rev. Lett.*, 2(10), 1959.

[95] T. Fukuyama and A. J. Silenko. Derivation of Generalized Thomas-Bargmann-Michel-Telegdi Equation for a Particle with Electric Dipole Moment. *Int. J. Mod. Phys. A*, 28(1350147), 2013.

[96] A. J. Silenko. Spin precession of a particle with an electric dipole moment: contributions from classical electrodynamics and from the thomas effect. *Phys. Scr.*, 90(6), 2015.

[97] I. M. Ternov, Y. M. Loskutov, and L. I. Korovina. Possibility of polarization of an electron beam due to relativistic radiation in a magnetic field. *Sov. Phys. - JETP*, 14(921), 1962.

[98] A. A. Sokolov and I. M. Ternov. On polarization and spin effects in the theory of synchrotron radiation. *Sov.Phys.Dokl.*, 8(12), 1964.

[99] A. A. Sokolov, D. V. Gel'tsov, and M. M. Kolesnikova. Exact derivation of the synchrotron-radiation equation. *Russ. Phys. J.*, 14(4), 1971.

[100] D. Potaux and et al. (Orsay Storage Ring Group). Status report on ACO. *Proc. 8th Int. Conf. on High-Energy Accelerators (CERN)*, 1971.

[101] V. N. Baer. Radiative polarization of electrons in storage rings. *Sov. Phys. Usp.*, 14(695), 1972.

[102] U. Camerini, D. Cline, J. Learned, A. K. Mann, and L. K. Resvanis. Measurement of the radiative electron polarization in a 2.4-GeV storage ring. *Phys. Rev. D*, 12(1855), 1975.

[103] W. W. MacKay, J. F. Hassard, R. T. Giles, M. Hempstead, K. Kinoshita, F. M. Pipkin, Richard Wilson, and L. N. Hand. Measurement of the Υ mass. *Phys. Rev. D*, 29(11), 1984.

[104] D. P. Barber. A review of polarized electron and positron beams. *Proceedings of the 2nd European Particle Accelerator Conference (EPAC 90)*, 1, 1990.

[105] R. Assmann and J. P. Koutchouk. Spin tune shifts due to optics imperfections. *Divisional report CERN SL/94-13AP*, 1994.

[106] C. Steier, W. V. Drachenfels, F. Frommberger, M. Hoffmann, D. Husmann, J. Keil, S. Nakamura, and T. Nakanishi. Crossing intrinsic depolarizing resonances in ELSA with pulsed betatron tune jump quadrupoles. *Proc. 1997 Particle Accelerator Conf. (Vancouver) (Piscataway, NJ: IEEE)*, 5(3098), 1999.

[107] C. W. Leemann, D. R. Douglas, and G. A. Krafft. The continuous electron beam accelerator facility: CEBAF at the Jefferson Laboratory. *Ann. Rev. Nucl. Part. Sci.*, 51(1), 2001.

[108] R. Engels. Entwicklung eines universellen Lambshift-Polarimeters für polarisierte Atomstrahl-Targets wie an ANKE/COSY. *PhD thesis, Universität zu Köln*, 2002.

[109] W. E. Lamb and R. C. Retherford. Fine Structure of the Hydrogen Atom by a Microwave Method. *Phys. Rev.*, 72(241), 1947.

[110] J. N. Eckstein, A. I. Ferguson, and T. W. Hänsch. High-Resolution Two-Photon Spectroscopy with Picosecond Light Pulses. *Phys. Rev. Lett.*, 40(847), 1978.

[111] R. Engels, R. Emmerich, J. Ley, G. Tenckhoff, H. Paetz gen. Schieck, M. Mikirtytchiants, F. Rathmann, H. Seyfarth, and A. Vassiliev. Precision Lamb-shift polarimeter for polarized atomic and ion beams. *Rev. Sc. Instrum.*, 74(4607), 2003.

[112] R. Engels, R. Emmerich, K. Grigoryev, H. Schieck gen. Paetz, J. Ley, M. Mikirtychyants, F. Rathmann, J. Sarkadi, H. Seyfarth, G. Tenckhoff, and A. Vasilyev. Background reduction by a getter pump around the ionization volume of a Lamb-shift polarimeter and possible improvements of polarized ion sources. *Rev. Sc. Instrum.*, 76(053305), 2005.

[113] R. Engels, R. Gorski, K. Grigoryev, M. Mikirtychyants, F. Rathmann, H. Seyfarth, H. Ströher, P. Weiss, L. Kochenda, P. Kravtsov, V. Trofimov, N. Tschernov, A. Vasilyev, M. Vznuzdaev, and H Paetz gen. Schieck. Measurement of the nuclear polarization of hydrogen and deuterium molecules using a Lamb-shift polarimeter. *Rev. Sci. Instrum.*, 85(103505), 2014.

[114] H. F. Glavish. A strong field ionizer for an atomic beam polarized ion source. *Nucl. Instr. Meth.*, 65(1), 1968.

[115] W. Wien. Untersuchungen über die electrische Entladung in verdünnten Gasen. *Ann. Phys.*, 301(440), 1898.

[116] P. Pradel, F. Roussel, A. S. Schlachter, G. Spiess, and A. Valance. Formation of $H(n = 2)$ atoms by the nearly resonant process H^+ in Cs. Multiple collision processes. *Phys. Rev. A*, 10(797), 1974.

[117] J. L. McKibben, G. P. Lawrence, and G. G. Ohlsen. Nuclear spin filter. *Phys. Rev. Lett.*, 20(1180), 1968.

[118] M. Mikirtychyants, R. Engels, K. Grigoryev, A. Vasilyev, D. Chiladze, A. Kacharava, S. Mikirtychyants, F. Rathmann, J. Sarkadi, R. Schleichert, H. Seyfarth, H. Stroeher, D. Prasuhn, B. Lorentz, S. Barsov, and S. Dymov. First experiments with the polarized internal gas target at ANKE/COSY. *J. Phys.: Conf. Ser.*, 295(012148), 2011.

[119] T. D. Arber, K. Bennett, C. S. Brady, A. Lawrence-Douglas, M. G. Ramsay, N. J. Sircombe, P. Gillies, R. G. Evans, H. Schmitz, A. R. Bell, and C. P. Ridgers. Contemporary particle-in-cell approach to laser-plasma modelling. *Plasma Phys. Control. Fusion*, 57(113001), 2015.

[120] Y. Wu, L. Ji, X. Geng, Q. Yu, N. Wang, B. Feng, Z. Guo, W. Wang, C. Qin, X. Yan, L. Zhang, J. Thomas, A. Hützen, M. Büscher, T. P. Rakitzis, A. Pukhov, B. Shen, and R. Li. Polarized electron-beam acceleration driven by vortex laser pulses. *New J. Phys.*, 21(073052), 2019.

[121] M. Wen, M. Tamburini, and C. H. Keitel. Polarized laser-wakefield-accelerated kiloampere electron beams. *Phys. Rev. Lett.*, 122(214801), 2019.

[122] P. Mora and T. M. Antonsen, Jr. Kinetic modeling of intense, short laser pulses propagating in tenuous plasmas. *Phys. Plasmas*, 4(217), 1997.

[123] Y. S. Derbenev and A. M. Kondratenko. Polarization kinetics of particles in storage rings. *Zh. Eksp. Tear. Fiz.*, 64(1918), 1973.

[124] J. D. Jackson. On understanding spin-flip synchrotron radiation and the transverse polarization of electrons in storage rings. *Rev. Mod. Phys.*, 48(417), 1976.

[125] S. R. Mane. Electron-spin polarization in high-energy storage rings. I. Derivation of the equilibrium polarization. *Phys. Rev. A*, 36(105), 1987.

[126] J. Schwinger. On the classical radiation of accelerated electrons. *Phys. Rev.*, 75(1912), 1949.

[127] V. N. Baier and V. M. Katkov. Radiative polarization of electrons in a magnetic field. *Sov. Phys. - JETP*, 25(944), 1966.

[128] X. Geng, L. Ji, B. Shen, B. Feng, Z. Guo, Q. Han, C. Qin, N. Wang, W. Wang, Y. Wu, X. Yan, Q. Yu, L. Zhang, and Z. Xu. Spin-dependent radiative deflection in the quantum radiation-reaction regime. *New J. Phys.*, 22(013007), 2020.

[129] X. Geng, Z. Bu, Y. Wu, Q. Han, C. Qin, W. Wang, X. Yan, L. Zhang, B. Shen, and L. Ji. Generalizing the Sokolov-Ternov effect for radiative polarization in intense laser fields. arXiv:1912.03625v2 [physics.plasm-ph], 2020.

[130] A. Di Piazza, K. Z. Hatsagortsyan, and C. H. Keitel. Quantum Radiation Reaction Effects in Multiphoton Compton Scattering. *Phys. Rev. Lett.*, 105(220403), 2010.

[131] C. P. Ridgers, J. G. Kirk, R. Duclous, T. G. Blackburn, C. S. Brady, K. Bennett, T. D. Arber, and A. R. Bell. Modelling gamma-ray photon emission and pair production in high-intensity laser–matter interactions. *J. Comput. Phys.*, 260(273), 2014.

[132] D. L. Burke, R. C. Field, G. Horton-Smith, J. E. Spencer, D. Walz, S. C. Berridge, W. M. Bugg, K. Shmakov, A. W. Weidemann, C. Bula, K. T. McDonald, E. J. Prebys, C. Bamber, S. J. Boege, T. Koffas, T. Kotseroglou, A. C. Melissinos, D. D. Meyerhofer, D. A. Reis, and W. Ragg. Positron Production in Multiphoton Light-by-Light Scattering. *Phys. Rev. Lett.*, 79(1626), 1997.

[133] D. Del Sorbo, D. Seipt, T. G. Blackburn, A. G. R. Thomas, C. D. Murphy, J. G. Kirk, and C. P. Ridgers. Spin polarization of electrons by ultraintense lasers. *Phys. Rev. A*, 96(043407), 2017.

[134] D. Seipt, D. Del Sorbo, C. P. Ridgers, and A. G. R. Thomas. Theory of radiative electron polarization in strong laser fields. *Phys. Rev. A*, 98(023417), 2018.

[135] D. Seipt, D. Del Sorbo, C. P. Ridgers, and A. G. R. Thomas. Ultrafast polarization of an electron beam in an intense bichromatic laser field. *Phys. Rev. A*, 100(061402(R)), 2019.

[136] G. L. Kotkin, V. G. Serbo, and V. I. Telnov. Electron (positron) beam polarization by Compton scattering on circularly polarized laser photons. *Phys. Rev. ST Accel. Beams*, 6(011001), 2003.

[137] W. Pauli and S. Flügge. *Handbuch der Physik: Band V., Prinzipien der Quantentheorie I.* Springer Berlin, 1958.

[138] B. M. Garraway and S. Stenholm. Observing the spin of a free electron. *Phys. Rev. A*, 60(63), 1999.

[139] A. A. Pomeranskii and I. B. Khriplovich. Equations of motion of a spinning relativistic particle in external fields. *J. Exp. Theor. Phys.*, 86(839), 1998.

[140] C. Huang, W. An, V. K. Decyk, W. Lu, W. B. Mori, F. S. Tsung, M. Tzoufras, S. Morshed, T. Antonsen, B. Feng, T. Katsouleas, R. A. Fonseca, S. F. Martins, J. Vieira, L. O. Silva, E. Esarey, C. G. R. Geddes, W. P. Leemans, E. Cormier-Michel, J.-L. Vay, D. L. Bruhwiler, B. Cowan, J. R. Cary, and K. Paul. Recent results and future challenges for large scale particle-in-cell simulations of plasma-based accelerator concepts. *J. Phys.: Conf. Ser.*, 180(012005), 2009.

[141] J.-L. Vay. Simulation of plasma accelerators with the particle-in-cell method. arXiv:2008.07300 [physics.comp-ph], 2020.

[142] J. D. Jackson. *Classical Electrodynamics*. Wiley, New York, ISBN: 978-0-47-143132-9, 1975.

[143] A. Pukhov. Particle-in-cell codes for plasma-based particle acceleration. *Proceedings of the CAS-CERN Accelerator School: Plasma Wake Acceleration*, 1(181), 2016.

[144] J. P. Boris. Relativistic plasma simulation-optimization of a hybrid code. In *Proceeding of Fourth Conference on Numerical Simulations of Plasmas*, 1970.

[145] A. Pukhov. Three-dimensional electromagnetic relativistic particle-in-cell code VLPL (Virtual Laser Plasma Lab). *J. Plasma Phys.*, 61(3), 1999.

[146] A. Pukhov. High Performance 3D PIC Code VLPL: Virtual Laser Plasma Lab. *MPQ-Report*, 2019.

[147] K. Yee. Numerical solution of initial boundary value problems involving Maxwell's equations in isotropic media. *IEEE Transactions on Antennas and Propagation*, 14(302), 1966.

[148] L. Reichwein, A. Hützen, M. Büscher, and A. Pukhov. On the robustness of spin polarization for magnetic vortex accelerated proton bunches in density down-ramps. *Plasma Phys. Control. Fusion*, 63(085011), 2021.

[149] X. Li, P. Gibbon, A. Hützen, M. Büscher, S. Weng, M. Chen, and Z. Sheng. Polarized proton acceleration in ultraintense laser interaction with near-critical-density plasmas. *Phys. Rev. E*, 104(015216), 2021.

[150] Y. Wu, L. Ji, X. Geng, Q. Yu, N. Wang, B. Feng, Z. Guo, W. Wang, C. Qin, X. Yan, L. Zhang, J. Thomas, A. Hützen, A. Pukhov, M. Büscher, B. Shen, and R. Li. Polarized electron acceleration in beam-driven plasma wakefield based on density down-ramp injection. *Phys. Rev. E*, 100(043202), 2019.

[151] Y. Wu, L. Ji, X. Geng, J. Thomas, M. Büscher, A. Pukhov, A. Hützen, L. Zhang, B. Shen, and R. Li. Spin filter for polarized electron acceleration in plasma wakefields. *Phys. Rev. Applied*, 13(044064), 2020.

[152] Jülich Supercomputing Centre (JSC) Forschungszentrum Jülich. JURECA: General-purpose supercomputer at Jülich Supercomputing Centre. *JLSRF*, 2(A62), 2016.

[153] K. I. Popov, W. Rozmus, V. Y. Bychenkov, N. Naseri, C. E. Capjack, and A. V. Brantov. Ion Response to Relativistic Electron Bunches in the Blowout Regime of Laser-Plasma Accelerators. *Phys. Rev. Lett.*, 105(195002), 2010.

[154] L. L. Ji, A. Pukhov, I. Y. Kostyukov, B. F. Shen, and K. Akli. Radiation-Reaction Trapping of Electrons in Extreme Laser Fields. *Phys. Rev. Lett.*, 112(145003), 2014.

[155] F. Sylla, A. Flacco, S. Kahaly, M. Veltcheva, A. Lifschitz, G. Sanchez-Arriaga, E. Lefebvre, and V. Malka. Anticorrelation between Ion Acceleration and Nonlinear Coherent Structures from Laser-Underdense Plasma Interaction. *Phys. Rev. Lett.*, 108(115003), 2012.

[156] K. Strathmann. Vermessung von Gasjetsmittels Interferometrie. *Bachelor thesis, HS Emden-Leer*, 2016.

[157] C. D. Keith, J. Brock, C. Carlin, S. A. Comer, D. Kashy, J. McAndrew, D. G. Meekins, E. Pasyuk, J. J. Pierce, and M. L. Seely. The Jefferson Lab Frozen Spin Target. *Nucl. Instrum. Methods. Phys. Res. A*, 684(27), 2012.

[158] I. Engin, M. Büscher, O. Deppert, L. Di Lucchio, R. Engels, S. Frydrych, P. Gibbon, A. Kleinschmidt, A. Lehrach, M. Roth, F. Schlüter, K. Strathmann, and F. Wagner. Towards a Laser-driven polarized ^{3}He ion-beam source. *PoS Proc. Sci.*, PSTP 2015(002), 2015.

[159] H. Soltner, M. Büscher, P. Burgmer, I. Engin, B. Nauschütt, S. Maier, and H. Glückler. A Permanent-Magnet Array to Maintain ^{3}He Gas Polarization Inside a Glass Vessel for Applications in High-Energy Laser Physics. *IEEE Transactions on Applied Superconductivity*, 36(1), 2016.

[160] R. Engels, H. M. Awwad, K. Grigoryev, L. Huxold, M. Martic, A. Rolofs, W. Sartison, H. Ströher, M. Büscher, A. Vasilyev, L. Kochenda, P. Kravtsov, V. Trofimov, and M. Vznudaev. Production and Storage of Polarized H_2, D_2 and HD Molecules. *Proc. 23rd International Spin PhysicsSymposium (SPIN2018)*, 033, 2018.

[161] T. P. Rakitzis, P. C. Samartzis, R. L. Toomes, L. Tsigaridas, M. Coriou, D. Chestakov, A. T. J. B. Eppink, D. H. Parker, and T. N. Kitsopoulos. Photofragment alignment from the photodissociation of HCl and HBr. *Chem. Phys. Lett*, 364(1), 2002.

[162] T. P. Rakitzis and T. N. Kitsopoulos. Measurement of Cl and Br photofragment alignment using slice imaging. *J. Chem. Phys.*, 116(9228), 2002.

[163] T. P. Rakitzis, P. C. Samartzis, R. L. Toomes, T. N. Kitsopoulos, Alex Brown, G. G. Balint-Kurti, O. S. Vasyutinskii, and J. A. Beswick. Spin-Polarized Hydrogen Atoms from Molecular Photodissociation. *Science*, 300(5627), 2003.

[164] T. P. Rakitzis. Pulsed-Laser Production and Detection of Spin-Polarized Hydrogen Atoms. *ChemPhysChem*, 5(1489), 2004.

[165] D. Sofikitis, L. Rubio-Lago, M. R. Martin, D. J. Brown Ankeny, N. C.-M. Bartlett, R. N. Zare, and T. P. Rakitzis. Preparation of highly polarized nuclei: Observation and control of time-dependent polarization transfer from $H^{35}Cl$ molecular rotation to ^{35}Cl nuclear spin. *Phys. Rev. A*, 76(012503), 2007.

[166] D. Sofikitis, L. Rubio-Lago, L. Bougas, A. J. Alexander, and T. P. Rakitzis. Laser detection of spin-polarized hydrogen from HCl and HBr photodissociation: Comparison of H- and halogen-atom polarizations. *J. Chem. Phys.*, 129(144302), 2008.

[167] A. T. J. B. Eppink, D. H. Parker, M. H. M. Janssen, B. Buijsse, and W. J. van der Zande. Production of maximally aligned O(1D) atoms from two-step photodissociation of molecular oxygen. *J. Chem. Phys.*, 108(1305), 1998.

[168] D. A. Chestakov, D. H. Parker, K. V. Vidma, and T. P. Rakitzis. Photofragment alignment in the photodissociation of I_2 from 450 to 510 nm. *J. Chem. Phys.*, 124(024315), 2006.

[169] R. J. Van Brunt and R. N. Zare. Polarization of Atomic Fluorescence Excited by Molecular Dissociation. *J. Chem. Phys.*, 48(4304), 1968.

[170] O. S. Vasyutinskii. Contribution to the theory of the effect of orientation of atoms produced in photodissociation of molecules. *Sov. Phys. JETP*, 54(855), 1981.

[171] D. Sofikitis, P. Glodic, G. Koumarianou, H. Jiang, L. Bougas, P. C. Samartzis, A. Andreev, and T. P. Rakitzis. Highly Nuclear-Spin-Polarized Deuterium Atoms from the UV Photodissociation of Deuterium Iodide. *Phys. Rev. Lett.*, 118(233401), 2017.

[172] D. Sofikitis, C. S. Kannis, G. K. Boulogiannis, and T. P. Rakitzis. Ultrahigh-Density Spin-Polarized H and D Observed via Magnetization Quantum Beats. *Phys. Rev. Lett.*, 121(083001), 2018.

[173] B. Friedrich and D. Herschbach. Polarization of Molecules Induced by Intense Nonresonant Laser Fields. *J. Chem. Phys*, 99(15686), 1995.

[174] B. Friedrich and D. Herschbach. Manipulating Molecules via Combined Static and Laser Fields. *J. Phys. Chem. A*, 103(10280), 1999.

[175] EKSPLA. SL330 series - SBS Compressed Picosecond Nd:YAG Lasers. *https://ekspla.com/wp-content/uploads/Product/Nanosecond-Lasers/SL330/SL330-datasheet-20181107.pdf*, Accessed 16 September 2020.

[176] D. W. Forslund, J. M. Kindel, and E. L. Lindman. Theory of stimulated scattering processes in laser-irradiated plasmas. *Phys. Fluids*, 18(1002), 1975.

[177] Germany Max-Planck Institute for Chemistry Mainz. Absorption cross sections of hygrogen bromide HBr at room temperature. *http://joseba.mpch-mainz.mpg.de/spectral_atlas_data/cross_sections_plots/Hydrogen%20halides/HBr_139-286nm_log.jpg*, Accessed 08 August 2020.

[178] H. Keller-Rudek, G. K. Moortgat, R. Sander, and R. Sörensen. The MPI-Mainz UV/VIS Spectral Atlas of Gaseous Molecules of Atmospheric Interest. *Earth Syst. Sci. Data*, 5(365), 2013.

[179] G. Scoles, D. Bassi, U. Buck, and D. C. Laine. *Atomic and Molecular Beam Methods: Vol. 1.* New York: Oxford University Press, ISBN: 978-0195042801, 1988.

[180] F. B. Dunning and R. G. Hulet. *Atomic, Molecular, and Optical Physics: Atoms and Molecules: Volume 29B.* Elsevier Science, ISBN: 978-0-124-75976-3, 1996.

[181] H. Pauly. *Atom, Molecule, and Cluster Beams I.* Springer-Verlag Berlin Heidelberg, ISBN: 978-3-540-66945-6, 2000.

[182] P. L. Owen and C. K. Thornhill. Aeronaut. Research Council (U.K.). *Rept. Mem.*, 2616, 1948.

[183] H. Ashkenas and F. S. Sherman. *Rarefied Gas Dynamics.* Academic Press, ISBN: 978-0-1200-2075-1, 1966.

[184] K. L. Saenger. Pulsed molecular beams: A lower limit on pulse duration for fully developed supersonic expansions. *J. Chem. Phys.*, 75(2467), 1981.

[185] A. Nass and E. Steffens. Direct simulation of low-pressure supersonic gas expansions and its experimental verification. *Nucl. Instrum. Methods Phys. Res. A*, 598(653), 2009.

[186] B. Broderick, V. Chernyak, A. Smolin, O. Vasyutinskii, and A. Suits. Imaging detection of spin-polarized hydrogen atoms. *Chem. Phys. Lett.*, 635(350), 2015.

[187] R. Sharma, R. Kumar, and S. P. Sharma. Absolute ionization cross sections of hydrogen bromide by electron impact. *AIP Conference Proceedings*, 2220(130024), 2020.

[188] Sirah Lasertechnik GmbH. Cobra-Stretch Dye Laser. *http://www.sirah.com/laser/pulsed-lasers/cobra-stretch*, Accessed 29 December 2020.

[189] Sirah Lasertechnik GmbH. Boston 500. *http://www.sirah.com/laser/pulsed-lasers/boston-500*, Accessed 29 December 2020.

Acknowledgment

I wish to express my sincere thanks and appreciation to everyone who made this work possible and who accompanied me during the time of my doctorate. In particular, I am deeply grateful to:

Prof. Dr. **Markus Büscher** for giving me the opportunity to write my PhD thesis at PGI-6, which provided an excellent environment for my research. Thank you for personally supporting and supervising my project as first reviewer. I truly thank you for giving me your fullest trust and valuing my scientific abilities. At the same time, I profoundly appreciate you always having an open door for me. You have constantly motivated me and made it possible for me to develop further by participating in numerous conferences as well as in collaboration meetings in Shanghai and on Crete, as lecturer and group leader at the Hadron Physics Summer School 2018, as tutor for the nuclear and particle physics lecture at the Heinrich Heine University Düsseldorf (HHUD) or as supervisor of students – I have really learned for life.

Prof. Dr. **Axel Görlitz** for becoming the second reviewer of this thesis and also my dedicated mentor at Heinrich Heine University Düsseldorf (HHUD). Thank you for being available as a personal contact throughout my studies. Not least due to your advertisement for studying (medical) physics in the context of the award of the Dr. Hans Riegel Fachpreis 2011, I have taken this great path.

Prof. Dr. **Sebastian M. Schmidt** for the privilege of preparing my doctoral thesis in the PGI and the IKP as a member of your board doctoral program.

Prof. Dr. **Andreas Lehrach**, thank you for being my second supervisor at FZJ. For all questions concerning accelerator physics you were my first contact person. You always encouraged me, especially when presenting our research results on the big stage during the annual MT meetings. Due to the important exchange with you I have gained a lot of experience – not only in scientific respects.

Prof. Dr. **Paul Gibbon** for the mentoring concerning theoretical questions in laser-plasma as well as computational physics. Especially towards the end of my PhD thesis you were an important advisor for the interpretation of my simulation results. During our numerous discussions you shared your huge expertise with me and, thus, contributed to the success of this work. Many thanks for that.

Dr. **Ralf Engels** for not only letting me transform your nuclear physics lab into half a laser lab, but especially for your excellent supervision during the experimental realization of the polarized proton target. You taught me the important tricks in the lab, and had always time to answer my open questions in a patient way. With you there is always enthusiasm for new ideas and a positive mood, at least as long as we are not discussing world politics or healthy diet.

Valantis Kannis and **Lukas Huxold** for the many hours together in the lab, where we laughed a lot besides searching for *the* peak. I am sure all three of us are now experts in vacuum chamber venting. Thank you Valantis for your support in evaluating the experimental results, thank you Lukas for loosening one or the other screw that was too tight for me.

Prof. Dr. **Claus M. Schneider** (PGI-6), Prof. Dr. **Hans Ströhner** (IKP-2) and Dr. **Ralf Gebel** (IKP-4) for providing the resources and for being open to new research topics as heads of your respective institutes. Thank you for enabling me to do my work in three different institutes and, thus, to combine nuclear physics with laser-plasma physics, which contributed to the success of this work.

Prof. Dr. **Alexander Pukhov**, Dr. **Johannes Thomas**, **Lars Reichwein** for always having an open door in the TP1 for a Jülich experimental physicist concerning questions around theoretical laser-plasma physics and the VLPL code. Special thanks to Prof. Dr. Alexander Pukhov for implementing the spin dynamics in your VLPL code, the first PIC code with this feature, making a decisive contribution for obtaining the presented simulation results. Another very special thank you goes to you, Johannes. You have always guided and mentored me since the beginning of my Bachelor studies. Thank you for sharing your knowledge in countless discussions and thank you for your patience with me during the evaluation of the simulation results. Besides our many hours together in your office, be it because of the simulations or because of the preparation for the nuclear and particle physics exercise group, also our culinary experiences in China remain unforgotten. Thank you Lars, for helping me towards the end of a PhD time to analyze the simulation results, and for helping me to defeat Python over and over again.

Prof. Dr. **T. Peter Rakitzis** for always being available for me and taking the time to answer my many questions in detail. Thank you also for keeping an eye on our experimental developments from remote Crete and for your expertise. Thanks Prof. Dr. **Dimitris Sofikitis** for your visit to FZJ, which helped me understand a lot about the photo-dissociation process by hands on.

Prof. Dr. **Ruxin Li** for welcoming me as the dean of SIOM already four times in Shanghai, for giving me the opportunity to work with his wonderful team and to gain important experience in the field of laser-driven particle acceleration. Thanks to our constant scientific exchange, Prof. Dr. **Baifei Shen**, Prof. Dr. **Liangliang Ji**, Dr. **Jiancai Xu**, Dr. **Lingang Zhang**, **Yitong Wu** and **Xuesong Geng**, and our good collaboration, from which many joint publications have resulted, I have decisively broadened my horizons, both scientifically and culturally. Further thanks to Dr. **Meng Wen** from Hubei University for pushing forward the polarized laser-induced proton acceleration in our joint paper.

The whole ***Ju*SPARC group** for the revealing discussions, feedbacks and helpful solution approaches in our weekly group meetings. Besides the scientific exchange, personally or later virtually due to COVID-19, there was also time for a chat, which undoubtedly contributed to the good mood in our group.

The whole team of the **Scientific IT Systems (PGI/JCNS-TA)** for greatly solving any computer issues, fixing every bug and implementing all requested features even after normal business hours. Thank you.

Dr. **Olaf Felden** who always kept an eye on the safety regulations for us and made the operation of the experiment possible. I thank Dr. **Andreas Nass** for your open ear during short discussions in the corridor and your large treasure of spare parts, which we were allowed to help ourselves. Dr. **Thomas Sefzick**, I appreciate that you have always been available with your support for all electronic questions. Many thanks to **Guido D'Orsaneo** who more or less voluntarily slipped into the heavy breathing equipment for every gas bottle change. I further thank the whole teams of the **technical constructions and mechanical workshops at the PGI and the IKP** for always finding quick solutions for technical problems and mastering all corresponding challenges. Without them, the development and commissioning of the experiment would have been impossible.

Sarah Heidtfeld and **Bharti Parashar** for our time together in the first women's office in PGI-6 until COVID-19 separated us. I thank you for the friendly atmosphere and the nice conversations in between, where physics was not always the number one topic.

Frank Hartmann for taking the time to read through my work during your Christmas vacation and – hopefully – catching every mistake.

My final, special thanks go to **my family** and **friends** for the invaluable support, constructive criticism and nerves you have invested in me. Thank you **Sebastian** for your encouragement and patience and for dragging me off the desk at the right moments. I could not have achieved this goal without you. Thank you dear ones – for everything.

Appendix

A Supplementary information for Fig. 3.2

Year	1st Author	Source	Lab	Laser Parameters					Max. Proton Energy (MeV)
				Laser	Pulse duration (fs)	Intensity (W/cm^2)	Fluence I*tp (J/cm^2)	Wavelength (µm)	Energy (J)	
2000	Snaveley	https://doi.org/10.1103/PhysRevLett.85.2945	LLNL	NOVA PW	500	3,0E+20	1,5E+08	1,064	500	58
2000	Clark	https://doi.org/10.1103/PhysRevLett.84.670	RAL-CLF	VULCAN	1000	5,0E+19	5,0E+07	1,064	50	30
2000	Hatchett	https://doi.org/10.1063/1.874030	LLNL		500	3,0E+20	1,5E+08	1,064		55
2001	Zepf	https://aip.scitation.org/doi/pdf/10.1063/1.1351824	RAL-CLF	VULCAN PW	1200	1,0E+20	1,2E+08	1,064	90	40
2001	Murakami	https://doi.org/10.1063/1.1390333	OSAKA,	GEKKO MII	450	5,5E+18	2,5E+06	1,064	25	10
2002	Mackinnon	https://doi.org/10.1103/PhysRevLett.88.215006	LLNL	Jan USP	100	1,0E+20	1,0E+07	0,8	10	24
2003	Fritzler	https://doi.org/10.1063/1.1616661	LOA		40	6,0E+19	2,4E+06	0,8	0,84	10
2003	Spencer	https://doi.org/10.1103/PhysRevE.67.046402	RAL-CLF	ASTRA	60	7,0E+18	4,2E+05	0,8	0,2	1,5
2004	McKenna	https://doi.org/10.1103/PhysRevE.70.036405	RAL-CLF	VULCAN PW	700	2,0E+20	1,4E+08	1,064	400	44
2004	Maksimchuk	https://doi.org/10.1134/1.1768582	Michigan	CUOS	400	5,0E+19	2,0E+07	0,8	5	12
2005	Fuchs	https://doi.org/10.1103/PhysRevLett.94.045004	LULI	LULI 100 TW	320	6,0E+19	1,9E+07	1,064	30	20
2006	Robson	https://doi.org/10.1038/nphys476	RAL-CLF	VULCAN PW	1000	6,0E+20	6,0E+08	1,064	400	60
2006	Schwoerer	https://doi.org/10.1038/nature04492	U. Jena	JETI	80	3,0E+19	2,4E+06	0,8	0,6	1,2
2006	Neely	https://doi.org/10.1063/1.2220011	U. Lund		33	1,0E+19	3,3E+05	0,8		4
2008	Flippo	https://doi.org/10.1063/1.2987678	LANL		500	4,0E+19	2,0E+07	1,054	100	50
2008	Ceccotti	https://doi.org/10.1088/0741-3335/50/12/124006	CEA-Saclay	UHI	65	5,0E+18	3,3E+05	0,8		5,5
2008	Nishiuchi	https://doi.org/10.1063/1.2928161	KYOTO		34	3,0E+19	1,0E+06	0,8		4
2009	Antici	https://doi.org/10.1088/1367-2630/11/2/023038	LULI	LULI 100 TW	320	1,0E+19	3,2E+06	1,064		12
2009	Gaillard	http://meetings.aps.org/Meeting/DPP10/Session/NI3.4	LANL	Trident	600	2,0E+20	1,2E+08	1,054	80	65
2012	Haberberger	https://doi.org/10.1038/nphys2130	UCLA	Neptune	100000	6,0E+16	6,0E+06	10	60	20
2012	Ogura	https://doi.org/10.1364/OL.37.002868	KYOTO		40	1,0E+21	4,0E+07	0,8	10	40
2013	Green	https://doi.org/10.1063/1.4879641	RAL-CLF	GEMINI	50	5,0E+20	2,5E+07	0,8	30	30
2013	Zeil	https://doi.org/10.1007/s00340-012-5275-3	HZDR	DRACO	30	1,0E+21	3,0E+07	0,8	3	17
2016	Wagner	https://doi.org/10.1103/PhysRevLett.116.205002	GSI	PHELIX	500	1,0E+20	5,0E+07	1,05	200	85
2016	Wagner	https://doi.org/10.1103/PhysRevLett.116.205002	GSI	PHELIX	650	1,00E+20	6,50E+07	1,053	180	85
2016	Kim_IJ	https://doi.org/10.1063/1.4958654	CORELS	PW	30	6,1E+20	1,8E+07	0,8	27	93
2018	Higginson	https://doi.org/10.1038/s41467-018-03063-9	RAL-CLF	VULCAN PW	900	3,0E+20	2,7E+08	1,054	210	94
2018	Bin_JH	https://doi.org/10.1103/PhysRevLett.120.074801	RAL-CLF	GEMINI	50	2,0E+20	1,0E+07	0,8	5	30
2019	Polz	https://doi.org/10.1038/s41598-019-52919-7	U. Jena	POLARIS	217	3,50E+19	7,60E+06	1,05	2,5	20

B Exemplary v.ini file for VLPL simulations for set 3 in Sec. 7.6

```
&Domain                          # general information about the simulation domain
  Hx = 0.04                      # grid step size in x-direction
  Hy = 1                         # grid step size in y-direction
  Hz = 1                         # grid step size in z-direction
  Xlength = 400                  # simulation box length size in x-direction
  Ylength = 100                  # simulation box length size in y-direction
  Zlength = 100                  # simulation box length size in z-direction
  Ts = 0.02                      # time step
  Wavelength = 0.8e-4            # default laser wavelength, in this case 800 nm
  Nspecies = 3                   # number of particle species (including electrons)
  Npulses = 1                    # number of laser pulses
  NMovieFrames = 0               # number of fields to save for 2D real-time movie
  NMovieFramesH5 = 8             # number of fields to save in 3D regularly
  MaxwellSolver = 0              # 0 -> Yee; 1 -> NDF; 2 -> q1d
  CollisionIonizationIncluded = 0 # do we have collisional ionization of elements?
  PhotoRecombinationIncluded = 0  # do we have photo recombination?
  ParticlePusher = 0             # default:0 = energy conserving
  SilentTime = 0                 # particles do not respond to fields til this time
  BxExternal = 0                 # external B-field in x-direction, if any
  ByExternal = 0                 # external B-field in y-direction, if any
  BzExternal = 0                 # external B-field in z-direction, if any
/
&MPP_partition                   # controls the parallel partition
  Xpartition = 24                # 3D domain decomposition for parallel computing.
  Ypartition = 8                 # Here, 1536 processors with
  Zpartition = 8                 # 24x8x8 domain partitioning are used
/
&Controls                        # general controls
  Reload = 0                     # non-zero value if restart from a pre-saved point
  Nwrite = 0                     # number of control point
  Ndiagnose = 100                # code writes some info into v<pe>.log —files
  CPUstop = 0                    # code stops after this CPU time (seconds)
  PhaseStop = 1150.1             # code stops after this simulation time
  SavePeriod = 25                # code saves control points
  MovieFlag = 0                  # flag, whether 2D movie files should be produced
  MoviePeriod = 0                # 2D movie frames saved with this period in time
  MovieFlagH5 = 1                # flag, whether 3D movie frames should be saved
  MoviePeriodH5 = 10             # 3D movie frames saved with this period in time
  ShiftFlag = 1                  # flag, whether moving window should be done
  FirstShiftTime = 0             # time for the first shift of the moving window
  LastShiftTime = 1150.1         # no moving window shift after this time
  FieldFilterFlag = 0            # additional control parameter
  FieldFilterPeriod = .1         # additional control parameter
  WakeControlFlag = 0            # additional control parameter
  WakeControlTime = 551          # additional control parameter
  WakeControlPeriod = 551        # additional control parameter
  NullifyFieldsTime = 100e10     # additional control parameter
  NullifyFieldsXmin = 10         # additional control parameter
  NullifyFieldsXmax = 1e20       # additional control parameter
/
&Laser0                          # not used for the presented simulation series
/
&Pulse0                          # describes laser pulse
  a0 = 70                        # dimensionless laser amplitude
  Ypol = 1.0                     # value of y-polarization
  Zpol = 1.0                     # value of z-polarization
  Tprofile = 0                   # index of transverse laser profile
  Lprofile = 0                   # index of longitudinal laser profile
  Length = 12.5                  # pulse length parameter
  Ywidth = 6.7                   # pulse width in y-direction
  Zwidth = 6.7                   # pulse width in z-direction
  RiseTime = 0                   # additional parameter
  DropTime = 0                   # additional control paramter
  Xperiod = 0                    # additional control paramter
  Xcenter = 375                  # position of laser center, from the left boundary
  Ycenter = 0                    # position of laser center, from the optical axis
```

```
  Zcenter = 0                    # position of laser center, from the optical axis
  Yphase = 1.5708                # initial phase of the y-polarization
  Zphase = 0                     # initial phase of the z-polarization
  FromBoundary = XM              # from which boundary the pulse comes
  Kx = 1                         # wave vector x-direction
  Ky = 0                         # wave vector y-direction
  Kz = 0                         # wave vector z-direction
/
&Electrons                       # defines electron distribution
  Distribution = 0               # index of density distribution
  Density = 0                    # electron density measured in critical densities
  Begin = 400                    # parameter where plasma begins
  PlateauBegin = 650             # parameter where constant density of plasma begins
  PlateauEnd = 900               # parameter where constant density of plasma ends
  End = 1150                     # end of plasma
  Radius = 0.3                   # additional parameter
  RadiusX = 0.3                  # additional parameter
  RadiusY = 0.3                  # additional parameter
  RadiusZ = 0.3                  # additional parameter
  Px0 = 0.                       # initial momenta of particles in x-direction
  Py0 = 0.                       # initial momenta of particles in y-direction
  Pz0 = 0.                       # initial momenta of particles in z-direction
  PspreadX = 0e-4                # RMS spread of momentum in x-direction
  PspreadY = 0e-4                # RMS spread of momentum in y-direction
  PspreadZ = 0e-4                # RMS spread of momentum in z-direction
  P_perCell = 2                  # number of particles per cell for each cell
  LimitPerCell = 1e6             # limited number of particles per cell
  x0 = 0                         # additional parameter
  y0 = 0                         # additional parameter
  z0 = 0                         # additional parameter
  Delta = 0.                     # additional parameter
  Xperiod = 0                    # additional parameter
  Ycurvature = 0                 # additional parameter
  CurvatureBegin = 0             # additional parameter
  ScatterFlag = 0                # additional parameter
  InjectFlag = 0                 # additional parameter
  Zombie = 1                     # additional parameter
  Sx = 0                         # PIC particle polarization in x-direction
  Sy = 0                         # PIC particle polarization in y-direction
  Sz = 0                         # PIC particle polarization in x-direction
  RandomSx = 0                   # additional parameter
  RandomSy = 0                   # additional parameter
  RandomSy = 0                   # additional parameter
  RandomSz = 0                   # additional parameter
  mMoment = 1e-3                 # magnetic moment of particle species
  FollowUpPart = 0               # additional parameter
  FollowStride = 100000          # additional parameter
/
&Specie1                         # defines particle species
  Distribution = 0               # index of density distribution
  Density =  0.0122              # density of species measured in critical densities
  Begin = 400                    # parameter where plasma begins
  PlateauBegin = 650             # parameter where constant density of plasma begins
  PlateauEnd = 900               # parameter where constant density of plasma ends
  End = 1150                     # end of plasma
  Radius = 100e10                # additional parameter
  RadiusX = 1e10                 # additional parameter
  RadiusY = 0.95e10              # additional parameter
  RadiusZ = 0.95e10              # additional parameter
  Xperiod = 0                    # additional parameter
  x0 = 0                         # additional parameter
  y0 = 0                         # additional parameter
  z0 = 0                         # additional parameter
  Delta = 0.0                    # additional parameter
  Px0 = 0                        # initial momenta of particles in x-direction
  Py0 = 0                        # initial momenta of particles in y-direction
```

```
  z0 = 0                          # additional parameter
  Delta = 0.0                     # additional parameter
  Px0 = 0                         # initial momenta of particles in x-direction
  Py0 = 0                         # initial momenta of particles in y-direction
  Pz0 = 0.                        # initial momenta of particles in z-direction
  P_perCell = 2                   # number of particles per cell for each cell
  PspreadX = 0                    # RMS spread of momentum in x-direction
  PspreadY = 0                    # RMS spread of momentum in y-direction
  PspreadZ = 0                    # RMS spread of momentum in z-direction
  Beam = 1                        # RMS spread of momentum in x-direction
  Zombie = 0                      # additional parameter
  MassAE = 1                      # particle mass in atomic units
  InjectFlag = 0                  # additional parameter
  AtomType = 1                    # atom number in periodic table
  InitialState = 1                # initial ionization state
  Sx =  0                         # PIC particle polarization in x-direction
  Sy =  1                         # PIC particle polarization in y-direction
  Sz =  0                         # PIC particle polarization in z-direction
  RandomSx = 0                    # additional parameter
  RandomSy = 0                    # additional parameter
  RandomSz = 0                    # additional parameter
  mMoment = 1.793                 # magnetic moment of particle species
  FollowUpPart = 0                # additional parameter
  FollowStride = 100000           # additional parameter
/
&Specie2                          # defines particle species
  Distribution = 0                # index of density distribution
  Density =  0.0122               # density of species measured in critical densities
  Begin = 400                     # parameter where plasma begins
  PlateauBegin = 650              # parameter where constant density of plasma begins
  PlateauEnd = 900                # parameter where constant density of plasma ends
  End = 1150                      # end of plasma
  Radius = 1e10                   # additional parameter
  RadiusX = 1e10                  # additional parameter
  RadiusY = 0.95e10               # additional parameter
  RadiusZ = 0.95e10               # additional parameter
  Xperiod = 0                     # additional parameter
  x0 = 0                          # additional parameter
  y0 = 0                          # additional parameter
  z0 = 0                          # additional parameter
  Delta = 0.0                     # additional parameter
  Px0 = 0.                        # initial momenta of particles in x-direction
  Py0 = 0.                        # initial momenta of particles in y-direction
  Pz0 = 0.                        # initial momenta of particles in z-direction
  P_perCell = 2                   # number of particles per cell for each cell
  PspreadX = 0                    # RMS spread of momentum in x-direction
  PspreadY = 0                    # RMS spread of momentum in y-direction
  PspreadZ = 0                    # RMS spread of momentum in z-direction
  Beam = 1                        # additional parameter
  Zombie = 0                      # additional parameter
  MassAE = 35                     # particle mass in atomic units
  AtomType = 17                   # atom number in periodic table
  InjectFlag = 0                  # additional parameter
  InitialState = 2                # initial ionization state
  Sx = 0                          # PIC particle polarization in x-direction
  Sy = 0                          # PIC particle polarization in y-direction
  Sz = 0                          # PIC particle polarization in z-direction
  RandomSx = 0                    # additional parameter
  RandomSy = 0                    # additional parameter
  RandomSz = 0                    # additional parameter
  mMoment = 0                     # magnetic moment of particle species
  FollowUpPart = 0                # additional parameter
  FollowStride = 100000           # additional parameter
/
```

```
&Synchrotron                    # defines the radiation reaction module
  SynMin = 100000               # minimum gamma-factor of particle
/
&Movie                          # defines fields to be saved for real-time 2D movie
  Frame0 = n0                   # frame in which the parameter is stored
  Frame1 = ex                   # frame in which the parameter is stored
  Frame2 = ey                   # frame in which the parameter is stored
  Frame3 = ez                   # frame in which the parameter is stored
  Frame4 = bx                   # frame in which the parameter is stored
  Frame5 = by                   # frame in which the parameter is stored
  Frame6 = bz                   # frame in which the parameter is stored
/
&MovieHDF5                      # defines fields to be saved in 3D format
  Frame0 = n0                   # frame in which the parameter is stored
  Frame1 = n1                   # frame in which the parameter is stored
  Frame2 = n2                   # frame in which the parameter is stored
  Frame3 = bz                   # frame in which the parameter is stored
  Frame4 = ex                   # frame in which the parameter is stored
  Frame5 = s1x                  # frame in which the parameter is stored
  Frame6 = s1y                  # frame in which the parameter is stored
  Frame7 = s1z                  # frame in which the parameter is stored
/
&Boundary_Xm                    # defines boundary condition at lower x-boundary
  FieldCondition = 1            # field boundary condition (0-periodic, 1-open)
  ParticlesCondition = 1        # particles boundary condition (0-periodic, 1-open)
/
&Boundary_Xp                    # defines boundary condition at upper x-boundary
  FieldCondition = 1            # field boundary condition (0-periodic, 1-open)
  ParticlesCondition = 1        # particles boundary condition (0-periodic, 1-open)
/
&Boundary_Ym                    # defines boundary condition at lower y-boundary
  FieldCondition = 0            # field boundary condition (0-periodic, 1-open)
  ParticlesCondition = 1        # particles boundary condition (0-periodic, 1-open)
/
&Boundary_Yp                    # defines boundary condition at upper y-boundary
  FieldCondition = 0            # field boundary condition (0-periodic, 1-open)
  ParticlesCondition = 1        # particles boundary condition (0-periodic, 1-open)
/
&Boundary_Zm                    # defines boundary condition at lower z-boundary
  FieldCondition = 0            # field boundary condition (0-periodic, 1-open)
  ParticlesCondition = 1        # particles boundary condition (0-periodic, 1-open)
/
&Boundary_Zp                    # defines boundary condition at upper z-boundary
  FieldCondition = 0            # field boundary condition (0-periodic, 1-open)
  ParticlesCondition = 1        # particles boundary condition (0-periodic, 1-open)
/
&Histogramm                     # not used for the presented simulation series
/
```

C Data sheet of the *EKSPLA SL330 series* laser system

PICOSECOND LASERS

PL2210 • PL2230 • PL2250 • PL3140 • SL212 • SL230 • SL330

SL330 SERIES

SBS Compressed Picosecond Nd:YAG Lasers

SL 300 series lasers are an excellent solution for applications that require high energy picosecond pulses.

Pulse compression during backward-stimulated Brillouin scattering (SBS), used in EKSPLA SL300 series lasers, is a simple and cost-efficient way to generate picosecond pulses, with the unique capability of producing pulses with tunable duration.

An electro-optically Q-switched Single Longitudinal Mode (SLM) nanosecond generator is the heart of the system. Instead of external narrow linewidth diode lasers, the selective properties of Fabry-Perrot etalon, and a laser cavity are used to produce SLM pulses with a smooth temporal envelope. In scientific literature this method of generating SLM pulses is known as a selfseeding technique.

Pulse compression is done in a SBS-cell. Depending on the geometry of interaction, a pulse with duration in the 170–1500 ps range can be produced. Pulse duration can be tuned in discrete steps when a variable pulse duration option (-VPx) is installed.

After SBS compression, the pulse is directed to a multi-pass power amplifier system for amplification to up to 500 mJ energy. Temperature controlled harmonics generators, based on angle-tuned KD*P and KDP crystals and harmonic separation optics, are available as standard options. Each wavelength has a separate output port.

A power supply and cooling units are placed in a standard 19" rack that requires little space under an optical table.

The very low jitter of the optical pulse relative to the Q-switch triggering pulse ensures reliable synchronization of the laser with external equipment.

For customer convenience the laser can be controlled from a user-friendly remote control pad or RS232 interface.

The remote pad allows easy control of all laser parameters and features a backlit display that is easy to read even when wearing laser safety eyewear.

Alternatively, the laser can be controlled from a personal computer with supplied software for a Windows™ operating system. LabView™ drivers are supplied as well.

FEATURES

- *Innovative and cost-efficient design*
- *Up to **500 mJ** per pulse at 1064 nm*
- ***150 ps** pulse duration*
- *Self seeding SLM master oscillator*
- *More than 10^5 : 1 pre-pulse contrast ratio*
- *Low jitter external triggering*
- *Versatile synchronization possibilities*
- *Variable pulse duration option*
- *LabVIEW™ drivers for convenient control from PC via RS232 port*
- *Remote control via keypad*
- *Compact laser head and power supply cabinet*

APPLICATIONS

- *Plasma research*
- *Medical*
- *Material ablation and deposition*
- *Holography*
- *Absorption spectroscopy of laser induced plasmas*
- *Satellite ranging*
- *EUV light source development for photolithography*
- *OPCPA pumping*

EKSPLA SAVANORIU AV. 237, LT-02300 VILNIUS, LITHUANIA TEL +370 5 2649629 E-MAIL SALES@EKSPLA.COM WWW.EKSPLA.COM REV. 20181107

PICOSECOND LASERS

SL330 SERIES

SPECIFICATIONS [1]

Model	SL330	SL332	SL333	SL334
Max. pulse energy:				
at 1064 nm	30 mJ	150 mJ	250 mJ	500 mJ
at 532 nm [2]	12 mJ	70 mJ	120 mJ	240 mJ
at 355 nm [3]	7 mJ	40 mJ	80 mJ	140 mJ
at 266 nm [4]	4 mJ	25 mJ	40 mJ	80 mJ
at 213 nm [5]	2 mJ	10 mJ	15 mJ	25 mJ
Pulse energy stability (StdDev) [6]:				
at 1064 nm	6 %	4 %		
at 532 nm	8 %	7 %		
at 355 nm	10 %	9 %		
at 266 nm	13 %	12 %		
at 213 nm	15 %	15 %		
Pulse duration at 1064 nm (FWHM) [7]	150±20 ps			170±20 ps
Pulse duration stability at 1064 nm [8]	10 % (StdDev)			
Repetition rate [9]	10 or 50 Hz	10 Hz		5 Hz
Linewidth	≤0.1 cm^{-1}			
Polarization	linear, >50:1			
Optical pulse jitter [10]	0.5 ns			
Beam profile [11]	Hat Top, >70% fit to Gaussian			
Beam pointing stability at 1064 nm [12]	50 µrad			
Beam divergence [13]	<0.5 mrad			
Beam height	170±5 mm			
Pre-pulse contrast ratio	10^5 : 1			
Beam diameter [14]	~4 mm	~8 mm	~10 mm	~12 mm
PHYSICAL CHARACTERISTICS				
Laser head size (W × L × H)	255 × 790 × 240 mm	305 × 990 × 260 mm		
Electric cabinet size (W × L × H)	550 × 600 × 530 mm	550 × 600 × 850 mm		
Umbilical length	2.5 m			
OPERATING REQUIREMENTS				
Water consumption (max. 20 °C)	< 10 liters/min			
Room temperature	18–27 °C			
Relative humidity	10–80 % (non-condensing)			
Power requirements [15]	208 or 230 V AC, single phase, 50/60 Hz			208 or 380 V AC, three phase, 50/60 Hz
Power consumption [16]	<1.5 kVA	<2.5 kVA	<3.5 kVA	<3.5 kVA

[1] Due to continuous improvement, all specifications are subject to change without notice. Parameters marked typical are not specifications. They are indications of typical performance and will vary with each unit we manufacture. Unless stated otherwise, all specifications are measured at 1064 nm.

[2] For -SH option. Outputs are not simultaneous. Please inquire for pulse energies at other wavelengths.

[3] For -TH option. Outputs are not simultaneous. Please inquire for pulse energies at other wavelengths.

[4] For -FH option. Outputs are not simultaneous. Please inquire for pulse energies at other wavelengths.

[5] For -FiH option. Outputs are not simultaneous. Please inquire for pulse energies at other wavelengths.

[6] Averaged from 300 pulses.

[7] Variable pulse duration options are available with 170–500 ps or 500–1000 ns tuning range.

[8] Measured from 300 shots using 40 Gs/s oscilloscope and photodetector with 50 ps rise time.

[9] Inquire for up to 50 Hz custom pulse repetition rates.

[10] In external triggering mode with two separate triggering pulses for flashlamps and Q-switch. Low jitter sync pulse is available for user equipment triggering.

[11] Improved Gaussian fit profile is available on request.

[12] RMS value measured from 300 shots.

[13] Full angle measured at the $1/e^2$ point at 1064 nm.

[14] Beam diameter is measured at 1064 nm at the $1/e^2$ level.

[15] Three phase 208 or 380 V AC mains are required for 20 or 50 Hz versions.

[16] For 5 or 10 Hz pulse repetition rate.

PICOSECOND LASERS

SL330 SERIES

OPTIONS

▸ Variable pulse duration options -VPx and -VPCx

SL series lasers offer a unique capability for tuning pulse duration. The tuning is done by changing the geometry of interaction in the SBS compressor. Two tuning ranges – 170–500 ps (option -VP1) and 500–1000 ps (option -VP2) – are available as standard options.

While the -VPx option requires manual tuning of optical layout components for pulse duration change, the -VPCx option provides motorized tuning that allows a change in pulse duration from a personal computer or laser control pad.

Note. Certain specifications may change when the laser is configured for variable pulse duration. Contact Ekspla for detailed data sheets.

OUTLINE DRAWINGS

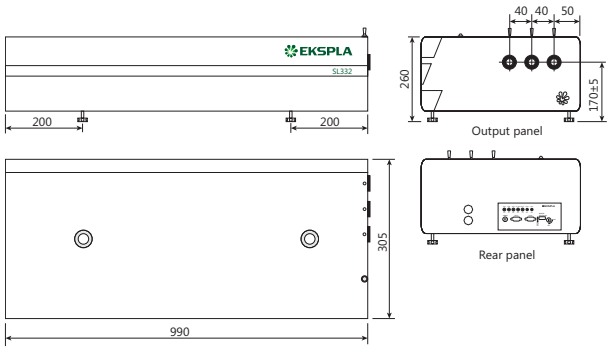

Fig 1. Dimensions of SL332, SL333 and SL334 lasers

APPLICATIONS

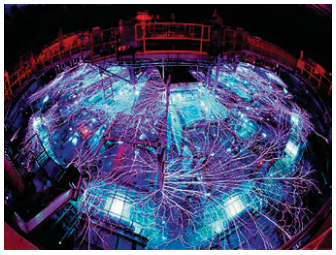

Fig 2. SL330 series laser used as a flash in high speed photography to illuminate wires as they explode
Courtesy of Dr. Randy Montoya, Sandia National Laboratories, USA

EKSPLA SAVANORIU AV. 237, LT-02300 VILNIUS, LITHUANIA TEL +370 5 2649629 E-MAIL SALES@EKSPLA.COM WWW.EKSPLA.COM REV. 20181107

PICOSECOND LASERS

SL330 SERIES

ORDERING INFORMATION

SL332-10-SH-VP1

- Model
- Pulse repetition rate in Hz
- Harmonic generator options:
  - SH → second harmonic
  - TH → third harmonic
  - FH → fourth harmonic
  - FiH → fifth harmonic
- Other options:
  - VP1 → 170–500 ps variable pulse duration, manual control
  - VP2 → 500–1000 ps variable pulse duration, manual control
  - VPC1 → 170–500 ps variable pulse duration, computer control
  - VPC2 → 500–1000 ps variable pulse duration, computer control
  - AW → water-air heat exchanger option. Please inquire Ekspla for more details

D Side and front views of the piezo valve from *Innovative Research Solutions GmbH*

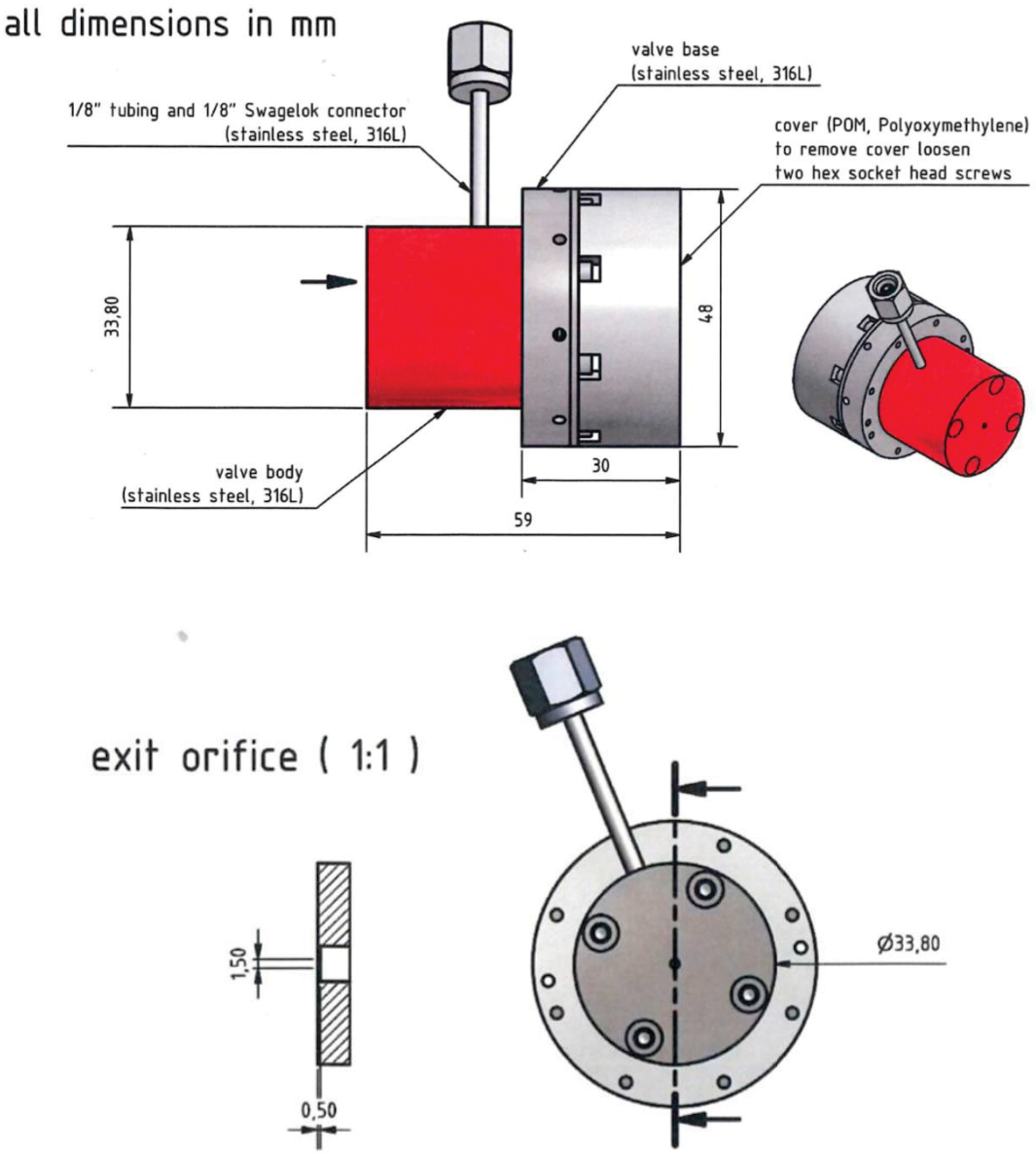

E Possible YAG-pumped dye-laser system for the polarized target, courtesy of *Sirah Lasertechnik GmbH*